

Mechanical Behavior of Tissue Simulants and Soft Tissues Under Extreme Loading Conditions

by
ZEYNEP ILKE KALCIOGLU

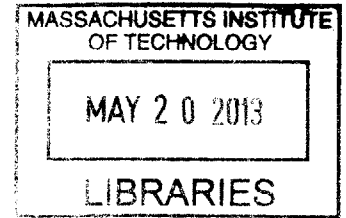
Bachelor of Science, Materials Science and Engineering
Sabanci University, Istanbul, Turkey, 2006

Submitted to the Department of Materials Science and Engineering
In partial fulfillment of the requirements for the degree of
DOCTOR OF PHILOSOPHY IN MATERIALS SCIENCE AND ENGINEERING
at the
MASSACHUSETTS INSTITUTE OF TECHNOLOGY

February 2013

© Massachusetts Institute of Technology, 2013. All rights reserved

ARCHIVES



Author: _____
Department of Materials Science and Engineering
26 September 2012

Certified by: _____
Krystyn J. Van Vliet
Paul M. Cook Career Development
Associate Professor of Materials Science and Engineering and Biological Engineering
Thesis Supervisor

Accepted by: _____
Gerbrand Ceder
Richard P. Simmons Professor of Materials Science and Engineering
Chair, Departmental Committee on Graduate Students

Mechanical Behavior of Tissue Simulants and Soft Tissues Under Extreme Loading Conditions

By
Zeynep Ilke Kalcioğlu

Submitted to the Department of Materials Science and Engineering
on September 28, 2012 in partial fulfillment of the requirements for the
Degree of Doctor of Philosophy in Materials Science and Engineering

Abstract

Recent developments in computer-integrated surgery and in tissue-engineered constructs necessitate advances in experimental and analytical techniques in characterizing properties of mechanically compliant materials such as gels and soft tissues, particularly for small sample volumes. One goal of such developments is to quantitatively predict and mimic tissue deformation due to high rate impact events typical of industrial accidents and ballistic insults. This aim requires advances in mechanical characterization to establish tools and design principles for tissue simulant materials that can recapitulate the mechanical responses of hydrated soft tissues under dynamic contact-loading conditions. Given this motivation, this thesis studies the mechanical properties of compliant synthetic materials developed for tissue scaffold applications and of soft tissues, via modifying an established contact based technique for accurate, small scale characterization under fully hydrated conditions, and addresses some of the challenges in the implementation of this method. Two different engineered material systems composed of physically associating block copolymer gels, and chemically crosslinked networks including a solvent are presented as potential tissue simulants for ballistic applications, and compared directly to soft tissues from murine heart and liver. In addition to conventional quasistatic and dynamic bulk mechanical techniques that study macroscale elastic and viscoelastic properties, new methodologies are developed to study the small scale mechanical response of the aforementioned material systems to concentrated impact loading. The resistance to penetration and the energy dissipative constants are quantified in order to compare the deformation of soft tissues and mechanically optimized simulants, and to identify the underlying mechanisms by which the mechanical response of these tissue simulant candidates are modulated. Finally, given that soft tissues are biphasic in nature, atomic force microscopy enabled load relaxation experiments are utilized to develop approaches to distinguish between poroelastic and viscoelastic regimes, and to study how the anisotropy of the tissue structure affects elastic and transport properties, in order to inform the future design of tissue simulant gels that would mimic soft tissue response.

Thesis Supervisor: Krystyn J. Van Vliet

Title: Paul M. Cook Career Development Associate Professor of Materials Science and Engineering

Acknowledgements

First, I would like to thank my advisor Krystyn J. Van Vliet who guided and supported me throughout my PhD studies, and taught me how to have confidence in myself. I could not be where I am now without all of her help, and for that I am gratefully thankful to her.

I am grateful to be a part of the Van Vliet group and I would like to thank all the former and present group members including Irene, Karen, Adam, John, Ranjani, Anna, Roza, Fei, Patrick and Meng for all the helpful discussions we had as well as for their amazing friendship throughout my PhD studies. I cannot imagine going through this journey without their support, and all the group lunches and activities we had together.

I would like to thank my thesis committee members including Professors Lorna J. Gibson and Darrell J. Irvine for their valuable support, contributions, and helpful discussions related to my research.

I also had a great number of fantastic collaborators throughout my PhD studies. I would like to thank Mark VanLandingham, Kenneth Strawhecker, Randy Mrozek and Joseph Lenhart, for the fruitful discussions and collaborations we had. I am grateful to Jim Smith and Stephen Goodes for all their patience with me and addressing all my questions, and needs about the nanoindenter.

I would also like to gratefully acknowledge G. Constantinides, Y. Hu, S. Peyton, D. Schmidt, F. Cebeci, T. Shazly, A. Robisson, Y. Mei, and Professors Suo, Hammond, Ortiz, Edelman, Anderson, and Griffith for all the collaborative works we have done together that have introduced me to new areas of research that expanded my vision. I would also like to thank Alan Schwartzman, not only for training me to use the facilities in the Nanolab, but also for all his help whenever we had a problem with our nanoindenter. I am thankful to Angelita Mireless, Stephanie Bright, and Elissa Haverty from the head office that helped me through the administrative aspects of doctoral research. I would also like to thank Schlumberger, CMSE, and Institute for Soldier Nanotechnologies for funding my research throughout my studies.

To my dear boyfriend Ruben and dearest friends including Joline, Roza, Burak, Orcun, Nabil, Melis, Sibel, Baris, Xiaoting, and Nihan, I would like to thank for being there for me and making it a lot easier to adapt living in a new country, and for all the good times we had together.

Finally, I am gratefully thankful to my family including my grandparents, and my parents Ferdi and Dilek Kalcioglu. I am thankful to my parents for their unlimited support, love and patience, for all the opportunities they have given to me, all the sacrifices they have made to make me the person I am today, and for making me feel like the luckiest person in the world. To them I dedicate this thesis.

Table of Contents

Abstract	2
Acknowledgements	3
Table of Contents	4
List of Figures	8
List of Tables	16
Chapter 1 Introduction	17
1.1 Motivation	17
1.2 Contact based deformation of compliant synthetic and biological materials via instrumented indentation	19
1.2.1 Current challenges: sample hydration, surface detection and tip sample interaction ..	20
1.2.2 Current interpretation of time dependent properties via indentation	23
1.3 Conventional macroscale methods for testing soft tissues and synthetic gels	24
under high loading rates	24
1.4 Current tissue simulant materials	26
1.5 Thesis organization	27
Chapter 2 Contact Deformation of Hydrated Polymers	30
2.1 Introduction	30
2.2 Implementation of a fluid cell in an instrumented indenter	31
2.2.1 Motivation and Background	31
2.2.2 Materials and Methods	32
2.2.3 Results and Discussion	33
2.2.3.1 Validation on water insensitive materials.	34
2.2.3.2 Application on compliant hydrated materials	35
2.2.4 Conclusions	37
2.3 Electrochemically controlled mechanical properties of a polymer nanocomposite	37
2.3.1 Introduction	37
2.3.2 Experimental Details	38
2.3.2.1 Material synthesis	38
2.3.2.2 Nanoindentation experiments and analysis	39
2.3.3 Results and Discussions	40
2.3.4 Conclusions	41

2.4	Micromechanical characterization of microporous PEG hydrogels for tissue scaffold applications.....	42
2.4.1	Materials and Methods.....	43
2.4.1.1	Poly(ethylene glycol) scaffold fabrication.....	43
2.4.1.2	Mechanical property characterization	43
2.4.2	Results and Discussions	44
2.4.3	Conclusions	46
2.5	High throughput nanomechanical screening of biomaterials for clonal growth of stem cells.....	47
2.5.1	Materials and Methods.....	47
2.5.1.1	Combinatorial array preparation and cell culture.....	47
2.5.1.2	Mechanical characterization	48
2.5.2	Results and Discussion	49
2.6	Conclusions	50
Chapter 3	Styrenic Block Copolymers as Potential Tissue Simulants	51
3.1	Introduction	51
3.2	Multiscale characterization of elastic and viscoelastic properties	52
3.2.1	Motivation and background	52
3.2.2	Materials.....	53
3.2.3	Multiscale characterization of Young’s modulus and energy dissipation	57
3.2.3.1	Methods	57
3.2.3.2	Analysis	59
3.2.3.3	Results.....	62
3.2.4	Multiscale characterization of relaxation modulus and relaxation times.....	66
3.2.4.1	Methods	66
3.2.4.2	Analysis	67
3.2.4.3	Results.....	68
3.2.4.4	Discussion	73
3.2.4.5	Summary	75
3.2.5	Conclusion.....	75
3.3	Quantification of impact resistance and energy dissipation via high rate impact indentation.....	76
3.3.1	Introduction	76
3.3.2	Experimental methods and analysis.....	78
3.3.2.1	Materials and tissues.....	78

3.3.2.2	High rate impact indentation experiments	78
3.3.2.3	Analysis of energy dissipation from indentation impact experiments	79
3.3.3	Results and Discussions	83
3.3.3.1	Impact resistance under dynamic impact loading	84
3.3.3.2	Energy dissipation under dynamic impact loading	87
3.3.4	Conclusions	91
3.4	Conclusions	92
Chapter 4	Crosslinked Networks as Potential Tissue Simulants for Ballistic Applications	93
4.1	Introduction	93
4.2	Materials	95
4.3	Comparison of gel and tissue rheology at low strains and rates	96
4.3.1	Experimental Methods	96
4.3.2	Results and Discussion	97
4.3.2.1	Effect of solvent vol% on the magnitude and rate dependence of G' , G'' , and $\tan \delta$	97
4.3.2.2	Effect of precursor chain stoichiometry on magnitude and rate dependence of G' , G'' and $\tan \delta$ for low and high molecular weight solvent	100
4.3.2.3	Effect of solvent molecular weight on the magnitude and rate dependence of G' , G'' , and $\tan \delta$	104
4.4	Impact indentation experiments	106
4.4.1	Experimental Methods	107
4.4.2	Results and Discussion	108
4.4.2.1	Effect of solvent loading vol% on impact resistance, energy dissipation capacity, and energy dissipation rate	108
4.4.2.2	Effect of precursor chain stoichiometry on impact resistance, energy dissipation capacity, and energy dissipation rate	110
4.4.2.3	Effect of solvent molecular weight on impact resistance, energy dissipation capacity, and energy dissipation rate	113
4.4.2.4	Comparison of impact response among gels and soft tissues	114
4.5	Concluding Remarks	118
Chapter 5	Elastic and Transport Properties of Hydrogels and Soft Tissues via Contact Mechanics	120
5.1	Introduction	120
5.2	Multiscale elastic and transport properties of polyacrylamide gels	121
5.2.1	Background and Motivation	121
5.2.2	Materials and Methods	122

5.2.2.1	Material synthesis	122
5.2.2.2	Macroscale load relaxation experiments.....	123
5.2.2.3	AFM enabled load relaxation testing.....	123
5.2.2.4	Analysis	124
5.2.3	Results	126
5.2.4	Discussion	129
5.2.5	Conclusions	135
5.3	Multiscale elastic and transport properties of soft tissues	135
5.3.1	Introduction	135
5.3.2	Experimental Details.....	137
5.3.3	Results and Discussion	138
5.3.3.1	Elastic and transport properties of heart	138
5.3.3.2	Elastic and Transport properties of liver.....	144
5.3.4	Conclusions	149
5.4	Conclusions	150
Chapter 6	Conclusions and Directions for Future Studies	151
6.1	Thesis Summary	151
6.2	Suggestions for future research	154
6.2.1	Computational modeling of gel response to high-rate deformation	154
6.2.2	Engineered protein based hydrogels as soft tissue simulants.....	154
6.2.3	Poroviscoelastic analysis of soft tissues	155
References	157
Appendix A	169
Appendix B	171
B.1	Polydimethylsiloxane (PDMS) gels.....	171
B.1.1	Experimental methods	171
B.2	Tissues from rat heart.....	174
Appendix C	176

List of Figures

Figure 1.1 (a) Robot assisted heart surgery, image from Ref. 4 (b) Torso cast using a tissue simulant gel, courtesy of U.S. Army Research Laboratory (c) Ballistic gelatin provides a comparison of penetration tests, image from Ref. 5.

Figure 1.2 Force displacement response of a synthetic polymeric gel via atomic force microscopy enabled indentation in air reveals large adhesion forces between the surfaces of the cylindrical flat punch probe (radius~900 nm) and the sample.

Figure 2.1 Schematic diagram (a) and photograph (b) of instrumented indenter apparatus capable of extended nanomechanical experiments in fully immersed environments on hydrated gels and tissues.

Figure 2.2 As expected, response of borosilicate glass under indentation with a sharp Berkovich diamond probe is statistically identical whether acquired in ambient air (●) or fully submerged in water (○); data intentionally offset at $P=0$ by 50 nm for clarity. Experimental details: Berkovich probe, $n=5$ for each testing condition, $P_{\max}=100$ mN, $t_{\text{load}}=t_{\text{unload}}=10$ s, $t_{\text{dwell}}=5$ s.

Figure 2.3 (a) Response of polyacrylamide gel to spherical indentation in air (blue) and water (green); inset shows repeatability of five replicate experiments in water. (b) Elastic moduli of PAAm gels as a function of mol%-bis measured by instrumented indentation are within the range reported by calibrated AFM-enabled indentation and rheological experiments. The former approach is amenable to rapidly mapping variations in this stiffness over surface areas $>\text{mm}^2$ or as a function of depth >1 μm , and with fewer experimental artifacts as discussed in the text. Error bars represent one standard deviation from mean. (c) Contact creep response of PAAm hydrogels demonstrates increased creep resistance for increased mol%-crosslinker, as expected.

Figure 2.4 Instrumented nanoindentation results for an $(\text{LPEI/PB})_{50}$ film immersed in aqueous 0.1 M KHPH. (a) Loading portion of the load-depth response for a film in the oxidized (black, +0.6 V) and reduced (blue, -0.2 V) state. (b) Corrected effective elastic moduli of the film subjected to two redox cycles. O.C.P. stands for open circuit potential. The error bars represent the standard deviation from $n=6$ measurements at different locations on the film.

Figure 2.5 The elastic modulus for fully hydrated porous gels with pore sizes of 7, 12, or 17 μm follows the predictive model (dashed black) described by Gibson and Ashby¹¹⁵ based on the elastic modulus of the solid, represented by nonporous gels (E_s , solid black). Errors are S.E.M. for 3 separate samples with 9 locations per sample.

Figure 2.6 Colony formation frequency versus polymer indentation elastic modulus in the hydrated state; the inset is in semi-log format to indicate the behavior at low modulus values. Data are sorted into groups of 20–25 spots as a function of increasing modulus. Abscissa error

bars represent the standard error of the modulus for a given group of 20–25 spots, and ordinate error bars represent the standard error of the mean of the colony-formation frequency of three replicates for a given group.

Figure 3.1 (a) Schematic illustrating length scales of liver tissue structural heterogeneity (adapted from Ref. 138), load is applied normal to the outer liver capsule for the experiments outlined in this chapter; (b) schematic illustrating length scales of heart wall structural heterogeneity (adapted from Ref. 139), load is applied normal to the outer fibrous layer; (c) 100/0 and 75/25 triblock/diblock styrenic copolymer discs of diameter ~ 2 cm; Atomic force microscopy (AFM) phase-lag image of (d) rat liver capsule, (e) fibrous layer of rat heart, (f) 75/25 triblock/diblock styrenic copolymer gel indicating segregated domains of triblocks and diblock-triblocks.

Figure 3.2 Styrenic block copolymers comprise AB diblocks of styrene-ethylene propylene (SEP), and ABA triblocks of styrene-ethylene butylene (SEBS). As the vol%-triblock increases, crosslinking density of the gel will increase, since in ABA (SEBS) triblocks, B blocks can form bridges between different micellar cores containing the A blocks (adapted from Ref. 147.)

Figure 3.3 (a) Load-displacement response for 100/0 triblock/diblock gel shows attraction toward and initiation of mechanical contact. Note that, prior to actual contact with the surface, electromagnetic coil current is expressed in units of load on the pendulum, to enable visual identification of contact. Point B is considered the initiation of mechanical contact, and W_p and W_e denote the dissipated and recovered work of this indentation, respectively. Adhesion of the probe to this sample persists from position δ_o to δ_{po} until the pull-off force F_{po} is attained. (b) On more compliant materials such as cardiac tissue, sharp transitions are not observed. Analysis of the pre-contact response (see text) shows that contact occurs at point B. Point A denotes the point at which the instrument software misidentified the contact initiation, based on a threshold increase in load or instantaneous contact stiffness dP/dh .

Figure 3.4 (a) Representative stress vs. strain responses from unconfined compression and (b) load vs. displacement responses from quasistatic indentation tests for triblock/diblock gels compared to heart and liver. Insets show only the gel response.

Figure 3.5 Comparison of Young's moduli (mean \pm standard error) inferred from unconfined compression (points) and $E_{O\&P}$ for tissues and E_{JKR} for tissue surrogate gels inferred from instrumented indentation (bars). Inset magnifies data for Young's moduli of heart and liver inferred from unconfined compression. (b) Energy dissipation calculated from indentation $P-h$ responses (mean \pm standard error) shows that tissues exhibit a lower energy dissipation capacity than the gels at quasistatic rates.

Figure 3.6 (a) Macroscale relaxation modulus of tissue surrogate gels and heart tissue. (b) Calculated τ and β by fitting stress vs. time response via Equation 3.5.

Figure 3.7 (a) Mesoscale relaxation modulus of triblock/diblock gels as a function of vol%-triblock. (b) Calculated τ and β as a function of vol%-triblock by fitting load vs. time response via Equation 3.5. Data represented as mean \pm standard error.

Figure 3.8 (a) Representative load vs. depth responses of 100/0 triblock/diblock gel as a function of immersion environment. Inset: optical microscope image of the gel adhering to the probe during AFM experiments in air. (b) Young's elastic modulus of 100/0 triblock/diblock gel as a function of immersion environment. Data represented as mean \pm standard error.

Figure 3.9 Representative load vs. time responses of the 100/0 triblock gel in air, in water, and in PBS+0.2% Pluronic® F108.

Figure 3.10 (a) Microscale relaxation modulus of 100/0 triblock/diblock gel as a function of immersion environment. (b) Calculated τ and β in different immersion environments.

Figure 3.11 Representative impact response and definition of terms used to quantify energy dissipation. (a) Pendulum displacement over time is described by damped harmonic oscillatory motion, here for a 100/0 triblock/diblock gel at an impact velocity of 5.8 mm/s. Quality factor Q is calculated via Equation (3.8), and can be recognized visually as the number of indentation impact cycles n required for the amplitude of oscillation h_o to fall by a factor of e . Here, $n \sim 2$ so $Q \sim 6$. (b) Velocity is calculated as the time derivative of displacement. Impact velocity v_{in} is the maximum velocity prior to contact, which defines the sample contact point x_{o1} . To objectively identify the position of the deformed surface, x_r is taken to be equivalent to the displacement x_{o2} which would be required to initiate contact with the sample in the next cycle. Thus x_r is the position of the relaxed surface following the initial impact. Rebound velocity v_{out} is defined as the velocity at displacement x_r . Penetration depth over the first impact cycle is defined as $x_{max} - x_{o1}$.

Figure 3.12 (a) Free oscillations of the pendulum-linear elastic wire spring system show that the damping due to the pendulum is small but not negligible. Pendulum damping constant b_p is calculated via Equation (3.13), ω_o and γ_m are extracted by fitting Equation (3.7) to the $h(t)$ response. (b) Differences in pendulum velocity for oscillations in air or immersed in fluid do not differ significantly, showing that immersion in aqueous environments contributes negligible additional damping.

Figure 3.13 Impact loading was conducted using a customized, pendulum-based nanoindenter. Raw displacement vs. time response for all materials at a maximum velocity of 7 mm/s corresponding to impact energy of 4 μ J shows a significant difference between the penetration depths and energy dissipation rates among all samples.

Figure 3.14 Maximum penetration depths varied as a function of (a) impact velocity; and (b) strain energy density. Liver tissue exhibited the lowest penetration resistance among all samples whereas 50/50 triblock/diblock gel exhibited the closest penetration resistance to heart tissue. (c) Force-displacement responses calculated from the $h(t)$ response of the first impact peak for an impact energy of $\sim 4 \mu$ J show significant hysteresis for all samples. As observed in (a) and (b), liver tissue exhibited the lowest penetration resistance.

Figure 3.15 (a) Velocity ratio v_{out}/v_{in} and (b) quality factor Q for the impact energies studied here provide means to compare the energy dissipation capacity and energy dissipation rate of each

sample, averaged over the range of impact velocities considered. Comparison of v_{out}/v_{in} shows that Perma-GelTM and 100/0 triblock/diblock gel exhibit the lowest energy dissipation capacity, whereas energy dissipation capacity of 50/50 triblock/diblock gel is similar to that of liver and heart tissues. Comparison of Q shows that both Perma-GelTM and 100/0 triblock/diblock gel dissipate the total energy more slowly, as compared to 50/50 triblock/diblock gel and tissues. Data indicated as mean \pm standard error.

Figure 3.16 Energy dissipation parameter K as a function of impact velocity provides a quantitative comparison among samples. While the tissues and 50/50 triblock/diblock gel dissipate nearly all of the imposed impact energy, Perma-GelTM and 100/0 triblock/diblock gel dissipate only 40-50% of the total energy at these impact velocities.

Figure 4.1 Chemical structures of the model system network components, adapted from Ref. 80.

Figure 4.2 Effect of 1.1 kg/mol solvent loading on (a) Storage modulus G' with silane:vinyl stoichiometry of 4:1, compared to heart and liver, as a function of frequency, (b) Log-log plot of G' versus polymer content for PDMS gels containing 1.1 kg/mol solvent, (c) Loss modulus G'' and (d) Loss tangent $\tan \delta$ of the gels at different loading values of 1.1 kg/mol solvent, with silane:vinyl stoichiometry of 4:1, compared to heart and liver, as a function of frequency.

Figure 4.3 (a, b) Storage modulus G' , (c) loss modulus G'' , and (d) loss tangent $\tan \delta$ of heart and liver tissue exhibit frequency dependence.

Figure 4.4 Effect of crosslinking density on (a) Storage modulus G' , (b) Loss modulus G'' , and (c) Loss tangent $\tan \delta$ of heart and liver tissues, and of PDMS gels containing 60 vol% of 1.1 kg/mol solvent.

Figure 4.5 Effect of crosslinking density on (a) Storage modulus G' , (b) Loss modulus G'' , and (c) Loss tangent $\tan \delta$ of heart and liver tissues, and of PDMS gels containing 60 vol% of 308 kg/mol solvent.

Figure 4.6 Frequency dependence of (a) Storage modulus G' , (b) Loss modulus G'' , and (c) Loss tangent $\tan \delta$ of gels with 4:1 silane:vinyl stoichiometry, containing 80 vol% of solvent with molecular weight of 1.1, 139, or 308 kg/mol.

Figure 4.7 Indenter displacement vs. time response from dynamic impact indentation of soft biological tissues and PDMS gels with 2:1 stoichiometry and 50% solvent loading differing only in solvent molecular weight. From these raw data, one can visually compare the maximum penetration depths (measure of impact resistance) and the number of impact cycles (related to energy dissipation rate).

Figure 4.8 Effect of solvent loading vol% for PDMS gels with silane:vinyl stoichiometric ratio of 4:1 and solvent molecular weight of 1.1 kg/mol (a) Maximum penetration depth x_{max} as a function of impact velocity: as the solvent loading % increases, the gels become less impact resistant; this effect is more pronounced at higher impact velocities. (b) Energy dissipation capacity K as a function of impact velocity: K increases as solvent loading % increases; this

effect is more pronounced at higher impact velocities. (c) Quality factor Q as a function of impact velocity: increasing the solvent loading% decreases Q (i.e., increases the energy dissipation rate). Data are represented as mean \pm standard error, and standard error bars may appear smaller than the symbols.

Figure 4.9 Effect of stoichiometric ratio of vinyl to crosslinking silane groups for PDMS gels with 60 vol% 1.1 kg/mol molecular weight solvent (a) Maximum penetration depths as a function of impact velocity: impact resistance of gels increases (lower x_{\max}) by increasing the crosslink density; this effect is more pronounced at higher impact velocities. Impact resistance of heart and liver tissues is matched by the PDMS gels. (b) Energy dissipation capacity K as a function of impact velocity: gels dissipate more energy at lower crosslinking densities. Energy dissipation capacity of the tissues is matched by the gels with lower crosslinking. (c) Quality factor Q as a function of impact velocity: gels dissipate energy more quickly (lower Q) as the crosslinking density decreases. Both heart and liver show comparable energy dissipation rates to the gels with lower crosslinking density. Data are represented as mean \pm standard error, and error bars may appear smaller than data symbols.

Figure 4.10 Effect of solvent molecular weight on impact response of PDMS gels with a 4:1 precursor chain stoichiometry and 80 vol% solvent loading: (a) Maximum penetration depths as a function of impact velocity: gels become more impact resistant as the molecular weight (MW) of the solvent increases; this effect is more pronounced at higher impact velocities. (b) Energy dissipation capacity K as a function of solvent MW: gels of larger solvent MW are more dissipative at a given impact velocity. (c) Quality factor Q as a function of impact velocity: increasing solvent MW increases the energy dissipation rate (lower Q), to the extent that for gels with MW > 1.1 kg/mol, energy was dissipated during the first impact cycle leading to Q values below the dashed line. Data are represented as mean \pm standard error.

Figure 4.11 (a) By changing the solvent loading vol% and silane:vinyl stoichiometry, we compare two different gels that both mimic the impact resistance of heart tissue for the impact velocities explored herein. (b) These two gel systems exhibit distinct energy dissipation capacities K (b) and quality factor Q (c). For the impact velocities considered, the gel with 60 vol% solvent of 1.1 kg/mol MW and silane:vinyl stoichiometry of 2.75:1 most closely mimics heart tissue by all three metrics of mechanical impact response.

Figure 4.12 (a) The two top candidates for matching liver tissue impact resistance are the PDMS gels with 60 vol% solvent/silane:vinyl stoichiometry of 2:1, and 80 vol% solvent/silane:vinyl stoichiometry of 4:1, both with solvent MW of 1.1 kg/mol. The two top candidates for matching energy dissipation capacity K (b) and quality factor Q (c) of liver tissue are the PDMS gels with 60 vol% solvent/silane:vinyl stoichiometry of 2.25:1, and 60 vol% solvent/silane:vinyl stoichiometry of 2.5:1, both with solvent MW of 1.1 kg/mol.

Figure 4.13 Effect of solvent loading vol%, silane:vinyl stoichiometric ratio (i.e. crosslinking density), and solvent molecular weight (MW) on maximum penetration depths x_{\max} , energy dissipation capacities K , and energy dissipation rates Q .

Figure 5.1 (a) Apparatus for load relaxation experiments at the macroscale, using a stainless steel spherical probe of radius 1 cm. Scale marker at left is in mm. (b) Schematic of load relaxation experiment conducted at the microscale, using a polystyrene spherical probe of radius 22.5 μm attached to the cantilever of an atomic force microscope. All experiments were conducted on fully hydrated polyacrylamide gels immersed in buffered saline solution.

Figure 5.2 (a) Load vs. time response for macroscale experiments ($R = 1$ cm) at three different maximum indentation depths (100, 200, and 400 μm), where relaxation times are on the order of 10s of hours. (b) Load vs. time response for microscale experiments ($R = 22.5$ μm) at three different maximum indentation depths (4, 6, and 8 μm), where relaxation times are on the order of a few seconds. Data are shown as mean \pm standard deviation among replicate experiments. Due to the high data density (see text), error bars are not displayed for all data points.

Figure 5.3 Macroscale and microscale load relaxation responses for polyacrylamide gels, for which load is normalized in the form $[F(t)-F(\infty)]/[F_o - F(\infty)]$. Data are shown as mean \pm standard deviation. Due to the high data density (see text), error bars are not displayed for all data points. These data do not fully collapse onto a single curve when time is not also normalized, at either the macroscale (a) or microscale (b), as would be expected for a linear viscoelastic response. These data collapse more completely onto a single curve when time is normalized by a^2 , as would be expected for a poroelastic response. Comparison of this collapse is shown in (c) and (f), as the standard deviation among the replicate curves for all maximum depths. Standard deviation is noticeably smaller when time is normalized, confirming dominance of the poroelastic regime at the macro- and microscales.

Figure 5.4 Load relaxation responses for polyacrylamide gels at six different indentation depths - spanning two orders of magnitude- for which load is normalized in the form $[F(t)-F(\infty)]/[F_o - F(\infty)]$. Data are shown as mean \pm standard deviation. Due to the high data density, error bars are not displayed for all data points. These data collapse onto a single curve when time is normalized by a^2 as is expected for a poroelastic response.

Figure 5.5 Macroscale (a) and microscale (d) load relaxation data where force is normalized by ah , but time is not normalized. Macroscale (b) and microscale (e) load relaxation response when force is normalized by ah and time is normalized by a^2 . Standard deviation among replicate curves for all indentation depths vs. time in macroscale (c) and microscale (f) tests when time is normalized vs. when time is not normalized. Data is shown as mean \pm standard deviation. Due to the high data density (see text), error bars are not displayed for all data points.

Figure 5.6 Macroscale (a) and microscale (d) load relaxation data where time is not normalized. Macroscale (b) and microscale (e) load relaxation response where time is normalized by a^2 . Force is normalized by F_o in all cases. Standard deviation among replicate curves for all indentation depths vs. time in macroscale (c) and microscale (f) experiments when time is normalized vs. when it is not normalized. Data is shown as mean \pm standard deviation. Due to the high data density (see text), error bars are not displayed for all data points.

Figure 5.7 (a) Heart tissue exhibits a layered heterogeneous structure (adapted from Ref. 139). (b) Load vs. time response of pericardium (load applied in direction A) at three different

maximum indentation depths (4.5, 7.5, and 9.5 μm), where relaxation times are on the order of a few seconds. (c) Load vs. time response of myocardium in circumferential direction (load applied in direction B) at three different maximum indentation depths (4.5, 6.5, and 8.5 μm) (d) Load vs. time response of myocardium in longitudinal direction (load applied in direction C) at three different maximum indentation depths (4.5, 7.5, and 9.5 μm). Probe radius is $R = 22.5 \mu\text{m}$, data are shown as mean \pm standard deviation among replicate experiments. Due to the high data density, error bars are not displayed for all data points.

Figure 5.8 Load relaxation data in direction A (a), direction B (d), and direction C (g) where time is not normalized. Load relaxation response in direction A (b), direction B (e), and direction C (h) where time is normalized by a^2 . Force is normalized by $[F(t)-F(\infty)]/[F_0 - F(\infty)]$ in all cases. Standard deviation among replicate curves for all indentation depths vs. time responses in direction A (c), direction B (f), and direction C (i) when time is normalized vs. when it is not normalized. Data is shown as mean \pm standard deviation. Due to the high data density, error bars are not displayed for all data points.

Figure 5.9 Shear modulus G (a), Diffusivity D (b), and Poisson's ratio ν (c), as a function of strain for three different directions (direction A: pericardium, direction B: myocardium circumferential, direction C: myocardium longitudinal) as shown in Figure 5.7a. Data are reported as mean \pm standard deviation.

Figure 5.10 (a) *top*: AFM-enabled load relaxation experiments are conducted with the Glisson's capsule attached (adapted from Ref. 138), *bottom*: Load vs. time response of liver capsule and parenchyma at three different maximum indentation depths (6.5, 9, and 11 μm) (b) *top*: AFM-enabled load relaxation experiments are conducted with the Glisson's capsule removed, *bottom*: Load vs. time response of liver parenchyma at three different maximum indentation depths (9, 12, and 14 μm). Probe radius is $R = 22.5 \mu\text{m}$, data are shown as mean \pm standard deviation among replicate experiments. Due to the high data density, error bars are not displayed for all data points.

Figure 5.11 Load relaxation data with capsule attached (a), and with capsule removed (d) where time is not normalized. Load relaxation response with capsule attached (b), and with capsule removed (e) where time is normalized by a^2 . Force is normalized by $[F(t)-F(\infty)]/[F_0 - F(\infty)]$ in all cases. Standard deviation among replicate curves for all indentation depths vs. time responses with capsule attached (c), and with capsule removed (f) when time is normalized vs. when it is not normalized. Data is shown as mean \pm standard deviation. Due to the high data density, error bars are not displayed for all data points.

Figure 6.1 Quantitative analysis of maximum penetration depths as a function of impact velocity for protein-based hydrogels in comparison to soft tissue response, inset shows an image of the gel (courtesy of Matthew Glassman from Olsen Lab, MIT ChemE). (b) Quality factor Q related to energy dissipation rate of the gels and soft tissues as a function of impact velocity.

Figure A.1 Comparison between the experimental data and the model fit shows excellent agreement.

Figure B.1 Representative load vs. displacement response from load relaxation experiments on PDMS gels immersed in PBS and PBS containing 3% Pluronic® F108 shows that adhesive forces between the probe and the sample surface are minimized when the gels are immersed in the solution containing pluronic.

Figure B.2 (a) Normalized force vs. time responses, and (b) calculated relaxation time τ values at different immersion environments. Data are represented as mean \pm standard deviation.

Figure B.3 (a) Load vs. displacement response of heart tissue in direction A; immersed in Krebs-Henseleit buffer vs. Krebs-Henseleit buffer+ 0.5 Pluronic®F108. (b) Adhesion force F_{po} as a function of time in the presence and lack of Pluronic®F108. Note that the values in the time axis are arbitrary, i.e. they do not represent the real time intervals, and the total time of the experiment is 3 hours (i.e. at $t=20$, real time is 3 h).

List of Tables

Table 2.1 Elastic moduli (E_s) extracted from indentations in ambient air and fully immersed in water, for borosilicate glass. These moduli are independent of the extent of hydration, as expected, and in good agreement with the range of elastic moduli widely reported by others (E_{lit}). Data are mean \pm one standard deviation.

Table 5.1 Shear modulus G , Poisson's ratio ν_s , diffusivity D , permeability κ and characteristic relaxation time τ as a function of indentation depth for two probes of radii R_1 and R_2 . Data are presented as mean \pm standard deviation.

Table 5.2 Shear modulus G , Poisson's ratio ν_s , diffusivity D , permeability κ as a function of indentation depth at three different directions. Data are presented as mean \pm standard deviation.

Table 5.3 Shear modulus G , Poisson's ratio ν_s , diffusivity D , permeability κ as a function of indentation depth with liver capsule attached and removed. Data are presented as mean \pm standard deviation.

Table B.1 Young's Elastic Modulus of PDMS as a function of the immersion environment. Data are represented as mean \pm standard deviation.

Chapter 1 Introduction

1.1 Motivation

Measurement of the mechanical properties of “soft tissues” is a central subject of biomechanics. Here, the term “soft tissues” implies the organized biopolymeric extracellular matrices filled with extracellular fluids and cells that carry out specific functions of anatomical organs, as distinct from the highly mineralized “hard tissues” such as cortical bone. We note at the outset that the term “soft” is a misnomer in terms of the actual mechanical response of such tissues, which are actually mechanically compliant and remarkably resistant to permanent deformation; we adopt this term only because it is used commonly in the medical and biomechanics communities. Although this subject of soft tissue mechanics has been investigated at the macroscale for many years, multi-scale measurement of the mechanical properties of soft tissues from organs such as heart and liver has attracted increasing interest due to an increase in the demand for tissue-engineered constructs and recent developments in computer-integrated and robot-aided surgery (Figure 1.1a) that require accurate computational models of tissue deformation under mechanical load. Mechanical response of soft tissues is due directly to their structural heterogeneity and anisotropy, and chemical interfaces between these structures: such tissues are hydrated composites of nanoscale molecular networks, microscale cells and protein matrices, and macroscale multi celled channels. Given this complex structure, contact-based indentation approaches have emerged as powerful means to quantify nano- and microscale mechanical properties in tissues and other biomaterials. However, continuing advancements in testing methods and indentation data analysis are necessary to increase this method’s utility in the accurate characterization of biomaterials. Given this motivation, this thesis will develop experimental and analytical avenues to evaluate the mechanical properties and responses of fully hydrated biomaterials addressing some of the current challenges.

Additionally, there is a growing need to quantify mechanical behavior of soft tissues under more dynamic loading conditions, to predict deformation and damage due to loading at high rates, including “impact events” such as vehicle collisions or ballistic and blast assaults that result in

penetrating wounds or blunt trauma. Recent fabrication of so called “tissue simulant” synthetic polymer gels (Figure 1.1b, c) has been leveraged to better understand how impact forces are transmitted through soft tissue in order to provide insight into damage as the result of an insult, and to design more effective protective systems¹. These materials mimic the mechanical response of soft tissue to an extent, and are often utilized in gathering pressure and velocity data during impact². These data are further utilized to validate finite element models in order to describe soft tissue response³. However, there are currently no synthetic materials that can replicate the dynamic mechanical deformation of tissues from critical organs – such as the heart and liver– with high fidelity, due chiefly to challenges in robust gel design and in multiscale mechanical characterization of both gels and tissues. A closer pairing of the mechanical properties of a well-defined synthetic material to biological tissue can improve the data collected from such engineered tissue simulants, ultimately helping to understand damage evolution and deformation to design protective materials accordingly, and to develop constitutive models of impact responses of tissues through computational studies. Thus, this thesis will study the structure-mechanical property relationship of physically associating block copolymer and crosslinked silicone network systems as potential tissue simulant gel systems in comparison to soft tissues from heart and liver. To achieve this quantitative comparison and correlation, we will demonstrate new methodologies to evaluate the local mechanical response and properties to penetrating mechanical impact loading. The goal of this study is to inform the design principles required for synthetic polymer gels that are optimized to predict the response of specific biological tissues to impact loading.

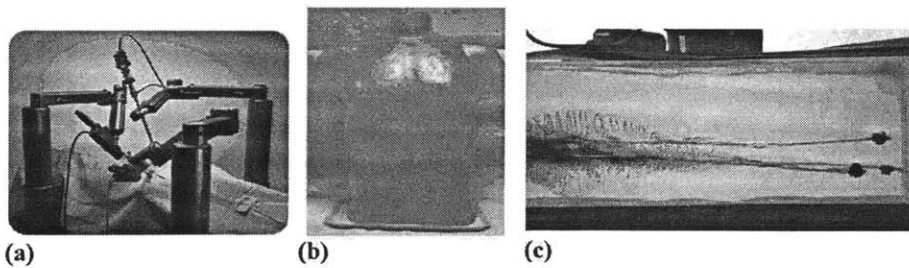


Figure 1.1 (a) Robot assisted heart surgery, image from Ref. 4 (b) Torso cast using a tissue simulant gel, courtesy of U.S. Army Research Laboratory (c) Ballistic gelatin provides a comparison of penetration tests, image from Ref. 5.

This introduction lays the foundation for the current state of contact based deformation of synthetic and biological materials via instrumented indentation (Section 1.2); detailing some of

the current challenges such as sample hydration, sample probe interactions, and surface detection (Section 1.2.1), and discussing some of the current analysis to time dependent mechanical properties (Section 1.2.2); conventional macroscale methods for testing soft tissues and synthetic materials under high rates (Section 1.3); current tissue simulant materials (Section 1.4), and thesis organization (Section 1.5).

1.2 Contact based deformation of compliant synthetic and biological materials via instrumented indentation

Understanding of the structure-mechanical property relationship in biological materials is critical for informing the design of tissue engineered constructs, and for advancing technologies for computer aided, robot integrated surgical planning systems. For many years, measurement methods for bulk materials such as unconfined compression⁶⁻⁷, uniaxial tension⁸⁻¹⁰, and aspiration¹¹ have been utilized to characterize the macroscale mechanical properties of synthetic polymeric materials and/or soft tissues. However, most biological systems such as soft tissues exhibit mechanical properties that are strongly dependent on length scales (e.g., impactor geometry and penetration depth, tissue striation layer thickness, mesh pore diameter, organ dimensions), and time scales (e.g., strain rate, velocity, polymer relaxation times, solvent diffusivity), due in part to hierarchical structure of biological polymers from the nanoscale and microscale that requires < micrometer level characterization. Given the small dimensions of the contact probe and resolution of depth, force, and time, instrumented indentation has recently emerged as a powerful tool for measuring mechanical properties of polymeric systems such as hydrogels¹²⁻¹³ and soft tissues such as liver¹⁴⁻¹⁷. This instrumentation and analysis were developed originally to characterize the elastic and plastic properties of metals and ceramics, and thus modifications of hardware, experimental methods, and analytical frameworks are required to extend such approaches to biological tissues and simulants thereof. Although most of the work mentioned above is focused on studying a composite response of the material system, indentation can also be used to measure local material properties in small samples and in structurally heterogeneous samples; this spatial resolution of mechanical response enables the testing of materials that are unsuitable for traditional mechanical testing techniques, including tissue samples from small-animal models.

When the loads or the depths of indentation are less than 100 nN or 100 nm, respectively, instrumented indentation is sometimes referred to as nanoindentation; the high mechanical compliance of soft tissues is such that typical indentation depths exceed this threshold, so hereafter we refer to the general acquisition and control of contact load, penetration depth, and time as simply instrumented indentation. As expected, adaptation of instrumented indentation for testing of compliant synthetic and biological materials creates several experimental challenges, and requires the development of analysis methods that could study mechanical responses of these complex systems, ranging from nonlinear elastic responses to strongly viscoelastic responses to strongly poroelastic responses. Section 1.2.1 introduces some of the current experimental challenges, and Section 1.2.2 discusses some of the current analysis methods utilized for characterizing mechanical properties of these materials.

1.2.1 Current challenges: sample hydration, surface detection and tip sample interaction

Most biological tissues are hydrated in their native state; some soft tissues exhibit water content up to 80 wt%¹⁸. Synthetic materials such as hydrogels used in tissue scaffold applications are also composed mainly of electrolyte (i.e., water and dissolved metal ions such as Na⁺ and Cl⁻). Hence, the ability to maintain sample hydration both during the preparation and testing of the sample is crucial for accurate characterization of mechanical properties¹⁹⁻²¹; failing to do so could lead up to a significant increase in modulus as shown in a study conducted on fully demineralized dentin²².

One method used for indentation-based mechanical characterization of hydrogels and soft tissues in a fully hydrated state is submersion of the sample in a fluid cell^{12,21-23}. However, meniscus forces acting upon the shaft of the indenter complicate the data acquisition and analysis²⁰, and specialized longer probes are required to protect the transducer from contact with the fluid²⁴. To avoid these challenges, researchers have been utilizing other methods to maintain sample hydration such as hydrating samples from the outer edges using sample insertion into a hydrated foam²⁵, spraying the sample surface with saline solution²⁶, or removing the fluid from the surface right before testing²⁷. However, these are not reliable techniques, given that these methods could only keep the sample moist rather than fully hydrated and dehydration could occur during the process of indentation. Note that although a single mechanical measurement via instrumented

indentation could require only seconds, the sensitivity of the measurement and the variability of structure and properties within biological samples requires many replicate trials that could require hours of data acquisition on a given sample. Chapter 2 addresses the challenge of sample hydration by modifying an existing platform to conduct experiments in fully immersed environments, and introduces different applications of this modification.

Another complication that could arise due to testing very compliant materials is the possible errors in detection of mechanical contact between the probe and the sample surface²⁸. To define the sample surface, most indentation techniques sense a change in the load measured on the order of $\sim 1\mu\text{N}$. Although this set point value results in negligible penetration depths on stiff materials, for more compliant polymeric materials and soft tissues, this force could already result in appreciable penetration of the probe into the sample, leading to errors in calculation of mechanical properties. To resolve this problem, researchers have been developing techniques including intentionally starting the indents out of contact with the sample, and a dynamic indentation method where the tip is oscillated in small amplitude while it is displaced²⁹. Given these current efforts, the problem of surface detection still resides to be one of the biggest challenges in testing of compliant materials. In Section 3.2.3.2.1 we introduce the development of another method in which data are collected prior to contact and the acquired load depth response is processed accordingly to resolve this issue.

Finally, one important challenge that arises with testing of compliant synthetic and biological materials at small length scales is the increase in the adhesive forces between the sample surface and the probe surface, which complicates both data acquisition and analysis. For such compliant materials, adhesive forces could be as large as the overall maximum load applied on the sample (Figure 1.2). The presence of significant tip-sample adhesion could lead to an increase in the energy dissipation during the indentation process, influencing the calculation of energy dissipation capacities. Further, presence of adhesion could result in erroneous calculation of mechanical properties such as the Young's elastic modulus of the material³⁰, due to an adhesion-driven increase in the probe-sample contact area.

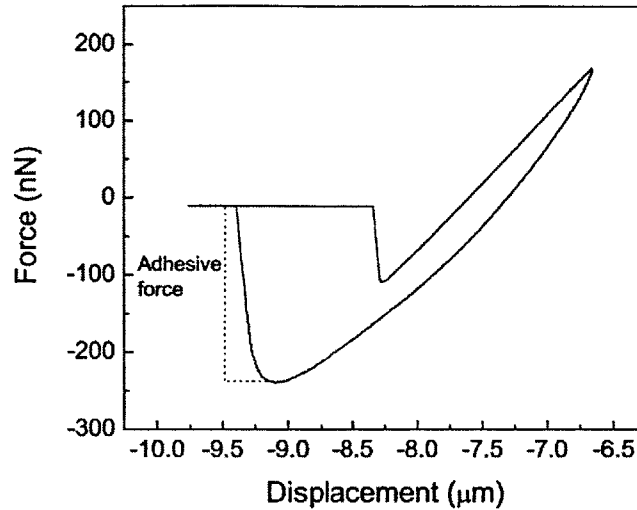


Figure 1.2 Force displacement response of a synthetic polymeric gel via atomic force microscopy enabled indentation in air reveals large adhesion forces between the surfaces of the cylindrical flat punch probe (radius~900 nm) and the sample.

To include the effect of adhesion in analysis, most researchers have utilized Johnson-Kendall-Roberts (JKR) contact based adhesion model in characterization of elastic properties³⁰⁻³¹, which is applicable for compliant samples and large surface areas³². Section 3.2.3 also utilizes this model to characterize time independent properties of polymeric materials developed as potential tissue simulant gels. Given that polymeric materials and soft tissues exhibit time dependent mechanical properties, more complex models that combine JKR analysis and viscoelasticity are also being developed^{31,33-34}; however, these methods have not been yet applied to many instrumented indentation studies of soft tissues.

Rather than including adhesion in the analysis, adhesive forces between the probe and the sample could be controlled by depositing chemicals on the surface of the probe³⁵, or by deposition of noninteracting fluids on the sample surface³⁶. Section 3.2.4 explores further effects of adhesion on load relaxation response of polymeric materials and how the deposition of noninteracting fluids on the sample surface mitigates adhesive forces. Given the current state of research in this field, continued development and application of adhesion models and/or experimental techniques to minimize adhesion are essential for accurate characterization of mechanical properties of soft tissues and polymeric materials.

1.2.2 Current interpretation of time dependent properties via indentation

Although most current literature documenting indentation of biomaterials utilize time-independent elastic analysis methods such as Oliver and Pharr method³⁷⁻³⁹, most biological materials actually exhibit time dependent behavior that requires more complex viscoelastic, poroelastic and/or poroviscoelastic analysis methods. This section will introduce some of these current analysis methods utilized in studying time dependent properties of synthetic and biological materials via indentation.

Most polymers and biological materials exhibit time-dependent behavior due to the viscoelastic response of the solid matrix. In order to study the time-dependent properties of a material via indentation, researchers have adapted two different approaches: the first is the application of an oscillatory displacement or force, and the second is the application of a step load or displacement and subsequent measurement of depth (creep) or force as a function of time (relaxation). This first approach, also called dynamic testing or dynamic indentation, is utilized to calculate elastic storage and loss moduli as a function of frequency⁴⁰⁻⁴³, and provides insight into the viscous dissipation of the material. The response obtained from second approach could be analyzed by applying analytical solutions of quasi-static contact between a rigid indenter and a linear viscoelastic solid to calculate creep compliance and relaxation modulus⁴⁴⁻⁴⁶. Alternatively, researchers have expressed these responses by idealizing the polymer as a viscoelastic model of springs and dashpots corresponding to a discrete spectrum of relaxation times^{12,47}. However, these approaches do not inform us about the microstructure of the material, and most of the above approaches assume that the material is deforming in the linear viscoelastic regime. Thus, there is still a need for development of appropriate models that could capture large-strain nonlinear viscoelastic response of soft tissues via indentation.

Another explanation for the observation of time dependency of mechanical properties of biological materials could be contributed to the presence of fluid flow. In order to study the flow of fluid through a saturated porous matrix, poroelasticity theory was developed by Biot⁴⁸ and Terzaghi⁴⁹ to study the migration of water in soil. Given that most biological materials are comprised mainly of aqueous electrolyte, this theory has been further extended to study elastic and transport properties of hydrogels and tissues^{13,50-53} via indentation. Although indentation

offers several advantages such as minimal specimen preparation, the ability to probe local properties, and the ability to extract the mechanical and transport properties simultaneously, extraction of the values of the constitutive parameters from the test output is not always straightforward. As there exist no analytical solutions to indentation of a poroelastic half-space recently, Oyen and Galli et al. have introduced a method to examine creep⁵² and stress relaxation⁵³ data from indentation using a poroelastic framework. However, this methodology requires finite element simulations or numerical implementation of the resulting boundary value problem that complicates data analysis. Other developments include presentation of a contact-based theoretical approach to extract simultaneously the mechanical and transport properties of hydrated gels from stress relaxation tests conducted via different probe geometries such as flat rigid circular, rectangular, conical, and spherical punches^{51,54-55}. However, the application of this methodology has been on macroscale contact areas and depths that requires hold times on the order of hours for the fluid to reach equilibrium; this duration is not feasible for testing biological materials that degrade over time. Chapter 5 adapts and extends this methodology to study the elastic and transport properties at micrometer length scales, minimizing the experimental times to enable poroelastic analysis of soft tissues.

Given that time dependency of mechanical behavior could arise due to viscoelastic and/or fluid permeation effects, a few researchers have started to work on the development and application of models that capture both effects⁵⁶. The determination of specific constitutive forms and the accompanying material parameters from experiments for the development of poroviscoelastic models is likely to be central to the future studies of indentation of biological materials.

1.3 Conventional macroscale methods for testing soft tissues and synthetic gels under high loading rates

Studying the response of biological tissues to impact loading at high rates is necessary to understand injury mechanisms and response of soft tissues to blunt trauma, and to develop tissue simulant gels that can be used as model torsos for ballistic protection applications. Although a growing number of reports characterize aspects of soft tissue mechanics under quasistatic⁵⁷⁻⁵⁸ and dynamic loading regimes⁵⁹⁻⁶⁰, effects of impact loading are less explored. This section will

summarize some of the conventional macroscale methods utilized in characterizing soft tissue response at higher rates.

Split Hopkinson pressure bar (SHPB) has been employed widely to investigate mechanical properties of engineering materials at high strain rates (10^3 s^{-1} - 10^4 s^{-1})⁶¹. Recently, SHPB has been modified to measure stress vs. strain response of compliant synthetic and biological materials such as tissue simulant gels⁶²⁻⁶³, liver⁶⁴, muscle⁶⁵⁻⁶⁶, skin⁶¹, and heart⁶⁷ under high rates relevant to insult and injury. This method requires dynamic stress equilibrium and constant strain rate deformation; thus, the low inherent strength and low mechanical impedance of soft tissues could lead to collection of experimental data that is inaccurate⁶⁴. In addition, specific sample dimensions (i.e., exact cylindrical shapes) are required, which complicates testing tissues from small-animal models; further, samples are tested in dry conditions that promote dehydration and structural degradation of the tissue over the testing period.

Other macroscopic studies include blunt impact tests of muscle and trochanteric soft tissues using a pendulum-like apparatus⁶⁸⁻⁶⁹. Lau and Viano utilized an impactor to study abdominal responses of rabbits using a disk with a diameter of 7.7 cm⁷⁰. Talantikite et al. also conducted pendulum impacts to study impact response of liver using an impactor with a diameter of 15 cm for impact velocities ranging from 1.5 m/s to 4.1 m/s⁷¹. Snedker et al. utilized falling weights and pneumatic projectile gun to study rupture criterion for bovine kidneys reporting strain energy densities at failure⁷². Lewis et al. has conducted impact tests on cartilage utilizing a 6 mm-diameter cylindrical instrumented impactor to study cell death after impact⁷³. Even though these studies inform us of the injury thresholds of specific organs, given that they are all macroscale techniques this limits the ability to test spatially localized impact response to study structure/property relationship of soft tissues. Further, the lack of studies on the impact response of tissues and tissue simulant gels under the same impact conditions hinders further design of tissue simulant gels that can accurately mimic soft tissue response such as impact resistance and energy dissipation capacities. Given this need, Chapter 3 introduces a new technique to conduct localized impact indentation experiments on potential tissue simulant gels and soft tissues from heart and liver in fully hydrated environments. The next section will introduce some of the current tissue simulant gels used to mimic the mechanical response of soft tissue to impact.

1.4 Current tissue simulant materials

For many years, ballistic gelatin has been used as a soft tissue simulant⁷⁴⁻⁷⁵ given that it is easy to process, relatively available, and cheap. Even though this gel, which is a thermoreversible hydrogel composed of crosslinked polypeptide chains, provides a qualitative insight of the bullet penetration and interaction into soft tissue, it has several downsides. These shortcomings include limited mechanical tunability⁷⁶ with a Young's elastic modulus $E \sim 100\text{-}150\text{ kPa}$ ⁷⁷⁻⁷⁸, narrow working temperature range for usable mechanical properties², and possible decomposition of the hydrated gels after a few days⁶². Rheology experiments conducted on ballistic gel from 0 °C to 30 °C have shown that storage modulus decreases drastically as a function of temperature suggesting a loss in the gelatin structure; this necessitates tests to be done below room temperature². Further, variability in the molecular weight distribution of natural driven gelatin could arise due to differences in properties from batch to batch, further complicating comparison of tests conducted at different facilities or labs². Thus, there is a need to design new tissue simulant gels that exhibit well defined crosslinking density or molecular weight, stable mechanical properties as a function of time, and mechanical tunability in order to mimic biological tissue as closely as possible.

Recent work on the design of a tissue simulant material with the aforementioned qualities has led to the development of physically associating gels (PAG), such as triblock copolymers possessing an ABA polymer structure including a midblock selective solvent (mineral oil). These materials offer superior environmental stability compared to ballistic gelatin⁶² and additional methods of tailoring the mechanical response including solvent loading, the incorporation of diblock polymer, and the ratio of the constituent blocks⁷⁹. One such system has been formulated from commercially available triblock copolymers consisting of polystyrene and polyisoprene^{2,62}. Multiscale mechanical characterization of these material systems have been conducted and compared to ballistic gelatin, utilizing low-rate unconfined compression and indentation methods, and high rate split-Hopkinson pressure bar (SHPB) methods. Even though these results are informative for the development of this field, more extensive work on these and similar systems are necessary in order to: (1) study the relation between composition and mechanical properties; and (2) compare mechanical response and energy dissipation characteristics attained at higher rates directly to those obtained for soft tissues from organs such as heart and liver under

comparable conditions. Only this direct comparison of conditions will provide insight into the design principles and approaches to modulate the mechanical response of tissue simulant gels, as required to mimic the response of soft biological tissues to concentrated impact loading. To address these issues, Chapter 3 introduces a new styrenic block copolymer system, and provides a detailed analysis of structure- mechanical property relationship under low and high rates compared to heart and liver tissue.

Recently, a new system comprising a crosslinked silicone network including an unpolymerized silicone solvent has been developed with a potential to be considered as tissue simulants for ballistic testing. The presence of an organic solvent within a cross-linked polymer network produces a polymer gel that is compliant and deformable, but will recover its shape due to the elastic nature of the polymer strands. Recent work by Mrozek et al. has demonstrated the ability to tailor the rate dependent mechanical response of polymer gels through the molecular weight of the solvent⁸⁰. Specifically, when the solvent molecular weight was larger than the entanglement molecular weight of the polymer, the gel exhibited significant stiffening with increasing strain-rate. This insight demonstrates the potential to incorporate and tailor the strain rate dependent response of these soft materials to provide a better match to the mechanical response of biological tissue. A significant advantage of this class of materials is the ability to tailor the properties by altering the material design including the polymer chemistry, network cross-link density, solvent type, solvent loading, solvent molecular weight, and through the incorporation of particulate filler. Of course, for this approach to be useful for the design of tissue simulants, the baseline elastic properties of the gels must approximate that of soft biological tissues. Chapter 4 provides a more detailed study on these material systems to gain insight into the tunability of mechanical properties, in order to ultimately match the mechanical response of soft tissues under impact loading.

1.5 Thesis organization

This thesis aims to (1) develop analytical and experimental techniques to study small scale mechanical behavior of compliant, synthetic and biological materials, in order to inform further design of tissue engineered constructs and computational models of soft tissues; and (2) study the structure-mechanical property relationship of potential tissue simulant gels in comparison to

two specific soft tissues obtained from heart and liver via conventional and newly developed experimental techniques. Together, successful achievement of these aims will inform the design of an environmentally stable, mechanically tunable tissue simulant gel that will more closely approximate the response of these tissues under impact loading. More generally, this thesis will provide new experimental and analytical tools to quantify key mechanical properties of and extract design principles from soft tissues and engineered polymer gels.

Chapter 1 included motivation for this thesis research and introduced indentation as a method to characterize mechanical properties of soft tissues and synthetic gels, mentioning some of the current challenges in implementing this technique to test compliant materials, as well as some of the current models utilized for extracting time dependent mechanical properties from contact based approaches. For high rate applications, a review of the conventional macroscale techniques was provided followed by an introduction of the current and potential future tissue simulant gels designed for ballistic applications.

Chapter 2 introduces a modification of a commercially available instrumented indenter to conduct experiments in fully hydrated conditions addressing the challenge of sample hydration reported in Section 1.2.1. In addition to the validation of the method, this chapter includes three studies that utilize this modification to develop new material systems for biological applications (Aim 1).

Chapter 3 provides a detailed analysis of multiscale mechanical properties of physically associated styrenic block copolymer gel systems as potential tissue simulants in comparison to heart and liver tissue under low rates (Aim 2), utilizing the tool developed in Chapter 2; addressing some of the challenges that arise in the indentation of compliant materials mentioned in Section 1.2 (Aim 1). Chapter 3 also introduces a new technique developed for conducting localized high rate impact tests on compliant materials under fully hydrated conditions (Aim 2). This technique is further implemented to study the tunability of impact resistance, energy dissipation capacities, and energy dissipation rates of the block copolymer system in comparison to heart and liver tissues (Aim 2).

Chapter 4 introduces a new system comprising a crosslinked silicone network including a nonreactive solvent as potential tissue simulants, and investigates the mechanical properties of this new system in comparison to heart and liver using conventional techniques as well as tools developed in Chapters 2 and 3 (Aim 2).

Chapter 5 provides a new method to characterize poroelastic properties of compliant materials at small length scales, and utilizes this methodology to study structure-mechanical property relationship of heart and liver tissue layers in order to inform the design of tissue engineered constructs, computational models of tissue mechanics (Aim 1), and design of tissue simulant gels (Aim 2).

Finally, Chapter 6 presents broad conclusions, unique contributions of this thesis, and suggested directions for future research.

Chapter 2 Contact Deformation of Hydrated Polymers

2.1 Introduction

This thesis aims to study the structure-property relationship of soft tissues and tissue simulant gels designed for ballistic applications. This understanding will lead to the development of environmentally stable, mechanically tunable, better-matched tissue simulant gels, and will aid the development of computational models of impact loading on anatomical organs. Recently, instrumented indentation has become a popular technique for measurement of local mechanical properties of biological materials, due in part to the high force resolution and spatial resolution of mechanical probing afforded by this method. However, a longstanding challenge in accurate mechanical characterization of engineered and biological tissues via instrumented indentation is the maintenance of stable sample hydration.

To this end, in this chapter we present the modification of a commercially available instrumented indenter to conduct experiments under fully hydrated conditions. Section 2.2 introduces the modification of the platform and the validation of this method. Various applications are introduced in the rest of this chapter; Section 2.3 investigates the electrochemically controlled mechanical properties of a polymer nanocomposite, Section 2.4 studies the tunable mechanical properties of PEG hydrogels for 3-D tissue scaffold applications, and Section 2.5 introduces the high-throughput mechanical characterization of biomaterials developed for clonal growth of stem cells utilizing the modified platform. The tools developed in this chapter are further implemented in Chapter 3 and Chapter 4 in order to conduct impact indentation experiments under hydrated environments required for accurate characterization of tissue simulant gels and biological soft tissues.

2.2 Implementation of a fluid cell in an instrumented indenter

The following study is part of a publication from 2008 with coauthors G. Constantinides, M. McFarland, J. F. Smith, and K. J. Van Vliet⁸¹, and is reprinted with the permission of Elsevier.

2.2.1 Motivation and Background

Accurate mechanical characterization of hydrogels and engineered and biological tissues requires both stable sample hydration and high instrument signal resolution. Although mechanical properties of compliant, hydrated polymers are increasingly inferred from indentation force-depth ($P-h$) responses acquired via atomic force microscopes (AFMs)⁸²⁻⁸³, several aspects of this cantilever-based deformation preclude straightforward, accurate mechanical characterization (e.g., limited maximum force/depth range ($\sim 1 \mu\text{N}/10 \mu\text{m}$), limited probe materials/geometries, and objective identification of initial contact points). Instrumented indentation employs comparably rigid load frames to impose normal probe-surface contact that can be mapped rapidly over cm-scale surface areas⁸⁴, surmounting these challenges for imposed forces $> \mu\text{N}$. With notable exception^{12,23,30}, indenters are typically operated in ambient air on dry samples. Given the increasing effort to quantify and mimic the mechanical properties of tissues^{22,85}, robust mechanical analysis of biological/synthetic polymers in fully hydrated states is required. One option that has been used recently for hydrated testing of biological materials is submerging the sample in a fluid cell with a vertical loading assembly, but data acquisition and analysis are complicated by meniscus forces acting on the shaft of the indenter, and specialized probes with long shafts are required. Other solutions include submerging the sample prior to testing and removing from the fluid prior to indentation, or applying several drops of fluid to the surface prior to indentation⁸⁵; these approaches are not robust, given that dehydration can occur during the course of experiments that tend to span at least one hour to acquire sufficient replicate trials.

Here, we describe the modification of an instrumented indenter to accommodate mechanical characterization of biological and synthetic tissues in liquid media, and demonstrate accurate acquisition of force-displacement data that can be used to extract elastic and viscoelastic properties of hydrated gels. More specifically, we demonstrate the validity of this approach via elastoplastic analysis of relatively stiff, water-insensitive materials of elastic moduli $E > 1000$ kPa (borosilicate glass), and then consider the viscoelastic response and representative mechanical properties of compliant, synthetic polymer hydrogels (polyacrylamide-based

hydrogels of varying mol%-biscrosslinker) with $E < 500\text{kPa}$. These capabilities are particularly important to materials design and characterization of macromolecules, cells, explanted tissues, and synthetic extracellular matrices as a function of spatial position, degree of hydration, or hydrolytic/enzymatic/corrosion reaction times.

2.2.2 Materials and Methods

To validate the modified apparatus, several synthetic and biological materials were probed in the fully hydrated, immersed state at 24°C . Borosilicate glass was obtained from VWR. Polyacrylamide (PAAm)-based hydrogels (10% bis-tris NovaGel of proprietary composition, Invitrogen) and freshly synthesized PAAm of $2\times 2\times 0.5\text{ mm}$ and varying mol%-bis crosslinker, prepared on amine-derivitized glass slides, were stored in water throughout testing.

The instrumented indentation platform modified for liquid-immersed experiments (NanoTest, Micro Materials, Ltd., Wrexham, UK) relies on a vertical pendulum that rotates about a frictionless pivot. This configuration confers horizontal loading, normal to a vertically mounted sample, and has been used widely in mechanical characterization of metal, ceramic, and polymeric surfaces⁸⁶. Force application proceeds via an electromagnetic coil/magnet at the pendulum top, and displacement is acquired via a capacitor positioned behind the indenter (Figure 2.1a). Upon calibration of displacement (nm/V), force ($\mu\text{N}/\text{V}$), and frame compliance (nm/ μN)⁸⁷, the P/h resolutions were $0.1\ \mu\text{N}/0.1\ \text{nm}$, respectively. As shown in Figure 2.1, the extended, stainless steel indenter mount is immersed within the liquid cell; this cell inclusive of mounted samples is positioned via automated stage displacement. The indenter automatically contacts the sample in two stages: (1) With the pendulum held against a mechanical stop by an arbitrarily low force, the sample stage moves towards the indenter at low velocity until contact displaces the pendulum from its rest position. Displacement is detected at capacitive sensor resolution of $<0.1\text{nm}$, upon which stage motion ceases and the indenter falls away from the surface. (2) The specimen retracts a known distance; the indenter is slowly moved into contact at the now-defined measurement plane, at a location laterally displaced from the original site to avoid initial contact damage. The force applied to the indenter at this point is determined from an initial calibration procedure that finds the coil current required to move the indenter to the

measurement plane. Liquids can be added before/after this operation, and exchanged intermittently.

We first validated the accuracy of P - h acquisition and inferred properties of a relatively water-insensitive material, borosilicate glass (repetitions, $n=8$) using a diamond Berkovich indenter. Trapezoidal loading functions to maximum load P_{\max} of 100 mN were used, with dwell and un/loading times of 5 s and 10 s, respectively. We then indented PAAm-based hydrogels ($n=8$ for each mol%bis) in air and in water, with dwell and un/loading times of 20 s and 10 s, respectively; a ruby spherical probe of 1 mm diameter was chosen to reasonably approximate linear viscoelastic deformation and to induce comparable strains on all samples to $h_{\max}=1500$ nm. Indentation modulus E_r was calculated from the unloading slope dP/dh evaluated at P_{\max} and the indenter area function $A_c(h_c)$ obtained through parallel indentations on quartz, according to established analyses for elastoplastic materials⁸⁸. E_r of gels (E_{gel}) was corrected for finite sample thickness on a stiff glass substrate ($E_{\text{substrate}}=69$ GPa; $\nu=0.3$) for the measured ratio of geometrically calculated contact radius a to measured sample thickness t ⁸⁹. For comparison with AFM-enabled indentation of PAAm hydrogels, P - h responses were acquired in an AFM fluid-cell (PicoPlus, Agilent) with Si_3N_4 cantilevers of nominal spring constant $k=0.1\text{N/m}$ (Veeco), and E_s calculated as in Reference⁹⁰. Using the 1 mm-diameter probe, we also conducted contact creep experiments on PAAm hydrogels. Samples were rapidly loaded (1s) to $P_0=200$ μN (PAAm); the resulting depth increase $h(t)$ was monitored over 30 s. Responses were analyzed using a linear viscoelastic Kelvin-Voigt model expressed by⁹¹:

$$h^{3/2}(t) = \left(\frac{3}{4} \sqrt{\frac{3P_0^2}{4RE_1^2}} \right) \left(\left(\frac{E_1 + E_2}{E_2} \right) - \left(\frac{E_1}{E_2} \right) e^{-\left(\frac{E_2 t}{3\eta} \right)} \right) \quad (2.1)$$

2.2.3 Results and Discussion

As shown in Figure 2.1, the horizontal-loading configuration confers significant advantages for indentation in liquids, obviating vertical-loading effects due to variation in buoyancy and surface tension during vertical indenter displacement through liquid. In absolute terms such forces are quite small, but can be significant for the nanoscale forces and/or displacements relevant to compliant hydrogels¹² or tissues. Vertical sample orientation requires adhesion to a rigid backplate.

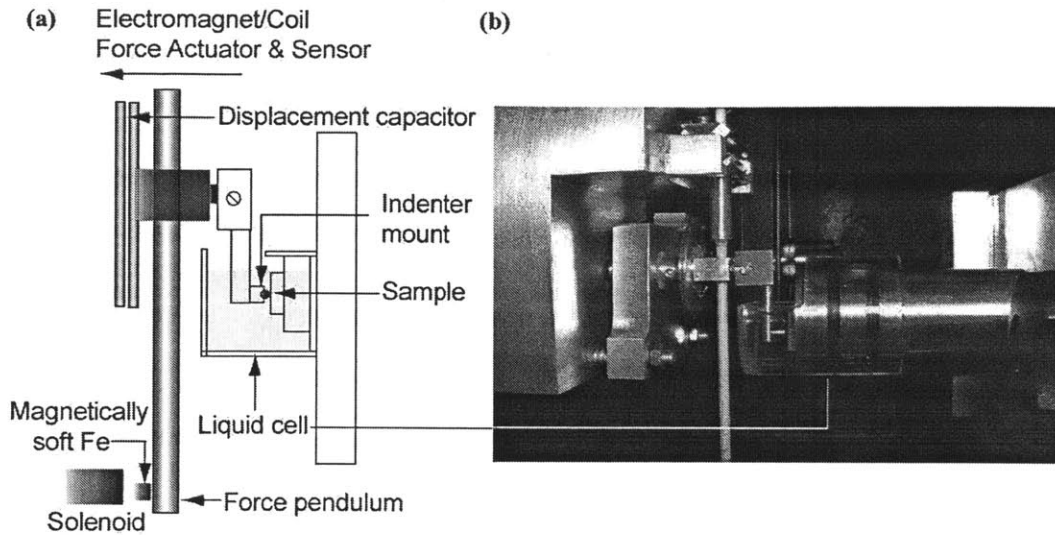


Figure 2.1 Schematic diagram (a) and photograph (b) of instrumented indenter apparatus capable of extended nanomechanical experiments in fully immersed environments on hydrated gels and tissues.

2.2.3.1 Validation on water insensitive materials.

To demonstrate that $P-h$ precision/accuracy were preserved following instrument modifications and introduction of liquids, experiments were conducted on borosilicate glass that was not expected to absorb/react appreciably with water. Excellent repeatability of borosilicate indentations was observed in water, and $P-h$ responses in air/water were indistinguishable (Figure 2.2). In addition, we found good agreement between calculated E_s and that reported in the literature (Table 2.1).

Table 2.1 Elastic moduli (E_s) extracted from indentations in ambient air and fully immersed in water, for borosilicate glass. These moduli are independent of the extent of hydration, as expected, and in good agreement with the range of elastic moduli widely reported by others (E_{lit}). Data are mean \pm one standard deviation.

Sample	Fluid	E_s [GPa]	E_{lit} [GPa]
Borosilicate Glass	air	67.67 ± 0.99	65-70
	water	69.83 ± 0.82	65-70

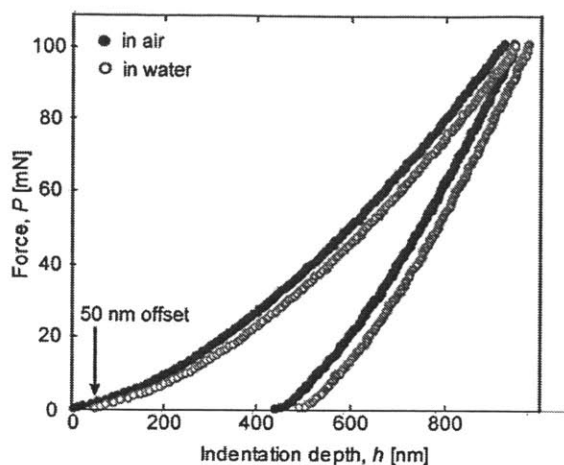


Figure 2.2 As expected, response of borosilicate glass under indentation with a sharp Berkovich diamond probe is statistically identical whether acquired in ambient air (●) or fully submerged in water (○); data intentionally offset at $P=0$ by 50 nm for clarity. Experimental details: Berkovich probe, $n=5$ for each testing condition, $P_{\max}=100$ mN, $t_{\text{load}}=t_{\text{unload}}=10$ s, $t_{\text{dwell}}=5$ s.

2.2.3.2 Application on compliant hydrated materials

To demonstrate validity on compliant, hydrated materials, experiments were conducted on PAAm-gels. As expected, $P-h$ responses of PAAm-based electrophoresis gels depended strongly on whether the materials were in a dried or fully hydrated state, with excellent repeatability of the hydrated response (Figure 2.3a, $n=5$). Significant increases in penetration depth upon full hydration were correlative with 1000-fold decreases in stiffness ($E_{\text{gel,water}}=266\pm 27$ kPa; $E_{\text{gel,air}}=295\pm 26$ MPa). Figure 2.3b shows that this approach can also be used to determine E_{gel} as a function of synthesis conditions such as mol%-bisacrylamide crosslinker, commonly employed to tune PAAm-hydrogel stiffness to approximate tissues including fat, brain, and muscle⁹². Although rigorous viscoelastoplastic analysis is beyond the scope of this section⁹³, un/loading rates were optimized to enable reasonable approximation of storage elastic moduli of these polymers according to the Oliver and Pharr method⁹⁴. Figure 2.3b shows that E_{gel} obtained via indentation in this liquid cell agreed reasonably well with those obtained for gels of similar composition via AFM-enabled indentation by us and by others⁹⁵, and via conventional rheology⁹². Since gel architecture and stiffness depend strongly on both mol%-bis and vol%-water during synthesis, better agreement is not expected among disparate hydrogels. Figure 2.3b confirms the required sensitivity of this apparatus to measure elastic properties of synthetic gels/biological tissues with stiffness on the order of ~ 10 kPa. This comparison underscores the

need for consideration of finite sample thickness when such compliant gels are characterized via indentation: elastic mismatch between the specimen and the underlying, stiffer substrata can incur significant errors in calculated E_s ⁸⁹.

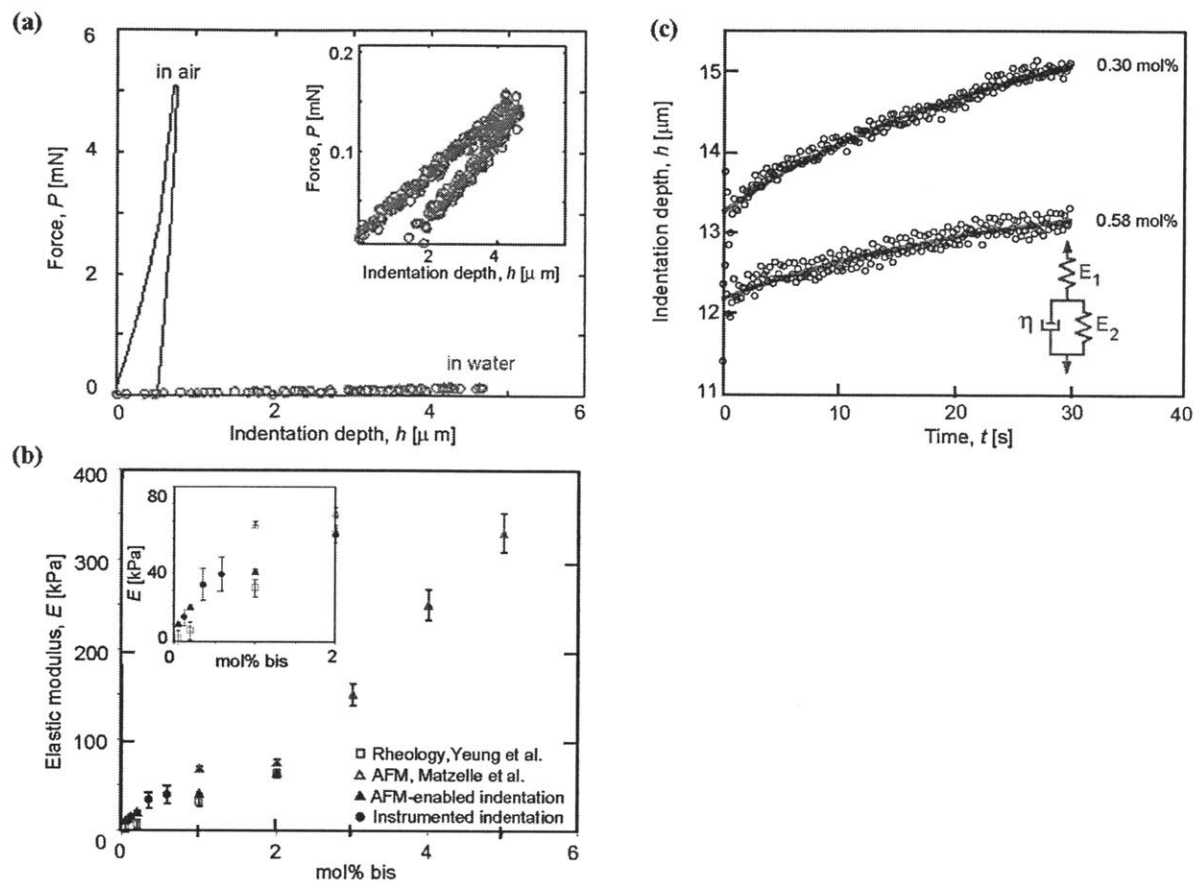


Figure 2.3 (a) Response of polyacrylamide gel to spherical indentation in air (blue) and water (green); inset shows repeatability of five replicate experiments in water. (b) Elastic moduli of PAAm gels as a function of mol%-bis measured by instrumented indentation are within the range reported by calibrated AFM-enabled indentation and rheological experiments. The former approach is amenable to rapidly mapping variations in this stiffness over surface areas $>\text{mm}^2$ or as a function of depth $>1 \mu\text{m}$, and with fewer experimental artifacts as discussed in the text. Error bars represent one standard deviation from mean. (c) Contact creep response of PAAm hydrogels demonstrates increased creep resistance for increased mol%-crosslinker, as expected.

As one goal of synthetic hydrogel design is to match tissues that exhibit time dependent mechanical properties, we also conducted analysis of hydrogels via contact creep experiments. The Kelvin-Voigt model reasonably approximated creep responses of PAAm (Figure 2.3c). As expected, increased bis-crosslinker from 0.30 mol% to 0.58 mol% decreased creep compliance and increased effective storage moduli $E_1=E_s$ of PAAm (10 kPa and 12 kPa, respectively). These

E_s agree within a factor of 4 with those inferred from elastic unloading (Figure 2.3b), with discrepancy attributable in part to significantly different assumptions of analytical models used to estimate E_s from creep compliance and elastic unloading, respectively.

2.2.4 Conclusions

In summary, we have developed and demonstrated an approach to enable nano- to microscale indentation of fully immersed, hydrated polymers and tissues that maintains accurate acquisition of high precision force and displacement signals. The following sections detail three different case studies; the first case study utilizes this method to characterize the mechanical properties of an electrochemically controlled nanocomposite, the second study investigates the tunable mechanical properties of PEG hydrogels as 3-D tissue scaffolds, and the third study conducts a high-throughput nanomechanical screening of biomaterials for clonal growth of stem cells via using the modified platform developed in this section.

2.3 Electrochemically controlled mechanical properties of a polymer nanocomposite

The following study is part of a publication with coauthors D. Schmidt, F. Cebeci, S. Wyman, C. Ortiz, P. Hammond, and K. J. Van Vliet⁹⁶, and is reprinted with the permission of Ref. 96 © 2009 American Chemical Society. A direct link to the article is at:

<http://pubs.acs.org/articlesonrequest/AOR-cTSkq7ENdwwbBhIsRXrK>.

2.3.1 Introduction

Stimuli-responsive polymeric materials have attracted much interest for a variety of applications including drug delivery, biological and chemical sensing, separations, and mechanical actuation, among others⁹⁷⁻¹⁰¹. Control over the mechanical properties of a surface is of particular interest for the modulation of cellular behavior, as it is well known that adhesion of cells to surfaces can be modulated via the stiffness of those surfaces^{82,102}. Stimuli-responsive composite materials open up the possibility of tuning percolative behavior, which can dramatically alter mechanical, electrical, optical, and other composite properties¹⁰³⁻¹⁰⁴. In this work, we have designed and characterized an electrochemically-responsive polymer nanocomposite thin film with actively-tunable mechanical properties, utilizing the modified platform described in Section 2.2. Electrochemical stimuli are advantageous, in comparison with temperature or pH changes, in that they can be applied reversibly, rapidly, and locally (i.e., at an electrode instead of throughout the

bulk). Moreover, the structure and function of biological molecules, cells, and organisms, for example, may be inadvertently altered by large changes in temperature or pH, whereas application of a small voltage maintains a comparatively mild environment.

More specifically, here we characterize the electrochemically-controlled mechanical behavior of electroactive layer-by-layer (LbL) thin films containing Prussian Blue (PB) nanoparticles as the polyanion and linear polyethyleneimine (LPEI) as the polycation. Specifically, we applied -0.2 V (vs. Ag/AgCl) to reduce the particles from the PB state to the Prussian White (PW) state, and +0.6 V to oxidize the particles back to the PB state. Upon electrochemical reduction, the negative charge on the particle surface and interior was doubled as estimated from the valence of the two redox states. In response to the excess negative charge created in the film, cations and water from electrolyte solution entered the film to maintain electroneutrality. Instrumented nanoindentation was used to measure the mechanical properties of films in the oxidized and reduced states. To our knowledge, this is the first direct observation of mechanical property manipulation carried out in an electrochemical cell with a redox-active thin film.

2.3.2 Experimental Details

2.3.2.1 *Material synthesis*

All of the synthesis described in this section was conducted by Daniel Schmidt in the Hammond Group, MIT Chemical Engineering. Linear polyethyleneimine (LPEI) ($M_n = 25,000$) was purchased from Polysciences. Iron(II) chloride tetrahydrate, potassium ferricyanide, potassium hydrogen phthalate (KHPh), and 3-mercapto-1-propanesulfonic acid (MPS) were purchased from Sigma Aldrich. Potassium chloride was purchased from Mallinckrodt Baker. All chemicals were used as received. Indium tin oxide (ITO)-coated glass slides (CD-50IN-CUV) were purchased from Delta Technologies, Limited.

2.3.2.1.1 Synthesis of Prussian Blue Nanoparticles

Synthesis of PB nanoparticles was carried out as described previously¹⁰⁵. Briefly, 50 mL of aqueous 10 mM $\text{FeCl}_2 \cdot 4\text{H}_2\text{O}$ was added dropwise to an equivalent volume of aqueous 50 mM $\text{K}_3[\text{Fe}(\text{CN})_6]$ and 50 mM KCl with vigorous stirring. The dark green mixture was immediately submitted to dialysis against a regenerated cellulose membrane with a 3500 Da molecular weight cutoff to remove excess $\text{K}_3[\text{Fe}(\text{CN})_6]$ and KCl. The resulting blue nanoparticle suspension was

adjusted to pH 4 with potassium hydrogen phthalate (KHPH) (final concentration of 1 mM) and hydrochloric acid.

2.3.2.1.2 Assembly of LPEI/PB Films

Films were assembled on ITO-coated glass slides. ITO-coated slides were cleaned by sonication in a 4% solution of Micro-90 detergent for 15 minutes, following by two 15 minute sonication cycles in deionized water. LPEI solutions were prepared in deionized water at a concentration of 10 mM based on the polymer repeat unit. The solution pH was adjusted to the desired value with HCl and NaOH. (LPEI/PB)_n films, where n denotes the number of bilayers, were assembled by dip coating using an automated Zeiss HMS Series programmable slide stainer. Briefly, substrates were immersed in an LPEI solution for 10 minutes followed by three separate deionized water rinse baths (adjusted to pH 4 with KHPH and HCl) for a total of 3 minutes. Next the substrates were immersed in a PB solution for 10 minutes followed by the same cascade rinse cycle. Slight differences in initial film thickness from sample to sample can be attributed to slight variations in pH of the solutions used for the deposition process.

2.3.2.2 *Nanoindentation experiments and analysis*

Nanoindentation on (LPEI/PB)₅₀ films on ITO-glass was conducted by a pendulum-based instrumented nanoindenter (NanoTest, Micro Materials, Ltd.) with a force resolution of 1 μN and a displacement resolution of 0.1 nm. Films assembled on ITO-coated glass were adhered to an aluminum support with a thin layer of cyanoacrylate and all of the experiments were conducted with the sample fully immersed in 0.1 M KHPH, using the modified platform for *in situ* liquid experiments⁸¹ described in Section 2.2. An electrochemical cell was set up within the liquid cell with the film as the working electrode, a Pt wire as the counter electrode, and a silver wire as a pseudo-reference electrode. The potential was controlled with an EG&G 263A potentiostat/galvanostat. Samples were indented with a spherical indenter of radius $R=5\ \mu\text{m}$, both in the oxidized and reduced states ($n=6$ locations for each condition), with loading, dwell, and unloading times of 10s, 10s, and 2s, respectively. A maximum depth of 40 nm was chosen to induce comparable, low strains on all samples (~10%), and the corresponding maximum loads ranged between 80 to 200 μN. Film elastic modulus inferred from indentation, E_i , was calculated through a finite-thickness correction of Hertzian elastic contact, using the model of Dimitriadis et al.,¹⁰⁶ (see Appendix A) in order to count for mechanical contributions from the underlying stiff

ITO-glass substrate for the measured film thickness of 224 ± 13 nm (as measured via profilometry).

2.3.3 Results and Discussions

The mechanical behavior of the (LPEI/PB) composite films on ITO-glass, in response to electrochemical redox of PB within the films, was analyzed with instrumented nanoindentation in aqueous conditions. Instrumented, spherical nanoindentation enabled determination of the effective elastic modulus of the composite films, fully immersed in 0.1 M KHPH at room temperature. Figure 2.4a shows typical load-depth responses for an (LPEI/PB)₅₀ film in the oxidized state (+0.6 V) and the reduced state (-0.2 V). Clearly, the film was more compliant in the reduced state. This increased compliance is consistent with increased hydration of the film as it swells in response to doubling of the PB charge state (data not shown). From these data, an effective elastic modulus, E_i , for the hydrated composite film was determined, correcting for the finite thickness of each film and the stiffness of the underlying ITO substrate. Figure 2.4b shows E_i of a film subjected to two redox cycles. After allowing the film to swell in the electrolyte solution for 2 hours, the modulus was measured to be 3.40 ± 1.03 GPa. Subsequent electrochemical reduction of the film reduced E_i further to 1.75 ± 0.26 GPa, a decrease of nearly 50%. Upon re-oxidation of the film, E_i returned to 3.54 ± 0.64 GPa; subsequent electrochemical reduction then reduced E_i to 2.14 ± 0.6 GPa. Measurements at each potential were taken over the course of 1 h and exhibited excellent repeatability, attesting to the stability of the films and the reversibility of the switching. As expected, the indentation elastic modulus of the film in the absence of an applied potential (i.e., at the open circuit potential) was equal to that at +0.6 V, since the PB redox state is largely unchanged between the open circuit potential (typically +0.3 V to +0.4 V) and +0.6 V (Figure 2.4b). For reference, an (LPEI/PB)₅₀ film in the dry state exhibited $E_i = 6.92 \pm 1.03$ GPa (data not shown).

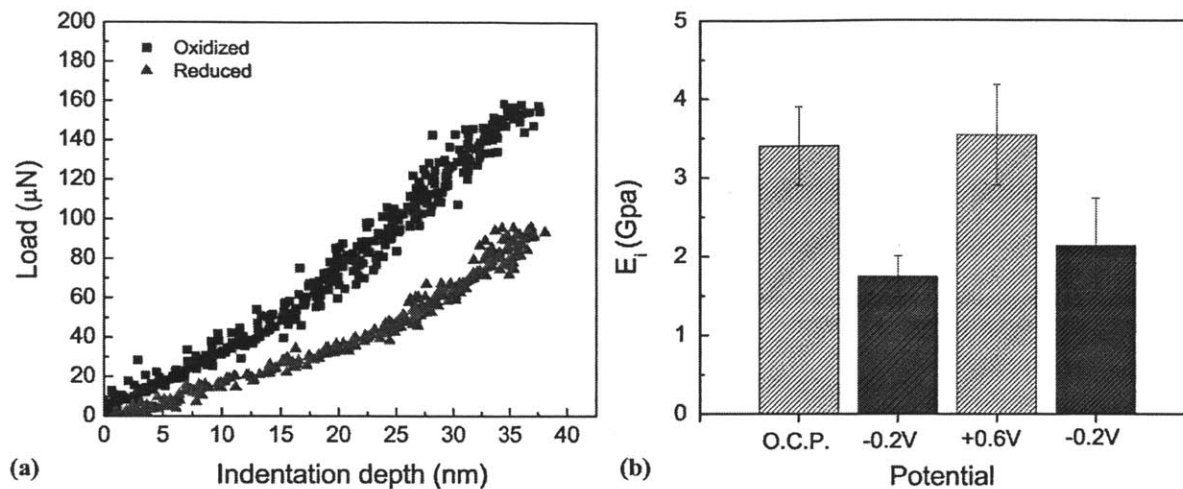


Figure 2.4 Instrumented nanoindentation results for an $(\text{LPEI/PB})_{50}$ film immersed in aqueous 0.1 M KHPH. (a) Loading portion of the load-depth response for a film in the oxidized (black, +0.6 V) and reduced (blue, -0.2 V) state. (b) Corrected effective elastic moduli of the film subjected to two redox cycles. O.C.P. stands for open circuit potential. The error bars represent the standard deviation from $n=6$ measurements at different locations on the film.

As expected, the elastic modulus of the film decreased upon immersion in the electrolyte solution, and then decreased further upon electrochemical reduction of the film. During swelling, the incoming water serves as a plasticizer to reduce cohesive polymer-polymer and polymer-nanoparticle interactions in the film. Furthermore, incoming ions can break ionic crosslinks in the film, thereby giving polymer segments additional degrees of translational freedom, rendering the film less stiff. Jaber and Schlenoff recently showed that the elastic modulus of layer-by-layer films can be decreased substantially (for relatively small degrees of swelling)¹⁰⁷ by increasing the ionic strength of the surrounding solution, which decreases the ionic crosslink density in the film¹⁰⁸. Here we maintained the ionic strength of the electrolyte constant, but instead induced locally increased ionic strength within the film by exploiting PB redox chemistry.

2.3.4 Conclusions

In this section, we have described the electrochemically-triggered modulus reduction of a polymer nanocomposite film containing Prussian Blue nanoparticles and linear polyethyleneimine utilizing the method developed in Section 2.2. Reduction of the Prussian Blue (PB) in the films to Prussian White doubled the negative charge on the nanoparticle surface and interior. An influx of ions and water from the surrounding solution occurred to maintain electroneutrality in the film and results in film swelling and decreased mechanical stiffness of the

composite. A future system that could be engineered to achieve rapid, dramatic mechanical changes with only slight changes in degree of swelling could be applied to the control of cellular behavior on surfaces. For example, on/off switching of cell adhesion could allow cells to be guided to particular locations within microfluidic devices or cells could be triggered to differentiate for tissue engineering applications or fundamental studies. The system reported here, however, is likely too stiff to modulate cellular behavior. Nonetheless, we have introduced a new framework for electrically modulating the stiffness of a composite. We believe that this work could serve as a starting point for further studies on mechanomutable coatings with potential future applications in micro- and nanoscale devices.

2.4 Micromechanical characterization of microporous PEG hydrogels for tissue scaffold applications

The following study is part of a publication from 2011 with coauthors S. Peyton, J. Cohen, A. Runkle, D. Lauffenburger, L. Griffith, and K. J. Van Vliet¹⁰⁹, and is reprinted with the permission of Wiley.

Design of 3D scaffolds that can facilitate proper survival, proliferation, and differentiation of progenitor cells is a challenge for clinical applications involving large connective tissue defects. One of the metrics that has to be considered for the design of tissue scaffolds is the mechanical properties of the substrate typically defined by elastic moduli, given that the stiffness of the substrate is known to regulate cell migration¹¹⁰, alter cell adhesion¹¹¹, and affect cell differentiation¹¹². In this section, the modified platform for conducting experiments in fully immersed environments demonstrated in Section 2.2 was utilized to characterize the mechanical properties of 3-D scaffolds composed of microporous Poly(Ethylene Glycol) PEG hydrogels with tunable mechanical properties and pore sizes. Instrumented indentation was chosen over other conventional methods such as macroscale rheometry or microscale atomic force microscopy enabled indentation, since the former required very large amounts of material for testing, and the latter could not access the larger length scales and contact areas necessary to obtain a homogeneous mechanical response given the relatively large pore sizes in these hydrogels.

2.4.1 Materials and Methods

2.4.1.1 Poly(ethylene glycol) scaffold fabrication

The following synthesis was conducted by Shelly Peyton in the Griffith Lab, MIT Department of Biological Engineering. Three-dimensional (3D) scaffolds based on poly(ethylene glycol) (PEG) were fabricated by adapting a previously published system¹¹³. PEG-dimethacrylate (PEGDMA, average Mn 750 g/mol 14-15-mer, Sigma-Aldrich, St. Louis, MO) and PEG-methacrylate (PEGMA, average Mn 526, 10-11-mer, Sigma) were combined in various ratios (10-34% v/v PEGDMA/reaction solvent) with 0.05-0.6% v/v (PEGMA/reaction solvent) for ligand addition with 0.8% w/v 1-hydroxy-cyclohexylphenyl ketone initiator (Sigma) and buffered with 3:1 phosphate buffered saline (PBS):EtOH. For pore size analysis and migration experiments, 5 mM (0.05% v/v of reaction solution) of fluorescein-o-methacrylate (Sigma) was included to visualize the scaffolds.

Monodisperse poly(methyl methacrylate) microspheres (PMMA, Sigma) with nominal diameters of 20, 30, 40, 50, or 60 μm were concentrated to 65% (w/v) in 70% EtOH and pipetted into circular PDMS gaskets (6 mm x 1 mm, EMSdiazum, Hatfield, PA) adhered to Sigmacote-pretreated glass slides. The microspheres were shaken vigorously on an orbital shaker (350 rpm) until dry (4 hrs). 12 μL of the polymer solution was then added to the dried bead cake and photopolymerized via UV-light irradiation (3 min at 365 nm). Scaffolds were soaked for 3 days in tetrahydrofuran (THF) with regular solvent changes to leach away the PMMA templating beads and leave behind a macroporous PEG hydrogel. Two-dimensional (2D) hydrogels were made using the same PEGMA and PEGDMA formulations to compare with 3D results; polymer solutions were polymerized between glass plates separated by thin (180 μm) Teflon spacers, similar to previous studies¹¹¹. The resulting 2D hydrogels were soaked for 1 hour in THF to remove any unreacted monomers then reacted with adhesive ligand according to the same protocol for 3D scaffolds.

2.4.1.2 Mechanical property characterization

Instrumented indentation on macroporous hydrogels was conducted via a pendulum-based instrumented nanoindenter (NanoTest, Micro Materials, Ltd.) with a force resolution of 1 μN and a displacement resolution of 0.1 nm. Hydrogels made from PMMA bead diameters of 20, 40 and

60 μm and PEGDMA crosslinker contents of 10, 17 and 34% (v/v) were tested. Additionally, nonporous PEGDMA gels with similar dimensions and crosslinker content were prepared and tested in order to compare the results with predictions of macroscopic elastic moduli for the Gibson-Ashby cellular solid model¹¹⁴⁻¹¹⁵. This model correlates Young's elastic modulus of the solid of which the foam is comprised E_s to the Young's modulus of the elastomeric, open-celled foam E^* , according to the relation:

$$E^* = C[\rho^*/\rho_s]^n E_s \quad (2.2)$$

where C is a constant of proportionality related to void geometry and is ~ 1 for open-cell foams, ρ^*/ρ_s is the relative foam density and is 0.26 for this study assuming an ideal packing density of the templating beads according to the Kepler conjecture, and n is an exponent that defines whether the dominant mechanism of deformation is bending or axial stretching¹¹⁶. Hydrogels were adhered to a glass slide with a thin layer of cyanoacrylate-based adhesive and mounted on an aluminum support. All experiments were conducted with the sample fully immersed in PBS (150 mM NaCl) using a modified platform for *in situ* liquid experiments⁸¹. Samples were indented with a spherical indenter of radius $R = 1$ mm, ($n=9$ locations for each hydrogel sample), with loading, dwell, and unloading times of 10 s, 30 s, and 10 s, respectively. A maximum depth of 20 μm was chosen to contact as many pores as possible. The elastic modulus inferred from indentation E_i (equivalent to E^* of porous gels and E_s of nonporous gels) was calculated via analysis of the unloading response according to the method of Oliver and Pharr⁸⁸. Given that the adhesion forces between the probe surface and sample surface were negligible, and the property of interest was Young's elastic modulus, this method has been chosen over other analysis methods such as JKR.

2.4.2 Results and Discussions

Since the mechanical properties of the tissue scaffolds could play a role in cell adhesion, differentiation, and migration, these PEG hydrogels were also characterized mechanically. By varying the diameter of the templating beads from 20 to 60 μm , we achieved pore sizes ranging from 7 to 17 μm (measured in the hydrated state via confocal microscopy), independent of PEG crosslinker content. Elastic moduli increased with increasing volume percent of PEGDMA crosslinker (Figure 2.5), for both nonporous gels and porous hydrogels of identical composition for pore diameters of 7, 12 and 17 μm . E^* of these porous scaffolds varied from 3 kPa to 100

kPa for an increase in crosslinker from 10 to 34 v/v% PEGDMA. As expected, microscale porosity reduced the stiffness as a function of crosslinker as compared to the nonporous versions of these same gels ($56 \text{ kPa} < E_s < 7 \text{ MPa}$). Elastic moduli of the nonporous samples E_s represent the mechanical stiffness of the hydrogel material comprising the solid pore walls and struts of the porous samples. As the cells adhere directly to and migrate along these pore walls and struts, it is the mechanical stiffness of those regions—as opposed to E^* of the macroscopic porous hydrogel—that is expected to chiefly define the local mechanical environment of cells within the porous hydrogels. Despite this difference between macroscopic gel stiffness and the local effective mechanical environment of the adherent cell, quantification of the E^* for these porous hydrogels (Figure 2.5) is useful in that it allows comparison of elastic properties as commonly reported for tissues and other types of engineered scaffolds, when measured via micro- to macroscopic mechanical methods.

Here, we note that porous gels of 10 v/v% PEGDMA were too compliant to be tested experimentally using instrumented indentation; the topology of the microscale-porous gels also prohibited atomic force microscopy-enabled indentation. For these porous 10 v/v% PEGDMA gels, E^* was instead predicted by use of a validated Gibson and Ashby model¹¹⁵. This was achieved by measuring E_s for all nonporous gels and E^* for the 17 and 34 v/v% PEGDMA porous gels; these measured E_s and E^* for the stiffer porous gels were used to obtain n (the model mode of strut deformation in Equation 2.2). This model, with now validated values of n for each pore diameter, $C \sim 1$ and relative density $\rho^*/\rho_s = 0.26$, was then used to estimate E^* of the 10 v/v% porous gels. Although the model predicts that the macroscale elastic modulus is independent of pore diameter, we observed that E^* was greatest for the porous gels of largest diameter (17 μm) for all v/v% PEGDMA. These deviations are reasonably attributed to the neglect of poroelastic contributions in the “dry” cellular solid model of Gibson-Ashby, and other studies adopting the Gibson-Ashby model for open-cell foams have also reported this phenomenon¹¹⁷.

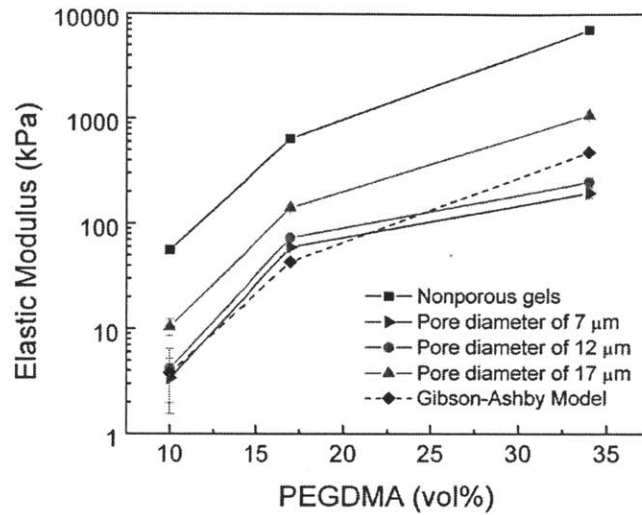


Figure 2.5 The elastic modulus for fully hydrated porous gels with pore sizes of 7, 12, or 17 μm follows the predictive model (dashed black) described by Gibson and Ashby¹¹⁵ based on the elastic modulus of the solid, represented by nonporous gels (E_s , solid black). Errors are S.E.M. for 3 separate samples with 9 locations per sample.

2.4.3 Conclusions

In this study, porous 3-D PEG hydrogels were designed as tissue scaffolds with tunable stiffness for cell adhesion and migration studies. Instrumented indentation with a modified platform for fully immersed experiments was implemented to characterize elastic moduli of compliant PEG gels ($E < 500$ kPa) with microscale heterogeneous structure. The ability to test relatively small samples sizes compared to conventional macroscale methods and the ability to access larger length scales compared to atomic force microscopy-enabled techniques rendered this method to be utilized for this study. For a given pore diameter, elastic modulus increased as a function of %-crosslinker. For a given %-crosslinker, $E_{\text{nonporous}} > E_{\text{porous}}$. Finally, the cellular solid model was applied to estimate mechanical properties of very compliant gels that could not be characterized by instrumented indentation.

2.5 High throughput nanomechanical screening of biomaterials for clonal growth of stem cells

The following study is part of a publication from 2010 with coauthors Y. Mei, K. Saha, S.R. Bogatyrev, J. Yang, A.L. Hook, S. Cho, M. Mitalipova, N. Pyzocha, F. Rojas, K.J. Van Vliet, M.C. Davies, M.R. Alexander, R. Langer, R. Jaenisch, and D.G. Anderson¹¹⁸, and is printed with permission of Nature Publishing group.

Human pluripotent stem cells (both human embryonic stem (hES) and induced pluripotent stem (hiPS) cells) are utilized currently for regenerative medicine¹¹⁹⁻¹²⁰ and human disease modeling¹²¹⁻¹²³. However, existing methods to grow human pluripotent stem cells are not well suited for genetic manipulation experiments and introduce animal components, increasing the risks of immune rejection. Here we employed a high-throughput approach to engineer new culture polymeric substrates that could be used to clonally expand human pluripotent stem cells in a chemically defined, xeno-free, feeder-free manner. To develop structure/function relationships between mechanical properties and biological performance, the reduced indentation elastic modulus E_r of all polymeric substrates was quantified using a high-throughput method demonstrated previously^{84,124} and as introduced in Section 2.2.

2.5.1 Materials and Methods

2.5.1.1 Combinatorial array preparation and cell culture

To facilitate rapid synthesis and analysis of synthetic substrates, Ying Mei and Dan Anderson from the Langer Lab, MIT Chemical Engineering, manufactured cell-compatible, biomaterial microarrays¹²⁵⁻¹²⁷. Polymer microarrays allow for rapid, nano-liter scale synthesis and analysis of libraries of polymeric surfaces on a standard glass microscope slide. Microarrays were prepared from 22 acrylate monomers with diversified hydrophobicity/hydrophilicity and crosslinking densities. The arrays were prepared by copolymerization between each of 16 “major” monomers and each of 6 “minor” monomers at 6 different ratios [100:0, 90:10, 85:15, 80:20, 75:25, 70:30 (v/v)]. In this way, arrays with 496 [16 + (16 x 5 x 6)] different combinations were created, primarily composed of the major monomer (70-100%), and to a lesser extent with the minor monomer (0-30%). These monomer mixtures were robotically deposited in triplicate on a non-cell adhesive layer of poly(hydroxyl ethyl methacrylate) covered conventional glass slides (75 mm x 25 mm), and then polymerized with a long-wave UV source. Polymer arrays were coated

with the fetal bovine serum (FBS) and were seeded at low cell density (40 hES cells per mm^2), to best model the ability of cells to grow in isolation. For each polymer, the colony formation frequency was measured by Dr. Ying Mei (Langer Lab, MIT) as the number of polymer spots on which cell colonies formed divided by the total number of replicate spots of the same kind of polymer on each array ($n=3-18$). See Reference¹¹⁸ for more detailed information on the cell culture.

2.5.1.2 Mechanical characterization

Nanoindentation was applied to the array polymer spots with an average diameter of 300 μm , height of ~ 15 μm with center-to-center distance of 740 μm by a pendulum-based instrumented nanoindenter (NanoTest, Micro Materials, Ltd.). Samples were immersed in phosphate buffered saline 1X (DPBS, Invitrogen) for at least 12 h prior to indentation to achieve equilibrium. The array slide was mounted on an aluminum support with a thin layer of cyanoacrylate, and all of the experiments were conducted with the sample fully immersed in PBS using a modified platform for *in situ* liquid experiments explained in Section 2.2⁸¹. Samples were indented with a spherical ruby indenter of radius $R = 500$ μm , ($n=3$ locations for each polymer spot), with loading and unloading rates of 0.5 mN/s, dwell of 10 s and a maximum load of 3 mN or a maximum depth of 600 nm, depending on whichever limit was achieved first. The average strains imposed on the polymer spots calculated from a/R , where a is the contact radius, was found out to be less than 5%. Reduced elastic modulus inferred from indentation, E_r , was calculated from the unloading slope dP/dh evaluated at maximum load P_{max} through Oliver and Pharr method⁸⁸, given that no adhesion was observed between the sample surfaces and the probe surface. These results are not corrected for finite sample thickness, however, indentation depth over sample thickness ratio h/t , was kept at less than 4% in order to minimize the errors that would arise from effect of the stiff substrate. Note that, for the tests conducted here, the Hertzian model utilized to correct for the finite sample thickness in Section 2.3.2.2 was not able to capture the loading response accurately, and thus could not be applied. If there is a substrate effect, even though it would change the absolute values of E_r , it is most likely not to affect the trends observed herein, given that the samples are of the same thickness.

2.5.2 Results and Discussion

A positive power-law correlation was observed between the indentation elastic modulus E_i of hydrated polymers and colony-formation frequency (Figure 2.6 inset). However, polymers with low reduced indentation modulus also exhibited a low water contact angle (data not shown), and many of these highly compliant polymers contained a hydrophilic major monomer and a hydrophilic minor monomer. Since the reduced indentation modulus measured in a hydrated state is heavily influenced by water swelling, the power-law correlation between elasticity and colony formation (Figure 2.6) therefore likely reflects the impacts of polymer hydrophobicity/hydrophilicity in the cases where a hydrophilic polymer swells to create a soft surface (indentation modulus < 0.2 GPa) that poorly supports colony formation. Figure 2.6 also demonstrates that, for the present array of hydrated polymers, colony formation is not strongly governed by polymer stiffness for E_i exceeding 0.2 GPa.

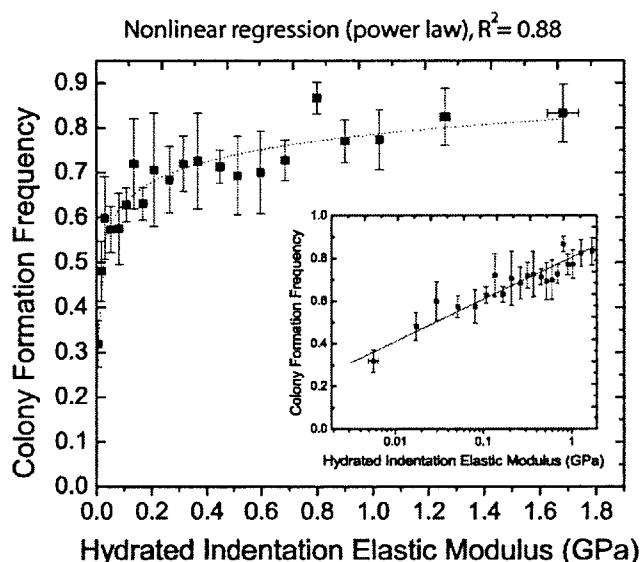


Figure 2.6 Colony formation frequency versus polymer indentation elastic modulus in the hydrated state; the inset is in semi-log format to indicate the behavior at low modulus values. Data are sorted into groups of 20–25 spots as a function of increasing modulus. Abscissa error bars represent the standard error of the modulus for a given group of 20–25 spots, and ordinate error bars represent the standard error of the mean of the colony-formation frequency of three replicates for a given group.

In summary, here we demonstrated a high-throughput combinatorial technique to characterize the elastic properties of a library of acrylate polymers, which were designed as potential synthetic substrates for clonal growth of human stem cells, under fully hydrated conditions. The

ability to conduct high-throughput characterization under fully hydrated environments provides a rapid and an accurate way to study key mechanical properties of biological material libraries.

2.6 Conclusions

Chapter 2 introduced the development of a new tool to conduct mechanical characterization under fully hydrated environments required for accurate testing of materials such as hydrogels and soft tissues. Validation of this method on water insensitive materials was followed by three different applications that utilized this tool to develop new material systems for biological applications including stimuli responsive polymers, 3-D tissue scaffolds with tunable mechanical properties, and synthetic substrates for clonal growth of human stem cells. Although elastic response is the primary mechanical design parameter for these three applications, for other applications such as the development of tissue simulant gels and tissue engineered constructs it is important to consider the time-dependent mechanical behavior, as well. Thus, in addition to the time independent elastic properties, Chapter 3 utilizes this tool to characterize viscoelastic properties and impact response under concentrated loading of soft tissues and potential tissue simulant gels, addressing the challenges related to testing and understanding the deformation mechanics of these material systems.

Chapter 3 Styrenic Block Copolymers as Potential Tissue Simulants

3.1 Introduction

There exists a growing need for new materials that are mechanically optimized to recapitulate the mechanical responses and energy dissipation of soft tissues. Such tissue-simulant materials can then be implemented as a standard test medium to test effects of ballistics on soft tissues, to rank protective garments in minimization of impact trauma, and to establish characterization tools and design principles for new flexible armor materials. The limited environmental stability and mechanical tunability of current materials in use (e.g., ballistic gelatin) underscore this need for innovation, and opportunities to develop such materials. This chapter studies the structure property relationship of triblock/diblock styrenic copolymers as potential tissue simulant gels in comparison to heart and liver tissue. Triblock/diblock styrenic copolymers are chosen as potential tissue simulants given that they have a flexible polymer backbone, include a low volatility solvent and exhibit good polymer-solvent miscibility for the temperature ranges of interest which makes them environmentally stable. Heart and liver are chosen as target organs to mimic since they are located in the chest and abdominal cavities, respectively, and are commonly damaged by high-impact mechanical insults. Studies of these systems include a combination of macro, micro, and nanoscale mechanical methodologies such as unconfined compression, pendulum-based impact loading, instrumented indentation, and atomic force microscopy (AFM). In Section 3.2.3, unconfined compression, instrumented indentation using the tool developed in Chapter 2, and AFM-enabled approaches are utilized to quantify elastic modulus, relaxation modulus, and viscoelastic relaxation time scales of these biological and synthetic materials. Section 3.3 investigates resistance to penetration and energy dissipative constants under the rates and energy densities of interest for ballistic applications via pendulum-based impact indentation.

3.2 Multiscale characterization of elastic and viscoelastic properties

This section focuses on capturing the elastic and viscoelastic properties of soft tissues and optimized simulants from the macroscale to microscale, utilizing conventional methods as well techniques developed in Chapter 2.

3.2.1 Motivation and background

Parts of the following study are from a publication in 2011 with coauthors M. Qu, K. Strawhecker, T. Shazly, E. Edelman, M. VanLandingham, J. Smith, and K. J. Van Vliet¹²⁸, and is reprinted with the permission of Taylor & Francis.

Mechanical properties of biological tissues have been investigated for many years⁵⁷⁻⁵⁸, using methods such as uniaxial tension^{10,129-130}, confined¹³¹ and unconfined compression¹³²⁻¹³³, and aspiration¹¹. Multi-scale measurement of such properties for so-called soft tissues has attracted increasing attention as the demand for tissue-engineered constructs has grown. Another motivation lies in developments in mechanical modeling of soft tissues which have an impact on medical practice in particular for surgery planning, tissue replacement engineering and trauma research¹¹. Due to this demand, there has been an increase in the reported multiscale quantitative measurements of the mechanical properties via experimental techniques such as indentation, which provides the unique capacity to measure spatially resolved mechanical properties in materials of small volume^{14,134-135}. However, to this extent, with notable exceptions^{14,37-38,136} most of the data in the literature are obtained using low rate, quasi-static loading conditions in dry environments^{6,17,132-133,137}. While these works are crucial for the development of the field, there is still a need of accurate characterization and analysis of multiscale mechanical properties of tissues under more biologically relevant, fully hydrated conditions.

Given this motivation, in this section we report multiscale analysis of the mechanical properties of heart and liver and styrenic block copolymers as potential tissue simulant gels for ballistic applications under biologically relevant, hydrated conditions. Through our multiscale experiments on these materials, we establish a searchable database that compares key mechanical properties such as elastic modulus, relaxation modulus, and viscoelastic relaxation time scales. More specifically, Section 3.2.3 focuses on multiscale characterization of elastic properties such as Young's elastic modulus of the potential tissue simulant gels (styrenic block copolymers) as a

function of composition in comparison to heart and liver tissue via unconfined compression (macroscale) and instrumented indentation (mesoscale) in fully hydrated environments. Since both soft tissues and styrenic block copolymers also exhibit time dependent behavior, Section 3.2.4 explores viscoelastic properties of tissue simulant gels and heart tissue via stress relaxation experiments at macroscale, mesoscale and microscale, focusing on the effect of composition and length scales on relaxation modulus and times. Together these studies will form a baseline for the design of tissue simulant gels that best represent and model soft tissue mechanical response under extreme loading conditions for ballistic applications, and will inform the mechanical modeling of soft tissues for other applications.

3.2.2 Materials

Synthetic materials considered as potential simulants of tissue impact response were organogels formed from styrenic block copolymers (Kraton Polymers) comprised of styrene (S) and either ethylene/butylene (EB) or ethylene/propylene (EP). Copolymer-based gel samples were prepared by Dr. Kenneth Strawhecker in the US Army Research Laboratories (ARL) in Aberdeen, MD by mixing SEBS triblock copolymer (Kraton G1652) with SEP diblock copolymer (Kraton G1701). The copolymers were dissolved at elevated temperature in light mineral oil (Mallinckrodt Chemicals, St. Louis, MO) at a volume ratio of 20:80 polymer to oil, forming gels upon cooling to room temperature. Each polymer-oil mixture was placed in a vacuum oven at 150°C and fully dissolved over 6 h with stirring every hour. The melt was then poured onto a flat surface to cool and gelate. Light mineral oil is a block selective solvent, i.e., a good solvent for the rubbery blocks and a poor solvent for the styrene blocks, and has a low vapor pressure facilitating development of physically associating gels that are stable in ambient conditions. Samples were mixed at triblock/diblock volume ratios of 100/0, 75/25 and 50/50, and cast to obtain final sample thickness of 4 mm.

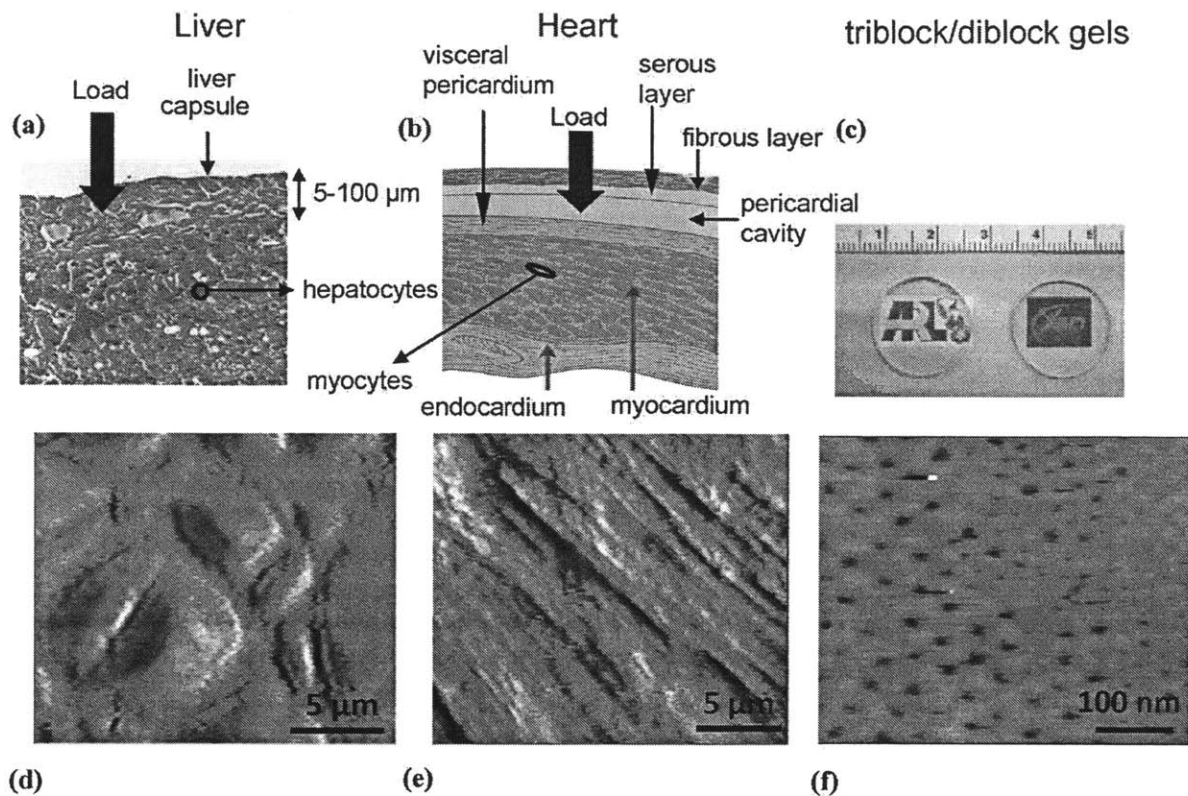


Figure 3.1 (a) Schematic illustrating length scales of liver tissue structural heterogeneity (adapted from Ref. 138), load is applied normal to the outer liver capsule for the experiments outlined in this chapter; (b) schematic illustrating length scales of heart wall structural heterogeneity (adapted from Ref. 139), load is applied normal to the outer fibrous layer; (c) 100/0 and 75/25 triblock/diblock styrenic copolymer discs of diameter ~ 2 cm; Atomic force microscopy (AFM) phase-lag image of (d) rat liver capsule, (e) fibrous layer of rat heart, (f) 75/25 triblock/diblock styrenic copolymer gel indicating segregated domains of triblocks and diblock-triblocks.

Tissues were harvested from liver and heart of healthy male, adult Sprague-Dawley rats (250-350 g). Soft tissues exhibit a striated or orthotropic anisotropy at the microscale dimensions. The external surface of the liver is covered with a collagenous dense connective tissue capsule called Glisson's capsule (Figure 3.1a). While the collagen fibrillar layer of the human liver capsule is 70-100 μm in thickness, rat liver's capsule is less than 5 μm in thickness³⁵. The liver parenchyma which lies under the liver capsule is composed of hepatic lobules where the diameter of each lobule is about 0.8-2mm¹⁴⁰. Each lobule consists of a roughly hexagonal arrangement of plates of hepatocytes radiating outward from a central vein in the center. Hepatocytes are 20-30 μm in diameter¹⁴¹, separated from each other by large capillary spaces called "liver sinusoids."

Similar to liver, heart also exhibits a layered heterogeneous structure. The heart wall is composed of three main layers; pericardium, myocardium, and endocardium (Figure 3.1b). Pericardium, which is composed of the visceral and parietal layers, is the outermost layer of the heart wall and serves as a protective barrier. Parietal pericardium, the bag that encloses the heart, consists of a 1-mm-thick layer (for human heart) of dense collagen (fibrous layer) with sparse interspersed elastic fibrils, and it is covered by a layer of mesothelial cells (serous layer). The visceral pericardium (epicardium or serous pericardium) is the surface of the heart itself and consists of a thin (<1 mm for human heart) layer of loose fibrous tissue covered by mesothelial cells (serous layer)¹⁴². For the rat hearts used in our studies, the thickness of the fibrous+serous layer of the parietal pericardium (Figure 3.1b) was measured to be 500 μm - 1 mm by a micrometer. A space (pericardial cavity) exists between the visceral and parietal pericardial layers, which holds a small amount of fluid¹⁴³. Myocardium is the middle layer comprised of cardiac muscle tissue which consists of distinct, individual cells named cardiac myocytes that have an average rest length of 120 μm and a rest width of 30 μm ¹⁴⁴. These cells align together to form sheets which are loosely connected by the collagen network, introducing anisotropy into the structure¹⁴⁵. Endocardium is the thin layer of tissue heart that lines the heart's chambers and valves.

On the other hand, the synthetic gels are structurally homogeneous at the microscale (Figure 3.1c). Approaching the nanoscale, however, structural anisotropy in the synthetic gels becomes apparent in terms of micelle formation Figure 3.1f). The difference in structures of these materials is observable in atomic force microscopy (AFM) phase contrast images, as shown in Figure 3.1d-f. These images were acquired using an AFM (3D Molecular Force Probe, Asylum Research, Santa Barbara, CA) in AC mode at a scan rate of 0.5 Hz; images were acquired in ambient air for synthetic organogels and in Krebs-Hensleit buffer for tissues. As schematized in Figure 3.2, AB (SEP) diblock chains contain the A block within the micellar core and the B block extending away from the micelle into the solution (i.e., adding no network connectivity). In contrast, the ABA (SEBS) triblock chains can form either loops when both A blocks are in the same micelle; chains when only one A block is in a micelle with the rest of the triblock extending into solution; or bridges when A blocks are in neighbouring micelles connected by the B block¹⁴⁶. Thus, the microstructure of these synthetic gels can be manipulated by tuning the

relative concentration of triblock to diblock, in that increasing the vol%-triblock will result in a higher crosslinking density of the gel. While the apparent diameters of the micelles in Figure 3.1f are slightly enlarged by the finite AFM probe size and probe-sample contact, these features are considerably smaller than the μm -scale structures such as cuboidal and elongated cells of the hepatic lobules and cardiac muscle tissue of liver and heart, respectively (Figure 3.1d-e).

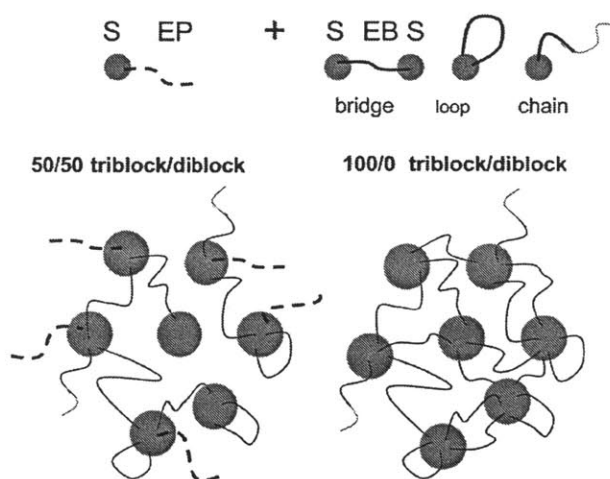


Figure 3.2 Styrenic block copolymers comprise AB diblocks of styrene-ethylene propylene (SEP), and ABA triblocks of styrene-ethylene butylene (SEBS). As the vol%-triblock increases, crosslinking density of the gel will increase, since in ABA (SEBS) triblocks, B blocks can form bridges between different micellar cores containing the A blocks (adapted from Ref. ¹⁴⁷.)

Throughout this chapter, all experiments involving animals were approved by the university IACUC protocol and compliant with NIH guidelines for animal care. The structure and mechanical behavior of these tissues depends strongly on hydration state²², and change with cell lysis and protein degradation *ex vivo*. Thus, all experiments were conducted within 3 hours post mortem. For both heart and liver tissue, discs of 8 mm diameter and thickness of 3 to 5 mm were prepared using a surgical punch, and all tissues were stored in Krebs-Henseleit buffer immediately after excision and throughout all experiments reported in this chapter. Note that both uniaxial compression and contact-based experiments on these tissues explained in the following sections proceeded normal to the tissue outermost layer, and were not varied to consider the full structural anisotropy of the tissue mechanical response. Rather, the loading directions were intended to replicate the expected loading direction of mechanical injury or impact to an intact tissue, which would typically proceed normal to the outermost (fibrous) layer of that tissue.

3.2.3 Multiscale characterization of Young's modulus and energy dissipation

In this section we characterize the elastic properties such as Young's elastic modulus, as well as energy dissipation capacities of triblock/diblock gels with different triblock vol%, and murine heart and liver tissues under low rates at macroscale and microscale length scales. The goals in this section are to understand the structure-property relationship of these gels, and to compare the gel responses to that of soft tissues at these quasistatic rates.

3.2.3.1 Methods

3.2.3.1.1 Quasistatic experiments via unconfined compression

For both gels and tissues, unconfined compression experiments were conducted by Dr. Kenneth Strawhecker in the US Army Research Laboratories (ARL) in Aberdeen, MD to ascertain the uniaxial stress-strain response of all materials at quasistatic loading rates. Compression of triblock/diblock gels of composition 100/0 ($n = 5$), 75/25 ($n = 4$) and 50/50 ($n = 4$) was conducted (AR 2000 Rheometer, TA Instruments) with 40 mm-diameter, parallel plate geometry. Sample diameter and thickness were maintained constant at 17.65 mm and 4 mm, respectively. Compression displacement rate was controlled at 25 $\mu\text{m/s}$ and a compression ramp (loading) was performed for 10 s (250 μm) leading to strain rates of 0.006 s^{-1} , followed immediately by a release ramp (unloading) at the same rate and time. Strains were determined from plate gap measurements and were approximately 5% for every sample. A thin layer of silicone oil (1000 cst) was used to lubricate the contact regions between the gels and the plates. A preloading normal force of 0.03-0.10 N was applied to the sample. For each specimen within a given material set, two complete load-displacement and thus duplicate stress-strain responses were obtained; a pause duration of 30-60 s between these duplicate trials was adopted to allow for recovery of these synthetic gels to the initial uncompressed state.

Compression of liver ($n = 5$) and heart ($n = 2$) in fully immersed buffer conditions were conducted (ElectroPlus E1000, Instron) for strain rates of 0.003 s^{-1} up to approximately 40% strain. These strain rates were chosen to be similar to the nominal strain rates applied to the gels. Although soft tissues are known to exhibit strain rate-dependent behavior, we did not explore a wider range of strain rates here since this was beyond the scope of these experiments. Samples discs of 8 mm diameter and 3.8 ± 0.3 mm thickness (heart) or 4.6 ± 0.4 mm thickness (liver)

were prepared using a surgical punch. For hepatic (liver) tissues, a single load-displacement cycle was acquired for each sample. For cardiac (heart) tissues, three load-displacement cycles and thus triplicate stress-strain responses were obtained; a pause duration of 60-120 s was adopted to allow for recovery of these hydrated tissues to the initial uncompressed state.

3.2.3.1.2 Quasistatic experiments through instrumented indentation

For both gels and tissues, instrumented indentation experiments were conducted to ascertain the mechanical response under contact loading at quasistatic rates, as well as to provide a comparison of elastic moduli under macroscale compression and microscale indentation. Here, the term ‘instrumented indentation’ will refer to acquisition of full load-depth cycles proceeding at quasistatic loading rates. All instrumented indentation measurements were conducted at ambient temperature $T_a = 24^\circ\text{C}$, using an instrumented indenter (NanoTest, Micro Materials Ltd.) that ensures force/displacement resolutions of $0.1 \mu\text{N}$ and 0.1 nm . Gels adhered readily and strongly to a bulk aluminum alloy support. Tissues were adhered to the aluminum support with a thin layer ($<5 \mu\text{m}$) of cyanoacrylate (Loctite, Henkel) and were fully immersed in Krebs-Hensleit buffer using the modified platform for fluid immersed experiments we have described in Chapter 2. In addition to acquiring load-depth responses in full contact with the sample surface, experiments were designed to acquire data prior to physical contact between the probe and the surface (pre-contact), and to acquire data until full separation of the probe from the surface; the latter portion of this dataset enabled quantification of the adhesion pull-off force F_{po} .

All materials were indented with a ruby sphere of radius $R = 1 \text{ mm}$. However, as discussed in Section 1.2.1 and 3.2.3.2.1, the accurate detection of contact loading on highly compliant materials is challenging and is aided by the use of probes with larger radii. Liver tissue was by far the most compliant sample considered in this study, and for the purposes of more accurate detection of contact this tissue was indented with a larger stainless steel sphere of $R = 2 \text{ mm}$; those data are reported herein. Maximum contact loads P_{max} for gels ($n = 10$ per composition), heart ($n = 10$) and liver tissue ($n = 10$) were chosen as 0.2 mN , 0.2 mN and 0.1 mN , respectively; the loading and unloading times for all samples was 10 s . Note that for soft tissues the resulting P_{max} after correcting the data for the physical contact point (see Section 3.2.3.2.1) was larger than 0.2 mN (Figure 3.4b). The resulting contact depths h_{max} of 10s of μm and contact diameters $2a$

correspond to projected contact areas at maximum load on the order of 10s of μm^2 for heart and 100s of μm^2 for liver; these projected areas are on the order of tissue cell diameters and pore diameters of biological extracellular matrices. The average strains imposed on these materials under such conditions can be approximated from contact geometry as $a/R^{3/2}$. Under this approximation, strains of 10% were attained for the synthetic gels, whereas average strains of $23 \pm 0.01\%$ and $28 \pm 0.002\%$ were attained for the heart and liver tissue samples, respectively.

3.2.3.2 Analysis

3.2.3.2.1 Ascertaining the physical contact point for soft and compliant materials

One major challenge in the indentation of compliant materials is accurate detection of the point at which actual physical contact and mechanical loading of the surface is initiated. Surface detection errors typically cause overestimation of the indentation elastic modulus inferred from indentation on soft and compliant materials²⁸. To more accurately define the initial contact point, we collected data prior to contact (pre-contact data), and post-processed our acquired load-depth ($P-h$) data accordingly. In the normal operation of this instrument, the pendulum displacement prior to contact is directly proportional to the applied electromagnetic coil current. This current is directly proportional to the applied force after contact is attained, and can be represented in units of “force” via the same conversion factor prior to actual contact. Therefore, a departure from linearity in the “force” vs. displacement response is an indication of surface contact with the spherical probe. Figure 3.3a illustrates this point for the $P-h$ response of 100/0 triblock/diblock gel, wherein we initially observe a line of constant slope dP/dh where the probe is far away from the surface (prior to point A in Fig. 3.3a). When contact occurs (point B in Figure 3.3a), the displacement signal increases abruptly; similar sharpness in this contact transition was observed for all synthetic gels considered. Data were thus analyzed and shifted such that this transition point corresponded to zero load and zero depth.

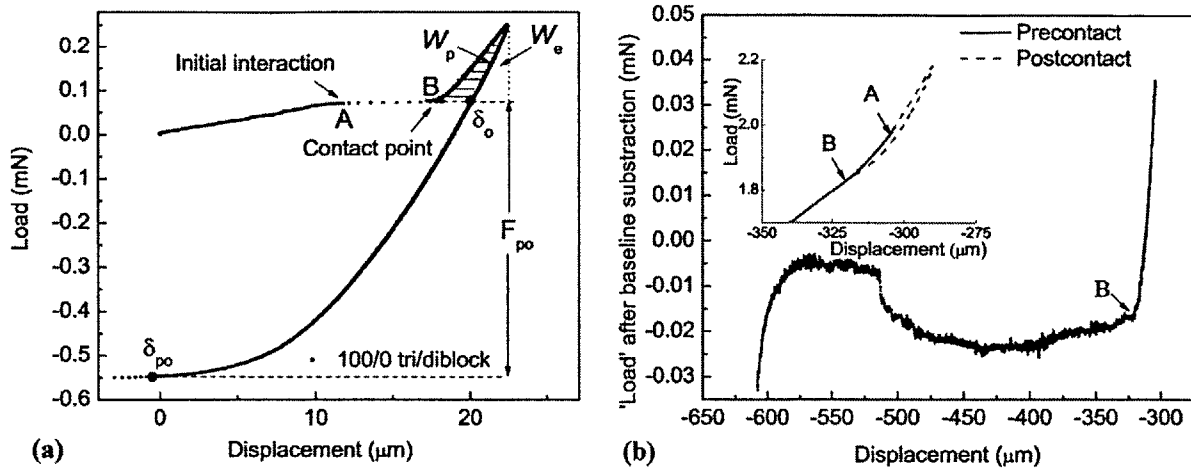


Figure 3.3 (a) Load-displacement response for 100/0 triblock/diblock gel shows attraction toward and initiation of mechanical contact. Note that, prior to actual contact with the surface, electromagnetic coil current is expressed in units of load on the pendulum, to enable visual identification of contact. Point B is considered the initiation of mechanical contact, and W_p and W_e denote the dissipated and recovered work of this indentation, respectively. Adhesion of the probe to this sample persists from position δ_o to δ_{po} until the pull-off force F_{po} is attained. (b) On more compliant materials such as cardiac tissue, sharp transitions are not observed. Analysis of the pre-contact response (see text) shows that contact occurs at point B. Point A denotes the point at which the instrument software misidentified the contact initiation, based on a threshold increase in load or instantaneous contact stiffness dP/dh .

For heart and liver tissues, however, a sharp transition upon contact was not observed (Figure 3.3b). As discussed below, the more gradual increase in dP/dh is attributable chiefly to the significantly greater elastic compliance of these tissues, as well as to the surface tension, charge, and roughness of these protein-rich biological tissues. Here, an objective estimate of contact was achieved by a linear regression fit to the initial portion of the pre-contact region for which the probe was visibly not in contact with the surface. Correction of the data via this baseline “tilt” then enables objective identification of the contact point (denoted as point B in Figure 3.3b). Data were thus analyzed and shifted such that this transition point corresponded to zero applied load and zero imposed indentation depth.

3.2.3.2.2 Calculating elastic modulus and energy dissipation from quasistatic deformation

For unconfined compression, E was calculated via least-squares linear regression to identify the slope of the stress vs. strain response over a defined strain range. Synthetic gels exhibited linear elastic deformation over the entire applied strain range, and thus linear regression was conducted on the entirety of the stress-strain response (Figure 3.4a). In contrast, the heart and liver tissues

exhibited highly nonlinear responses up to imposed maximum strains of 40% (Figure 3.4a). Thus linear regression was applied only over the linear region of the stress strain response (<10%).

The load-depth or P - h responses of the synthetic gels, obtained through instrumented indentation in ambient air, were analyzed to estimate the reduced elastic modulus of the sample E_r according to the Grunlan et al.¹⁴⁸ implementation of the JKR adhesion model³² that describes the effect of adhesion on elastic contact:

$$E_r = \frac{-3F_{po}}{(R)^{1/2}} \left[\frac{3(\delta_o - \delta_{po})}{3.3} \right]^{-3/2} \quad (3.1)$$

where R is the probe radius, F_{po} is the pull-off force that is measured to fully separate the probe from each sample under the corresponding loading and environmental condition, and the relative positions δ_{po} and δ_o are illustrated in Figure 3.3a. This implementation of the JKR theory does not require identification of the absolute contact point, and is thus less sensitive than other implementations to accurate identification of this contact point³¹. As discussed in Section 3.2.3.2.1, this analytical insensitivity is particularly advantageous for the analysis of materials as compliant as these tissue surrogate gels.

In contrast, the P - h response of tissues, obtained through instrumented indentation in fully immersed and hydrated conditions, exhibited no significant adhesion or pull-off force upon unloading. Therefore, E_r of tissues was calculated according to the method of Oliver and Pharr, which relates E_r to the unloading slope dP/dh , contact depth h_c , and indentation contact area taken as a geometric function of probe radius R and h_c ⁸⁸. Note that the quantity E_r combines the modulus of the indenter and the sample, and is defined as¹⁴⁹:

$$\frac{1}{E_r} = \frac{(1 - \nu_s^2)}{E_s} + \frac{(1 - \nu_i^2)}{E_i} \quad (3.2)$$

where the subscript s indicates the sample and i indicates the indenter. As the elastic moduli E_s of these gels and tissues is considerably lower than that of ruby or steel, E_r is effectively equivalent to $E_s/(1-\nu_s^2)$, the Young's elastic modulus of the sample as inferred from instrumented indentation and the (assumed or separately measured) Poisson's ratio ν_s of that sample. Herein, all elastic properties of the sample are reported as E_s , a calculation for which we assumed Poisson's ratio $\nu = 0.5$ for all samples.

To facilitate comparison with dynamic energy dissipation via impact loading, energy dissipation for each indentation P - h cycle was determined as the dissipated work W_p normalized by the total work of indentation W_t , where $W_t = W_p + W_e$ and W_e is the reversible work of indentation (as illustrated in Figure 3.3a). Here, subscript notation developed for indentation of elastoplastic materials is preserved, but it is noted that these gels and tissues are deformed within the viscoelastic regime; plastic deformation was not observed in terms of permanent deformation that was visible or measurable upon complete unloading at the conclusion of the experiment, but work is still dissipated over the load- and time-scales of these experiments and is quantified here as W_p .

3.2.3.3 Results

Figure 3.4 presents representative stress vs. strain responses from unconfined compression and load vs. displacement responses from quasistatic indentation tests for the triblock/diblock gels in comparison to heart and liver. Figure 3.4a showed that the gels exhibited a linear response for the strains explored here, and were much stiffer than both heart and liver. Heart and liver exhibited a linear response up to ~13% and 18% strain, respectively. Similarly, Figure 3.4b also demonstrated that gels were stiffer compared to soft tissues, with liver being the most compliant among all samples. Note that the indentation responses of soft tissues shown here are reported in post-processed format, to more accurately define initial contact. For liver, calculated contact depths h_c (~80 μm) were larger than the thickness of the liver capsule (~5 μm), suggesting that a volume-averaged mechanical response of the whole tissue is captured, rather than a response attributable to individual tissue layer(s). For heart, h_c (~30 μm) were smaller than the thickness of fibrous layer of the pericardium t (~1 mm). However, according to Dimitriadis et al., given that t (~1 mm) $< 12.8R$ (where $R = 1$ mm), an assumption of semi-infinite thickness of this layer relative to the contact depth is invalid¹⁰⁶. Further, calculated geometric contact volumes (via Equation 3.8) were $\sim 3 \times 10^{-3} \text{ mm}^3$, and strain volumes will be larger than these contact volumes. Therefore, we infer that the properties explored herein were not those of individual layer(s), but rather represented a composite response including multiple layers of the heart wall.

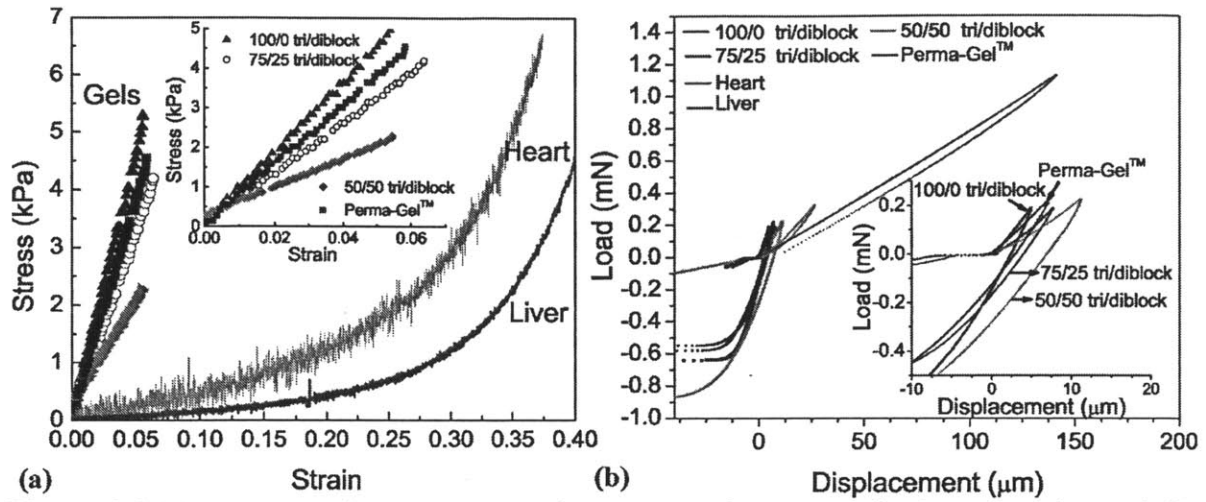


Figure 3.4 (a) Representative stress vs. strain responses from unconfined compression and (b) load vs. displacement responses from quasistatic indentation tests for triblock/diblock gels compared to heart and liver. Insets show only the gel response.

From the responses shown above we calculated and compared the effective elastic modulus E_s of the tissues to that of the polymeric tissue simulants, in order to investigate the extent to which the elastic properties of the tissues could be replicated by these gels. For the gels, elastic moduli inferred from macroscale experiments and microscale indentation experiments agreed reasonably well (Figure 3.5a), in that calculated E for each sample were within a factor of two from each other; generally, E calculated from macroscale experiments indicated lower elastic moduli for a given sample.

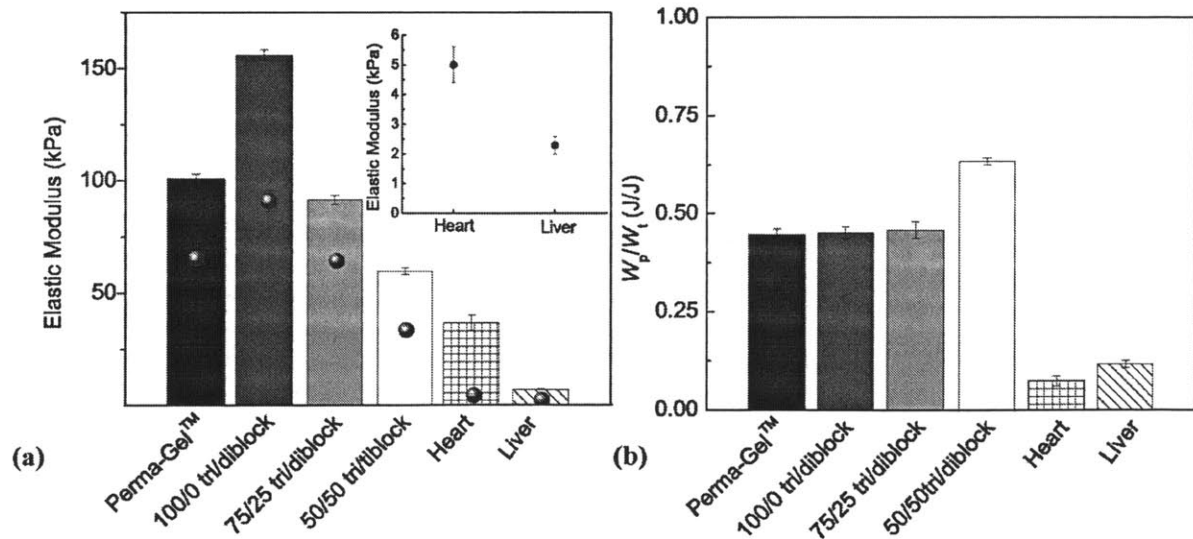


Figure 3.5 Comparison of Young's moduli (mean \pm standard error) inferred from unconfined compression (points) and $E_{O\&P}$ for tissues and E_{JKR} for tissue surrogate gels inferred from

instrumented indentation (bars). Inset magnifies data for Young's moduli of heart and liver inferred from unconfined compression. (b) Energy dissipation calculated from indentation $P-h$ responses (mean \pm standard error) shows that tissues exhibit a lower energy dissipation capacity than the gels at quasistatic rates.

The finite discrepancies in calculated E from may be attributed to either experimental uncertainties and/or to differences in the volumes of material analyzed. For the tissues, this discrepancy can be attributed in part to higher strains achieved at microscale experiments (i.e., accessing the nonlinear regime) and/or the difficulties in accurately accounting for sample dimensions in macroscale experiments. Appreciable curvature of sectioned tissues introduced uncertainty in calculation of the cross-sectional area over which loads were applied, and inherent variation in thickness of the sectioned tissue specimens; this tissue curvature was more pronounced in the cardiac muscle of the heart. These factors contribute uncertainty to calculations of the stress vs. strain responses, and thus the calculated elastic moduli via linear regression of defined portions of the stress-strain responses. Additionally, there exists a considerable difference in the cross-sectional areas sampled via unconfined compression and instrumented indentation of these tissues (mm^2 vs. μm^2), such that the indentation strain volume may not be sufficiently large to serve as a representative volume element of macroscopic mechanical response. Of course, this argument of length scale heterogeneity will not hold for the gels, as those amorphous-network materials exhibit a homogeneous structure at the length scales investigated by both methods. Here, the less than two fold increase in E inferred from instrumented indentation (e.g., $E_{1000} = 156.0 \pm 2.5$ kPa from indentation vs. $E_{1000} = 91.5 \pm 4.7$ kPa from unconfined compression) can be attributed in part to uncertainties in the magnitude of the probe radius R^{150} .

Beyond consideration of these method-dependent estimates of E , we found through either approach that E decreased significantly with increasing vol%-diblock of the synthetic gels. This was expected from the higher crosslinking concentration of the triblock phase¹⁵¹⁻¹⁵², since the replacement of SEBS chains by SEP chains induces a decrease in the number of bridges that can act as physical crosslinks that are formed between micelles. These results demonstrate that instrumented indentation can discern the mechanical difference between copolymers of different %triblock compositions and mechanical differences among tissues, even for very compliant gels and tissues ($E < 200$ kPa) under appropriate hydration conditions. Instrumented indentation also

clearly indicated that liver was the most compliant of all the materials studied here ($E_{liver} = 9.6 \pm 2.1$ kPa; $E_{heart} = 36.8 \pm 3.5$ kPa). Our results fall well within in the range of E reported previously for these tissues from macroscale uniaxial compression and tensile tests^{132-133,153}, further supporting the accuracy of our finding that hydrated liver tissue is more compliant than hydrated heart tissue.

Further, indentation results showed that the elastic moduli of the 50/50 tri/diblock gel was best matched to that of heart tissue ($E_{50/50} = 59.1 \pm 4.6$ kPa; $E_{heart} = 36.8 \pm 3.5$ kPa). This appears to indicate that the 50/50 tri/diblock gel is a candidate tissue simulant material to mimic the elastic properties of the tissues investigated herein. However, the concept of tissue simulant must be further defined in terms of utility – that is, defined by the range of deformation and deformation rates over which the mechanical response is intended to replicate that of tissue. To illustrate this point, Figure 3.5b compares the energy dissipation of these tissues and tissue simulant gels (as opposed to the effective elastic moduli) at these low loading rates and effective displacement rates (0.01 mN/s or 1 μ m/s). It is clear that the tissues dissipate considerably less energy than the gels at these rates.

Note also that the energy dissipation capacity of the 50/50 triblock/diblock is greater than that of the 100/0 triblock/diblock styrenic gel. From a materials design perspective, this increase in energy dissipation capacity within increasing vol%-diblock can again be rationalized by microstructural changes in the gel as a function of composition (see Figure 3.2). Decreasing the concentration of triblocks in the polymer will then decrease the number of bridges formed between micelles. These bridges are known to act as active chains in elastic energy restoration, and are treated as elastic springs¹⁴⁷. Therefore, a decrease in the number of bridges will have a negative impact on the materials capacity to recover elastic strain energy. In the context of the tissue surrogate candidates, of course, the goal is to recapitulate the energy dissipation capacity of these tissues at deformation rates of interest.

Thus, although $E_{50/50}$ is within 63% of E_{heart} , the capacity of each material to dissipate and restore imposed energy of contact deformation at these rates is significantly different. Indeed, for the initial intended application of these tissue simulant gels, it is the energy dissipation response at

high impact velocities that is of interest. Recapitulation of the quasistatic elastic moduli would thus be irrelevant if replication of the dynamic energy dissipation is not attained for the same material. (In other distinct applications, recapitulation of E at quasistatic loading rates would be the target property of the simulant, and in those cases instrumented indentation as outlined above would be the appropriate experiment, verified to be within a factor of two of macroscale E for the strain volumes attained herein.) Therefore, in order to determine whether the 50/50 triblock/diblock was a suitable tissue simulant material for the high rates of impact deformation of interest in this application, we conducted and analyzed impact indentation experiments on these gels and tissues under appropriate hydration conditions in Section 3.3.

3.2.4 Multiscale characterization of relaxation modulus and relaxation times

Following work has been published in 2010 in 27th Army Science Conference Proceedings with coauthors M. Qu, K. Strawhecker, M. VanLandingham, and K. J. Van Vliet¹⁵⁴.

Here, we characterize the viscoelastic stress relaxation response of heart and candidate tissue simulant gels composed of thermoplastic styrenic triblock/diblock copolymers. We explore the effects of gel composition and probe contact area on the relaxation modulus $E(t)$ and characteristic relaxation times τ of these tissue simulant gels, with comparisons to tissue response. We observe that $E(t)$ varies only as a function of vol-% triblock, whereas τ varies as a function of volume of the material probed. The latter variation is explained by the coupling between viscoelastic material deformation and probe-material adhesion. Finally, we find that heart tissue is more compliant and relaxes more quickly than the candidate tissue surrogate gels studied here.

3.2.4.1 Methods

Macroscale stress relaxation testing was conducted by Dr. Kenneth Strawhecker (ARL) using a rheometer (AR 2000, TA Instruments) for the gels and a universal load frame (Instron) for the tissues. Gel samples were punched (15 mm diameter) from ~4 mm thick sheets. A thin layer of silicone oil (1000 cst) was used to lubricate sample/plate contact regions. For heart tissue, discs of 8 mm diameter and thickness of 3 to 4 mm were prepared using a surgical punch. For the gels, applied strains were 7%, and for heart tissue, strains were held at 10% in order to confine the material behavior to the linear viscoelastic regime.

Mesoscale load relaxation testing was conducted on the gels using an instrumented indenter (TriboIndenter, Hysitron, Inc.) with a truncated cone of radius $R = 50 \mu\text{m}$. Indentation depths h were held constant at 500 nm with a rise time of 1 s and a hold time of 100 s. Because the change in the contact areas was 1% over this hold period, the probe geometry was approximated as a flat punch. Applied strains were calculated as the ratio h/R and were $\sim 1\%$. Note that the load relaxation response of heart tissue could not be characterized using this instrument, given that we did not have the necessary equipment (i.e., elongated shaft for the indenter) in order to test the tissue in fully hydrated conditions without damaging the electronics.

Microscale AFM-enabled indentation and load relaxation experiments were performed only on the 100/0 triblock/diblock gel (3D-MFP, Asylum Research). Modified plateau probes (PL2-FM, Nanosensors), which have nominal spring constants of $\sim 1\text{-}5 \text{ N/m}$, were used. PL2-FM probes have geometries similar to a “flat punch” with a plateau diameter of $1.8 \mu\text{m} \pm 0.5 \mu\text{m}$. Experiments were conducted in air, in water, and in PBS+0.2% Pluronic® F108 solution. Pluronic® F108 is a nonionic polyethylene-polyoxypropylene (PEO-PPO) block copolymer surfactant terminating in primary hydroxyl groups. Indentation experiments were conducted with a maximum force of 180 nN and a constant piezo velocity of $2.6 \mu\text{m/s}$ with no dwell period. For load relaxation experiments, indentation depths were held constant at $1 \mu\text{m}$ with a rise time of 1 s and a dwell period of 60 s to minimize drift. AFM phase images were acquired in air using AC mode at a scan rate of 0.5 Hz with sharp silicon cantilevers (OMCL AC240TS-W2, Olympus). Images of the gel-probe system were also acquired in air via optical microscopy.

3.2.4.2 Analysis

For macroscale stress relaxation experiments, relaxation modulus $E(t)$ can be calculated as:

$$E(t) = \sigma(t)/\varepsilon_o \quad (3.3)$$

where σ is instantaneous stress calculated from force normalized by cross-sectional sample area and ε_o is applied strain. For mesoscale and microscale load relaxation experiments, a linear viscoelastic model for indentation of a rigid flat punch into a homogeneous, isotropic material was used to fit the load vs. time response to calculate $E(t)$ which was expressed as a general Maxwell model¹⁵⁵:

$$E(t) = E_{\infty} + \sum_{i=1}^N E_i e^{-\lambda_i t} \quad (3.4)$$

where, E_{∞} , E_i are relaxation coefficients, λ_i are the reciprocals of relaxation times and N is the number of exponential terms in the Prony series. To calculate the relaxation time scales τ , normalized stress (at the macroscale) or normalized force (at the mesoscale and microscale) vs. time responses were described reasonably well using a stretched exponential of the KWW type¹⁵⁶:

$$x(t) = x_0 e^{-(t/\tau)^{\beta}} \quad (3.5)$$

where β describes the distribution of relaxation times with values between zero and unity.

For microscale AFM-enabled indentation experiments, Young's elastic modulus E was calculated by fitting the loading part of the load vs. time response, using the solution for indentation of a rigid flat punch indenter into a homogeneous, linear elastic and isotropic material¹⁵⁷:

$$E = P(1 - \nu^2)/(2hR) \quad (3.6)$$

where P is force and ν is Poisson's ratio that we assumed to be valued 0.5 for these gels.

3.2.4.3 Results

3.2.4.3.1 Macroscale Stress Relaxation

Macroscale relaxation modulus calculated via Equation 3.3 varied significantly as a function of composition (Figure 3.6a). First, instantaneous modulus E_0 calculated from $E(t=0)$ increased as the triblock vol-% was increased. This stiffening can be explained via the difference among samples in terms of the number of bridges formed between micelles that act as physical crosslinks (elastic springs). Only triblocks are capable of forming bridges, and thus increasing the triblock concentration increases the crosslink percentage as seen in Figure 3.2. Second, heart tissue exhibited the most compliant behavior. In order to match tissue response, theoretically these gels can be rendered more compliant by increasing vol-%diblock. However, in this material system, complete gelation could not be achieved for triblock composition <50 vol%.

Fits of the macroscale stress vs. time response via Equation 3.5 showed that relaxation times τ were on the order of 1000 s (Figure 3.6b). The long relaxation times found here is consistent

with macroscale stress relaxation experiments conducted on other styrenic triblock gels¹⁵⁸. Both τ and the distribution of relaxation times β were not strongly dependent on vol-% triblock. The relatively low value of β (compared to unity) indicated that there were multiple relaxation processes activated in this system. Further, heart tissue exhibited a much faster relaxation and a wider distribution of relaxation times.

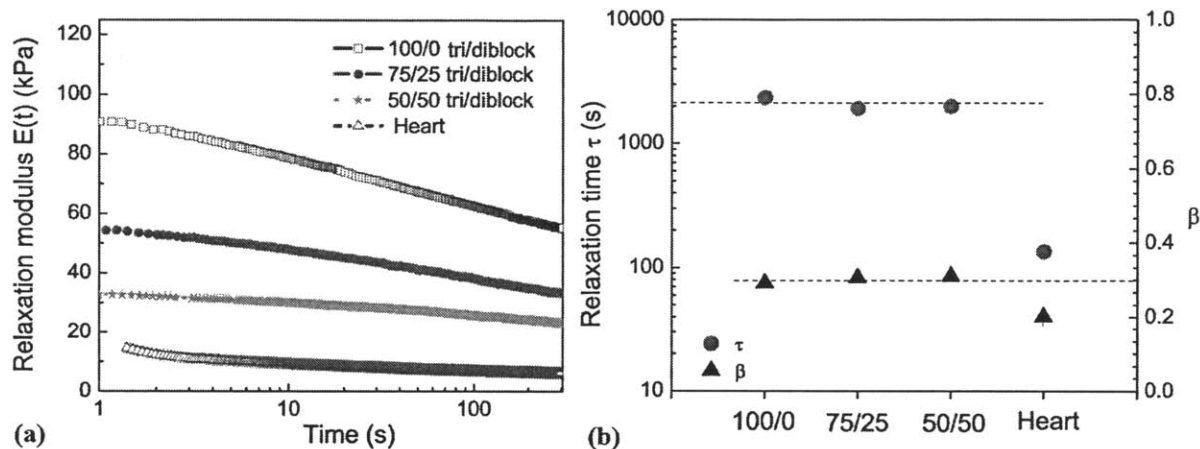


Figure 3.6 (a) Macroscale relaxation modulus of tissue surrogate gels and heart tissue. (b) Calculated τ and β by fitting stress vs. time response via Equation 3.5.

3.2.4.3.2 Mesoscale Load Relaxation

Mesoscale relaxation moduli of the triblock/diblock gels confirmed this macroscale result: increasing the vol-% triblock stiffens the gel (Figure 3.7a). Although the contact areas were orders of magnitude smaller than in those macroscale experiments (100s of μm^2 vs. mm^2 for the latter case), for a given sample, the difference in macroscale and mesoscale $E(t)$ was less than 50%. This general agreement between these length scales was expected in that, in both cases, contact areas were much larger than the micelle dimensions. Therefore, at these length scales, the gels exhibit a homogeneous mechanical response.

As in the macroscale experiment, the calculated mesoscale relaxation times were also on the order of 1000 s, and did not exhibit a significant dependence on vol-%triblock (Figure 3.7b). The distribution of relaxation times τ was on the order of 0.2-0.3, also similar to macroscale results.

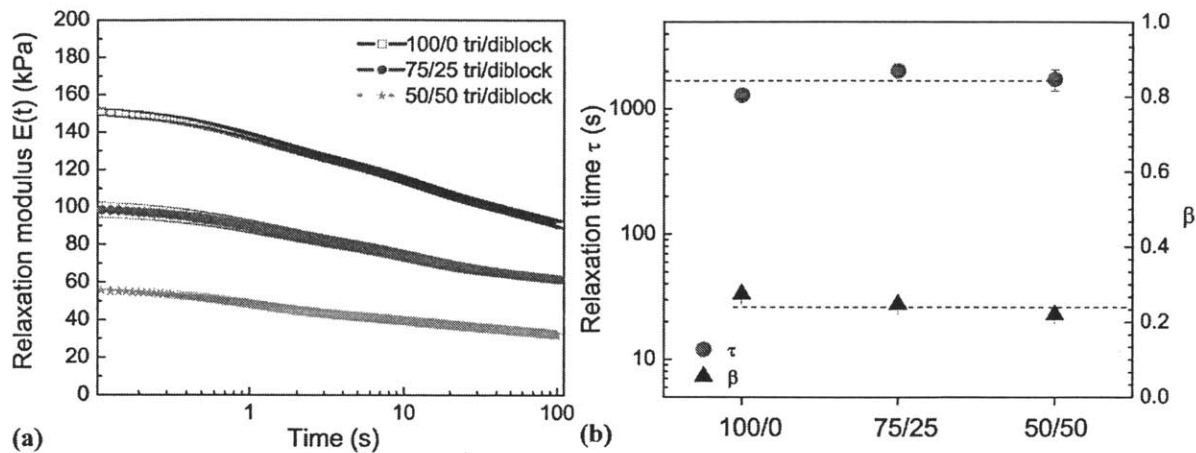


Figure 3.7 (a) Mesoscale relaxation modulus of triblock/diblock gels as a function of vol-%triblock. (b) Calculated τ and β as a function of vol-%triblock by fitting load vs. time response via Equation 3.5. Data represented as mean \pm standard error.

3.2.4.3.3 Microscale AFM-Enabled Load Relaxation

AFM-enabled relaxation experiments were conducted on the 100/0 triblock/diblock gel to investigate the effects of length scale on the characteristic relaxation time scales. Note that at these small contact areas, other factors such as adhesive forces between the probe and the sample can play a role in the measured relaxation times (Figure 3.8a inset). To investigate this potential contribution, experiments were conducted in air, in water, and in PBS+0.2% Pluronic® F108. In general, pluronic surfactants adsorb to hydrophobic surfaces with the PEO block extending into the solution and the more hydrophobic PPO block anchoring as loops and trains¹⁵⁹. Both in air and in water, adhesive forces between the gel and the probe were comparable to the applied maximum loads (Figure 3.8a). In PBS+0.2% Pluronic® F108, these adhesive forces were negligible when compared to maximum applied loads.

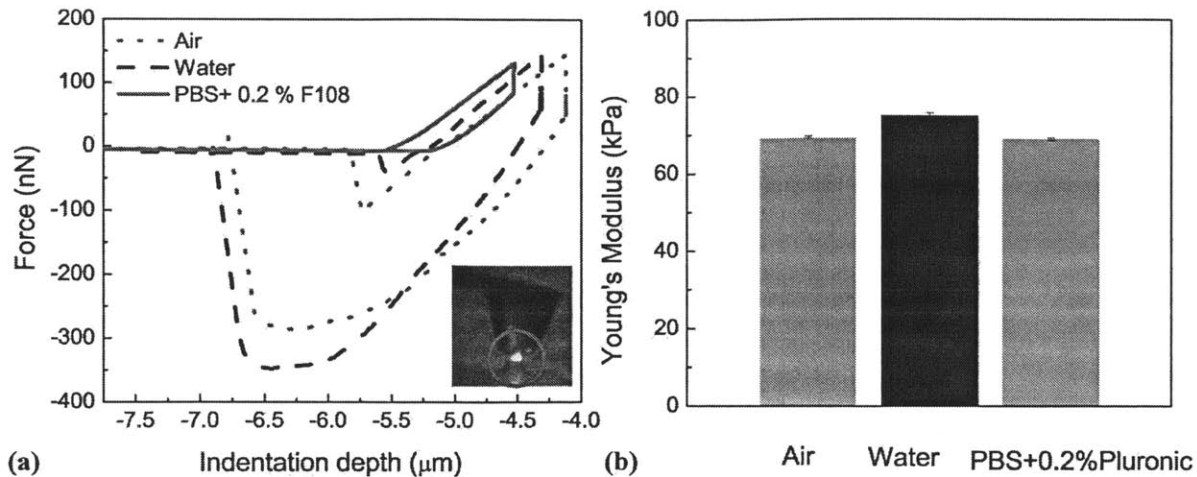


Figure 3.8 (a) Representative load vs. depth responses of 100/0 triblock/diblock gel as a function of immersion environment. Inset: optical microscope image of the gel adhering to the probe during AFM experiments in air. (b) Young's elastic modulus of 100/0 triblock/diblock gel as a function of immersion environment. Data represented as mean \pm standard error.

To investigate the effect of immersion environment on the surface mechanical properties of the gel, quasistatic indentation experiments were conducted via AFM. Young's moduli E were calculated from the load vs. indentation depth responses via Equation 3.6. The results showed that E did not change significantly as a function of environment (Figure 3.8b). Thus, we concluded that this surfactant reduced adhesion without changing the mechanical properties (of the material as measured at the surface via indentation) significantly.

Stress relaxation experiments were conducted in all three environments. The raw load vs. time responses showed that maximum forces obtained for all cases was comparable (Figure 3.9). It was observed that both in air and in water, environments conducive to higher adhesive forces, force relaxed more quickly. On the other hand, in PBS+0.2% Pluronic® F108 which enabled negligible adhesive forces, force relaxed more slowly.

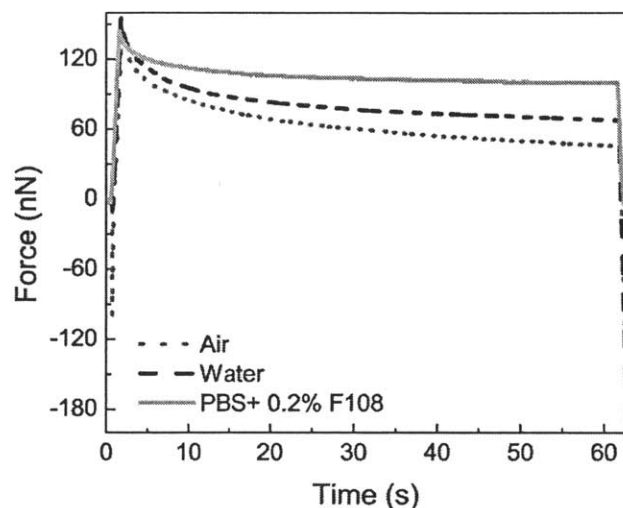


Figure 3.9 Representative load vs. time responses of the 100/0 triblock gel in air, in water, and in PBS+0.2% Pluronic® F108.

Quantitative analysis of $E(t)$ further demonstrated that immersing the sample in these solutions does not affect the instantaneous elastic moduli appreciably: E_o in air (63 ± 0.7 kPa) and in PBS+0.2% Pluronic® F108 (56 ± 0.4 kPa) were comparable (Figure 3.10a). In contrast, relaxation moduli $E(t)$ of this gel exhibited similar behavior in air and in water, but changed much more slowly over time in Pluronic® because the forces relaxed more slowly in the absence of appreciable probe-gel adhesion.

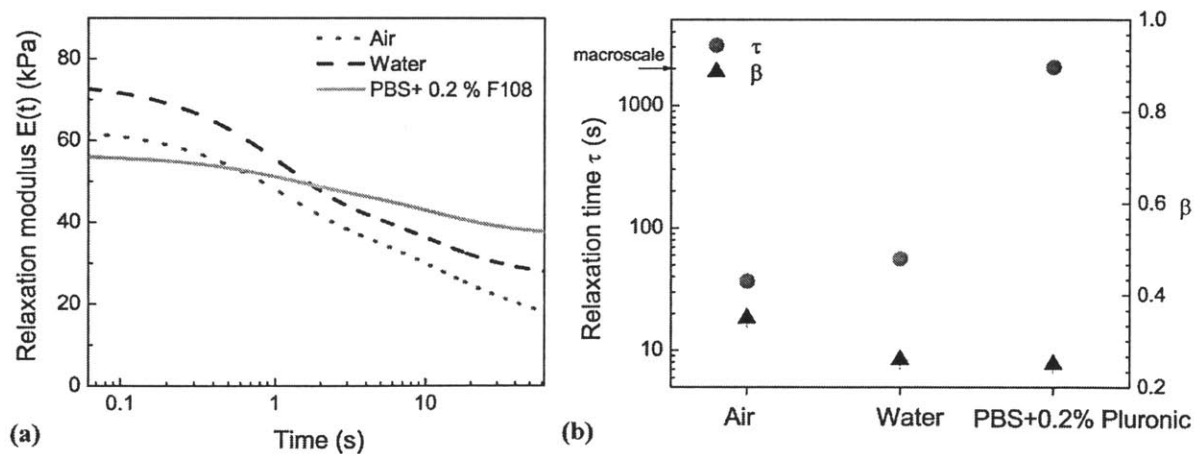


Figure 3.10 (a) Microscale relaxation modulus of 100/0 triblock/diblock gel as a function of immersion environment. (b) Calculated τ and β in different immersion environments.

The relaxation times calculated from load vs. time responses showed that both in air and in water, τ was on the order of 10s of seconds (Figure 3.10b). This relaxation time is two orders of magnitude smaller than that determined from macroscale and mesoscale experiments. In PBS+0.2% Pluronic® F108, τ was calculated to be on the order of 1000 s, and was thus comparable to that measured in larger scale experiments.

3.2.4.4 Discussion

3.2.4.4.1 Effect of Composition on $E(t)$ and τ

Both macroscale and mesoscale analyses showed that the relaxation modulus increases with increasing vol-% triblock. This result is explained by the replacement of SEBS chains by SEP chains, which induces a decrease in the number of bridges that form a network connecting the physical crosslinks (micelles). In contrast, τ and β did not show dependence on the vol-% triblock, i.e., on the stiffness of the gels. Similar results have also been shown previously on biological cells: τ and β calculated from stress relaxation experiments via AFM on human hepatoma cell line HEPG2 were independent of the estimated cell elastic modulus E^{160} . In general, relaxation time is strongly dependent on factors that affect molecular mobility within the material and is correlated inversely to the rate of molecular motion. For triblock systems, τ depends on temperature, endblock length, polymer volume fraction and aggregation number of micelles (number of endblocks per micelle)¹⁶¹. For the systems studied here, we did not vary the temperature, endblock length, or polymer volume fraction. Further, addition of diblock into a triblock system is expected to decrease the number of bridges and thus decrease the elastic modulus; however, it is not expected to affect the micelle aggregation number¹⁶¹. This lack of change in the micelle structure explains why τ and β did not depend on the triblock vol-%. Heart tissue exhibited more compliant behavior and shorter relaxation times than all the gels considered here. Although further increases in gel compliance cannot be achieved by changing the diblock ratio due to incomplete gelation, other factors such as chain length and polymer volume fraction can be tuned for designing tissue simulant gels with stiffness and relaxation time constants that are optimum for the application of interest.

3.2.4.4.2 Comparing $E(t)$ and τ at Different Contact Areas

This study investigates the relaxation modulus and time scales of triblock/diblock gels over a wide range of contact areas; macroscale (10s of mm²), mesoscale (100s of μm^2) and microscale

($\sim 1 \mu\text{m}^2$). The micelle diameters in Figure 3.1f are on the order of nm, and thus the 100/0 triblock/diblock gels are expected to deform homogeneously over the length scales investigated here. Therefore, $E(t)$, τ and β should not depend on the method of testing considered in the present study. Macroscale, mesoscale, and microscale relaxation experiments showed that the instantaneous elastic modulus E_o of these gels was indeed independent of the method of interest. For example, the 100/0 triblock/diblock gel exhibited an instantaneous modulus of 95 kPa, 150 ± 2 kPa and 63 ± 0.7 kPa calculated at the macroscale, mesoscale and microscale, respectively, which are all within 50% variation. Further, differences between our macroscale rheometry and indentation results can be attributed in part to uncertainties in defining the contact point (for mesoscale experiments) and to the assumption of manufacturer-provided AFM probe diameter (in microscale experiments).

In contrast to this length scale-independence for $E(t)$, studies conducted in air on the 100/0 triblock/diblock gel showed that τ varied significantly among these methods. As the contact areas decreased, τ decreased by two orders of magnitude ($\tau_{AFM} = 36 \pm 2$ s (in air) vs. $\tau_{macroscale} = 2340$ s (in air)). Because this gel was structurally homogeneous at the contact areas investigated here, the difference in the calculated τ values was attributed mainly to the increased contribution of adhesive forces to load relaxation that is observed at the small scales. As shown in the inset of Figure 3.8a, visualization of contact between the flat punch AFM probe and polymer gel surface in air provided evidence of capillary flow of the gel along the probe sidewalls. Immersing the gel in water can decrease the capillary and electrostatic forces; however, water immersion did not decrease the total adhesion force for this system. In previous studies of stress relaxation of cells via AFM, researchers have attempted to minimize adhesion by using chemically coated cantilevers, in order to make sure that the relaxation of the load is only due to viscoelastic nature of the material¹⁶². We also attempted several such chemical functionalization approaches for these AFM probes, but did not identify a surface functionality that significantly reduced adhesion in air. Here we observe that minimization of probe-sample adhesion via addition of a surfactant to the immersion environment results in a calculated τ of 2050 ± 388 s, which is comparable to macroscale results. Therefore, we conclude that in small-scale stress relaxation experiments, adhesion should be accounted for and minimized to accurately determine relaxation times. The errors arising from the effect of adhesion will be even more crucial for accurate characterization

of the mechanical properties of composite gels or soft tissues. In such structurally heterogeneous materials, the inferred mechanical properties will also depend on the volume of material probed.

3.2.4.5 Summary

In this study, we reported the relaxation modulus $E(t)$ and characteristic time scales τ of triblock/diblock gels as a function of composition and length scales, and compared the results with that of heart tissue. We concluded that $E(t)$ depends on vol-% triblock but did not depend on the volume of material probed over the length scales investigated. Relaxation times calculated from experiments conducted in air did not depend on the vol-% triblock, but could depend on the volume of material probed due to relatively stronger contributions of adhesion at smaller length scales. Relaxation time measured in air were two orders of magnitude smaller than relaxation times measured in PBS+0.2% Pluronic® F108, an immersion environment that minimizes probe-sample adhesion. Therefore, adhesion contributes significantly to load relaxation in small-scale experiments, and must be taken into account in order to decouple adhesive and viscoelastic properties.

3.2.5 Conclusion

In the present work we have combined macroscale unconfined compression, mesoscale indentation and microscale AFM techniques to characterize the structure property relationship of triblock/diblock gels as potential tissue stimulants in comparison to heart and liver tissue under quasistatic rates. For the indentation experiments, we developed a method to accurately define the actual contact points which can be further utilized for accurate testing of other compliant materials ($E < 100$ kPa). Multiscale quasistatic tests showed that the stiffness and the energy dissipation capacity of the triblock/diblock gels can be tuned by changing the vol%- triblock. Heart and liver tissue were found to be more compliant and dissipate less energy than these gels under quasistatic rates. Multiscale relaxation experiments showed that while relaxation modulus $E(t)$ could be tuned by changing the vol%-triblock, relaxation times τ could not be tuned. Heart tissue was found to relax quicker than the triblock/diblock gels. Finally, a method to decrease adhesive forces between the sample and the probe was demonstrated, and this adhesion mitigation was shown to be required for accurate analysis of relaxation response of triblock gels probed at the nanoscale.

3.3 Quantification of impact resistance and energy dissipation via high rate impact indentation

The following study has been published in 2011 in Philosophical Magazine A with coauthors by M. Qu, K. Strawhecker, T. Shazly, E. Edelman, M. VanLandingham, J. Smith, and K. J. Van Vliet¹²⁸, and is reprinted with the permission of Taylor and Francis.

The objective of this section is to characterize quantitatively the response of soft tissues and synthetic polymer simulants to concentrated-impact loading, and to compare the deformation of soft tissues and mechanically optimized simulants. Note that the characterization and design of tissue simulant materials can pivot on a range of applications, depending on the properties one intends to recapitulate. For example, one could choose to achieve similar pore sizes (structural surrogacy) or adherent cell morphology (biological surrogacy), or similar cutting resistance (mechanical performance surrogacy). The focus of the current section is surrogacy of the penetration resistance and the rate and extent of energy dissipation by the organogel candidates, as compared to specific soft tissues, under concentrated impact loading.

3.3.1 Introduction

There exists a growing need to quantify the mechanical behavior of tissues under dynamic loading conditions. Such studies enable prediction of the deformation and energetic dissipation under high-rate loading “impact events” such as industrial accidents, ballistic injuries, and blasts^{2,67}. In addition, there exists a concurrent need for tissue simulant materials, synthetic materials capable of simulating the mechanical responses of biological tissues. Tissue simulants serve as mechanical mimics of hydrated tissues, and can be examined in ambient conditions under controlled laboratory testing. These materials are used to help evaluate tissue-engineering designs and the efficacy of technologies including protective garments¹⁶³. Thus, tissue simulants must be synthesized reproducibly, and must enable application of repeated, defined loading conditions that are similar to the forces applied to the fully hydrated soft tissues they are intended to mimic mechanically.

A growing number of reports have quantified mechanical properties of soft tissues via a variety of quasistatic methods including macroscale tension, unconfined compression and microscale indentation experiments^{6,17,25,37-38,57,132,134}. Further, dynamic mechanical analysis of soft tissues have been explored via methods such as oscillatory

loading^{60,136,164-165} and indentation recovery¹⁶⁶. However, the mechanical response of soft tissues to impact loading at the high rates relevant to insult and injury is relatively less explored. Recent macroscopic studies have included falling-weight impact tests⁷², Kolsky or split Hopkinson pressure bar-based experiments^{63,65-67}, instrumented impacters⁷³ and blunt impact tests using a pendulum-like apparatus⁶⁸⁻⁶⁹. These macroscale approaches are certainly important as a first step in characterizing responses of soft tissues under impact loading, and can facilitate comparisons among tissue types. However, most such studies to date have explored the energy dissipation capacity of tissues in ambient air rather than fully hydrated environments that define the relevant structure and mechanical properties of biological tissues²². This shortfall motivates the design of new techniques that enable measurement of multiscale mechanical properties of hydrated tissues, under extreme loading conditions. Such methods could also aid in the development of highly compliant synthetic materials for a variety of biomedical and other applications.

Here, we demonstrate that contact loading via impact indentation can be employed to characterize the mechanical behavior of hydrated tissues and tissue surrogate materials under concentrated impact. We first adapt the experimental methods and analysis, initially proposed for metals and glassy polymers¹⁶⁷⁻¹⁶⁸, to address key differences in the application to soft tissues in hydrated environments. We then demonstrate the application of this approach to characterizing the impact energy dissipation and resistance to penetration of tissues and tissue simulant gels that are intended to replicate the tissue responses under impact loading conditions. Such analysis enables identification of design principles by which tissue simulant materials can be engineered to match better the dynamic response of specific soft tissues under comparable mechanical deformation states, rates, and insults. More specifically, we employed microscale contact-loading methods to quantify the mechanical response of murine liver and heart tissues. These tissues are located in the abdominal and chest cavities, respectively, and are commonly damaged by high-impact mechanical insults. We compared a commercially available tissue simulant, Perma-GelTM, with blends of styrenic triblock (ABA) and diblock (AB) copolymers². Dynamic impact loading indicated the opportunity to tune the energy dissipation of the block copolymers as a function of diblock content. Under the impact conditions of interest, we were thus able to identify design principles and triblock/diblock compositions that best matched the impact resistance and energy dissipation of hydrated heart and liver tissues.

3.3.2 Experimental methods and analysis

3.3.2.1 Materials and tissues

Two types of synthetic materials were considered as potential surrogates of tissue impact response, including Perma-GelTM (PERMA-GEL, Inc.), a commercial ballistic organogel of proprietary composition that is physically stable at room temperature¹⁶⁹; and gels formed from styrenic block copolymers (Kraton Polymers) with triblock:diblock volume ratios of 100/0, 75/25 and 50/50 as explained in Section 3.2.2. Heart and liver tissues were harvested as explained in Section 3.2.2.

3.3.2.2 High rate impact indentation experiments

For both gels and tissues, impact experiments were conducted to ascertain the dynamic response of materials under concentrated impact loading at elevated rates. Pendulum-based impact experiments were conducted using a commercial instrumented indenter (Micro Materials, Ltd.) as described previously¹⁶⁷⁻¹⁶⁸, using a stainless steel probe of radius $R = 2$ mm on all materials (see Figure 2.1a). Gels adhered readily and strongly to a bulk aluminum alloy support. Tissues were adhered to the aluminum support with a thin layer of cyanoacrylate (<5 μm , as compared to the 3 to 5 mm-scale thickness of these tissues). Tissue samples were fully immersed in Krebs-Hensleit buffer using the modified platform for fluid immersed experiments we have described in Chapter 2⁸¹. The force pendulum in this instrument is actuated to apply load via electromagnetic interaction between the conductive coil at its “top” toward the stationary magnetic plate positioned behind the coil, and articulates about a frictionless pivot of compliant leaf springs; displacement of the probe mounted rigidly toward the “bottom” of the pendulum is measured via a parallel-plate capacitor. To achieve impact loading, the pendulum position is maintained via a solenoid/magnet assembly below the probe, while the electromagnetic coil current above the probe is increased; shutting off the solenoid then releases the “loaded” pendulum such that the probe swings toward the sample with high kinetic energy. Resulting probe displacement is recorded as a function of time, until the probe comes to rest at the sample surface. Here, the physical limit stop (which sits behind the pendulum for quasistatic indentation experiments) was retracted to achieve both high impact velocities and high impact penetration depths into such compliant samples to remove this potential obstruction of the pendulum motion. Impact velocities investigated here ranged from 2 to 20 mm/s. For the probe of mm-scale radius

employed in the present experiments, the resulting strain energy density depends naturally on each material's resistance to penetration, and ranged from 0.4 to 20 kJ/m³ among all samples.

3.3.2.3 Analysis of energy dissipation from indentation impact experiments

In general, pendulum based impact tests conducted here can be fully described by damped harmonic oscillatory motion (Figure 3.11a). This response upon impact and subsequent oscillation against the sample is well fit by an exponentially decaying time-dependent function of the indenter displacement, upon impact and oscillation against a sample¹⁷⁰:

$$h(t) = h_0 \exp^{-\gamma t/2} \quad (3.7)$$

where $\gamma/2$ is the inverse of the decay time τ of the pendulum oscillation. Natural angular frequency ω is measured by $\omega = 2\pi/t^*$, where t^* is the measured period of oscillation.

Energy dissipation upon impacting the sample can be calculated as the effective quality factor Q of the damped oscillatory system. This Q is a dimensionless number that we here compute as:

$$Q = \omega/\gamma = 2\pi/(t^*\gamma) \quad (3.8)$$

for a measured $h(t)$ response. Equivalently, $Q/2\pi$ is the ratio of energy stored per cycle to energy lost per cycle¹⁷¹. For completeness, we note that qualitative differences in Q can be observed directly from the $h(t)$ response: the number of indentation impact cycles n required for the amplitude of oscillation to fall by a factor of e occurs over approximately Q/π cycles of oscillation (see Figure 3.11a)¹⁷⁰. Note that, Q of a system is large compared to unity for impact of materials and/or conditions exhibiting small rates of energy dissipation (i.e., more cycles of oscillation to achieve a given decrease in the depth of penetration or amplitude of oscillation). Conversely, a system of low Q will exhibit a higher energy dissipation rate; fully dissipating the total impact energy over a shorter duration of time.

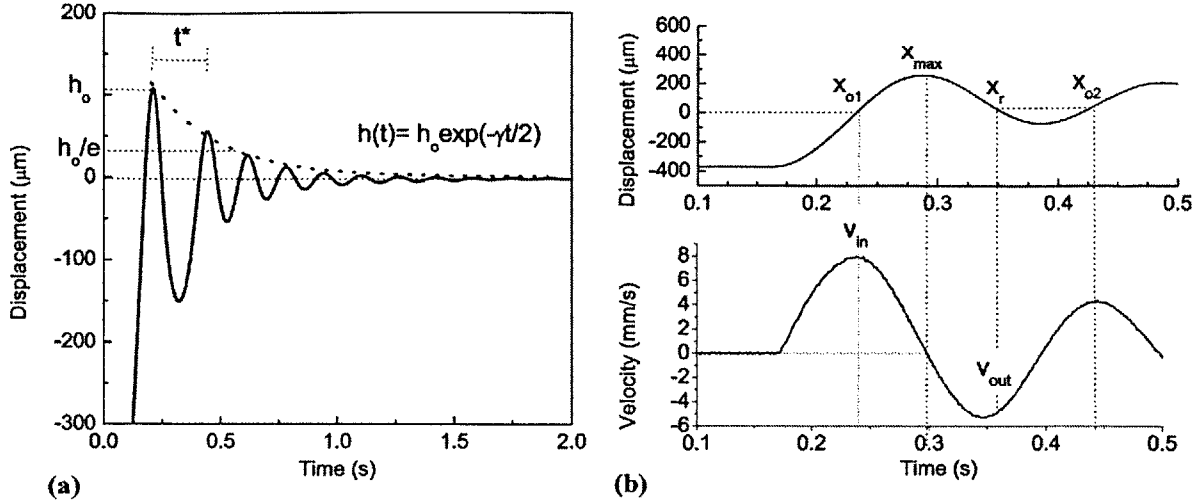


Figure 3.11 Representative impact response and definition of terms used to quantify energy dissipation. (a) Pendulum displacement over time is described by damped harmonic oscillatory motion, here for a 100/0 triblock/diblock gel at an impact velocity of 5.8 mm/s. Quality factor Q is calculated via Equation (3.8), and can be recognized visually as the number of indentation impact cycles n required for the amplitude of oscillation h_0 to fall by a factor of e . Here, $n \sim 2$ so $Q \sim 6$. (b) Velocity is calculated as the time derivative of displacement. Impact velocity v_{in} is the maximum velocity prior to contact, which defines the sample contact point x_{o1} . To objectively identify the position of the deformed surface, x_r is taken to be equivalent to the displacement x_{o2} which would be required to initiate contact with the sample in the next cycle. Thus x_r is the position of the relaxed surface following the initial impact. Rebound velocity v_{out} is defined as the velocity at displacement x_r . Penetration depth over the first impact cycle is defined as $x_{max} - x_{o1}$.

Energy dissipation upon impact can also be determined directly from analysis of the first impact cycle, rather than from the decay of oscillation that is used to determine Q , as the ratio of impact and rebound velocities (see Figure 3.11b). For each impact experiment, the following parameters were calculated from customized analysis scripts in MATLAB (The MathWorks, Inc.): impact (v_{in}) and rebound (v_{out}) velocities, displacement at which contact initiates (x_{o1}) displacement at maximum penetration (x_{max}) and displacement at minimum rebound velocity (x_r). Strain rates can be roughly estimated as $\dot{\epsilon} \sim v_{in}/x_{max}^{1/2}$. Impact energy E_{imp} was calculated from $E_{imp} = (1/2)mv_{in}^2$, and strain energy densities were calculated as impact energy normalized by the geometric contact volume of the spherical probe at x_{max} . Geometric contact volumes V were calculated from:

$$V = \frac{2\pi R^3 \left(1 - \cos\left(\text{Arcsin}\left(\frac{a}{R}\right)\right)\right) - \pi a^2 (R - x_{max})}{3} \quad (3.9)$$

where contact radius a is calculated from $a=2\pi R x_{\max} - \pi(x_{\max})^2$. Here, v_{out} is used to calculate the elastic energy that is recovered during the unloading portion of the first impact. If v_{out} corresponded exactly to the exit velocity upon loss of contact and if the energy dissipation mechanisms were solely due to inelastic deformation and local heating, $v_{\text{out}}/v_{\text{in}}$ would be termed the coefficient of restitution. In the gels studied herein, adhesion forces serve as an additional source of energy dissipation. We observed visually that the probe tended to remain in contact with the surface upon rebound; this is attributable to high adhesive forces between the probe and the sample, even under the fully hydrated and buffered conditions of these tissues. Therefore, we characterize these more complex collisions simply as $v_{\text{out}}/v_{\text{in}}$. This ratio was compared among materials at a given impact velocity and among impact velocities for a given material.

Both Q and $v_{\text{out}}/v_{\text{in}}$ quantify the energy dissipation of the sample-pendulum system. To distinguish the energy dissipation capacity of the sample alone, which we will define as the dimensionless parameter K , we must first calculate the energy dissipated and recovered by the pendulum as outlined below in Equations (3.10) – (3.14). In general, at any given displacement of the pendulum after impact is initiated, the impact energy is the total energy of the system (pendulum and sample) and can be defined as:

$$E_t^{\text{system}} = (1/2)m(v_{\text{in}})^2 = E_r^s + E_r^p + E_d^s + E_d^p \quad (3.10)$$

where E_r^s is the energy recovered by the sample, E_r^p is the energy restored to the system by the fully recovered displacement of the pendulum springs at v_{out} , E_d^s is the energy dissipated by the sample, and E_d^p is the energy dissipated by the pendulum. The latter dissipation can be attributed to sources such as Eddy current damping at the electromagnetic coil/magnet, air damping between the capacitor plates, etc. Note that the subscripts r and d indicate restored and dissipated energies, respectively; superscripts s and p denote the sample and pendulum, respectively. Total recovered energy at v_{out} is calculated from:

$$(1/2)m(v_{\text{out}})^2 = E_r^s + E_r^p \quad (3.11)$$

Therefore, to calculate accurately the energy dissipated only by the sample at v_{out} , we require calculation of E_d^p and E_r^p at v_{out} . The restored energy of the pendulum E_r^p is calculated from the relation:

$$E_r^p = (1/2)k_p(\Delta x)^2 \quad (3.12)$$

where $\Delta x = x_{\max} - x_r$ which is the distance the pendulum travels out of the impacted sample from its maximum penetration depth during the unloading portion of this impact, and k_p is the effective rotational stiffness of the pendulum at the indenter contact position.

To calculate the dissipated energy of the pendulum E_d^p the dynamic response of the pendulum must also be calibrated as we have detailed previously¹⁶⁸. Briefly, we determined the pendulum damping coefficient b_p (0.6 N-s/m) and pendulum quality factor Q_p (46.1) via analysis of $h(t)$ for abrupt loading experiments on a wire spring connected between the pendulum and opposing sample holder (Figure 3.12a). In order to provide analysis of multiple oscillations in a relatively short test period, the stiffness of this spring was chosen to be much higher ($k_{\text{spring}} = 4.457$ kN/m) than the low rotational stiffness of the pendulum ($k_p = 3$ N/m). This rotational stiffness was measured from the slope of force-displacement response prior to physical contact between the probe and the surface under quasistatic rates. The pendulum damping coefficient is calculated as:

$$b_p = (\gamma_m k_{\text{spring}}) / \omega_o^2 \quad (3.13)$$

where γ_m (3.5 s^{-1}) was determined from fitting Equation (3.7) to the $h(t)$ response of Figure 3.12a and the angular resonant frequency of the pendulum-wire spring system ω_o (161.6 rad-s^{-1}) was determined directly from this same $h(t)$ response. The magnitude of Q_p was determined as ω_o / γ_m . No significant damping due to the presence of liquid was observed (Figure 3.12b). Therefore, the energy dissipation and system damping analysis outlined here hold for experiments on both gels tested in air and tissues tested in aqueous Krebs-Hensleit buffer. Finally, the dissipated energy of the pendulum E_d^p is then calculated as:

$$E_d^p = \int_{x_o}^{x_{\max}} b_p \frac{\partial x}{\partial t} dx + \int_{x_{\max}}^{x_r} b_p \frac{\partial x}{\partial t} dx \quad (3.14)$$

Having calibrated pendulum energy dissipation, we can now consider the energy dissipated only by the sample under impact. Using Equations (3.10) – (3.12) and (3.14), we can calculate the quantity K , which is the energy dissipated by the sample normalized to the sum of the dissipated and recovered sample energy:

$$K = \frac{E_d^s}{E_t^{\text{system}} - E_r^p - E_d^p} \quad (3.15)$$

In summary, impact analysis provides three quantitative measures of energy dissipation: Q (Equation (3.8)), $v_{\text{out}}/v_{\text{in}}$, and K (Equation (3.15)). Note that while $v_{\text{out}}/v_{\text{in}}$ and K characterize the magnitude or extent of energy dissipation by the material during the first impact cycle, Q indicates the rate of energy dissipation.

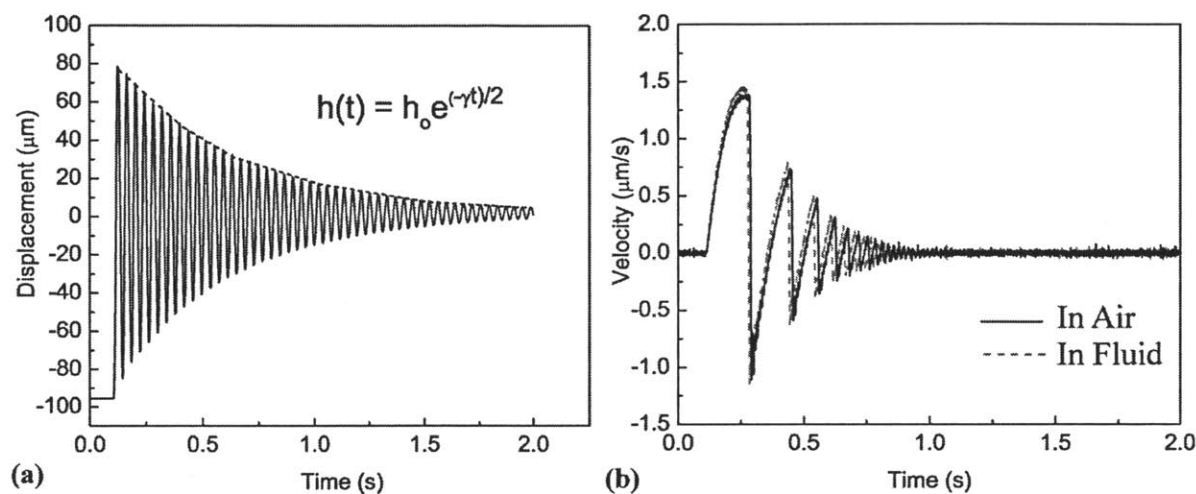


Figure 3.12 (a) Free oscillations of the pendulum-linear elastic wire spring system show that the damping due to the pendulum is small but not negligible. Pendulum damping constant b_p is calculated via Equation (3.13), ω_o and γ_m are extracted by fitting Equation (3.7) to the $h(t)$ response. (b) Differences in pendulum velocity for oscillations in air or immersed in fluid do not differ significantly, showing that immersion in aqueous environments contributes negligible additional damping.

3.3.3 Results and Discussions

Impact indentation experiments were conducted on Perma-GelTM, styrenic block copolymer gels, and liver and heart tissues at impact velocities up to 20 mm/s (corresponding to nominal strain rates up to 40 s^{-1}). Figure 3.13 shows representative impact responses of tissues and gels for an impact velocity of 7 mm/s and corresponding impact energy of 4 μJ . These raw displacement vs. time responses enable one to readily compare both the deformation response and the rate of energy dissipation among samples qualitatively. First, these data indicated that the hydrated tissues were more compliant than these gels, as the tissues exhibit the maximum deformation (i.e., depth of penetration) under a given impact velocity and impact energy. Among the styrenic block copolymers, Figure 3.13 shows clearly that the maximum penetration depth x_{max} increased with decreasing vol%- triblock. Perma-GelTM exhibited an intermediate deformation between that of the 75/25 and 50/50 triblock/diblock gels. Second, Figure 3.13 illustrates the rate of energy dissipation among samples in terms of the number of indentation impact cycles to

dissipate the total impact energy, as apparent from the number and duration of pendulum oscillations after impact. While Perma-Gel™ and 100/0 triblock/diblock gel dissipated impact energy most slowly, the tissues dissipated impact energy most quickly. Among the triblock/diblock styrenic gels, the number of cycles and time for complete energy dissipation increases with increasing vol%- triblock. In fact, Figure 3.13 shows that 50/50 triblock/diblock dissipated total impact energy almost as quickly as the tissues for this impact velocity. This qualitative comparison among impact displacement responses indicates that the rate of impact energy dissipation can be tuned toward that of heart and liver tissues by modulating the triblock concentration. Next, we quantitatively evaluate the impact responses in terms of penetration depth and energy dissipation capacity, under a range of impact velocities and strain energy densities.

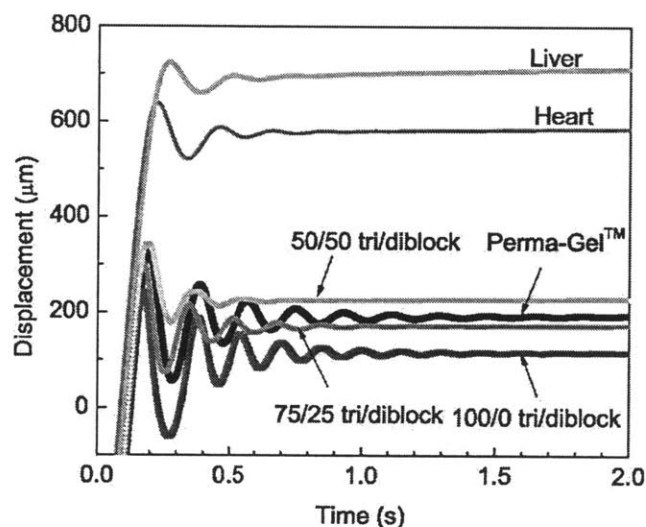


Figure 3.13 Impact loading was conducted using a customized, pendulum-based nanoindenter. Raw displacement vs. time response for all materials at a maximum velocity of 7 mm/s corresponding to impact energy of 4 μ J shows a significant difference between the penetration depths and energy dissipation rates among all samples.

3.3.3.1 Impact resistance under dynamic impact loading

To compare the penetration resistance of each sample quantitatively, displacement of the pendulum at maximum penetration x_{\max} is calculated as a function of impact velocity. For the range of impact energies studied here, the resistance of a material to impact penetration decreases with increasing impact velocity (Figure 3.14a); however, the trends of maximum penetration among the different materials as described above still hold. Note that, the maximum penetration depths attained on liver were larger than the thickness of the liver capsule ($\sim 5 \mu\text{m}$),

and comparable to the thickness of the pericardium (~ 1 mm) for heart. The corresponding contact volumes were on the order of 2 mm^3 and 1 mm^3 , respectively. Therefore, the reported tissue responses are representative of a composite response from multiple tissue layers. Here, the maximum impact velocities obtained for tissues were lower than that attained for gels. For the compliant hydrated tissues, an impact velocity $v_{\text{in}} > 8$ mm/s imposed via this probe would penetrate the tissue so deeply that the pendulum displacement would be physically halted due to mechanical collision of the electromagnetic coil into the stationary magnetic plate. Higher impact velocities on tissues could be attained via probes of larger radii, but with concurrent and nonlinear decreases in impact energy densities due to the high compliance of these tissues.

As expected, maximum penetration depth also varied with imposed strain energy density (Figure 3.14b). Although the maximum penetration depths obtained and velocities investigated here are still low compared to ballistic tests (mm/s compared to \sim m/s), the impact strain energy densities are high ($0.4 - 20 \text{ kJ/m}^3$) and comparable with macroscale impact tests such as pneumatic gun and falling weight impacts designed to replicate ballistic conditions ($15-60 \text{ kJ/m}^3$)⁷². The high strain energy density achievable in the present contact-based impact experiments is due simply to the fact that the contact volumes of impact indentation are over contact areas on the order of hundreds of μm^2 , as compared to contact areas on the order of cm^2 for macroscopic ballistic impact. Note that our reported impact energy densities represent an upper bound, as these are calculated from penetration depth and thus neglect the actual volume of material under significant strain beneath the impact contact. Actual contact areas and strain volumes will depend on whether the material is structurally homogeneous over the experiment length scales or exhibits structural heterogeneity. The lamellar structure of encapsulated and striated tissues imposes such uncertainties in strain energy density calculations.

Finally, the displacement vs. time response at the first impact peak can also be represented as a force vs. displacement response that allows visualization of hysteresis curves for a given impact velocity. For alternative probe geometries such as flat punch, this response can further be transformed to stress vs. strain, which is a metric that is reported by other macroscale pendulum-based impact approaches and split-Hopkinson pressure bar experiments⁶⁷⁻⁶⁸. The resistive force of the material is defined as $F = ma$, where a is the deceleration of the pendulum upon impact

and m is the mass of the pendulum (impacting object). This calculated force changes as a function of penetration and rebound depths (Figure 3.14c). Under similar impact energies, all samples exhibited significant hysteresis. The 100/0 triblock/diblock gel showed the stiffest response, and these gels were increasingly compliant with decreasing vol%- triblock. This trend is expected from the higher crosslinking concentration of the triblock phase^{2,151}: the replacement of SEBS chains by SEP chains induces a decrease in the number of bridges that can act as physical crosslinks between micelles. In contrast, liver tissue exhibited the most compliant response among all samples. The comparative compliance of liver tissue as compared to heart tissue at these elevated deformation rates is consistent with quasistatic mechanical comparisons of elastic moduli E between two tissue types, estimated via macroscale uniaxial compression, uniaxial tension, and indentation experiments^{17,132-133,153}.

Note that Figure 3.14c also underscores the difference in penetration depth between the gels and these tissues. If the goal of the tissue simulant gel is to dissipate the total impact energy at penetration depths comparable to these tissues, none of the gels considered here are viable candidates. The tunability of decreased penetration depth with increasing vol%- triblock is apparent in Figure 3.14a-c, but further decreases in vol%- triblock are not possible for this particular system due to incomplete gelation for < 50 vol%-triblock compositions. However, the bridging role of the triblocks in impact penetration resistance of such block copolymers provides a clear avenue for development of other tissue surrogate gels. Next, we compare the rate and extent of impact energy dissipation among these gels and tissues.

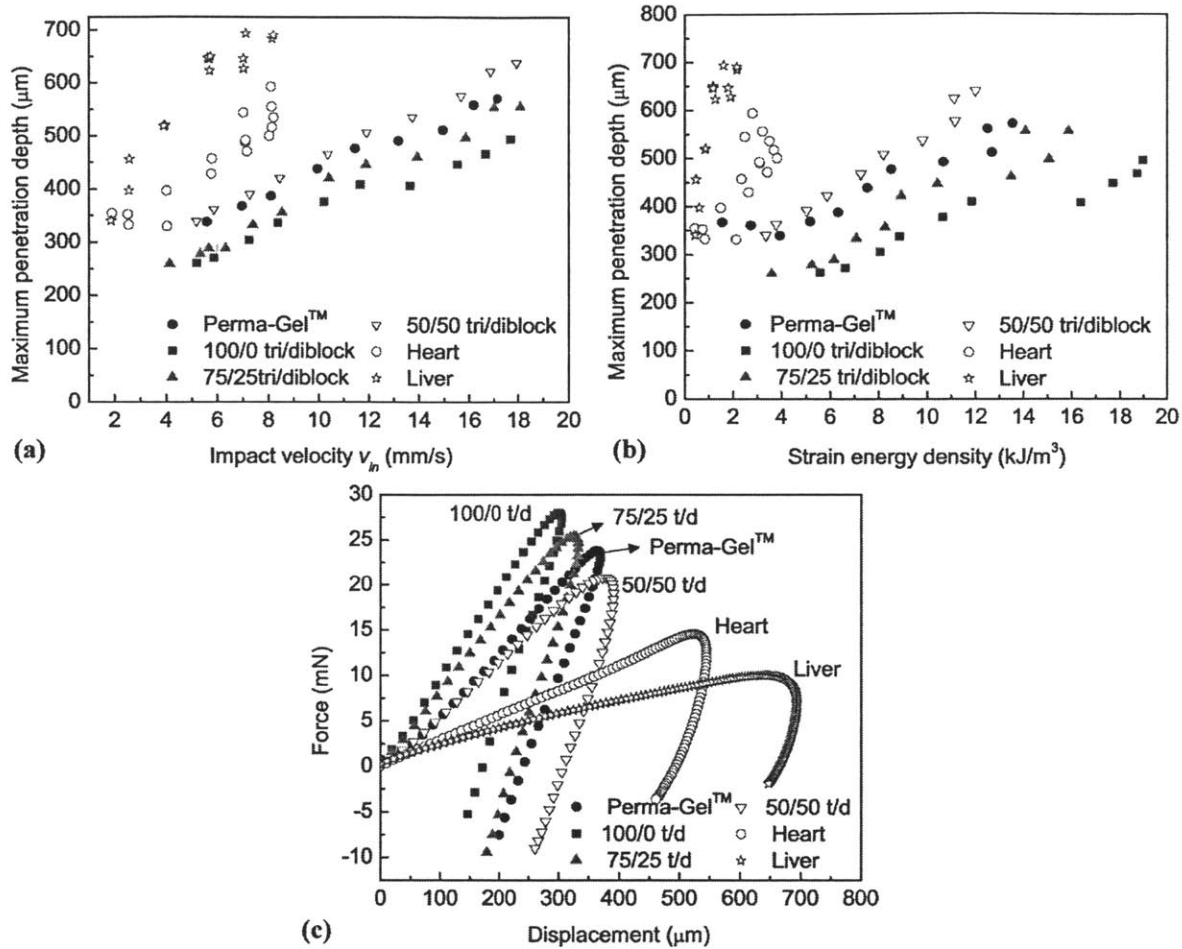


Figure 3.14 Maximum penetration depths varied as a function of (a) impact velocity; and (b) strain energy density. Liver tissue exhibited the lowest penetration resistance among all samples whereas 50/50 triblock/diblock gel exhibited the closest penetration resistance to heart tissue. (c) Force-displacement responses calculated from the $h(t)$ response of the first impact peak for an impact energy of $\sim 4 \mu\text{J}$ show significant hysteresis for all samples. As observed in (a) and (b), liver tissue exhibited the lowest penetration resistance.

3.3.3.2 Energy dissipation under dynamic impact loading

To compare the energy dissipation capacity of each pendulum-sample system quantitatively, two dimensionless parameters were considered. First, the velocity ratio v_{out}/v_{in} , which provides a measure of the material energy dissipation per impact; this reduction in velocity upon impact considers only the first instance of reversible penetration between the indenter probe and material, such that energy dissipated by the dynamic indentation event modulates v_{out}/v_{in} . Second, the quality factor Q as defined in Equation (3.8) provides a measure of the rate of energy

dissipation in the pendulum-sample system, determined over multiple impact events until complete dissipation of the impact energy.

Figure 3.15a and b show average v_{out}/v_{in} and Q , respectively, for the tissues and tissue simulant gels under the impact velocities considered herein. Both measures of energy dissipation indicate that tissues exhibit a higher impact energy dissipation capacity than the tissue simulant gels, at least over the velocities and impact energy densities of interest. That is, more energy is dissipated in a single impact cycle (larger v_{out}/v_{in}) and total impact energy is dissipated more quickly (lower Q) in these tissues. Note that the quality factor of the pendulum-based indenter reported in Section 3.3.2.3 is at least one order of magnitude higher than those observed on the more dissipative tissues and tissue simulant gels, suggesting that the materials tested here dissipate the impact energy faster than the pendulum-based indenter.

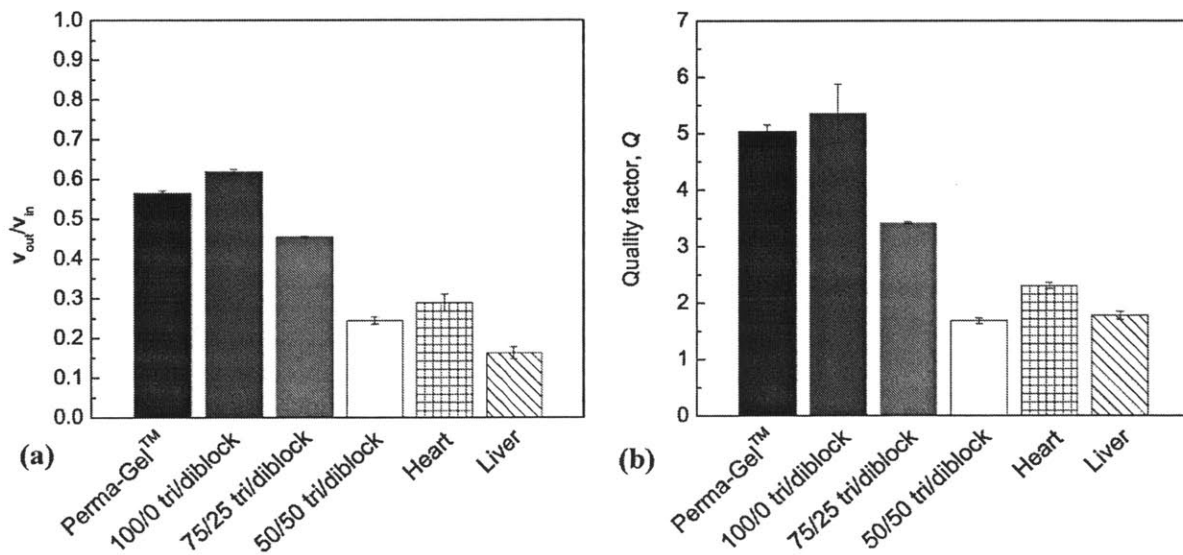


Figure 3.15 (a) Velocity ratio v_{out}/v_{in} and (b) quality factor Q for the impact energies studied here provide means to compare the energy dissipation capacity and energy dissipation rate of each sample, averaged over the range of impact velocities considered. Comparison of v_{out}/v_{in} shows that Perma-Gel™ and 100/0 triblock/diblock gel exhibit the lowest energy dissipation capacity, whereas energy dissipation capacity of 50/50 triblock/diblock gel is similar to that of liver and heart tissues. Comparison of Q shows that both Perma-Gel™ and 100/0 triblock/diblock gel dissipate the total energy more slowly, as compared to 50/50 triblock/diblock gel and tissues. Data indicated as mean \pm standard error.

Perma-GelTM and 100/0 triblock/diblock gel exhibited the lowest impact energy dissipation capacity among these materials, and liver tissue exhibited the greatest impact energy dissipation capacity. Although Perma-GelTM is more compliant than the 75/25 triblock/diblock gels (i.e., the maximum depth of penetration is larger at all impact velocities considered in Figure 3.14a), the dissipation capacity of this ballistic gel is less than that of the styrenic gel comprising 75 vol%-triblock. This result likely reflects differences in the proprietary copolymer gel formulation of Perma-GelTM relative to the model block copolymer gels, which alters the dynamic response of the network in a slightly different manner than simple diblock addition. Moreover, as the vol%-diblock was increased in these styrenic materials, energy dissipation capacity increased.

From a materials design perspective, this increase in energy dissipation capacity within increasing vol%-diblock can be rationalized by microstructural changes in the gel as a function of composition. As shown in Figure 3.2, these gels are comprised of nm-scale micelles which include the styrenic segments of multiple di- or triblocks. Only triblocks have the capacity to bridge styrenic segments. Thus, decreasing the concentration of triblocks in the polymer will decrease the number of bridges formed between micelles. These bridges act as active chains in elastic energy restoration, as effective elastic springs¹⁴⁷. Therefore, a decrease in the number of bridges will have a negative impact on the capacity of these gels to recover elastic strain energy. Finally, comparisons of Q among these materials showed that the 50/50 triblock/diblock ($Q = 1.68 \pm 0.05$) exhibited similar dissipation capacity rates as that measured for liver tissue ($Q = 1.77 \pm 0.07$).

To compare the high-rate response of each material quantitatively, the energetic dissipation parameter K (Equation (3.15)) was calculated as a function of impact velocity (Figure 3.16). In contrast to Q and v_{out}/v_{in} , K deconvolutes the finite damping of the impact pendulum from the impulse response of the sample. Liver tissue exhibited the highest magnitude of K , dissipating 95% of the impact energy at these impact energy densities; K_{liver} was independent of impact velocity. In contrast, K_{heart} was lower than that of liver and exhibited considerable velocity dependence. The tissue simulant gels exhibited composition-dependent K , with $K_{50/50}$ well matched to that of heart tissue to dissipate ~90% of the total impact energy. Tissue simulant gels exhibited either a weak, positive increase in K with impact velocity (75/25 and 50/50

triblock/diblock) or no discernible velocity dependence (100/0 triblock/diblock and Perma-GelTM). This contrast between the tissue types, as well as among the tissue simulant gels, remains an area of open interpretation that may be related to poroelastic effects (see Chapter 5), micellar reconfiguration within gels, and/or lamellar structural heterogeneity of tissues. Although beyond the scope of the current study, the methods outlined herein can be implemented in future work to explore independently the effects of penetration depth and contact volume on energy dissipation, e.g., through variation of the contact probe geometry for impact velocities of interest. Future applications of this method may also be designed to identify the possible additional contributions of nonlinear elastic deformation at these impact rates, provided that the macroscale stress-strain response of tissues or gels can be acquired to quantify any appreciable nonlinearity at the imposed strains and strain rates. Such implementations of the methods and analyses outlined here can enable multiscale analysis of energy dissipation in heterogeneous tissues, for distinct applications or models of scale-dependent deformation mechanisms.

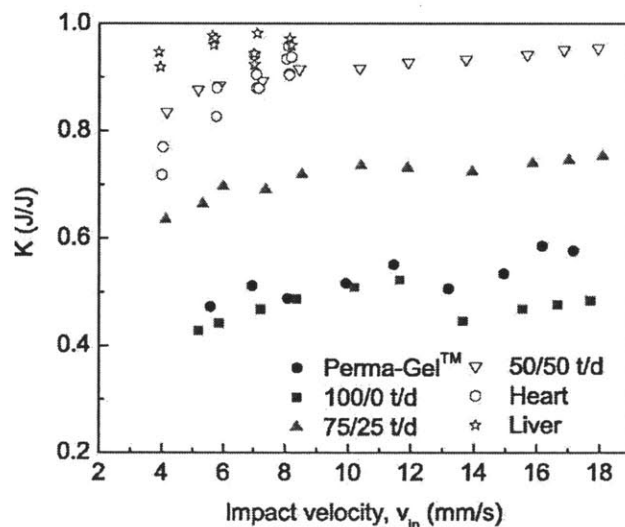


Figure 3.16 Energy dissipation parameter K as a function of impact velocity provides a quantitative comparison among samples. While the tissues and 50/50 triblock/diblock gel dissipate nearly all of the imposed impact energy, Perma-GelTM and 100/0 triblock/diblock gel dissipate only 40-50% of the total energy at these impact velocities.

At the high strain energy densities and velocities of primary interest for tissue simulant applications, this quantitative analysis of energy dissipation and penetration depth of a given contact probe enables identification of promising tissue simulant candidates. The 50/50

triblock/diblock styrenic gel is stable in air, and best replicates the extent of energy dissipation in the initial collision event that is exhibited by fully hydrated heart tissue (i.e., these materials exhibit K within 4% in Figure 3.16). Among the synthetic gels, this composition also exhibits penetration depths that are closest to those of heart tissue at all impact velocities (Figure 3.14a), though still exceeding the penetration resistance of heart tissue by at least ~15%. This gel also best replicates the energy dissipation rate of these tissues, exhibiting Q within 23% and 5% of heart and liver tissues, respectively. Note that there exists a competition between energy dissipation capacity K and energy dissipation rate Q in these gels, as apparent from the fact that the 50/50 gel compares more closely to the energy dissipation capacity of heart tissue and to the energy dissipation rate of liver tissue. Together these findings indicate that Perma-GelTM and the 100/0 and 75/25 triblock/diblock styrenic gels are suboptimal simulants for heart and liver tissues, in that these materials do not accurately predict impact loading resistance and impact energy dissipation capacity of these tissues. In contrast, the 50/50 triblock/diblock styrenic gel is a more suitable mechanical simulant of heart and liver tissue, in terms of the rates and extents of energy dissipation. As noted, further optimization of energy dissipation via this specific styrenic diblock/triblock gel is limited by the incomplete gelation for triblock composition <50 vol%. However, the present experiments elucidate the role of crosslinking bridges among micelles as a strong determinant of impact energy dissipation, and will guide design of future block copolymers for these tissue simulant applications.

3.3.4 Conclusions

The dynamic impact responses of styrenic triblock/diblock copolymer gels and a commercially available ballistic gel were studied and compared with those of fully hydrated liver and heart tissues. The specific tissue simulant application of interest required comparable penetration resistance and impact energy dissipation capacity of these gels to that of liver and heart tissues. Neither commercial Perma-GelTM nor block copolymers of high vol%- triblock accurately mimicked the responses of these tissues. However, observations of compositionally dependent energy dissipation capacity in the styrenic gels enabled development and demonstration of a 50/50 triblock/diblock gel that served as a reasonable simulant of impact energy dissipation capacity for these tissues. The instrumented dynamic impact indentation analyses detailed here

thus enable further modifications of these and other tissue simulant gels to quantitatively replicate the full energy dissipation response of hydrated soft tissues for a range of applications.

3.4 Conclusions

Chapter 3 considered triblock/diblock styrenic copolymers as potential tissue simulant gels. Quasistatic experiments formed a baseline for understanding structure property relationship of these tissue simulant gels. These systematic experiments from a materials engineering perspective have enabled the identification of the underlying mechanisms by which the mechanical response of these tissue simulant candidates are modulated. Although elastic modulus and relaxation modulus values were tunable with composition, relaxation times exhibited a lack of tunability which could be disadvantageous for tissue simulant applications. Chapter 5 further explores different mechanisms that could affect relaxation response of candidate material systems and soft tissues.

A new method to quantify and compare impact resistance and energy dissipation of soft tissues and candidate tissue simulants under concentrated impact loading was established. Importantly, by comparing biological soft-tissues and engineered tissue simulants under identical impact conditions, it was shown that compositional variation of these triblock/diblock gels affords a relatively close matching of energy dissipation capacities, but not of impact resistances. Further, we were not able to decouple impact resistance and energy dissipation capacities via tuning the composition. In order to overcome these limitations, Chapter 4 utilizes a chemically crosslinked PDMS network that is loaded with a non-reactive PDMS solvent as potential tissue simulant gels with enhanced mechanical tunability.

Chapter 4 **Crosslinked Networks as Potential Tissue Simulants for Ballistic Applications**

The following study is under preparation for publication with coauthors R. Mahmoodian, R. Mrozek, J. Lenhart, and K. J. Van Vliet.

4.1 Introduction

Chapter 3 explored block copolymer styrene-based gels containing a mid-block selective solvent for use as tissue simulants. Compared to the commonly used tissue simulant ballistic gelatin, these materials were environmentally stable, and offered additional methods of tailoring the mechanical response including the incorporation of diblock polymer, and the ratio of the constituent blocks. However, restricted tunability of the impact resistance, as well as the lack of ability to decouple impact resistances and energy dissipation capacities of this system, necessitates the design of new tissue simulant gels that can recapitulate the mechanical response of various “soft tissues” under concentrated impact loading.

A recently developed alternative system with strong potential for tissue simulants comprises a chemically crosslinked polydimethylsiloxane (PDMS) network loaded with a non-reactive PDMS solvent⁸⁰. Presence of a solvent in a cross-linked polymer network produces a polymer gel that is compliant and deformable, but will recover its shape due to the elastic nature of the polymer strands. These networks are considered to comprise so-called elastic chains that are joined by both ends to the gel structure, pendant chains (or dangling chain ends) that are joined only by one end to the gel, and free (or soluble or guest) chains that are not attached to the network¹⁷³. By altering the concentration of these different types of polymeric chains, as well as the corresponding molecular weight, both the elastic and viscoelastic properties of the system can plausibly be tuned¹⁷³⁻¹⁷⁹. Thus, a significant advantage of this class of materials is the ability to tailor the properties by altering the material design including the polymer chemistry, network cross-link density, solvent type, solvent loading, solvent molecular weight, and the incorporation of particulate filler.

While most synthetic gel design exploits a cross-linked polymer network swollen with small molecule solvents, recent work has also demonstrated the ability to tailor the rate dependent mechanical response of PDMS gels through the molecular weight of the solvent⁸⁰. Specifically, when the solvent molecular weight was larger than the entanglement molecular weight of the polymer, the gel exhibited significant stiffening as the strain rates increased, shown by small-strain rheological measurements. In addition, the deformation rate at which the stiffening initiated scaled with the characteristic molecular weight dependence of the reptation time, as $\tau_{\text{REPT}} \sim \text{MW}^{3.4}$. This insight demonstrates the potential to incorporate and tailor the strain rate dependent response of these compliant gels to provide a better match to the complex nonlinear, time-dependent mechanical response of biological soft tissues. However, for this approach to be useful for the design of tissue simulants, the approach must be implemented in a modulus regime relevant for many biological tissues. Further, development of such gels for ballistic and tissue simulant applications requires that the mechanical response and energy dissipation characteristics are attained at high rates relevant to impact loading, and that these properties be compared directly with those obtained for soft tissues under comparable conditions.

To that end, this chapter presents the mechanical and impact properties of a library of polydimethylsiloxane (PDMS) gels (see Section 4.2) along with murine heart and liver tissues. Section 4.3 provides a survey of the rheological properties of these tissue simulant candidates to investigate the effects of solvent loading percentage, crosslinking density, and solvent molecular weight on storage modulus G' , loss modulus G'' , and loss tangent $\tan \delta$. Such studies are useful in understanding the relationships between the network structure and mechanical properties. In Section 4.4, impact resistance and energy dissipation capacities and rates are quantified via impact indentation for the tissue simulant candidates and for murine heart and liver. Together the results and discussion presented in this chapter inform the design principles required for synthetic polymer gels that are optimized to predict the response of specific biological tissues to impact loading. These results will provide insight for further tuning of this gel system to match the impact response of other soft tissues.

4.2 Materials

Tissue simulant gels described in this section were synthesized by Dr. Randy Mrozek in the US Army Research Laboratories (ARL) in Aberdeen, MD. Vinyl-terminated PDMS (v-PDMS) and methyl-terminated PDMS (m-PDMS) were mixed with 800 ppm of a platinum-cyclovinylmethylsiloxane complex by mechanical mixing for 15 min. A tetrafunctional silane crosslinker, tetrakis(dimethylsiloxy)silane, was added at 4.0 molar equivalents of hydride to vinyl functionality and stirred for an additional 10 min. The networks were formed in the presence of solvent (m-PDMS)(Figure 4.1). The linear precursor v-PDMS chain length was 117 kg/mol. The samples were degassed by vacuum and cured for 72 h at 82 °C. Different PDMS samples were prepared by varying the solvent vol% loading and molecular weight, and the molar ratio of silane crosslinking groups to vinyl. This ratio was varied from 4:1 to 2:1 (4:1, 3:1, 2.75:1, 2.5:1, 2.25:1 and 2:1). Solvent loading was varied from 10 vol% to 80 vol% (10, 30, 40, 50, 60, 70, 75 and 80%). Solvent molecular weights studied were 1.1, 139, and 308 kg/mol.

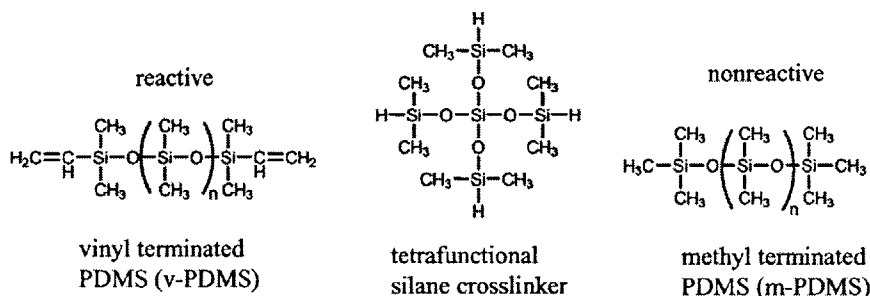


Figure 4.1 Chemical structures of the model system network components, adapted from Ref. ⁸⁰.

Heart and liver organs were harvested from adult rats (see Section 3.2.2). All experiments involving animals obeyed the University IACUC protocol and the NIH guidelines for animal care. For both heart and liver tissues, discs of 8 mm diameter and thickness of 3 to 5 mm were prepared using a surgical punch, and all tissues were stored in Krebs-Hensleit buffer immediately after excision and throughout all experiments reported herein.

4.3 Comparison of gel and tissue rheology at low strains and rates

The thesis author's contribution to this macroscale rheological component of the study included guiding the design of the gels, part of data analysis, as well as drafting of the figures and discussion presented in this section.

Due to the complexity of mechanical characterization at higher rates, dynamic mechanical measurements via rheology at low strains and shear rates was conducted as to provide an understanding of the impact of solvent loading percentage, precursor chain stoichiometric ratio, and solvent molecular weight on storage modulus G' , loss modulus G'' , and loss tangent $\tan \delta$ (i.e., G''/G' often employed as a measure of the dissipation of deformation energy¹⁸⁰) in order to provide a baseline for exploring the impact behavior of gel systems, and to compare these parameters to those obtained for heart and liver tissue. This survey of a library of candidate gels does not ignore the reality that differences in loading rates and configurations as well as contact geometries (bulk sample response vs. local response in concentrated impact indentation) can affect the mechanical response and the corresponding observed trends therein, but increases the efficiency of tissue simulant identification. As the correlations between gel composition, network structure, and mechanical response under these conditions guide our design of tissue simulants for impact applications, here we discuss the rheological results and interpretation in detail.

4.3.1 Experimental Methods

Rheological measurements on PDMS gels were conducted by Dr. Randy Mrozek (ARL) adopting a torsion geometry (MCR 501, Anton Paar, Austria) at 25°C inside an environmentally controlled oven, using rectangular samples of approximately 12 × 4.5 × 28 mm. Strain sweeps were conducted to detect the linear viscoelastic region (i.e., strains at which the measured elastic modulus remained independent of strain) at an oscillation frequency of 1 Hz, upon which 1% strain level was deemed appropriate. Frequency sweeps were conducted at 1% shear strain at a range of 0.01-1 Hz. Three to five replicate experiments were conducted on each sample (n = 3-5). Oscillatory shear rheological measurements of heart and liver tissues (n=3 for each tissue source) were conducted by Dr. Roza Mahmoodian in the Van Vliet Group (MIT), using parallel plate geometry at 37°C (MCR 501, Anton Paar, Austria) within 5 h post-mortem. A strain magnitude of 1% was chosen, at which frequency sweeps were conducted in the range of 0.1-10 Hz. Tissues were adhered to the bottom plate using a thin layer of cyanoacrylate and a profiled top plate was utilized to ensure a secure grip on the sample. Gel data are reported as the median

of replicate experiments on the same sample with an error of less than 5%, and tissue data are reported as the mean of replicate experiments on samples from unique animal donors with an error of less than 30%.

4.3.2 Results and Discussion

4.3.2.1 Effect of solvent vol% on the magnitude and rate dependence of G' , G'' , and $\tan \delta$

The effect of solvent vol% on the viscoelastic properties of similar PDMS-based gels was investigated previously for gels containing up to 50 vol% solvent⁸⁰. Since those gels were considerably stiffer (at 50 vol % $G' \sim 40$ kPa) than soft tissues (< 10 kPa), here we considered higher solvent loadings in an attempt to access elastic moduli in the range of soft tissues. Thus, PDMS gels were made containing 60, 70, 75, 80, and 85 vol % solvent at the optimum stoichiometry (ratio of crosslinking silane groups to vinyl) of 4:1 with a solvent molecular weight of 1.1 kg/mol. Remarkably, the materials uniformly gelled at solvent loading up to 80 vol %. At 85 vol %, the gel consistency was inconsistent with large portion of uncured precursor. Rheology measurements were reported as a function of frequency from 0.01 Hz to 1 Hz (Figure 4.2). As expected, the storage modulus G' decreased as the solvent loading increased from 10% to 80% by approximately two orders of magnitude; this finding holds at any given loading frequency (Figure 4.2a). This decrease in stiffness with increased solvent loading can be attributed to the microstructural changes in the crosslinked network structure such as the dilution of networked polymer chains, screening of the network entanglements, and the enhanced formation of loop defects which could reduce the effective crosslink density¹⁸¹. It was also observed that G' is not significantly dependent on frequency over the ranges investigated here. However, study of an extended frequency range for tissues demonstrates strain rate dependent behavior as expected (Figure 4.3). Figure 4.2b shows the log-log relation between G' measured at 1 Hz and the polymer content. These data are well fitted by a straight line, indicating a power law behavior with a scaling factor (slope of line) of 2.5 that is slightly larger than the theoretical value of 2.3 for a network formed in a theta solvent¹⁸². Finally, at the highest solvent loadings, these gels exhibit storage moduli similar to those of heart tissue; however, for more compliant tissues such as liver, even higher solvent loadings would be necessary to achieve mechanical fidelity under such loading conditions.

The increase in the solvent vol% from 10% to 80% resulted in a decrease in the loss modulus G'' by approximately two orders of magnitude (Figure 4.2c) and an enhancement in the strain rate dependence of loss tangent (Figure 4.2d). This can be understood by the fact that one energy dissipation mechanism is migration of the solvent and dangling chain ends in the network. Both of these diffusion processes are affected by the entanglement density in the system, which depends on the concentration of the pendant chains, solvent molecular weight and the amount of solvent in the system. In the present system, increasing the low molecular weight solvent loading % screens these entanglements from each other, resulting in an overall decrease in the entanglement density and thus a decrease in G'' (Figure 4.2c). G'' increased as a function of frequency regardless of the solvent loading %, since at higher frequencies or shorter times, the polymer chains have insufficient time to rearrange or disentangle when stress is applied. As a result, physical entanglements persist longer than the time allowed by the oscillation frequency, thus physically constraining the chains and contributing to viscous dissipation. In contrast, at low frequencies, physical entanglements are created and broken quickly compared to the rate of deformation so they do not contribute to drag¹⁸³. Note that $\tan \delta$ values for the gels were below 0.1, suggesting these gels stored rather than dissipated most imposed mechanical energy at these frequencies. Heart and liver tissues, however, were more dissipative than the gels at the shear loading frequencies considered.

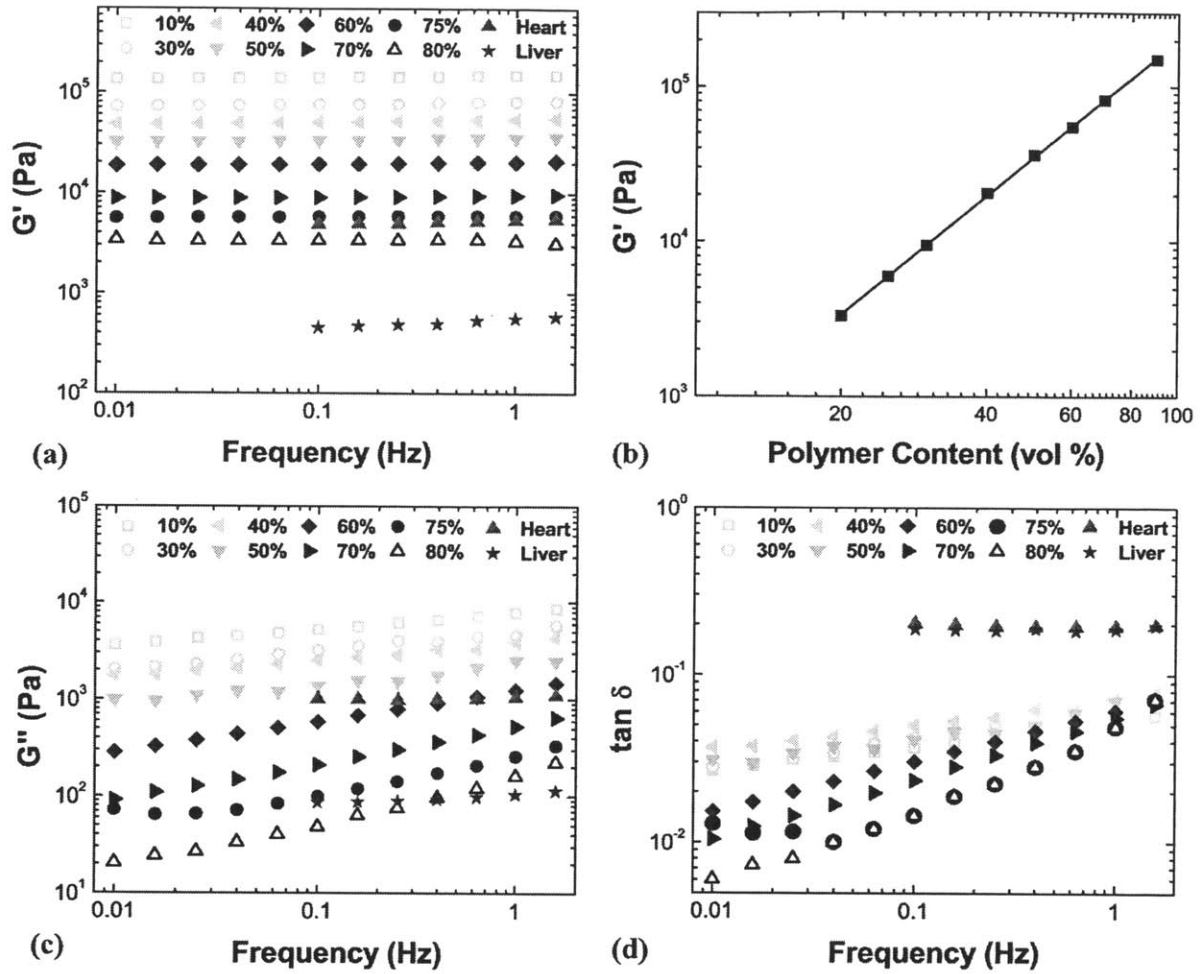


Figure 4.2 Effect of 1.1 kg/mol solvent loading on (a) Storage modulus G' with silane:vinyl stoichiometry of 4:1, compared to heart and liver, as a function of frequency, (b) Log-log plot of G' versus polymer content for PDMS gels containing 1.1 kg/mol solvent, (c) Loss modulus G'' and (d) Loss tangent $\tan \delta$ of the gels at different loading values of 1.1 kg/mol solvent, with silane:vinyl stoichiometry of 4:1, compared to heart and liver, as a function of frequency.

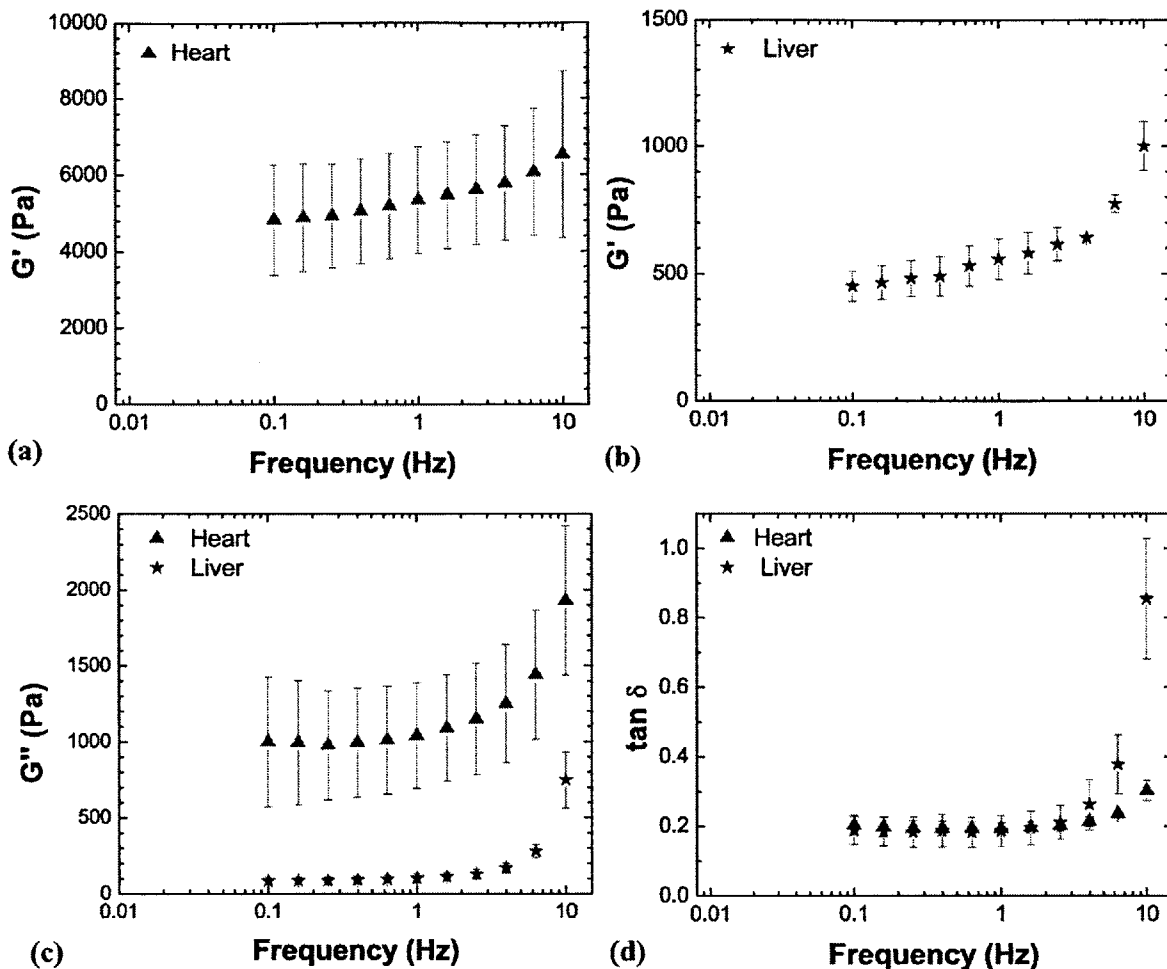


Figure 4.3 (a, b) Storage modulus G' , (c) loss modulus G'' , and (d) loss tangent $\tan \delta$ of heart and liver tissue exhibit frequency dependence.

4.3.2.2 Effect of precursor chain stoichiometry on magnitude and rate dependence of G' , G'' and $\tan \delta$ for low and high molecular weight solvent

As established previously⁸⁰, regardless of the solvent molecular weight, changes in silane:vinyl stoichiometry alter the network structure, and hence alter the mechanical behavior of these PDMS gels. When the crosslinker ratio is low, v-PDMS does not react completely, resulting in a decreased crosslink density and an increase in the incorporation of dangling chain ends, which lowers the number of elastically active junctions in the network¹⁷⁴. A junction is elastically active when three or more of its sites are independently connected to the network, and the chains connecting the junctions are elastically active when both are attached to elastically active junctions. Excess crosslinker also results in a decreased crosslink density, due to excessive end-capping of the precursor species. Previously, by monitoring the effect of crosslinker

concentration on the storage modulus of cured gels, the optimum stoichiometry for this system was determined as 4:1 silane:vinyl⁸⁰. The precursor chain molecular weight was chosen to be much higher than the MW_{ENT} of PDMS (117 kg/mol vs. 29 kg/mol). This leads to a network with mechanical properties that are dictated chiefly by the trapped entanglements among polymer chains, rather than properties that depend only on the chemical crosslinks⁸⁰. To determine the effect of stoichiometry at solvent loadings and molecular weights employed here, we examined gels at a range of crosslinker ratios (4:1 to 2.25:1), solvent-loaded at 60 vol%, with solvents comprising either the lowest (1.1 kg/mol) or highest (308 kg/mol) molecular weight.

Figure 4.4a shows that decreasing the stoichiometry (for the 1.1 kg/mol MW solvent gel) from 4:1 to 2.25:1 leads to an order of magnitude decrease in the storage modulus. This trend can be attributed to an increase in the density of dangling chain ends and/or the presence of unreacted precursor chains in the network that act effectively as a solvent. Since the equilibrium shear modulus of the network is proportional to the concentration of elastically active chains and fraction of trapped entanglements¹⁷⁵, decreased stoichiometry thus correlates with decreased storage moduli. By varying the crosslinker stoichiometry, we were able to identify gels that exhibited stiffness in the range of heart tissue; however, further modifications are necessary to match the more compliant tissues such as liver. Loss modulus G'' did not change significantly as a function of crosslinker ratio (Figure 4.4b). Gels became more dissipative as the crosslinking density decreased which could be attributed to an increase in the dangling chain end density since these pendant chains have more potential to dissipate energy as compared to elastic chains¹⁷³(Figure 4.4c); however, dissimilar to the effect of solvent loading on energy dissipation (Figure 4.2d), frequency dependence of the loss tangent remained unaffected at these frequencies. Magnitudes of energy dissipation were similar for gels and tissues at higher frequencies.

Similar to the effect of solvent loading vol%, decreasing the stoichiometric ratio did not affect the strain rate dependency of G' of the PDMS gels for the frequencies investigated here. Previous reports have indicated that G' was almost frequency independent for networks formed exclusively with elastically active chains¹⁷⁵; however, this is not the case for these PDMS gels, as decreasing silane:vinyl stoichiometry is known to introduce dangling chain ends and guest

chains in the network. These chains can behave as elastic chains when the involved entanglements cannot relax at higher frequencies (i.e., times shorter than the relaxation time of chains), leading to a higher G' at those frequencies. In fact previous rheological measurements of PDMS gels formed with different precursor chain stoichiometries in the absence of solvent revealed an increased frequency dependence of storage modulus as the amount of crosslinker was decreased, deviating from the optimum 4:1 stoichiometry⁸⁰. The reason that we do not observe this effect is plausibly attributed to the screening of these entanglements due to the presence of the low molecular weight guest chains in the present system (1.1 kg/mol, compared to the entanglement molecular weight MW_{ENT} of PDMS ~29 kg/mol)¹⁸⁴. Due to the decreased entanglement, the dangling ends do not reptate or exhibit short reptation/relaxation times given that the relaxation time of a linear pendant chain increases exponentially with the number of entanglements with which the chain is involved¹⁸⁵⁻¹⁸⁶. Since these pendant chains contribute to the non-equilibrium viscoelastic properties at frequencies higher than the inverse of their terminal relaxation time¹⁸⁷, frequency regimes accessed in the present study may be too small to observe any strain rate- or frequency-dependence.

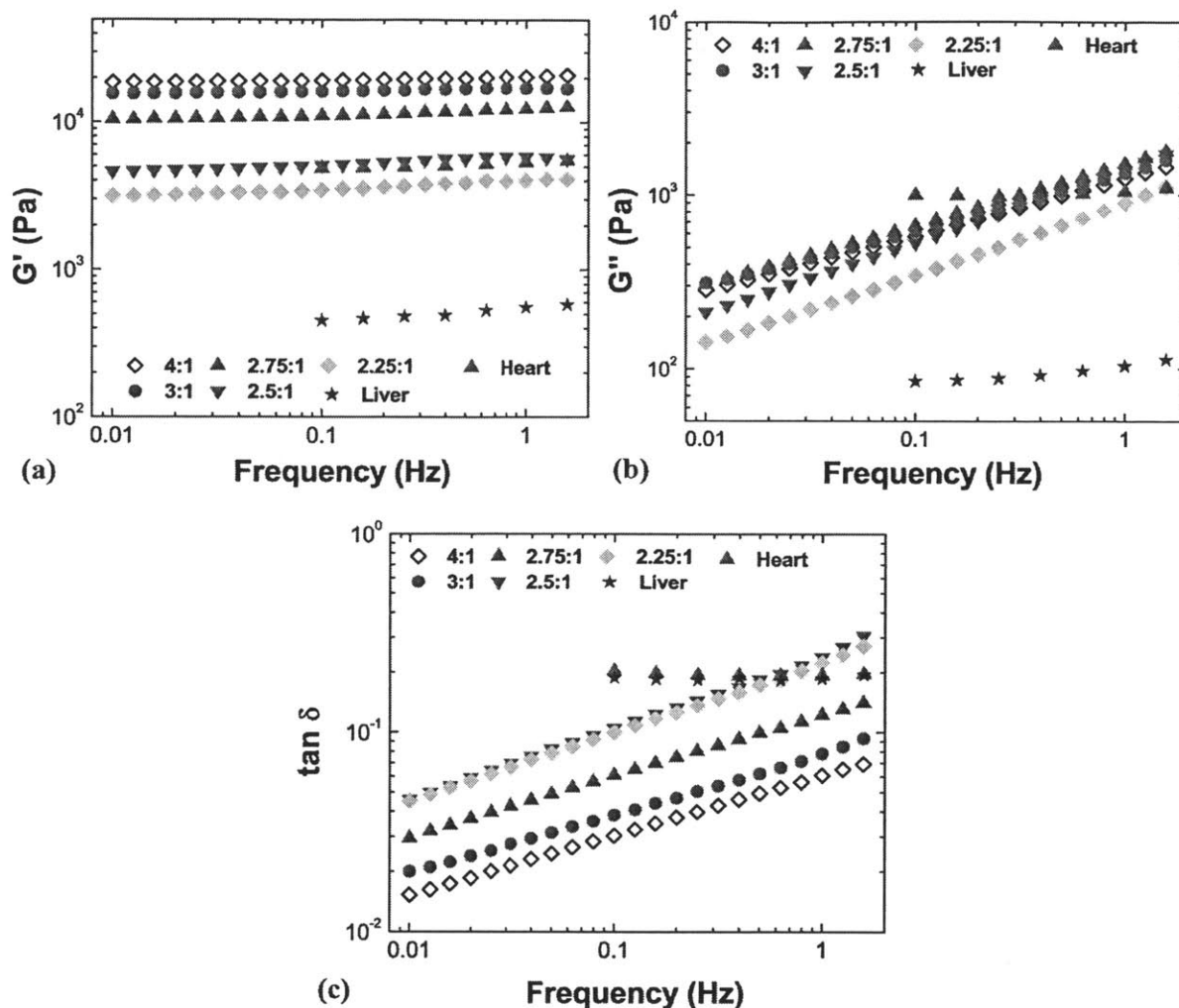


Figure 4.4 Effect of crosslinking density on (a) Storage modulus G' , (b) Loss modulus G'' , and (c) Loss tangent $\tan \delta$ of heart and liver tissues, and of PDMS gels containing 60 vol% of 1.1 kg/mol solvent.

This hypothesis is supported by our results obtained of gels comprising 308 kg/mol solvent, which significantly exceeds the entanglement molecular weight of PDMS (~ 29 kg/mol¹⁸⁴). For these gels, decrease in the silane:vinyl stoichiometry from 4:1 to 2.25:1 hence decrease in the crosslinking density and the number of dangling chain ends correlated with increased frequency-dependence of G' (Figure 4.5a), suggesting that the dangling chain ends entangle with the solvent. At high frequencies, these entanglements will act as effective crosslinking points and thus the dangling chain ends can contribute to the storage modulus¹⁷⁴. These gels exhibited

higher loss moduli compared with gels comprising solvent of lower molecular weight (Figure 4.5b), and they became more dissipative as the silane:vinyl ratio was decreased (Figure 4.5c).

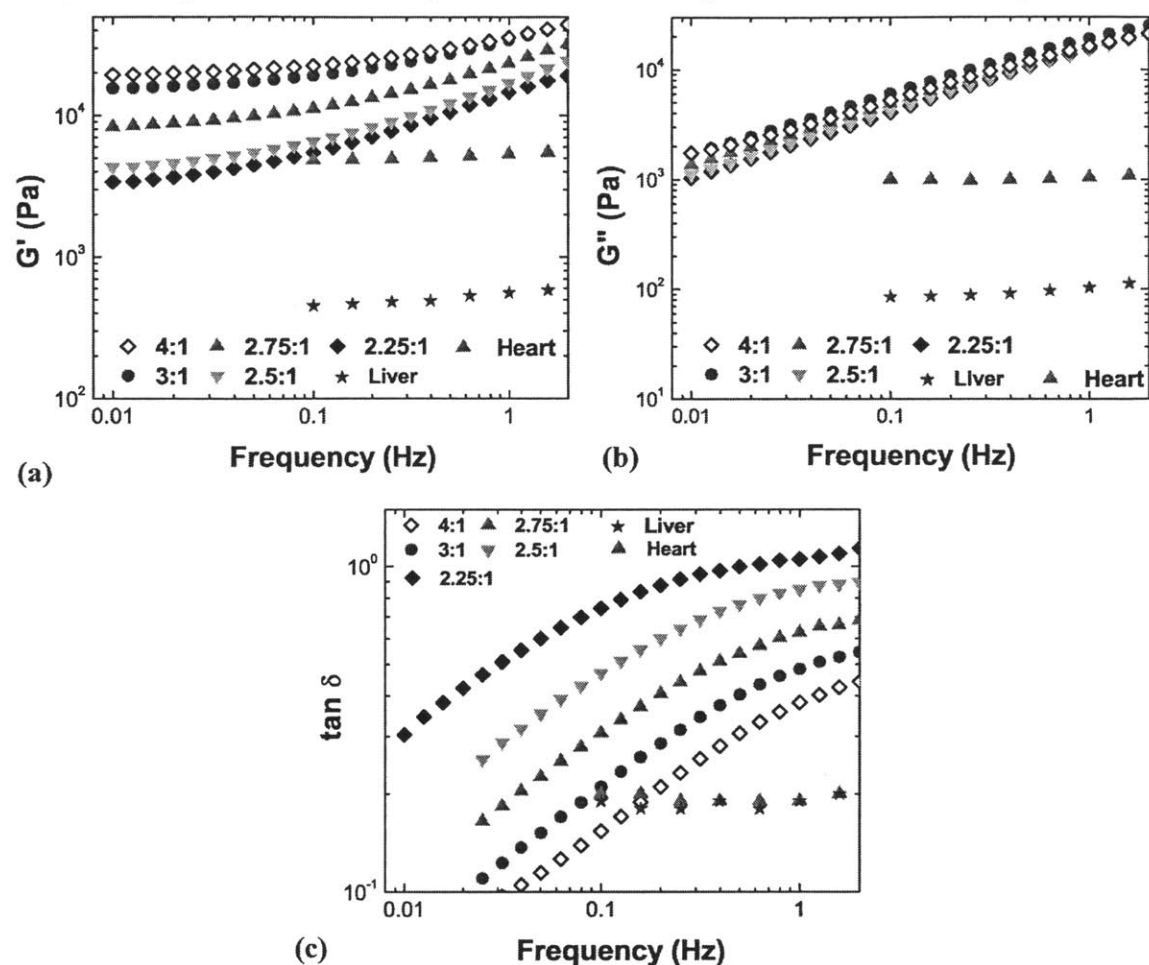


Figure 4.5 Effect of crosslinking density on (a) Storage modulus G' , (b) Loss modulus G'' , and (c) Loss tangent $\tan \delta$ of heart and liver tissues, and of PDMS gels containing 60 vol% of 308 kg/mol solvent.

4.3.2.3 Effect of solvent molecular weight on the magnitude and rate dependence of G' , G'' , and $\tan \delta$

Effects of solvent molecular weight on the viscoelastic properties of the present gel system was investigated in detail previously⁸⁰. Here, we extend that study to gels with higher solvent vol%, which are consequently more compliant and thus more suitable for soft-tissue simulant applications. Rheological measurements were obtained of PDMS gels with a 4:1 silane:vinyl stoichiometry and solvent loading of 80 vol% for three different solvent molecular weights (1.1, 139 and 308 kg/mol) to broadly span the entanglement molecular weight of PDMS (~29 kg/mol).

Our results indicate that increasing the solvent molecular weight did not significantly affect the storage modulus at low loading frequencies, but did induce an enhanced frequency dependence of the storage modulus (Figure 4.6a). As it was shown previously that the network microstructure was insensitive to solvent molecular weight (or “size”), this effect was attributed to decreased diffusion of the entangled solvent at higher molecular weights⁸⁰. Hence, the increase in the number of entanglements caused by larger solvents is considered the determining factor that leads to longer relaxation times of the dangling chains relative to the deformation rate. At higher frequencies, these entanglements act as elastic chains and contribute to the stiffness. In addition, relaxation times of the free chains trapped in the network (i.e., the solvent) also increase as the solvent molecular weight increases^{185,188}. These free chains behave as elastic chains when the observation time scale is shorter than the relaxation time of the guest chains¹⁸⁹, which can lead to an increase in G' at higher frequencies. The storage modulus of gels containing low-MW solvent exhibited frequency dependence similar to that of heart and liver tissues. Energy dissipation of these gels increased with increasing solvent MW (Figure 4.6 b, c), which can be attributed to the increase in chain entanglements and thus to the higher number of entanglements that must be disrupted to facilitate chain migration.

In conclusion, this rheological survey of a large library of PDMS gels indicates that the storage modulus could be tuned to match that of soft tissues at the frequencies studied herein, chiefly by decreasing the crosslinking density and increasing the solvent loading. When the solvent molecular weight was lower than the entanglement molecular weight of PDMS, changing the solvent loading or the crosslinker density did not impact the frequency dependence. By increasing the solvent molecular weight to 308 kg/mol, we obtained gels that exhibited an increased frequency dependence, though this frequency dependence exceeded that of heart and liver tissues for the strain rates investigated here.

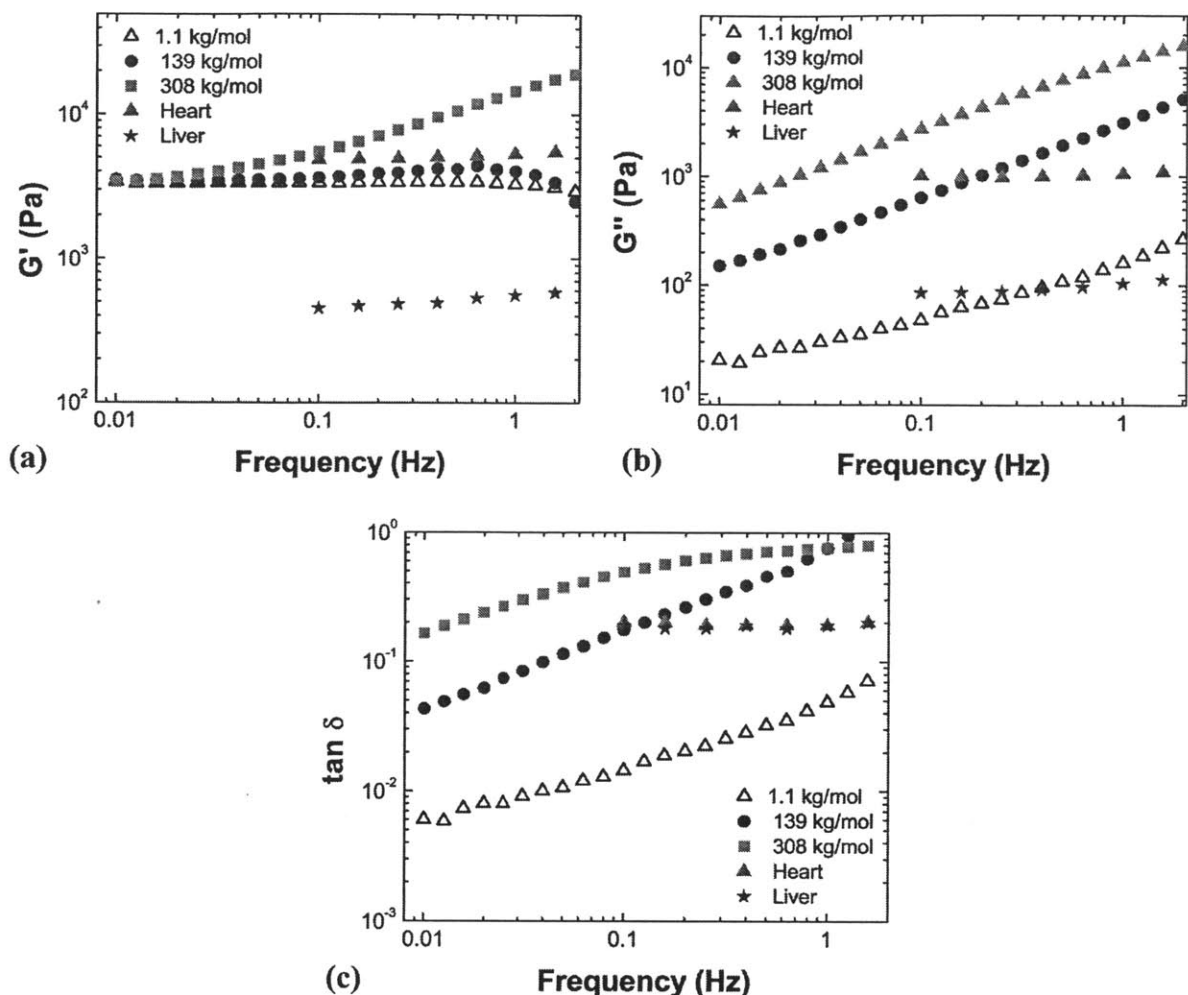


Figure 4.6 Frequency dependence of (a) Storage modulus G' , (b) Loss modulus G'' , and (c) Loss tangent $\tan \delta$ of gels with 4:1 silane:vinyl stoichiometry, containing 80 vol% of solvent with molecular weight of 1.1, 139, or 308 kg/mol.

4.4 Impact indentation experiments

Following the design baseline obtained from rheological measurements of PDMS gels, impact indentation experiments were conducted to study the gel response in comparison to soft tissues at high rates under concentrated impact loading. Thus, we investigated impact resistance, as well as the capacities and rates of energy dissipation, of PDMS gels as a function of solvent loading vol%, crosslinking density, and solvent molecular weight for impact velocities ranging from 0.4 to 2 cm/s. Although these impact velocities are relatively small compared to other macroscale impact testing methods such as pneumatic gun and falling weight impact tests, the calculated strain energy densities spanning a range of 2-20 kJ/m³ are comparable to other macroscale

impact tests (15-60 kJ/m³)⁷². The results presented in this section provide insights into design principles and approaches to modulate the mechanical response of tissue simulant gels to concentrated impact loading to enable the development of biofidelic tissue simulants.

4.4.1 Experimental Methods

Gel samples were cut into rectangular shapes with a thickness of 4 mm, and a width and length greater than 1 cm. Heart and liver tissues were harvested from three different animals and tested within 3 h post-mortem. Impact indentation was conducted on all tissues and gels with a stainless steel cylindrical probe ($R = 1$ mm) at 25°C using a commercially available pendulum-based instrumented nanoindenter (Micro Materials Ltd., UK). The instrument was modified previously and calibrated to enable impact indentation of compliant and adhesive materials in fully hydrated conditions¹²⁸ (see Section 3.3.2.2). Experiments were conducted at impact velocities ranging 0.4 - 2 cm/s leading to nominal strain rates $\dot{\epsilon}$ up to 30 s⁻¹ approximated by $\dot{\epsilon} \sim v_{in}/x_{max}$. Strain energy densities (SED) were calculated as impact energy normalized by the geometric contact volume of the cylindrical probe at maximum penetration depths:

$$SED = \frac{1/2mv_{in}^2}{\pi R^2 x_{max}} \quad (4.1)$$

where m is the mass of the pendulum (0.17 kg), and x_{max} is the maximum penetration depth calculated from the displacement time response of the pendulum (Section 3.3.2.3). For the experiments conducted here, calculated SED values ranged from 2-20 kJ/m³ due to the relatively small probe contact area and volume. Tissue samples obtained from murine heart and liver were tested under the same conditions in a fully hydrated state; penetration proceeded normal to the outer fibrous layer of the tissue as schematized in Figure 3.1 a, b. Given the maximum penetration depths attained in these experiments, measured displacement-time responses were attributed to the overall response of the tissue, rather than to individual tissue layers. Replicate experiments were conducted at each impact velocity for both PDMS gels ($n=3$) and tissues ($n=5$). Probe displacement was recorded throughout successive impact cycles until the probe came to rest (Figure 4.7). Impact resistance, energy dissipation capacity K , and quality factor Q related to energy dissipation rate were computed from the acquired displacement vs. time traces as explained in Section 3.3.2.3. Data are represented as mean \pm standard error. Although the anticipated application of the PDMS gels as tissue simulants is in air, due to their highly adhesive nature these gels were immersed in an aqueous solution containing 3% Pluronic® F108

during mechanical characterization. Note that, in Chapter 3, this aqueous solution was shown to minimize adhesive forces between the probe surface and styrenic block copolymer gel surface (Section 3.2.4.3.3), and Appendix B shows that immersing other PDMS gels in solution containing pluronic minimizes adhesive forces, as well. This immersion enabled quantification of gel impact response with minimized surface interactions between this specific probe and the samples; future studies could be undertaken to compare energy dissipation as a function of probe material. Separate paired experiments were conducted in air and fluid to verify negligibility of the contribution of fluid drag forces to the overall damping of the system, and ensure that testing in fluid did not affect the measured properties of the samples.

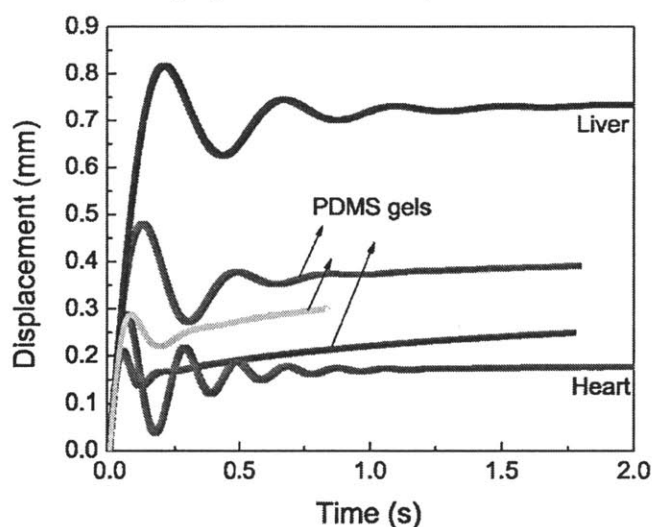


Figure 4.7 Indenter displacement vs. time response from dynamic impact indentation of soft biological tissues and PDMS gels with 2:1 stoichiometry and 50% solvent loading differing only in solvent molecular weight. From these raw data, one can visually compare the maximum penetration depths (measure of impact resistance) and the number of impact cycles (related to energy dissipation rate).

4.4.2 Results and Discussion

4.4.2.1 Effect of solvent loading vol% on impact resistance, energy dissipation capacity, and energy dissipation rate

Impact indentation experiments were conducted on heart and liver tissues and on PDMS gels with silane:vinyl stoichiometry of 4:1, solvent molecular weight of 1.1 kg/mol, and a range of solvent loading including 60, 70, 75 and 80 vol%. As expected, maximum penetration depths increased as the solvent loading increased (Figure 4.8a), indicating that the gels become less impact resistant with increasing solvent vol%. This is in agreement with small-strain Rheology

(Figure 4.2a), which showed decreased storage modulus G' with increased in solvent loading vol%, and is consistent with increased formation loop defects and screening of physical entanglements^{181,190}. Increased solvent loading also led to an increase in the impact velocity-dependence of penetration resistance (Figure 4.8a), and in the energy dissipation capacity defined as K (Figure 4.8b). Finally, energy dissipation was faster (lower Q) for higher solvent loadings (Figure 4.8c). Impact resistance of heart tissue was matched most closely by the gel comprising 70 vol% solvent. However, this gel dissipated less energy in the first impact event (lower K) and dissipated this energy more slowly (higher Q) than both heart and liver tissues under the impact velocities considered. Although the gel comprising 80 vol% solvent most closely approached the impact resistance, the energy dissipation capacity and rate of liver tissue, all of these gels were in fact more impact resistant and exhibited lower capacities and rates of energy dissipation than liver tissue. Thus, although trends as a function of solvent loading are clear, modulation of only this parameter is insufficient to mimic the impact behavior of either of these soft tissues.

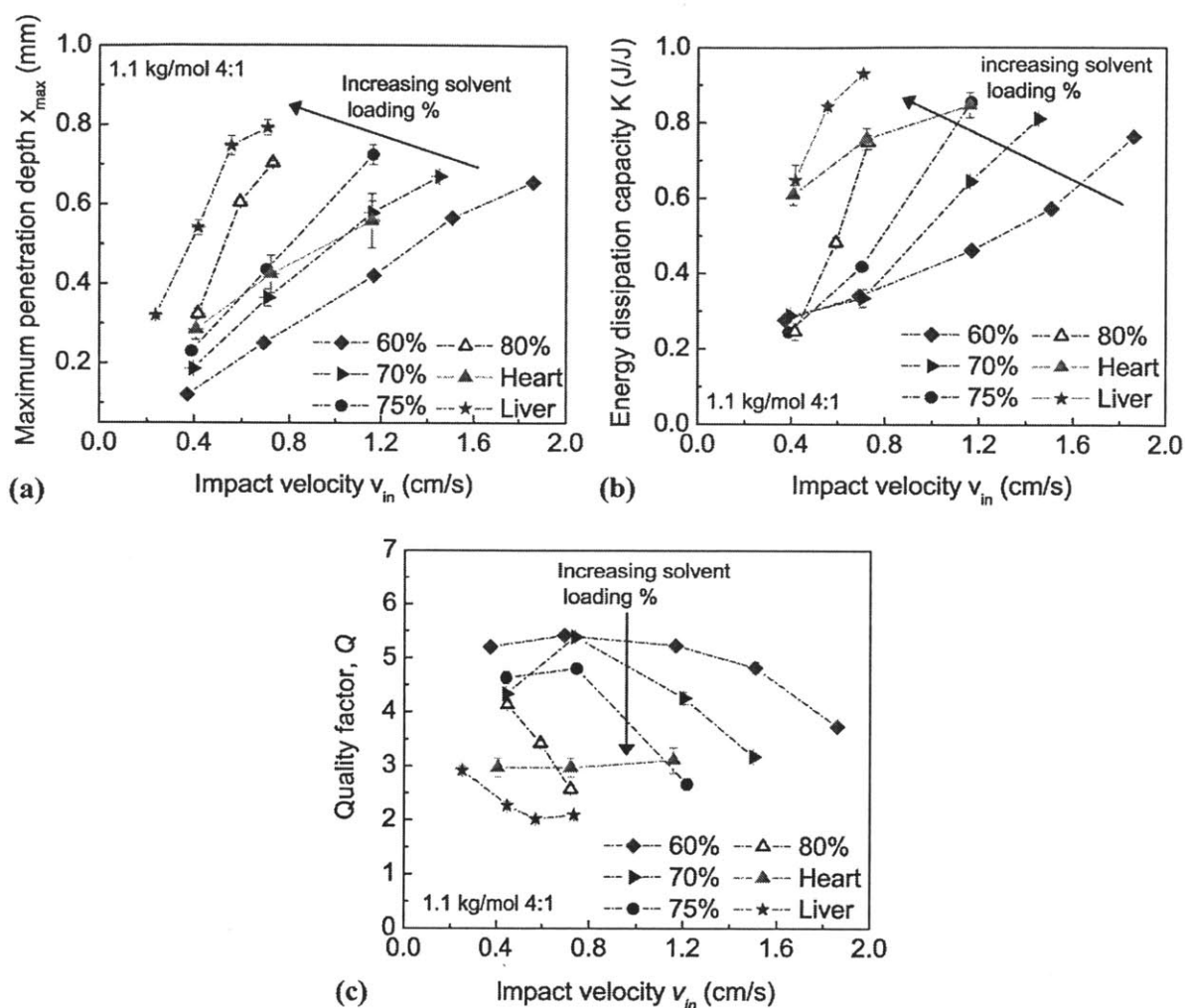


Figure 4.8 Effect of solvent loading vol% for PDMS gels with silane:vinyl stoichiometric ratio of 4:1 and solvent molecular weight of 1.1 kg/mol (a) Maximum penetration depth x_{max} as a function of impact velocity: as the solvent loading % increases, the gels become less impact resistant; this effect is more pronounced at higher impact velocities. (b) Energy dissipation capacity K as a function of impact velocity: K increases as solvent loading % increases; this effect is more pronounced at higher impact velocities. (c) Quality factor Q as a function of impact velocity: increasing the solvent loading% decreases Q (i.e., increases the energy dissipation rate). Data are represented as mean \pm standard error, and standard error bars may appear smaller than the symbols.

4.4.2.2 Effect of precursor chain stoichiometry on impact resistance, energy dissipation capacity, and energy dissipation rate

To investigate the effect of precursor chain stoichiometry (representing the crosslink density within the present range) on impact responses, PDMS gels loaded with solvent of 1.1 kg/mol molecular weight at 60 vol% were considered; precursor chain stoichiometric ratios ranged from

2:1 to 4:1. Figure 4.9a shows that impact resistance of these gels increased for a given impact velocity as the crosslinking density increased (i.e., as stoichiometry varied from 2:1 to 4:1). These trends agree well with macroscale rheology, for which increasing crosslinking density resulted in increased storage modulus (Figure 4.4a). Gels of highest crosslinking densities (3:1 and 4:1 ratio) exhibited similar maximum penetration depths, indicating that further increases in crosslinker density would be unlikely to further decrease x_{\max} ; the stoichiometric ratio is already optimal at 4:1⁸⁰. Increasing the amount of crosslinker resulted in lower energy dissipation capacities (lower K , Figure 4.9b) and lower energy dissipation rates (higher Q , Figure 4.9c), due ostensibly to an increase in the elastic chains and a decrease in the incorporation of dangling chain ends. Impact resistance and energy dissipation rate of heart tissue were best matched by gels comprising 60 vol% of 1.1 kg/mol solvent at a precursor stoichiometric ratio of 2.75:1. Impact resistance of liver tissue was best matched by gels comprising 60 vol% of 1.1 kg/mol solvent at a precursor stoichiometric ratio of 2:1, though this candidate tissue simulant dissipated more energy than liver tissue (higher K).

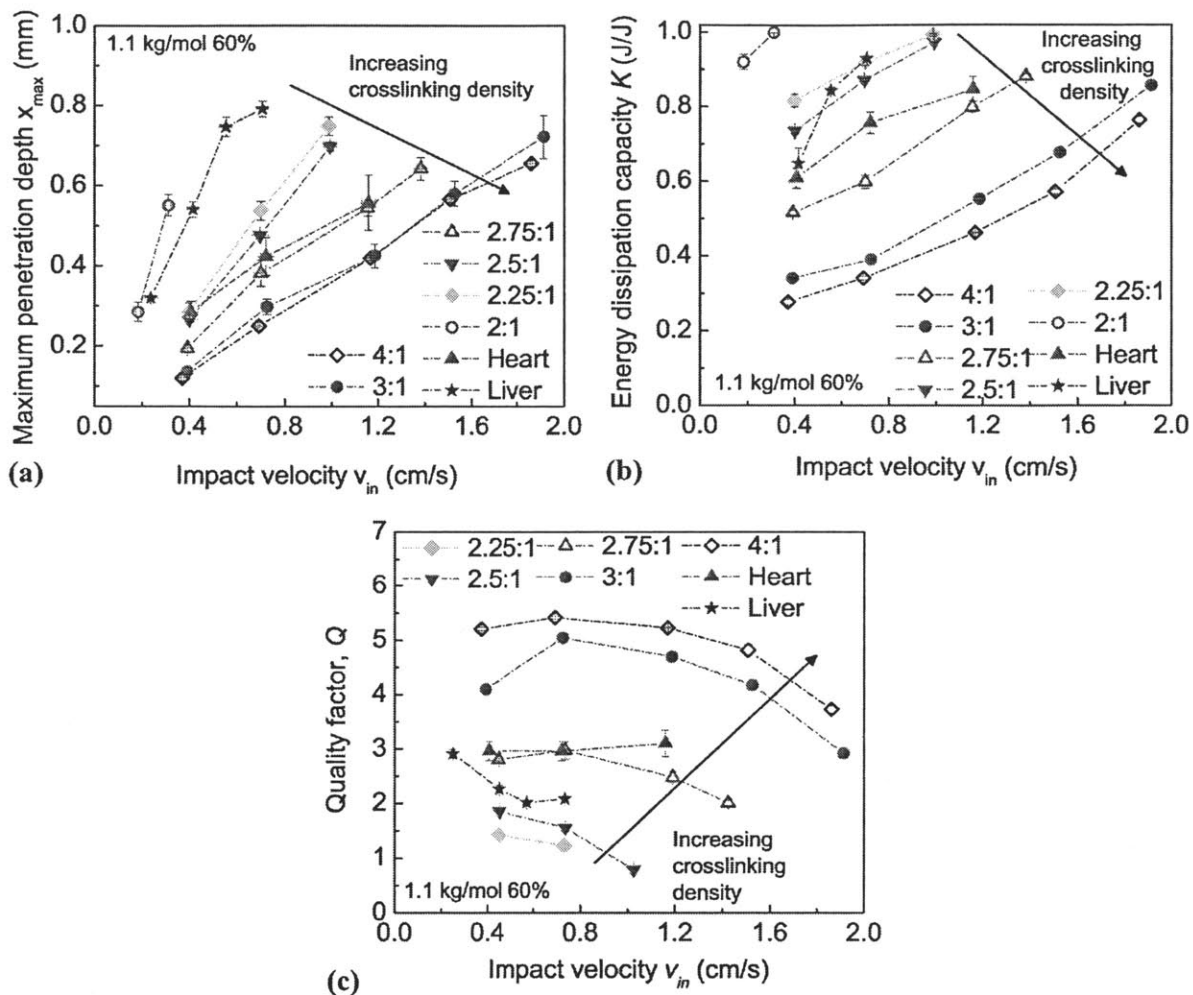


Figure 4.9 Effect of stoichiometric ratio of vinyl to crosslinking silane groups for PDMS gels with 60 vol% 1.1 kg/mol molecular weight solvent (a) Maximum penetration depths as a function of impact velocity: impact resistance of gels increases (lower x_{max}) by increasing the crosslink density; this effect is more pronounced at higher impact velocities. Impact resistance of heart and liver tissues is matched by the PDMS gels. (b) Energy dissipation capacity K as a function of impact velocity: gels dissipate more energy at lower crosslinking densities. Energy dissipation capacity of the tissues is matched by the gels with lower crosslinking. (c) Quality factor Q as a function of impact velocity: gels dissipate energy more quickly (lower Q) as the crosslinking density decreases. Both heart and liver show comparable energy dissipation rates to the gels with lower crosslinking density. Data are represented as mean \pm standard error, and error bars may appear smaller than data symbols.

4.4.2.3 Effect of solvent molecular weight on impact resistance, energy dissipation capacity, and energy dissipation rate

Impact indentation experiments were conducted on PDMS gels with solvent loading of 80 vol% and precursor chain stoichiometric ratio of 4:1 for solvent molecular weights of 1.1, 139 and 308 kg/mol. Figure 4.10a shows that impact resistance of these gels increased with increasing molecular weight of the solvent (lower x_{\max}). Further, the dependence of impact resistance on impact velocity was enhanced with increasing solvent molecular weight, recalling the macroscale rheological trends of increased frequency dependence of storage moduli with increasing solvent molecular weight. Such increased stiffness and impact resistance are consistent with the concept of an increased number of physical entanglements as the solvent molecular weight surpasses MW_{ENT} . Energy dissipation capacity (Figure 4.10b) and rate (Figure 4.10c) also increased substantially as the solvent molecular weight surpassed MW_{ENT} , which could be attributed to increased physical entanglements and to correspondingly decreased solvent mobility. In fact, gels of solvent molecular weights of 139 kg/mol and 308 kg/mol dissipated most or all of the energy during the first impact leading to $K \sim 1$ and quality factor values less than unity (dashed line). We note that, although adhesion was mitigated to the extent possible in these experiments, gel adhesion to the impact probe surface was qualitatively greater at higher solvent molecular weights; this could serve as an additional mechanism for energy dissipation. We conclude from these results that gels comprising solvents of lower molecular weight are favored candidates to approximate the impact response of heart and liver tissues for the impact velocities explored in this study.

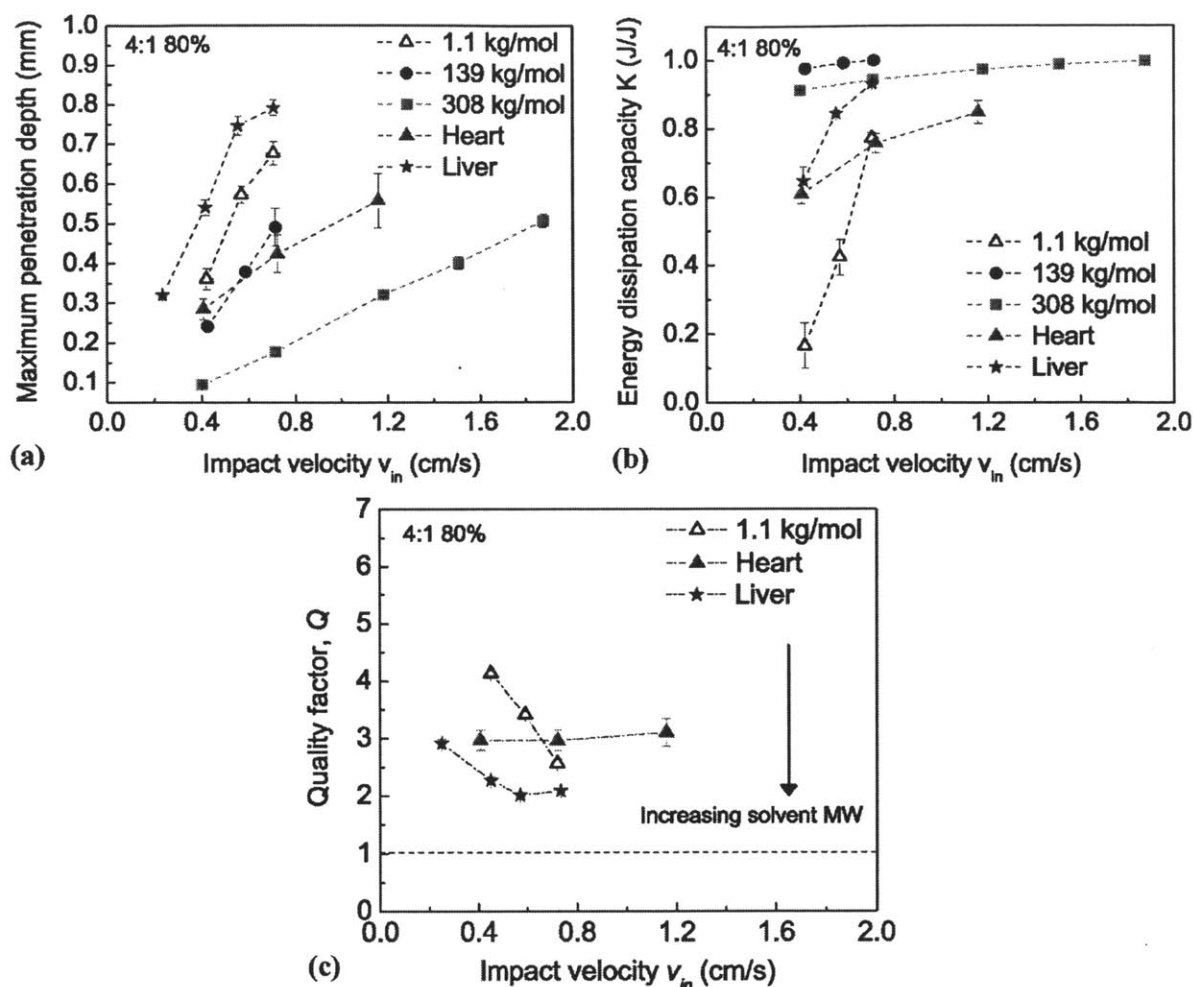


Figure 4.10 Effect of solvent molecular weight on impact response of PDMS gels with a 4:1 precursor chain stoichiometry and 80 vol% solvent loading: (a) Maximum penetration depths as a function of impact velocity: gels become more impact resistant as the molecular weight (MW) of the solvent increases; this effect is more pronounced at higher impact velocities. (b) Energy dissipation capacity K as a function of solvent MW: gels of larger solvent MW are more dissipative at a given impact velocity. (c) Quality factor Q as a function of impact velocity: increasing solvent MW increases the energy dissipation rate (lower Q), to the extent that for gels with $MW > 1.1$ kg/mol, energy was dissipated during the first impact cycle leading to Q values below the dashed line. Data are represented as mean \pm standard error.

4.4.2.4 Comparison of impact response among gels and soft tissues

The above discussion makes clear that the three design parameters considered (solvent vol%, solvent molecular weight, and precursor ratio) can result in coupled or competing effects on the impact performance metrics of interest (x_{max} , K , and Q). Quantification and understanding of this coupling allows us to move from many iterative experiments to reasonably predictive design of

impact performance. Here, we demonstrate the tuning of these knobs to realize a tissue simulant for heart tissue impact response, and discuss how these same principles can be extended toward design of mechanical tissue simulants for other, more compliant tissues such as liver.

Heart - Our impact indentation experiments showed that two gels exhibited similar impact resistance (i.e., maximum penetration depths x_{\max}) to that of heart tissue for the impact velocities studied here (Figure 4.11a). These gels comprised solvent of 1.1 kg/mol molecular weight, with loading/precursor chain stoichiometry of 70 vol%/4:1 or 60 vol%/2.75:1. In these gel families, we observed that impact resistance could be tuned by opposing design parameters: increasing the solvent loading from 60 vol% to 70 vol% increased x_{\max} , and increasing the crosslinking density (changing the stoichiometry from 2.75:1 to 4:1) decreased x_{\max} . Although these two gels exhibited similar impact resistance, the candidate with the lower solvent loading and crosslinking density dissipated more energy during the first impact bounce (larger K), and dissipated this energy more quickly (lower Q); thus, this tissue simulant candidate better matches the impact response of heart tissue (Figure 4.11b, c). Therefore, by tuning the crosslinker density and solvent loading, we were able to decouple and individually tune these three metrics of impact energy behavior, and thus to realize a tissue simulant candidate for murine heart tissue.

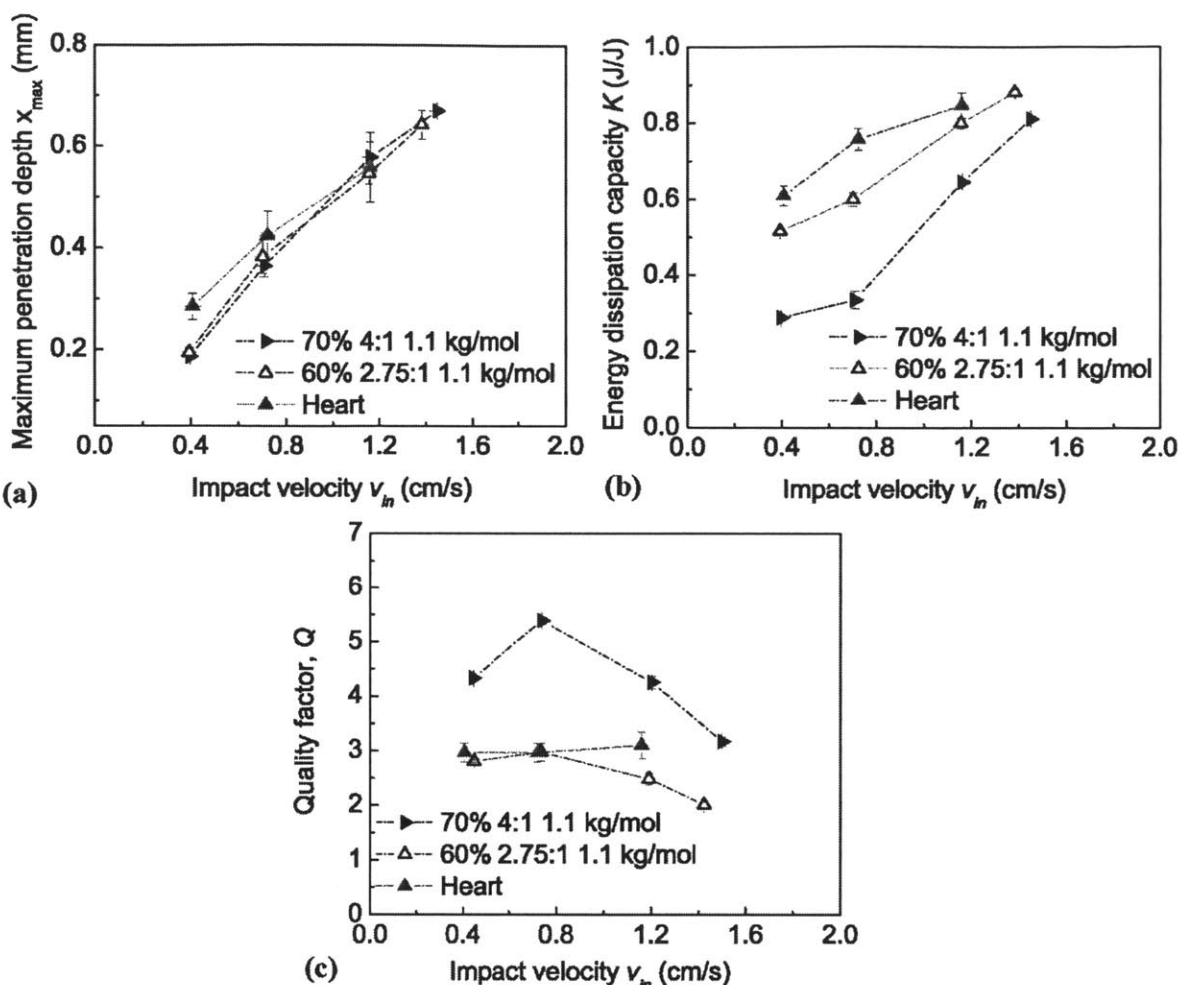


Figure 4.11 (a) By changing the solvent loading vol% and silane:vinyl stoichiometry, we compare two different gels that both mimic the impact resistance of heart tissue for the impact velocities explored herein. (b) These two gel systems exhibit distinct energy dissipation capacities K (b) and quality factor Q (c). For the impact velocities considered, the gel with 60 vol% solvent of 1.1 kg/mol MW and silane:vinyl stoichiometry of 2.75:1 most closely mimics heart tissue by all three metrics of mechanical impact response.

Liver - We identified several gels that exhibited either maximum penetration depths (Figure 4.12a), energy dissipation capacities (Figure 4.12b), or energy dissipation rates (Figure 4.12c) that were similar to those of liver tissue for the impact velocities studied here. However, unlike for the case of heart tissue, none of these gels captured the impact response of liver tissue by all metrics. For example, gels with a composition of 80 vol%-4:1-1.1 kg/mol and 60 vol%-2:1-1.1 kg/mol exhibited x_{max} similar to liver tissue, while the former dissipated less energy and the latter dissipated more energy than liver. Further increasing the molecular weight of the 80% 4:1 gel

from 1.1 to 139 kg/mol increased the energy dissipation capacities but also decreased the maximum penetration depths significantly. On the other hand, gel systems with a composition of 60 vol%-2.5:1-1.1 kg/mol and 60 vol%-2.25:1-1.1 kg/mol exhibited similar energy dissipation capacities to liver but yielded much lower maximum penetration depths.

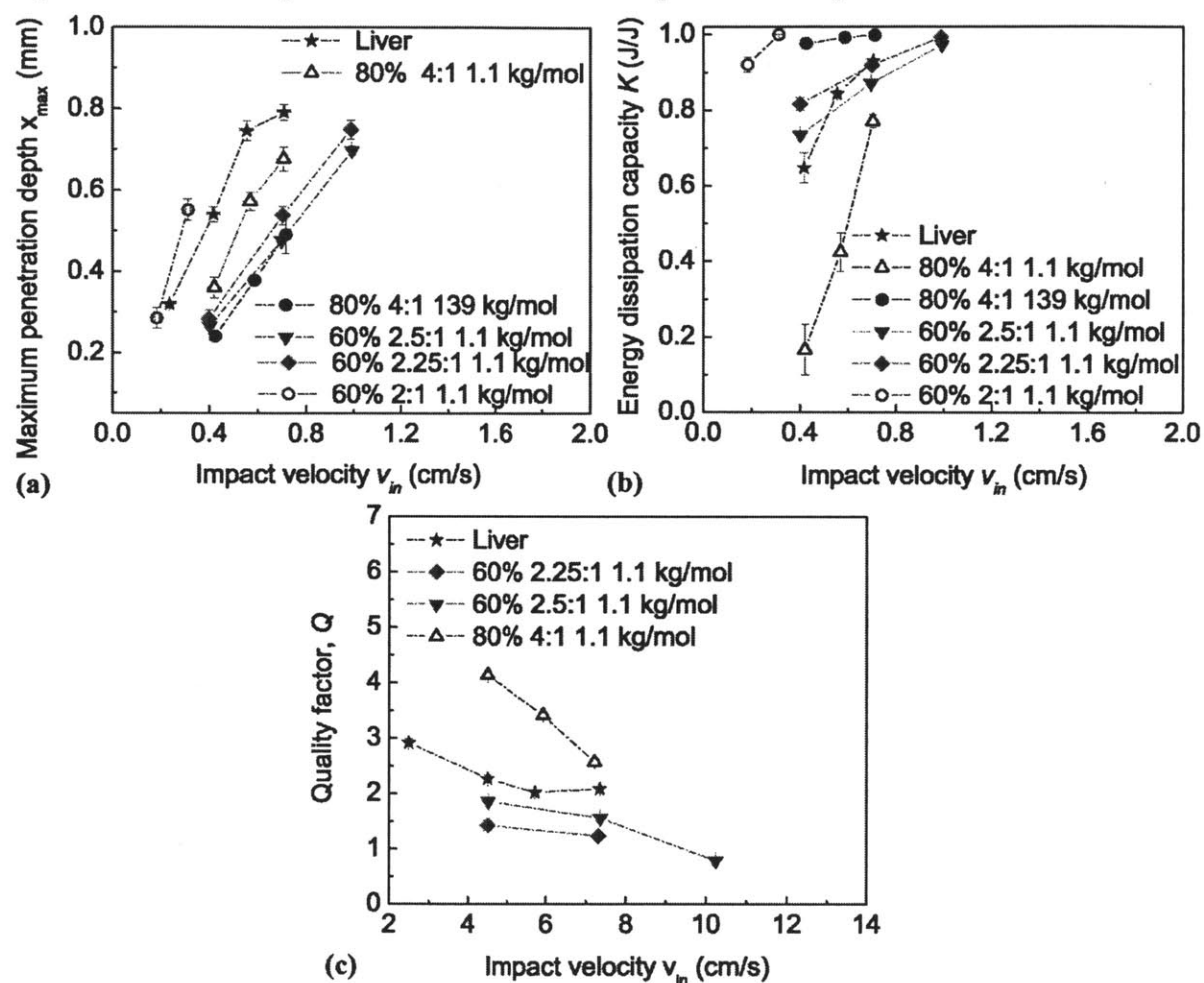


Figure 4.12 (a) The two top candidates for matching liver tissue impact resistance are the PDMS gels with 60 vol% solvent/silane:vinyl stoichiometry of 2:1, and 80 vol% solvent/silane:vinyl stoichiometry of 4:1, both with solvent MW of 1.1 kg/mol. The two top candidates for matching energy dissipation capacity K (b) and quality factor Q (c) of liver tissue are the PDMS gels with 60 vol% solvent/silane:vinyl stoichiometry of 2.25:1, and 60 vol% solvent/silane:vinyl stoichiometry of 2.5:1, both with solvent MW of 1.1 kg/mol.

Although it is beyond the scope of the current study to further optimize these gels toward liver tissue simulants, we can draw on the design parameters identified above to now suggest further iterations toward that aim. Based on the PDMS gels considered herein, an improved liver tissue

simulant could plausibly be attained by increasing the solvent loading vol% in gels with low crosslinking density (between 60% to 70% for 2.25:1 or 2.5:1 gels); this tuning would be expected to increase the maximum penetration depths (Figure 4.13). However, this increase in the solvent vol% would also likely increase the energy dissipation capacities (Figure 4.13) to exceed that of liver. To compensate for this increase, silane:vinyl ratio (i.e. crosslinking density) could be increased only slightly (precursor ratios between 2.5:1 and 2.75:1) to achieve lower energy dissipation capacities (Figure 4.13) without significantly impacting the maximum penetration depths. Another potential design route would be selection of a stoichiometric ratio between 2:1 and 2.5:1 to obtain similar maximum penetration depths to liver, and slightly decreasing the solvent loading (between 50-60 vol%) in order to decrease energy dissipation capacities without significantly increasing maximum penetration depths.

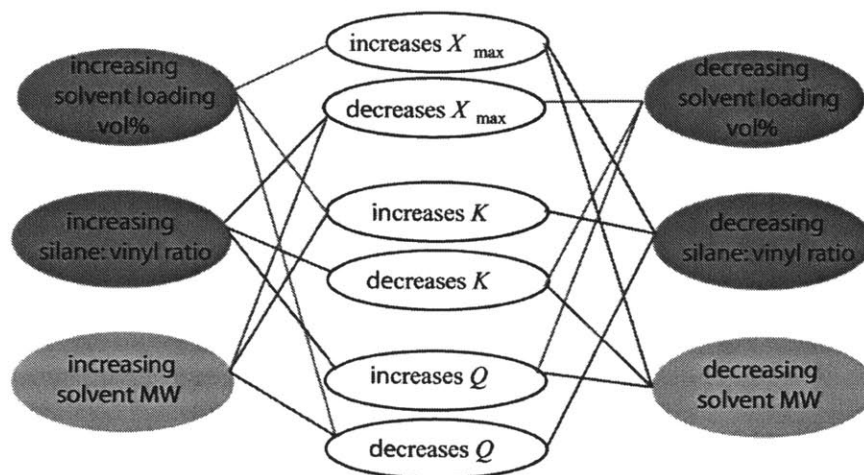


Figure 4.13 Effect of solvent loading vol%, silane:vinyl stoichiometric ratio (i.e. crosslinking density), and solvent molecular weight (MW) on maximum penetration depths x_{max} , energy dissipation capacities K , and energy dissipation rates Q .

4.5 Concluding Remarks

Chapter 4 explored and identified design principles required to simultaneously optimize key response metrics of impact response for PDMS gels, and tailored those gels to mimic the impact resistance and energy dissipation capacity and rate of soft tissues as closely as possible. Macroscale rheology was conducted as a baseline survey to establish trends for this gel family, and impact indentation was conducted to establish design principles for mimicking impact response of heart and liver. From the former survey, it is found that storage modulus and impact

resistance could be increased by decreasing the solvent loading, increasing the crosslinking density, and increasing solvent molecular weight. From the latter impact loading, it is observed that energy dissipation capacity and energy dissipation rate could be increased by decreasing the crosslinking density and increasing the solvent vol%. By varying the silane:vinyl stoichiometric ratio and solvent loading, the impact resistance and energy dissipation capacity and rate of the gels were decoupled, which enables independent tuning of these material characteristics for tissue-specific applications. Further, under identical impact loading conditions, specific gel compositions were identified that replicated the impact penetration resistance, energy dissipation capacity and rate of heart tissue with reasonable fidelity. These findings inform the design of synthetic gels to recapitulate the response of specific biological materials under impact.

Chapter 5 Elastic and Transport Properties of Hydrogels and Soft Tissues via Contact Mechanics

5.1 Introduction

Given the complex structure of native tissues, understanding the structure-property relationship of soft tissues is critical for the robust design of tissue simulant gels for ballistic applications that can accurately mimic the mechanical deformation of soft tissues. In Chapter 3 and Chapter 4, we have utilized elastic and viscoelastic models to characterize the mechanical properties of heart and liver in comparison to tissue simulant gels with the aim to design a gel that would recapitulate soft tissue response at high rates (i.e., short time scales). However, soft tissues are biphasic in nature: they contain solid and fluid components that both deform and that can interact during mechanical loading. Thus, a portion of the time dependence of the mechanical response is associated with the flow of the fluid through the tissue. Understanding the role of the fluid flow in the mechanical response is particularly crucial when the relaxation time scales of the fluid is in the range of the experimental time scales, which is the case for applications such as the design of tissue-engineered constructs and/or developments in computer-integrated and robot-aided surgery that require accurate computational models of tissue deformation under low rate mechanical loading (i.e., longer time scales). The aim of this chapter is to characterize elastic and transport properties of heart and liver as a function of tissue structure via a contact based poroelastic analysis – a mechanical theory that incorporates fluid motion through a porous elastic network. This framework is applied to contact-based indentation experiments, which offer particular advantages for tissue analysis including minimal specimen preparation requirement, the ability to probe local properties, and the capacity to measure mechanical and transport properties simultaneously. However, extraction of the values of the constitutive parameters from the test output of such experiments is not always straightforward. In Section 5.2, we introduce a recently developed contact mechanics-based approach in order to characterize the elastic and transport properties of soft tissues at smaller length scales and shorter time scales. Here, in conjunction with the Z. Suo group at Harvard University’s School of Engineering and Applied Sciences, we confirm the validity of a continuum-scale poroelastic model as applied to

homogeneous hydrogels at the nanoscale. This enables us to explore time-dependent properties due to fluid flow through the gels. Finally, in Section 5.3 we introduce the application of this method on murine heart and liver.

5.2 Multiscale elastic and transport properties of polyacrylamide gels

The following study was published in Soft Matter in 2012 with coauthors R. Mahmoodian, Y. Hu, Z. Suo, and K.J. Van Vliet¹⁹¹, and is reproduced by permission of The Royal Society of Chemistry (RSC). <http://pubs.rsc.org/en/content/articlelanding/2012/sm/c2sm06825g>

5.2.1 Background and Motivation

Instrumented indentation is a well-established approach to measure mechanical properties of materials. Initially utilized to characterize elastic and plastic properties of metals and ceramics⁸⁸, such experiments have been applied more recently to characterize viscoelastic and poroelastic regimes in relatively more compliant materials including polymeric gels and so-called soft tissues^{12,38,53,81,85,134,192-194}.

Polymeric gels, consisting of a network of cross-linked polymer chains swollen with a solvent, are a class of gels with widespread application in which the solid network deformation and solvent flow are coupled. Scherer¹⁹⁵⁻¹⁹⁶ provided the analytical foundation¹⁹⁷⁻¹⁹⁸ and a novel test¹⁹⁸ to obtain elastic and viscoelastic properties and permeability of aerogel beams in bending. However, this beam-bending approach is difficult to implement for increasingly compliant materials (Young's elastic modulus $E < 1$ MPa). Hui et al. recently presented a contact-based theoretical approach to extract simultaneously the mechanical and transport properties of hydrated gels via cylindrical punch indentation¹⁹⁷, whereby the load relaxation response was related to the shear modulus, Poisson's ratio, diffusivity, and permeability of a gel. To extend this load relaxation approach to other indenter geometries, Lin et al. and Hu et al. utilized finite element analyses to obtain semi-analytical relations between the initial and fully relaxed load for a flat rigid circular punch,¹⁹⁹ rigid rectangular punch⁵⁴, and conical and spherical punches⁵⁰⁻⁵¹.

One important characteristic of gels and other fluid-filled materials is that mechanical response can depend on both the time scale and length scale of measurement. Since the time dependence of a linear viscoelastic response is independent of the contact diameter, whereas the poroelastic response is dependent on contact diameter, the aforementioned approaches provide a means to

distinguish between load relaxation resulting from viscoelastic relaxation of the gel network and that resulting from solvent flow. In fact, Hu et al.⁵⁰⁻⁵¹ adopted a facile scaling means to identify dominance of the poroelastic deformation regime, so that experiments could be designed to extract both the elastic and transport properties of gels. To date, however, these methods have been applied only at the macroscale level for probe diameters on the order of cm. Since the poroelastic relaxation time τ scales quadratically with contact diameter, relaxation times in such experiments are on the order of hours. This length-time scale coupling renders experiments quite time consuming, which constrains the range of material systems that can be studied. In particular, it is not feasible to analyze the poroelastic response of soft biological tissues or degradable gels that require mechanical analysis under hydrated conditions over durations that are shorter than the degradation timescales that naturally affect structure and properties. Further, macroscale analysis of poroelastic properties restricts treatment of materials such as striated tissues that exhibit structural transitions at smaller (e.g., μm) length scales.

In this section, we sought to extend and validate the load relaxation approach of Hu et al. to smaller length and time scales, which would enable future studies on degrading or structurally heterogeneous gels and tissues. We compared analysis at the micro- and macroscale levels for a polyacrylamide (PAAm) hydrogel to determine whether poroelasticity could be identified as the dominant regime at the microscale, and to determine whether the elastic and transport properties could be extracted accurately and more rapidly than possible at the macroscale.

5.2.2 Materials and Methods

5.2.2.1 Material synthesis

Acrylamide stock solution was prepared by mixing 40% w/v acrylamide, 2% bis-acrylamide solution (Bio-Rad) and distilled water in a ratio of 1:2:2. After degassing the solution for 20 min, gels were synthesized by adding initiators of 10% w/v ammonium persulfate solution and N,N,N',N'-tetramethylethylenediamine (TEMED) to the stock solution. For macroscale experiments, three different gels were cast into 60 mm-diameter polystyrene Petri dishes to form a hydrated thickness of 1 cm. For microscale experiments, three different gels from the same batch synthesis were cast onto silane-treated glass slides. Prior to casting, glass slides were treated with 5 vol% glutaraldehyde, which was then aspirated and rinsed, to ensure that the gels

adhered well to the glass substrate. Gels measured 22 mm × 22 mm in-plane with a hydrated thickness of 500 μm. After 30 min gelation at room temperature, gels were submerged in phosphate buffered solution (DPBS, Invitrogen) and were maintained fully hydrated at 4°C for two weeks prior to testing to attain swelling equilibrium.

5.2.2.2 Macroscale load relaxation experiments

Macroscale load relaxation experiments were conducted by Yuhang Hu in the Suo Lab, Harvard School of Engineering and Applied Sciences using a custom-built load frame with a force resolution of 50 μN and a displacement resolution of 1 μm, as described previously⁵¹. Experiments were conducted via a stainless steel spherical probe of 1 cm radius (Figure 5.1a). The instrument was programmed to approach the surface of PAAm gels at a rate of 2 μm/s, until a positive slope of the force-displacement response was recorded. Upon contact detection, indenter displacement was increased with a rise time of 2 sec to attain three maximum indentation depths h_{\max} = 100, 200, or 400 μm. For each maintained depth, load relaxation measurements were acquired in triplicate over approximately 20, 40, and 110 h, respectively. Gels were fully submerged in phosphate-buffered saline (PBS, 150 mM NaCl, Invitrogen) solution in all experiments.

5.2.2.3 AFM enabled load relaxation testing

Microscale load relaxation experiments (Figure 5.1b) were conducted using atomic force microscope (AFM)-enabled indentation (3D Molecular Force Probe, Asylum Research, Santa Barbara, CA). Cantilevers with spherical polystyrene probes (Novascan) with nominal probe radius of 22.5 μm and spring constant k = 14.0 N/m were used; actual values of k were determined experimentally for each cantilever¹⁹⁴. Upon automatic contact detection (based on cantilever deflection), indenter displacement was increased at a velocity of 50 μm/s to attain three maximum depths h_{\max} = 4, 6 and 8 μm. For each maintained depth, 45 replicate load relaxation experiments were acquired over 20 – 30 sec, with a sampling rate of 250 Hz to acquire sufficient data for accurate analysis. To examine repeatability and potential structural heterogeneities at this lower length scale, n = 45 replicate measurements at each depth were attained by acquiring five replicate measurements (within an area of 80 μm × 80 μm) at three different locations on each of three samples.

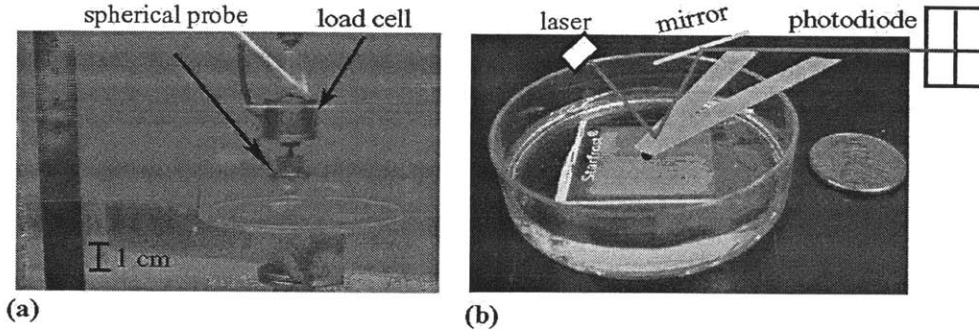


Figure 5.1 (a) Apparatus for load relaxation experiments at the macroscale, using a stainless steel spherical probe of radius 1 cm. Scale marker at left is in mm. (b) Schematic of load relaxation experiment conducted at the microscale, using a polystyrene spherical probe of radius 22.5 μm attached to the cantilever of an atomic force microscope. All experiments were conducted on fully hydrated polyacrylamide gels immersed in buffered saline solution.

5.2.2.4 Analysis

We adapted the method of Hu et al.⁵⁰⁻⁵¹, to analyze the acquired load relaxation responses. We summarize here the necessary equations to identify the dominance of the poroelastic deformation regime and the extraction of elastic and transport properties. After an indenter is pressed into a gel to a fixed depth h , the force on the indenter relaxes as a function of time $F(t)$. At sufficiently short times, the gel behaves as an incompressible material because there is no time for fluid to leave the network, while at extended times it acts as a compressible material. For a spherical indenter pressed into an incompressible elastic solid, the force on the indenter is given by²⁰⁰

$$F_0 = 16/3 Gah \quad (5.1)$$

Where F_0 is the resulting force at $t = 0$, G is the shear modulus, and a is the radius of contact computed from $a = \sqrt{R\delta}$. The ratio of the initial force F_0 and fully relaxed force at long times F_∞ is related to the Poisson's ratio of the solid ν_s as:

$$\frac{F_0}{F_\infty} = 2(1 - \nu_s) \quad (5.2)$$

From the experimental data, G and ν_s can be readily determined using Eqs. (5.1)-(5.2). Since the relevant length scale in this problem is the radius of contact a , the normalized time takes the form t/τ , where characteristic relaxation time constant τ is calculated as the ratio of the diffusivity D to contact area a by the relation: $\tau = D/a^2$. The force $F(t)$ is given for a spherical indenter as:

$$\frac{F(t) - F_{\infty}}{F_0 - F_{\infty}} = 0.491 \exp(-0.908\sqrt{\tau}) + 0.509 \exp(-1.679\tau) \quad (5.3)$$

where the magnitudes of prefactors were obtained by Hu et al. from finite element simulations⁵¹. In the present analysis, the dominant mechanism of load relaxation was determined by normalizing the force according to Eq. (5.3) and the time by a^2 . Relaxation time of a material that behaves linear viscoelastically is independent of contact diameter, whereas poroelastic relaxation time is length scale dependent. Therefore, by normalizing time by the relevant length scale (a^2), it is possible to differentiate between these two regimes. In other words, if after normalizing time by a^2 , the normalized force-time responses collapse, it is inferred that poroelastic relaxation was dominant. The opposite is concluded if little or no length scale dependence is observed. To render this distinction, we conducted the following analysis for both the macroscale and microscale experiments: First, we averaged the replicate load-relaxation responses at each maximum indentation depth ($n=3$ indentation depths). This resulted in three output curves for data with only force normalized (Figure 5.3a, b), and three output curves for data with both force and time normalized (Figure 5.3d, e). Next, for a clearer manifestation of this distinction, for each type of normalization, we calculated the standard deviation among all of the replicate load-relaxation responses from the three indentation depths tested (Figure 5.3c, f). Note that the standard deviation among these responses is defined here to reflect a measure of dispersion among relaxation responses measured for distinct maximum depths, while still including the experimental variation among responses at a given maximum depth. This approach serves as a means to quantify the effect of time normalization on the collapse of the response curves. For each time point, these standard deviations were calculated as:

$$s = \left(\frac{1}{n} \sum_{i=1}^n (y_i - \bar{y})^2 \right)^{\frac{1}{2}} \quad (5.4)$$

where $n = 9$ for macroscale and $n = 135$ for microscale experiments (corresponding to all the replicate responses from all the indentation depths tested), y_i represents the normalized force value at that particular time point for a particular output curve, and \bar{y} is the average of all the normalized force values at that time point. Smaller standard deviation for a specific normalization scheme was interpreted as stronger collapse, allowing identification of the dominant regime. Previously, other forms of force normalization were used to assist in this

classification⁵⁰⁻⁵¹. Our rationale for departure from those approaches is addressed in Section 5.2.4.

Since F_0 , F_∞ and $F(t)$ are known from experiment, the only unknown parameter in Eq. (5.3) is diffusivity D . To extract D , an optimization algorithm custom-written by Dr. Roza Mahmoodian in Van Vliet Group, MIT Department of Materials Science and Engineering was used in MATLAB (The MathWorks, Natick, MA) to find the best fit of Eq. (5.3) to the experimental force-time response. Permeability κ is then calculated from:

$$\kappa = \frac{D(1 - 2\nu_s)\eta}{2(1 - \nu_s)G} \quad (5.5)$$

where η is the solvent viscosity which is assumed to be equal to that of water (0.89×10^{-3} Pa.s)⁵² for PAAm gels. The characteristic relaxation times for the micro- and macroscale experiments are listed in Table 5.1. Unpaired t-tests were utilized to detect statistically significant differences among the values obtained at different maximum indentation depths (GraphPad Software, Inc., La Jolla, CA).

5.2.3 Results

Table 5.1 shows the experimentally measured load relaxation response obtained for PAAm gels at the macroscale (Figure 5.2a) and the microscale (Figure 5.2b), indicated as the average among replicate experiments at each maximum depth. It is observed from these graphs that the time required for full relaxation exceeded tens of hours for macroscale experiments (up to 110 h), as compared to a few seconds for microscale experiments. Macroscale contact radii (1.0 – 2.0 mm) were three orders of magnitude larger than those in microscale experiments (9.5 – 13.4 μ m).

Length scale dependence of relaxation time is a clear manifestation of the poroelastic response. In contrast, linear viscoelastic relaxation is independent of contact diameter. Therefore, by normalizing time by the relevant length scale (a^2), it is possible to differentiate between the poroelastic and linear viscoelastic regimes. This point is illustrated in Figure 5.3, in which load is normalized according to Eq. (5.3). At both the micro- and macroscale, normalization of the time by a^2 resulted qualitatively in the collapse of these responses onto a single curve (Figure 5.3b, e), and quantitatively to a lower standard deviation among the averaged curves acquired at three different maximum depths (Figure 5.3c, f). This qualitative and quantitative assessment of the

load relaxation responses confirms that the poroelastic response is dominant for these gels at both the macro- and microscales.

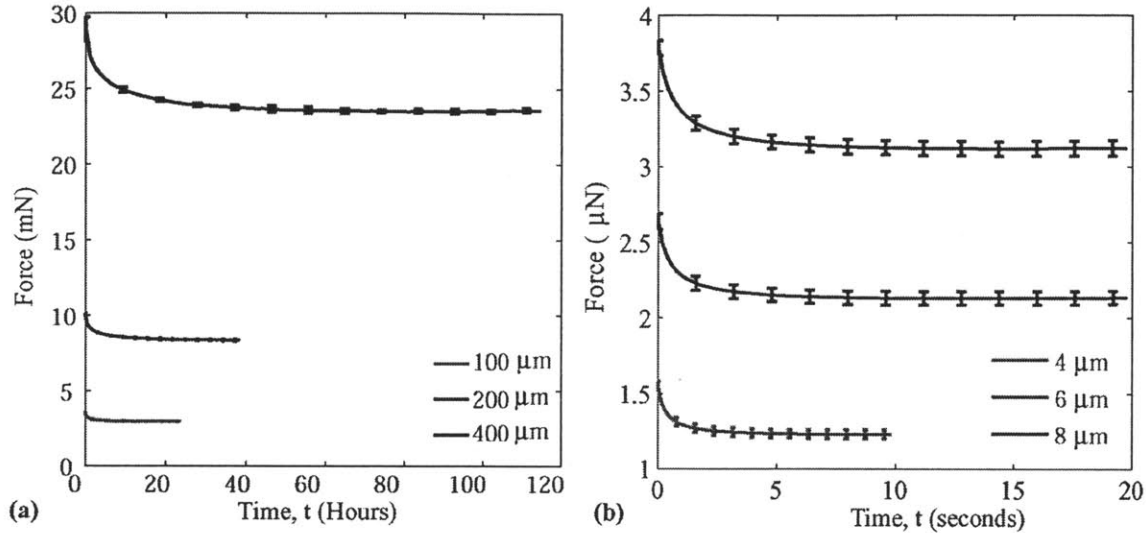


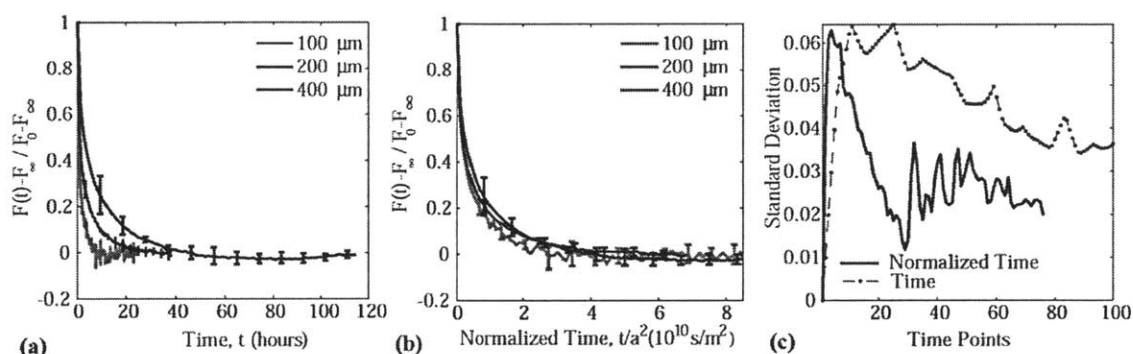
Figure 5.2 (a) Load vs. time response for macroscale experiments ($R = 1$ cm) at three different maximum indentation depths (100, 200, and 400 μm), where relaxation times are on the order of 10s of hours. (b) Load vs. time response for microscale experiments ($R = 22.5$ μm) at three different maximum indentation depths (4, 6, and 8 μm), where relaxation times are on the order of a few seconds. Data are shown as mean \pm standard deviation among replicate experiments. Due to the high data density (see text), error bars are not displayed for all data points.

Table 5.1 Shear modulus G , Poisson's ratio ν_s , diffusivity D , permeability κ and characteristic relaxation time τ as a function of indentation depth for two probes of radii R_1 and R_2 . Data are presented as mean \pm standard deviation.

Indentation depth	Shear modulus G (kPa)	Poisson's ratio ν_s	Diffusivity D (10^{-10} m^2/s)	Permeability κ (10^{-18} m^2)	τ (s)
400 μm ($R_1=1$ cm)	6.78 ± 0.20	0.39 ± 0.020	1.80 ± 0.25	4.78 ± 0.16	22.2×10^3
200 μm ($R_1=1$ cm)	6.70 ± 0.01	0.40 ± 0.007	1.97 ± 0.12	4.93 ± 0.86	10.2×10^3
100 μm ($R_1=1$ cm)	6.60 ± 0.10	0.41 ± 0.010	2.03 ± 0.00	5.82 ± 0.17	4.9×10^3
8 μm ($R_2=22.5$ μm)	6.21 ± 0.10	0.39 ± 0.004	1.70 ± 0.25	4.24 ± 0.51	1.06
6 μm ($R_2=22.5$ μm)	6.53 ± 0.13	0.38 ± 0.005	1.67 ± 0.26	4.35 ± 0.60	0.81
4 μm ($R_2=22.5$ μm)	6.73 ± 0.19	0.37 ± 0.005	1.60 ± 0.15	4.31 ± 0.31	0.56

Mechanical and diffusive properties are reported in Table 5.1, calculated according to Eqs. (5.1) – (5.3) and (5.5). The excellent agreement in all calculated properties (less than 20% difference) for experiments that analyzed the same gel over 10s of hours (with cm-scale probes) and <10s of seconds (with μm -scale probes) validates the application of load relaxation analysis at the microscale. Note that the characteristic poroelastic time τ is not a constant for a given material (i.e., for a given gel or tissue), but rather depends strongly on the deformation length scale defined by the experiment; here, τ varied over five orders of magnitude for the range of contact radii a that varied over three orders of magnitude.

MACROSCALE



MICROSCALE

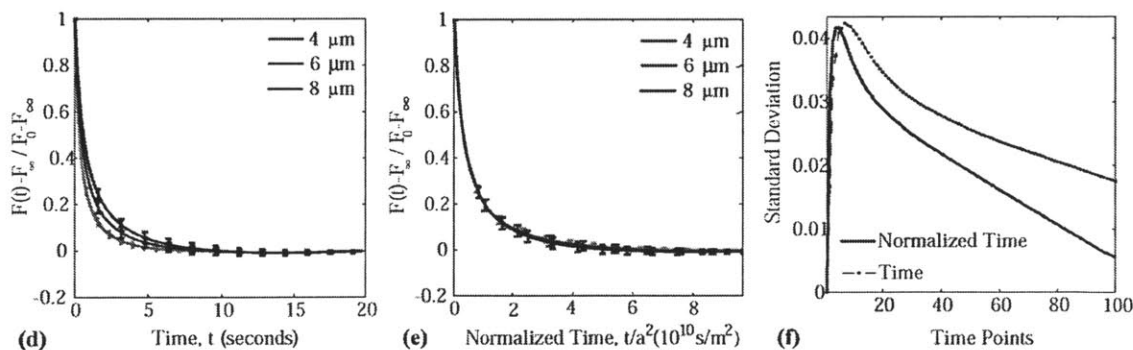


Figure 5.3 Macroscale and microscale load relaxation responses for polyacrylamide gels, for which load is normalized in the form $[F(t) - F(\infty)]/[F_0 - F(\infty)]$. Data are shown as mean \pm standard deviation. Due to the high data density (see text), error bars are not displayed for all data points. These data do not fully collapse onto a single curve when time is not also normalized, at either the macroscale (a) or microscale (b), as would be expected for a linear viscoelastic response. These data collapse more completely onto a single curve when time is normalized by a^2 , as would be expected for a poroelastic response. Comparison of this collapse is shown in (c) and

(f), as the standard deviation among the replicate curves for all maximum depths. Standard deviation is noticeably smaller when time is normalized, confirming dominance of the poroelastic regime at the macro- and microscales.

5.2.4 Discussion

In the present study we assessed the applicability of method of Hui et al.,¹⁹⁷ as extended by Hu et al.⁵⁰⁻⁵¹ to the study of μm -scale experiments. Within the context of this theory, contact based measurements of stress relaxation provide a simpler means to determine the permeability and compressibility of gels, which would otherwise have to be obtained from independent measurements of shear modulus, longitudinal elastic modulus,²⁰¹⁻²⁰² and diffusivity.²⁰³ By appropriately analyzing stress relaxation experiments at the microscale using the above approach, time required for experiments is greatly reduced, providing for convenient and reliable characterization of swollen gels and other classes of hydrated porous materials.

When an indenter is pressed into a gel, the load decays (relaxes) in a time-dependent manner. There are two distinct mechanisms of relaxation: viscoelastic relaxation as exhibited by dry elastomers, due to conformational changes of the polymer chains, and the fluid-induced (poroelastic) relaxation; a combination of both relaxation mechanisms is also possible as seen in soft tissues and elastomers swollen with solvent. Pavesi et al. have reported a viscoelastic relaxation time of ~ 3 ms for polyacrylamide chains as measured by pulsed NMR spectrometry at a frequency of 38 MHz²⁰⁴, which is at least two orders of magnitude smaller than the poroelastic relaxation times reported here; Weiss and Silberberg reported viscoelastic time scales of $\sim 0.09 - 0.16$ s for polyacrylamide gels of similar concentrations²⁰⁵. While the relaxation times of a homogeneous material that behaves linear viscoelastically does not depend on length scales⁵⁰, the characteristic poroelastic relaxation time of an indentation experiment is of the order of a^2/D ¹⁹⁷. Normalization by appropriate length scales can thus provide physical insight to distinguish between dominance of these two regimes, which is particularly advantageous when these relaxation times are of similar order. In the present study, we designed experiments that accessed poroelastic relaxation as the dominant mechanism in the PAAm gels. This is in agreement with the findings of Galli et al.⁵³, who showed better matching of microindentation ($R = 400 \mu\text{m}$) load relaxation responses obtained for similar PAAm gels via finite element simulations assuming a poroelastic constitutive model as compared to a viscoelastic constitutive

model. If the material behaved linear viscoelastically, one would expect to observe no differences in the normalized force decay as a function of different maximum indentation depths. However, Figure 5.3a, d show that this is not the case for the present PAAm gels, at either the macroscale or microscale. When additionally normalizing time by a^2 , it becomes apparent in Figure 5.3b, e that collapse of the responses onto a single curve is attained. This point is further underscored by the collapse of all of the normalized responses acquired at both the macroscale and microscale in a single graph (Figure 5.4), spanning four orders of magnitude in contact areas (μm^2 to mm^2). Quantitative comparisons of this strength of collapse are enabled by calculation of the standard deviation among the normalized responses, at both the macroscale and microscale (Figure 5.3c, f).

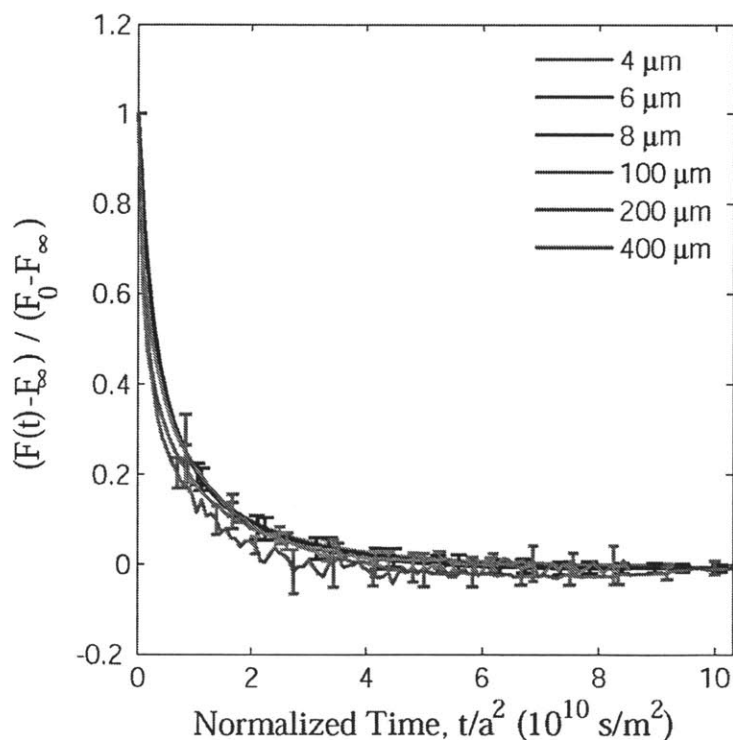
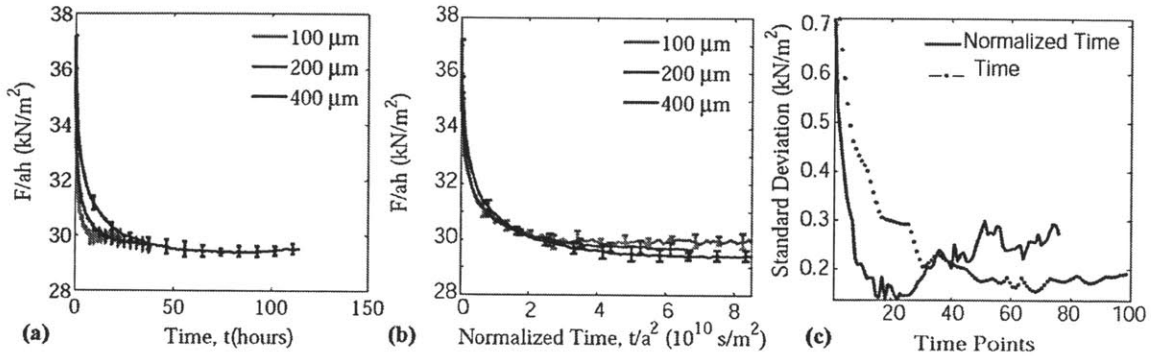


Figure 5.4 Load relaxation responses for polyacrylamide gels at six different indentation depths - spanning two orders of magnitude- for which load is normalized in the form $[F(t)-F(\infty)]/[F_0 - F(\infty)]$. Data are shown as mean \pm standard deviation. Due to the high data density, error bars are not displayed for all data points. These data collapse onto a single curve when time is normalized by a^2 as is expected for a poroelastic response.

Here, note that we have normalized force according to Eq. (5.3). We wish to contrast this approach to other approaches that normalize instantaneous force by ah or by the initial force

F_0 .^{50-51,197} This form of force normalization has been presented previously without comment;⁵¹ here, we recognize and discuss the advantage of this choice over other approaches. The normalization of force as shown in Figure 5.3 makes no *a priori* assumptions about how G or ν_s of the material may vary as a function of indentation depth. In contrast, normalization by ah assumes that both G and ν_s are invariant with depth into a sample, and normalization by F_0 assumes that ν_s is invariant with depth. Figure 5.5 demonstrates the misinterpretations that can result by normalizing force by ah , using our data on PAAm gels as an example: at the macroscale, a poroelastic-dominant response is inferred due to the stronger collapse for time expressed as t/a^2 (Figure 5.5a-c), and at the microscale normalization by ah gives inconclusive results regarding the poroelastic dominance of load relaxation (Figure 5.5d-f). That approach assumes G and ν_s are exactly constant with indentation depth, which we show in Table 5.1 is not the case for the microscale experiments; statistical analysis indicated significant differences ($p < 0.0001$) among the means of both G and ν_s obtained at the three different indentation depths. Galli et al. also noted, via comparison of experiments with finite element simulations, that G and ν_s were not identically constant with depth in similar hydrogels⁵³. These differences could arise from experimental errors at small length scales due to underestimating the contact area or surface interactions between the probe and the sample²⁰⁶. However, even when such differences are statistically significant but small (<10% variation in G here among the three microscale indentation depths), this can directly affect conclusions drawn about poroelastic dominance. For example, that normalization approach falsely indicates that the poroelastic and viscoelastic relaxation times are similar – and that poroelastic relaxation mechanisms are not dominant – under microscale deformation of these hydrogels.

MACROSCALE



MICROSCALE

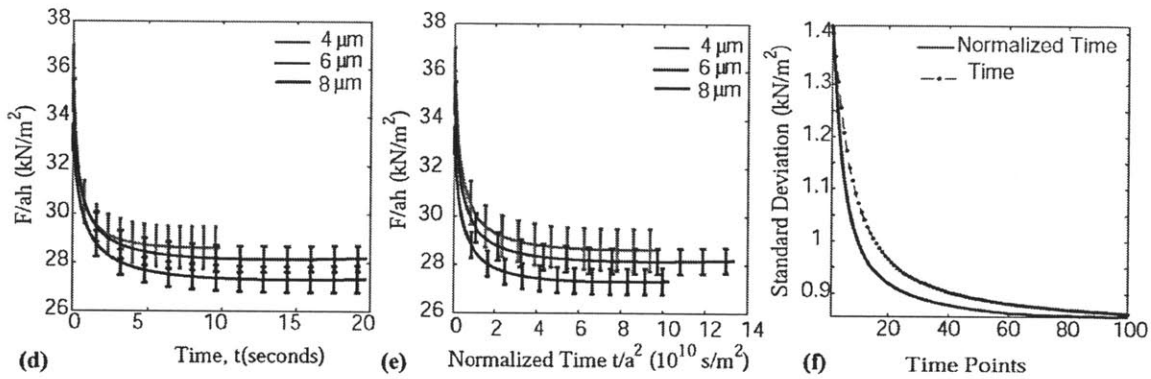


Figure 5.5 Macroscale (a) and microscale (d) load relaxation data where force is normalized by ah , but time is not normalized. Macroscale (b) and microscale (e) load relaxation response when force is normalized by ah and time is normalized by a^2 . Standard deviation among replicate curves for all indentation depths vs. time in macroscale (c) and microscale (f) tests when time is normalized vs. when time is not normalized. Data is shown as mean \pm standard deviation. Due to the high data density (see text), error bars are not displayed for all data points.

Similarly, Figure 5.6 shows normalization by F_0 also gives inconclusive results regarding the poroelastic dominance of load relaxation, due to the assumption of constant ν_s . Thus, although we adopt a continuum framework which assumes implicitly that the mechanical and transport properties within the deformed material volume are homogeneous, we advocate the present approach of force normalization that refrains from making any implicit assumption regarding of the magnitude of mechanical properties over greater length scales.

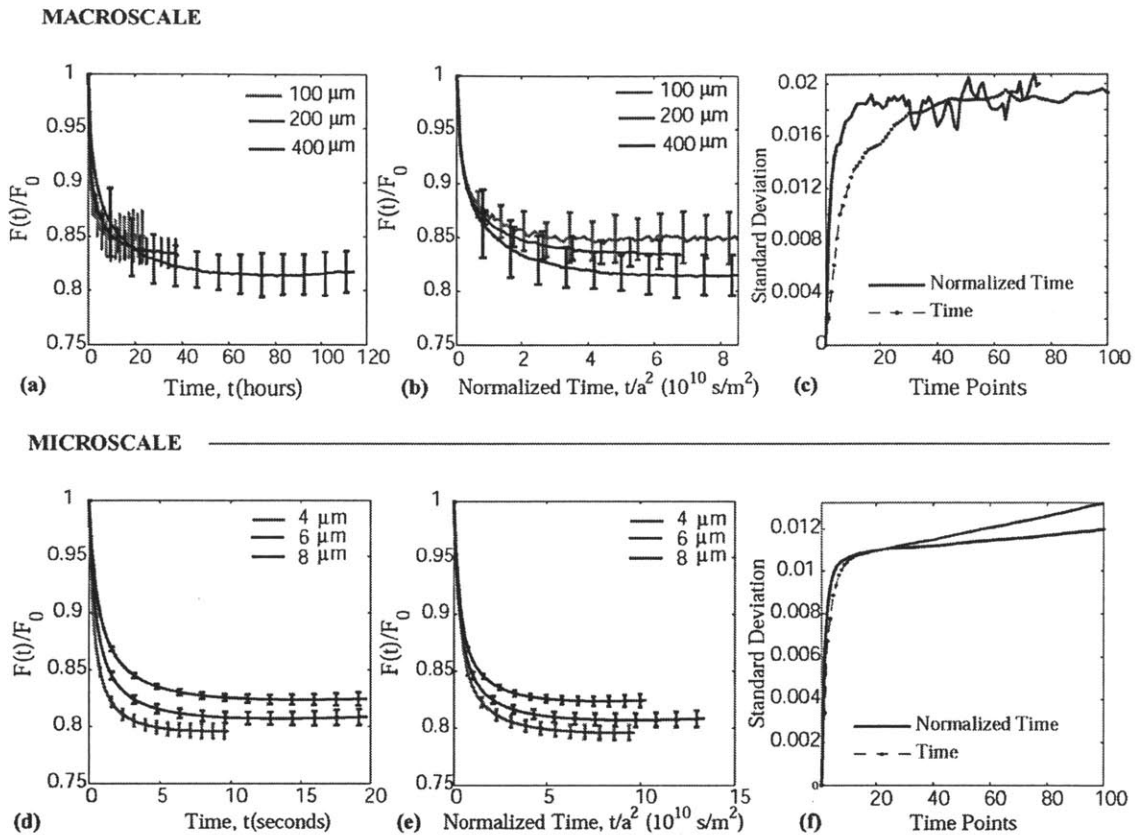


Figure 5.6 Macroscale (a) and microscale (d) load relaxation data where time is not normalized. Macroscale (b) and microscale (e) load relaxation response where time is normalized by a^2 . Force is normalized by F_o in all cases. Standard deviation among replicate curves for all indentation depths vs. time in macroscale (c) and microscale (f) experiments when time is normalized vs. when it is not normalized. Data is shown as mean \pm standard deviation. Due to the high data density (see text), error bars are not displayed for all data points.

Although there is wide variation in levels of reported detail for polyacrylamide hydrogels (e.g., %crosslinker, %initiator, and vol% water at reaction initiation), we obtained properties that were in good agreement with those previously reported. For similarly prepared PAAm gels, Weiss et al.²⁰⁵ reported elastic properties measured via force torsion pendulum-based viscoelastometry to obtain $G' = 0.3 - 6$ kPa; those authors separately measured transport properties in the same gels via fluid shear flow to obtain $\kappa = 7 \times 10^{-18}$ to 1.1×10^{-15} m^2 . This agrees well with our finding of $G \sim 7$ kPa and $\kappa \sim 4 \times 10^{-18}$ m^2 via a single experimental approach (Table 5.1). Weiss et al. concluded that the network became less permeable as the gel concentration and crosslinking density increased. Since storage moduli are also related directly to gel concentration and

crosslinking density²⁰⁷, this trend can explain the difference among permeability measured for different PAAm hydrogels. For example, Galli et al.⁵³ measured lower permeability ($\kappa = 5.6 \times 10^{-20}$ to 1.2×10^{-19} m²) for much stiffer PAAm gels ($G \sim 100$ kPa) than those considered here. With the present method, we also found internally consistent results between the properties obtained for identically prepared samples that were examined at the microscale over (O)10 seconds and at the macroscale over (O)10s hours; see Table 5.1. Thus, this approach can now be extended reliably to the microscale, with markedly decreased experimental time.

Note that although the elastic and transport properties are defined by the solid and fluid composition of the hydrogel itself, the measured poroelastic relaxation time is also a function of the experimental length scales. This natural variation of τ with length, and the requirement that sufficient relaxation occur to enable fitting of the relaxation response to obtain poroelastic properties, give rise to important considerations of experimental design at the microscale. The key to achieving reliable results with this approach is ensuring that the poroelastic relaxation time extends well beyond the rise time t_r (i.e., the time required for the instrument to reach maximum indentation depth, after which measurement of load relaxation commences). We found that calculated relaxation times (here, 0.6 to 1 s) should be at least an order of magnitude larger than the shortest achievable rise times (for our instrument, 0.08 - 0.16 s) to capture sufficient relaxation required of robust fits to Eq. (5.3) and thus robust property calculations. Generally, this minimum rise time corresponds to the maximum achievable displacement rates of a particular instrument, since true step-displacements or step-loads are not possible in practice. Thus, given t_r we can estimate a lower-bound value for τ to capture material relaxation response. Since τ is a function of both diffusivity and contact area as $\tau \sim a^2/D$, one can estimate the contact areas required to maximize poroelastic relaxation times for a given material by assuming an initial estimate of diffusivity D . For the AFM-enabled load relaxation experiments conducted herein, the largest available contact areas and shortest rise times (fastest displacement rates) were chosen to maximize the calculated relaxation time τ and to minimize relaxation during the initial displacement to attain h_{\max} , respectively. To maximize the contact areas, we selected the largest AFM-cantilevered probe radius commercially available ($R = 22.5\mu\text{m}$) and a stiff cantilever ($k_c = 14$ N/m); the latter consideration increased the maximum accessible forces, and hence the maximum indentation depths, to result in larger contact areas and consequently in longer

relaxation times (see Appendix C). For materials of greater fluid permeability than those considered here, the contact depths and/or probe diameter must be increased in order to capture the poroelastic relaxation response.

5.2.5 Conclusions

In conclusion, we have demonstrated that the mechanical and transport properties of poroelastic materials can be measured via microscale load relaxation. This extension of macroscale analysis was enabled by designing experiments that accessed the poroelastic regime, and identified this regime as the dominant relaxation mechanism without making *a priori* assumptions regarding the properties of the material. As there exist no analytical solutions to indentation of a poroelastic half-space, previous demonstration of this method at the macroscale obviated inference of such properties via finite element simulations or numerical implementation of the resulting boundary value problem. Our present validation of this approach for μm -scale contact radii and contact depths significantly reduces the required experiment time scale from $>10\text{s}$ of hours to $<10\text{s}$ of seconds. This decreased duration extends the applicability of contact-based analysis of poroelasticity to a wider range of materials, including synthetic hydrogels and biological tissues that can degrade quickly with time. We will demonstrate applications to such tissues in the next section.

5.3 Multiscale elastic and transport properties of soft tissues

5.3.1 Introduction

Biological soft tissues such as heart and liver are known to be highly inhomogeneous and structurally anisotropic (see Section 3.2.2). Given the hierarchical structure of biological polymers from the nanoscale and microscale, biological soft tissues exhibit complex nonlinear, time-dependent behavior that is also site- and direction-specific; this complexity makes it challenging to match the blast or ballistic response of tissue with traditional hydrogels or organogels. Further, soft-tissue comprises coupled solid-fluid interactions that confer mechanical responses ranging from nonlinear elastic to strongly viscoelastic to strongly poroelastic. Thus characterization of these tissue properties is necessary in order to design a gel that could capture soft tissue response at higher rates under concentrated impact loadings, as well as for

applications such as the design of tissue engineered constructs and development of computer integrated and robot aided surgery.

The viscoelastic character of heart^{164,208-213} and liver is well-documented^{60,214-217}. However, soft tissues comprise a framework of connective tissues and cells (solid matrix) surrounded by the fluid-filled extracellular space (fluid). Thus, more recently biphasic and poroelastic models that take into account both the deformation of the solid framework as well as the fluid flow have been applied extensively to characterize the biomechanical behavior of certain soft tissues such as cartilage^{40,218-220}. On the other hand, only a few researchers have investigated the poroelastic properties of heart and liver. Tsaturyan et al. has conducted stress relaxation experiments on myocardium via macroscale oscillatory techniques to conclude that extracellular fluid filtration plays an important role in the mechanical behavior of passive cardiac muscle, in addition to viscoelastic deformation²⁰⁸. The significance of poroelasticity in cardiac muscle mechanisms has been further confirmed by Yang et al., via comparison of their theoretical predictions with published experimental results²⁰⁹. These authors have further developed a theoretical model based on nonlinear poroelasticity in order to characterize the poroelastic properties of myocardium, emphasizing the lack of experimental data in this field²²¹. Ng et al. have also conducted poroelastic analysis of the myocardium based on finite element method in order to investigate how myocardium perfusion is influenced by myocardial stress²²², and Chappelle et al. introduced a poroelastic model to study cardiac perfusion²²³. Further, Raghunathan et al. applied poroviscoelastic (PVE) models to simulate the biomechanical response of liver tissue in unconfined compression stress relaxation experiments²²⁴. Jordan et al. have also used a biphasic poroelastic model to mimic the nonlinear viscoelastic response of porcine liver through FEM studies²²⁵, and Evans et al. applied a PVE finite element model to determine material parameters from nanoindentation tests conducted on liver tissue¹³⁵.

Although the works mentioned above provide a starting point for studies of the biomechanics of heart and liver tissue, there is still a need for the development and application of explicit poroelastic and poroviscoelastic analysis techniques for future studies of these tissues. Thus, in this section we are proposing to use a contact-based indentation technique explained in Section 5.2 to characterize elastic properties such as shear modulus G and Poisson's ratio ν and transport

properties such as diffusivity D and permeability κ of heart and liver tissue, as a function of directionality with respect to tissue layers. The advantages of this technique are the ability to extract elastic and transport properties simultaneously, and to conduct experiments at smaller length and time scales in order to study mechanical properties of tissues that degrade over time and also exhibit structural heterogeneities.

5.3.2 Experimental Details

Heart (n=9) and liver (n=3) organs were harvested from adult rats. All experiments involving animals obeyed the University IACUC protocol and the NIH guidelines for animal care. All tissues were stored in Krebs-Hensleit containing 0.5% Pluronic® F108 buffer immediately after excision and throughout all experiments reported herein. Microscale load relaxation experiments were conducted using atomic force microscope (AFM)-enabled indentation (3D Molecular Force Probe, Asylum Research, Santa Barbara, CA) at 37°C within 3 h post-mortem. Spherical polystyrene cantilevers (Novascan) with nominal probe radius of 22.5 μm and spring constant $k = 14.0 \text{ N/m}$ were used; actual values of k were determined experimentally for each cantilever¹⁹⁴.

For heart, load was applied along three different orthogonal directions (n=3 hearts per loading direction, and n=3 different maximum depths per each heart), in order to access the properties of pericardium and myocardium separately (Figure 5.7a), with n=10 replicate measurements per heart for each of three maximum depths. For each liver, load was applied normal to the tissue surface with the Glisson's capsule attached, and normal to the parenchyma after the capsule has been removed, with n=10 replicate measurements at each configuration for each of three maximum depths (Figure 5.10). Upon automatic contact detection (based on cantilever deflection), indenter displacement was increased at a velocity of 100 $\mu\text{m/s}$ to attain three maximum depths ranging between 4 μm and 14 μm . For each maintained depth, load relaxation experiments were acquired over 10 – 30 sec, with a sampling rate of 250 Hz to acquire sufficient data for accurate analysis. For each maximum depth attained, average strain is calculated as a/R where a is the contact radius, and R is the radius of the probe. Data were analyzed as outlined in Section 5.2.2.4. For each fit, R^2 values are calculated from²²⁶:

$$R^2 = \frac{[\sum(y - y_{est})^2]}{[\sum(y - \bar{y})^2]} \quad (5.6)$$

where y , y_{est} and \bar{y} values are the experimental values, theoretical values, and the mean of y values respectively. Unpaired t-tests were utilized to detect statistically significant differences among the values obtained at different maximum indentation depths (GraphPad Software, Inc., La Jolla, CA).

5.3.3 Results and Discussion

5.3.3.1 Elastic and transport properties of heart

Load relaxation experiments were conducted on heart tissue, with loading applied along three different directions (Figure 5.7a). To characterize the elastic and transport properties of parietal pericardium, load was applied along direction A. Dimitriadis et al. mentioned that when $t > 12.8R$ where t is the sample thickness and R is the radius of the probe, an assumption of semi-infinite thickness is a reasonable approximation¹⁰⁶. In this case, given that $\sim 500 \mu\text{m} - 1 \text{ mm}$ thick fibrous+serous layers of the parietal pericardium of rat heart $> 12.8 \times 22.5 \mu\text{m}$, it is most likely that the response we observed was not affected by the mechanical properties of the underlying layers such as myocardium and endocardium. To characterize the elastic and transport properties of myocardium we applied load both along the circumferential (B) and longitudinal (C) directions, since myocardium has been recognized as an anisotropic tissue with tensile mechanical properties dictated by cardiac muscle fiber orientation^{153,227}. More specifically, myocardial fibers are organized in a spiral arrangement, with subepicardial and subendocardial fibers running predominantly parallel to the long axis of the cavity and midmyocardial fibers arranged for the most part circumferentially²²⁸. Raw load vs. displacement responses showed that for a given maximum depth, the maximum forces attained in the direction of the parietal pericardium (Figure 5.7b) was lower than the maximum forces attained for the circumferential (Figure 5.7c) and longitudinal (Figure 5.7d) loading directions of the myocardium, suggesting that the pericardium is more compliant than the myocardium.

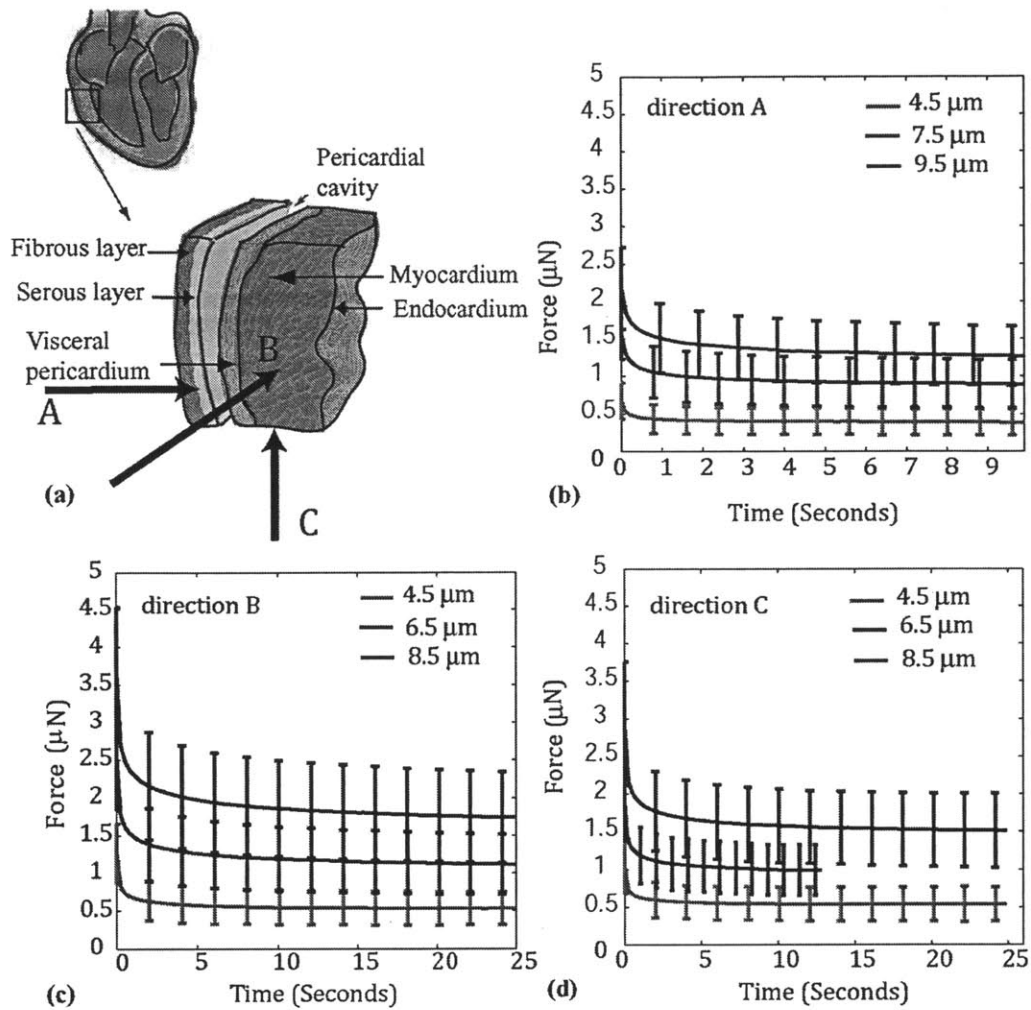


Figure 5.7 (a) Heart tissue exhibits a layered heterogeneous structure (adapted from Ref. 139). (b) Load vs. time response of pericardium (load applied in direction A) at three different maximum indentation depths (4.5, 7.5, and 9.5 μm), where relaxation times are on the order of a few seconds. (c) Load vs. time response of myocardium in circumferential direction (load applied in direction B) at three different maximum indentation depths (4.5, 6.5, and 8.5 μm) (d) Load vs. time response of myocardium in longitudinal direction (load applied in direction C) at three different maximum indentation depths (4.5, 7.5, and 9.5 μm). Probe radius is $R = 22.5 \mu\text{m}$, data are shown as mean \pm standard deviation among replicate experiments. Due to the high data density, error bars are not displayed for all data points.

For each direction, in order to differentiate between the poroelastic and linear viscoelastic regimes we graphed the normalized force vs. time (Figure 5.8a, d, g) and also the normalized force vs. time normalized by the relevant length scale a^2 (Figure 5.8b, e, h) as explained in

Section 5.2. For all loading directions, normalization of the time by a^2 resulted qualitatively in the collapse of these responses onto a single curve, suggesting the dominance of poroelastic relaxation. However, quantitatively the difference between the standard deviation among the curves acquired at three different maximum depths when time was normalized vs. when time was not normalized was less than 10% (Figure 5.8c, f, i). These findings suggest that at these length scales, we cannot conclude strongly that either poroelastic or viscoelastic relaxation was dominant; rather, both mechanisms played an important role in the relaxation response under these conditions. Accessing the time scales over which poroelastic relaxation is dominant is possible by utilizing larger probes (i.e., larger contact areas), which would increase the poroelastic relaxation times without affecting the viscoelastic relaxation time. However, this would further result in an overall increase in the total experimental time as well, which is disadvantageous for testing soft tissues that degrade over time.

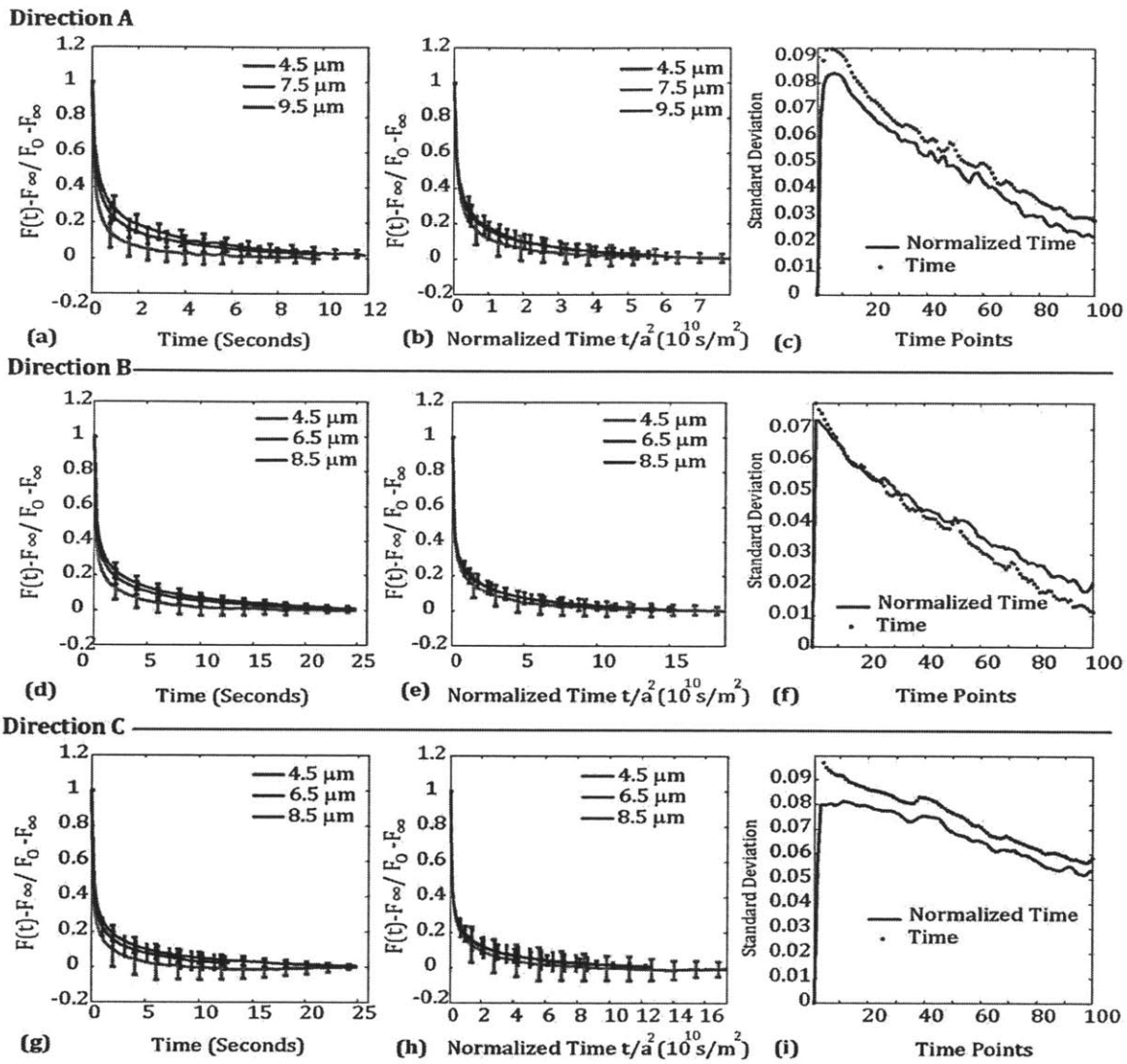


Figure 5.8 Load relaxation data in direction A (a), direction B (d), and direction C (g) where time is not normalized. Load relaxation response in direction A (b), direction B (e), and direction C (h) where time is normalized by a^2 . Force is normalized by $[F(t)-F(\infty)]/[F_0-F(\infty)]$ in all cases. Standard deviation among replicate curves for all indentation depths vs. time responses in direction A (c), direction B (f), and direction C (i) when time is normalized vs. when it is not normalized. Data is shown as mean \pm standard deviation. Due to the high data density, error bars are not displayed for all data points.

Table 5.2 Shear modulus G , Poisson's ratio ν_s , diffusivity D , permeability κ as a function of indentation depth at three different directions. Data are presented as mean \pm standard deviation.

Indentation depth	Shear modulus G (kPa)	Poisson's ratio ν_s	Diffusivity D (10^{-10} m ² /s)	Permeability κ (10^{-17} m ²)
4.5 μ m (direction A)	2.8 \pm 1.1	0.08 \pm 0.2	3.7 \pm 1.9	6.1 \pm 4.2
7.5 μ m (direction A)	3.3 \pm 0.9	0.05 \pm 0.17	2.7 \pm 1.0	4.0 \pm 2.6
9.5 μ m (direction A)	3.1 \pm 0.7	0.09 \pm 0.14	2.4 \pm 1.1	3.5 \pm 2.4
4.5 μ m (direction B)	5.1 \pm 1.7	-0.25 \pm 0.25	2.5 \pm 1.3	3.3 \pm 2.8
6.5 μ m (direction B)	5.9 \pm 1.5	-0.17 \pm 0.22	1.6 \pm 0.6	1.5 \pm 1.1
8.5 μ m (direction B)	5.9 \pm 1.5	-0.08 \pm 0.17	1.5 \pm 0.5	1.4 \pm 0.9
4.5 μ m (direction C)	4.5 \pm 1.7	-0.05 \pm 0.17	2.0 \pm 0.9	2.3 \pm 1.5
6.5 μ m (direction C)	4.8 \pm 1.6	-0.04 \pm 0.18	2.2 \pm 0.9	2.3 \pm 1.2
8.5 μ m (direction C)	4.7 \pm 1.5	0.05 \pm 0.13	2.1 \pm 1.0	2.1 \pm 1.0

The model by Hu et al. assumes that the poroelastic relaxation is the dominant mechanism, and our data cannot conclusively demonstrate poroelastic dominance. Nevertheless, here we apply that model to extract shear modulus G , poisson's ratio ν_s , diffusivity D and permeability κ (Table 5.2), and compare our results with other results from literature. R^2 values from the fits are calculated to be between 0.88-0.92 using Equation 5.6, suggesting the model to be a fairly good fit given that $R^2=1$ if the fit were perfect. As we speculated from the raw load vs. displacement response, we observe that $G_{\text{pericardium}}$ (direction A) < $G_{\text{myocardium}}$ (direction B&C) ($p < 0.05$), indicating that the pericardium is more compliant than the myocardium (Figure 5.9a). Statistical analysis (see Section 5.3.2) also showed a statistically significant difference in G when load is applied in the circumferential (direction B) vs. longitudinal (direction C) direction of the myocardium, except at the lowest strain of $\sim 45\%$; however, the difference in stiffness that we observe is less than what Engelmayr et al. has reported for rat myocardium tested under uniaxial tension along those two directions¹⁵³. This could be attributed to the difference between the tests methods (tension vs. compression) and/or to a large transmural change in fiber angles and possibility that the regions that are indented exhibit a relatively uniform fiber orientation. Sacks et al. has also mentioned that biaxial mechanical testing of right ventricle free wall myocardium is complicated by the fact that the fiber orientation is relatively uniform and that specimens

typically have a 30 to 40 deg range of transmural fiber angles²²⁷. In addition, contact radii in our experiments are $O(\sim 10 \mu\text{m})$, so it is possible that our sample volumes probe only a single myocyte, rather than the more composite response of the fiber-collagen network. We also observe that G does not depend on the strain that is exerted on the tissue, suggesting that we could be accessing a linear viscoelastic regime of the stress vs. strain response of pericardium and myocardium tissues. Calculated G values here are found to be within the range of values reported in Section 3.2.3.3, as well as previously reported values in literature. For example, Lieber et al. has conducted atomic force microscope enabled-indentation on rat myocytes and reported an elastic modulus E of 35-43 kPa ($G \sim 12-15$ kPa for $\nu=0.5$), Langer et al. calculated the elastic modulus of the left ventricular myocardium to be ~ 20 kPa ($G \sim 7$ kPa for $\nu=0.5$)

Figure 5.9b shows that diffusivity of aqueous electrolyte through the pericardium (direction A) was larger than diffusivity in the myocardium (circumferential, direction B). Statistical analysis (Section 5.3.2) also showed that diffusion coefficient depended on the directionality of the applied load on the myocardium, except at the lowest strain of 45% ($p < 0.05$). Previously, Garrido et al. utilized pulsed field gradient nuclear magnetic resonance methods combined with nuclear magnetic resonance imaging to determine the water diffusion anisotropy in perfused rat hearts at 37°C. He also found that the diffusion coefficient depends on the orientation of the applied gradient g ; when g was parallel to the rat epicardial surface, the observed diffusivity was $1.8 \pm 0.4 \times 10^{-9} \text{ m}^2/\text{s}$, whereas when g was perpendicular to it, diffusivity was $2.5 \pm 0.5 \times 10^{-9} \text{ m}^2/\text{s}$ ²²⁸. Zocchie et al. also reported a value of $\sim 2 \times 10^{-9} \text{ m}^2/\text{s}$ for the diffusivity of sucrose and Na^+ in parietal pericardium of rabbits²²⁹. Both these values are an order of magnitude larger than the values calculated here. A reason for this difference could be attributed to the presence of perfusion in those experiments, whereas in our experiments heart samples were not perfused. On the other hand, calculated permeability values here were in the range of reported values for other soft tissues. Swartz et al. has reported hydraulic permeability values ranging from 10^{-13} to $10^{-16} \text{ m}^4/\text{N}\cdot\text{s}$ for rat abdominal muscle, cartilage and rat dermis²³⁰ (compared to $\sim 10^{-14} \text{ m}^4/\text{N}\cdot\text{s}$ calculated here by κ/μ where $\mu = 0.00089 \text{ Pa}\cdot\text{s}$ ⁵²). Note that calculated permeability is directly dependent on the effective pore size⁵², and thus also known to exhibit a dependence on the applied strain on the material²³¹. For both the pericardium and the myocardium (circumferential,

direction B), we also observed a statistically significant difference when we compare permeability values at lowest and highest strain.

Figure 5.9c shows that the mean values of the calculated Poisson's ratio ν_s ranged from -0.25 to 0.09, with the lowest values being associated with the load applied in direction B (circumferential direction of myocardium). These values are much lower than what Raghunathan et al. selected as a baseline value for his finite element modeling ($\nu=0.35$)²²⁴. Negative Poisson's ratio values observed here could appear when a material is preloaded or prestrained²³², and the act of cutting the tissue could have had the effect of squeezing out liquid from the tissue causing the tissue to behave like a precompressed material. It is also possible that the solid scaffold of these tissues exhibit an auxetic response. However, more experiments would need to be done to confirm this speculation.

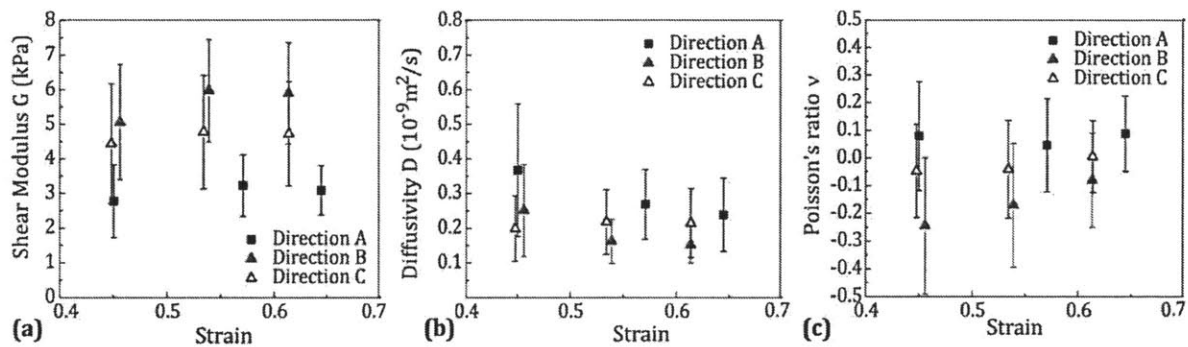


Figure 5.9 Shear modulus G (a), Diffusivity D (b), and Poisson's ratio ν (c), as a function of strain for three different directions (direction A: pericardium, direction B: myocardium circumferential, direction C: myocardium longitudinal) as shown in Figure 5.7a. Data are reported as mean \pm standard deviation.

5.3.3.2 Elastic and Transport properties of liver

Liver, like many other soft tissues, is structurally anisotropic and heterogeneous. To explore the effect of this anisotropy on the elastic and transport properties, load relaxation experiments on liver were conducted when the Glisson's capsule was attached and when the capsule was removed to expose the underlying parenchyma as show in Figure 5.10. Raw load vs. displacement responses showed that the maximum forces attained when the capsule was attached (Figure 5.10a) is higher than maximum forces attained when the capsule was removed (Figure 5.10b), even though the attained maximum depths were much smaller. This relative difference

suggests that the overall response when the capsule is attached is stiffer than the underlying parenchyma. Note that since the maximum depths attained here were comparable to the thickness of rat capsule ($\sim 5\mu\text{m}$), the response obtained when the load is applied (as in Figure 5.10a) is a composite mechanical response of the underlying parenchyma and the capsule.

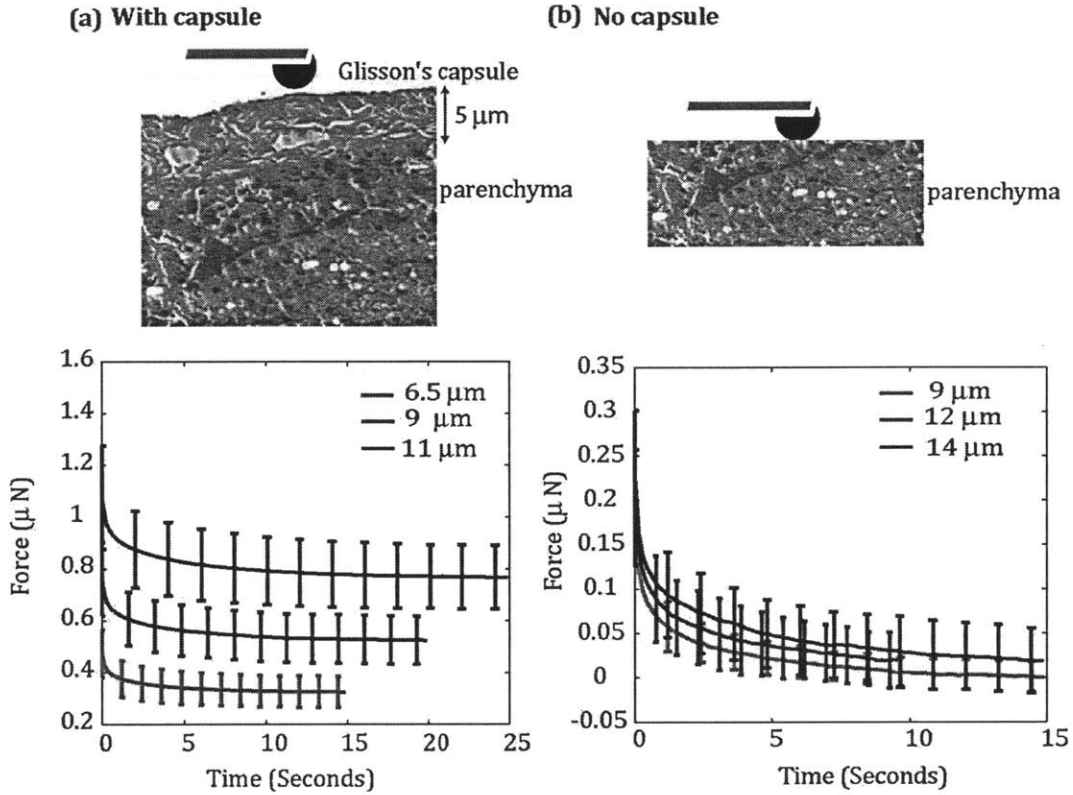


Figure 5.10 (a) *top*: AFM- enabled load relaxation experiments are conducted with the Glisson’s capsule attached (adapted from Ref. ¹³⁸), *bottom*: Load vs. time response of liver capsule and parenchyma at three different maximum indentation depths (6.5, 9, and 11 μm) (b) *top*: AFM- enabled load relaxation experiments are conducted with the Glisson’s capsule removed, *bottom*: Load vs. time response of liver parenchyma at three different maximum indentation depths (9, 12, and 14 μm). Probe radius is $R = 22.5 \mu\text{m}$, data are shown as mean \pm standard deviation among replicate experiments. Due to the high data density, error bars are not displayed for all data points.

Similar to the analysis for the PAAm hydrogels in Section 5.2.3 and heart tissue in Section 5.3.3.1, in order to differentiate between the poroelastic and linear viscoelastic regimes we graphed normalized force vs. time (Figure 5.11a, d) and normalized force vs. time normalized by the relevant length scale a^2 (Figure 5.11b, e). When load was applied with the capsule attached,

normalization of the time by a^2 resulted qualitatively in the collapse of these responses onto a single curve, suggesting the dominance of poroelastic relaxation (Figure 5.11b) However, quantitatively there was no difference between the standard deviation among the curves acquired at three different maximum depths when time was normalized vs. when time was not normalized (Figure 5.11c). When load is applied with the capsule removed, qualitatively it is not possible to draw a conclusion whether normalization of the time by a^2 improves the collapse of these responses onto a single curve. Quantitative comparison between the standard deviation among the curves acquired at three different maximum depths when time was normalized vs. when time was not normalized showed $<20\%$ difference (Figure 5.11f), favoring the dominance of poroelastic relaxation. However, given the small magnitude of this difference, at these length scales we cannot conclude that either poroelastic or viscoelastic relaxation is dominant, but rather both mechanisms play an important role in the relaxation response under these loading conditions.

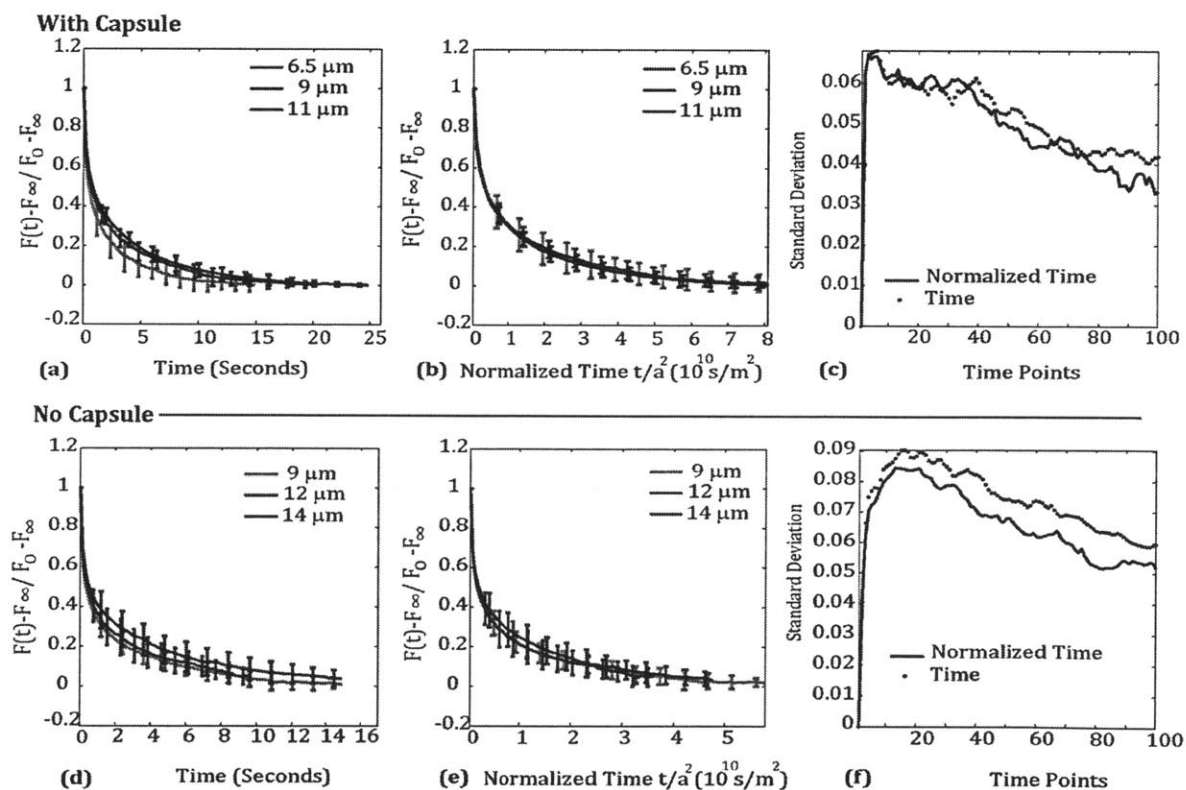


Figure 5.11 Load relaxation data with capsule attached (a), and with capsule removed (d) where time is not normalized. Load relaxation response with capsule attached (b), and with capsule

removed (e) where time is normalized by a^2 . Force is normalized by $[F(t)-F(\infty)]/[F_o - F(\infty)]$ in all cases. Standard deviation among replicate curves for all indentation depths vs. time responses with capsule attached (c), and with capsule removed (f) when time is normalized vs. when it is not normalized. Data is shown as mean \pm standard deviation. Due to the high data density, error bars are not displayed for all data points.

Although we could not conclusively attribute poroelastic dominance to the relaxation response of liver tissue, we again applied the framework of Hu et al. to extract elastic and transport properties of this tissue to compare with previous reports from different types of mechanical studies of liver. Table 5.3 reports the calculated values of shear modulus G , Poisson's ratio ν , diffusivity D , and permeability κ as a function of indentation depth, with and without the removal of the capsule ($R^2 \sim 0.9$ calculated from Equation 5.6). Calculated shear modulus G values when the capsule was attached was larger than G of the parenchyma by a factor of five. Hollenstein et al. also found that the Glisson's capsule may be responsible for a threefold increase in the measured stiffness of liver near the surface using an aspiration device²³³. The difference in the elastic moduli magnitudes can be attributed to the fact that the liver capsule is mostly composed of a tough fibrous supporting connective framework of densely interwoven collagen fibers²³³. Values reported here are comparable to our results in Section 3.2.3.3 from unconfined compression tests on liver ($E \sim 2$ kPa) as well as results from literature. Evans et al. has reported an elastic modulus of 2.62 kPa for native liver tissue with capsule, when the organ is not perfused¹³⁵. Liu et al. has measured the storage modulus G' of bovine liver to be 1-6 kPa for frequencies ranging from 0.006-20 Hz, utilizing oscillatory shear experiments⁵⁹. Cross et al. also estimated the Young's modulus of individual liver cells to be in the range of 1-2.5 kPa, as determined by atomic force microscopy-enabled indentation²³⁴. Note that here the contact radii for our experiments was on the order of ~ 15 μm , which is similar to the average hepatocyte cell diameter of 30 μm . Finally, shear modulus values did not depend on the applied strains, suggesting linear viscoelasticity in the stress vs. strain response at the strain ranges investigated (Figure 5.12a)

Diffusivity values calculated from the poroelastic model are on the same order as diffusivity values calculated for heart and PAAm hydrogels, and permeability κ values are calculated to be $\sim 3 \times 10^{-17}$ m^2 when capsule is attached. Kerdok et al. estimated hydraulic permeability k values of porcine liver from swelling tests to be $\sim 6 \times 10^{-9}$ $\text{m}^4/\text{N}\cdot\text{s}$, and Evans et al., has reported k values on

the order of $\sim 10^{-7}$ m⁴/N-s deduced from optimization of a PVE model of perfused bovine tissue^{135,217}. Even though, the k values calculated here ($\sim 3 \times 10^{-14}$ m⁴/N-s calculated by $k = \kappa/\mu$ where $\mu = 0.00089$ Pa-s) are smaller than what has been reported by Kerdok et al. and Evans et al., it is in the range of estimated permeability of articular cartilage and other soft tissues^{230,235-236}. Removing the capsule increases the diffusivity values by a factor of two (Figure 5.12b). This effect is also observed for the calculated permeability values where removing the capsule increases the permeability by an order of magnitude. The increase in permeability cannot be attributed to the difference in applied strains since increasing the strain should decrease the permeability²³¹; however, the opposite trend is observed here. A reason for this increase in permeability values could be due to the differences between the morphology of the capsule and the underlying parenchyma. Since permeability is directly proportional to the pore size⁵², these findings suggest that the average pore size in the capsule – which is composed of a fibrous connective framework of densely interwoven collagen fibers²³³ – could be smaller than in the parenchyma.

Finally, Poisson's ratio ν_s that represents the inherent compressibility of the drained solid matrix is calculated to be ~ 0.3 when the capsule is attached. This value is comparable to the value 0.35 reported in literature, obtained from the fit of numerical analysis to experimental data^{224,236}. Poisson's ratio values calculated when the load was applied only on the parenchyma were not in the range that is physically possible, and thus are not reported here. This error could rise from the observation that adhesive forces in the stress relaxation experiments conducted on the liver parenchyma are comparable to the maximum forces attained, which could affect magnitude of the fully relaxed forces at long times F_∞ resulting in a miscalculated ν_s since ν_s is related to F_∞ by Equation 5.2. Our studies on heart tissue showed that further immersing the tissue in Krebs-Henseleit buffer that included 0.5 wt% Pluronic® F108, which was shown to minimize adhesion in Section 3.2.4, did not minimize the adhesive forces between the probe surface and the tissue sample surface (Appendix B). Therefore, this methodology could not be applied here to minimize adhesion. This increase in the adhesive forces could be attributed to the surgical manipulation of the parenchymal surface prior to testing in order to remove the liver capsule and/or to the differences in the structure of the two different layers.

Table 5.3 Shear modulus G , Poisson's ratio ν_s , diffusivity D , permeability κ as a function of indentation depth with liver capsule attached and removed. Data are presented as mean \pm standard deviation.

Indentation depth	Shear modulus G (kPa)	Poisson's ratio ν_s	Diffusivity D (10^{-10} m ² /s)	Permeability κ (10^{-17} m ²)
4.5 μ m (with capsule)	1.1 \pm 0.3	0.26 \pm 0.07	1.1 \pm 0.5	2.9 \pm 1.8
7.5 μ m (with capsule)	1.1 \pm 0.2	0.27 \pm 0.04	1.1 \pm 0.3	2.9 \pm 1.1
9.5 μ m (with capsule)	1.1 \pm 0.2	0.30 \pm 0.03	1.2 \pm 0.2	2.9 \pm 0.8
4.5 μ m (no capsule)	0.2 \pm 0.1	-	2.0 \pm 0.9	45 \pm 23
6.5 μ m (no capsule)	0.2 \pm 0.1	-	2.2 \pm 1.3	45 \pm 32
8.5 μ m (no capsule)	0.2 \pm 0.1	-	1.7 \pm 0.8	43 \pm 17

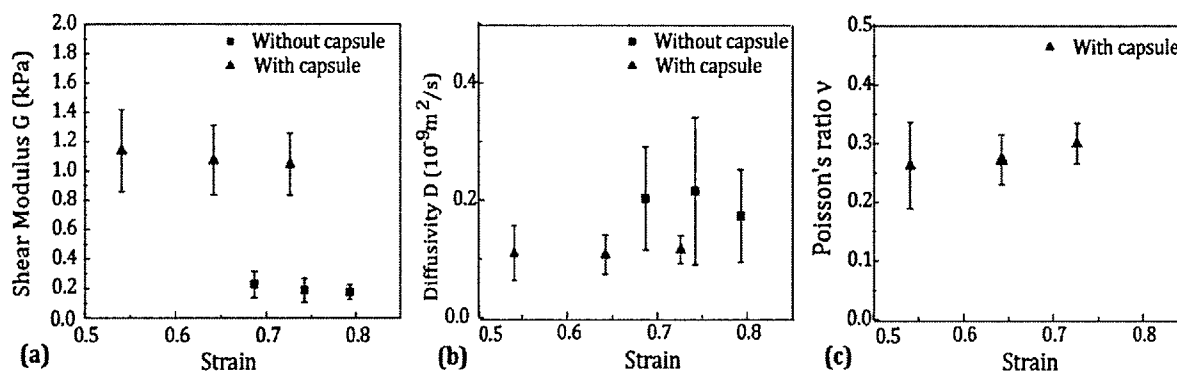


Figure 5.12 Shear modulus G (a), Diffusivity D (b), and Poisson's ratio ν_s (c), as a function of strain with capsule attached and removed. Data are reported as mean \pm standard deviation.

5.3.4 Conclusions

In conclusion, we have demonstrated that the elastic and transport properties of heart and liver can be measured via microscale load relaxation. Even though the experiments designed here were able to access the poroelastic regime, we were not able to conclusively identify this regime as the dominant relaxation mechanism. Nevertheless, calculated shear modulus G , Poisson's ratio ν , and permeability κ values were comparable to other values reported in literature – with the added advantage that we obtained all three properties from a single experiment. For heart, results demonstrated considerable differences in mechanical and elastic properties as a function of the direction of the applied load. For liver, existence of the liver capsule increased the overall stiffness and decreased the permeability of the tissue. Advantages of this method include ability to extract both elastic and transport properties simultaneously, and the ability to conduct

experiments at small length and time scales which gives access to characterizing individual layers of the tissue.

5.4 Conclusions

In order to study the effect of biphasic nature of soft tissues on tissue mechanics with the aim to inform the design of tissue simulant gels and tissue engineered constructs, and development of robot aided surgery, Chapter 5 addressed the application of a poroelastic model on contact based load relaxation experiments to extract the elastic and transport properties of hydrogels and soft tissues. As there exist no analytical solutions to indentation of a poroelastic half-space, previous demonstration of this method at the macroscale obviated inference of such properties via finite element simulations or numerical implementation of the resulting boundary value problem. Given that the poroelastic relaxation times depend on the contact areas, experiments were designed to validate this approach for μm -scale contact radii and contact depths, significantly reducing the required experiment time scale from $>10\text{s}$ of hours to $<10\text{s}$ of seconds, while keeping the poroelastic regime as the dominant relaxation mechanism without making *a priori* assumptions regarding the properties of the material. Excellent agreement was obtained between elastic and transport properties of homogeneous hydrogels calculated from macroscale and microscale experiments. Decrease in the duration times extended the applicability of this method to characterize the elastic and transport properties of heart and liver tissues that degrade quickly. Results showed that in addition to viscoelastic relaxation of the solid matrix, poroelastic relaxation due to fluid flow also plays a role in the time dependent mechanical properties of soft tissues. Further, the anisotropy of the tissue structure affected the calculated modulus and permeability values, which should be taken into consideration for the future design of tissue simulant gels.

Chapter 6 Conclusions and Directions for Future Studies

6.1 Thesis Summary

This thesis has presented novel experimental and analytical methods to study the mechanical properties of compliant hydrated materials such as hydrogels, soft tissues and tissue simulant gels. New experimental techniques were developed to address some of the challenges encountered during the indentation of compliant materials; such as sample hydration, sample adhesion and detection of contact surface. Two different systems -physically associating gels and crosslinked gels including a solvent- are introduced as potential tissue simulants for ballistic applications. In addition to conventional macroscale methods, a new technique was presented to evaluate the mechanical response and properties of tissue simulant materials to penetrating mechanical impact loading, in comparison to two specific soft tissues obtained from heart and liver. Finally, a poroelastic model of contact based relaxation experiments was applied to characterize the mechanical and transport properties of soft tissues in relation to tissue structure. The contributions of this thesis include: (1) development of novel experimental and data analysis techniques that can be utilized for contact based mechanical testing of compliant materials under low and high loading rates; and (2) a new mechanical property/impact resistance database comparing the penetration depth, stiffness, stress relaxation, poroelastic behavior and specific energy absorption of hydrated, soft tissues with that of engineered polymer gels.

Relevant conclusions and contributions of this thesis are summarized below:

Chapter 2 presented the development of a tool for conducting micro- and nano-scale indentation experiments under fully hydrated environments enabling characterization of mechanical properties of materials with in-solution applications. This development enabled the first direct observation of mechanical property manipulation carried out in an electrochemical cell with a redox-active thin film. Next, mechanically tunable porous tissue scaffolds were characterized via utilizing this method, and it was found that increasing the crosslinker percentage lead to an increase in the overall gel stiffness. Finally, high throughput nanomechanical screening of biomaterials for clonal stem cell growth was conducted in fully hydrated conditions; stiffness of

over 450 polymers was correlated with the colony formation frequency. These findings informed the effect of mechanical properties of the substrate on cell motility and proliferation.

Chapter 3 introduced two soft tissues from murine heart and liver organs, and physically associating styrene based triblock/diblock copolymer gels as tissue simulants. This chapter studied the structure-property relationship of these new materials in comparison to soft tissues, with the goal to design mechanically tunable, environmentally stable new tissue simulant gels for ballistic applications. First, low-rate macroscale unconfined compression and microscale indentation experiments were conducted to study elastic properties as a function of diblock percentage in comparison to soft tissues, utilizing the tool developed in Chapter 2. Next, macroscale, mesoscale, and microscale stress relaxation experiments were conducted to study the time-dependent viscoelastic properties. New techniques were presented for ascertaining the physical contact point for compliant materials, and for minimization of adhesion between the probe surface and the sample surface, utilizing accurate calculation of elastic and viscoelastic properties via contact based approaches. Increasing the diblock percentage in the system was found to decrease the overall elastic modulus and relaxation modulus, and to increase the energy dissipation capacity, but not affect the relaxation times. Both heart and liver tissues were more compliant, dissipated less energy and exhibited smaller relaxation times compared to the tissue simulants. Finally, to investigate the mechanical properties at higher strain energy densities and rates relevant to impact insult, a contact based impulse testing method developed originally for testing metals and ceramics was modified to study the impact resistance, and energy dissipation capacities and rates of the potential tissue simulants in comparison to heart and liver tissue. The gels became less impact resistant and dissipated more energy as the diblock percentage in the system decreased. Even though a gel with 50/50 triblock/diblock composition was found to exhibit similar energy dissipation capacities to heart and liver tissue, this system was found to exhibit limited tunability of impact resistance (i.e., maximum penetration depths) and strain rate dependency.

Chapter 4 studied a previously developed crosslinked PDMS gel system with a nonreactive PDMS solvent as potential tissue simulant gels in comparison to heart and liver tissue. First, macroscale rheology experiments were conducted to assess the effect of solvent loading

percentage, silane:vinyl stoichiometric ratio, and molecular weight of the solvent on storage G' , loss moduli G'' and loss tangent in order to study the relationships between the network structure and mechanical properties. Storage modulus was found to increase as a function of decreasing solvent loading percentage and increasing silane:vinyl stoichiometric ratio. Increasing the solvent molecular weight was found to not affect low frequency G' values, but enhanced strain rate dependency of G' , and increased the energy dissipation capacities significantly. Next, impact indentation experiments were conducted to study gel response in comparison to soft tissues at high loading rates under concentrated impact loading. These studies provided insights into design principles and approaches to modulate the mechanical response of tissue simulant gels to enable the development of biofidelic tissue simulants. Impact resistance increased as a function of decreasing solvent loading percentage, increasing silane:vinyl stoichiometric ratio, and increasing solvent molecular weight. Energy dissipation capacities and rates increased as the solvent loading percentage and solvent molecular weight increased, and stoichiometric ratio decreased. By varying the silane:vinyl stoichiometric ratio and solvent loading percentage, the impact resistance and energy dissipation capacity and rate of the gels were decoupled, which enabled independent tuning of these material characteristics for tissue-specific applications. Further, under identical impact loading conditions, specific gel compositions were identified that replicated the impact penetration resistance, energy dissipation capacity and rate of heart tissue with reasonable fidelity.

Chapter 5 addressed the application of a poroelastic model on contact based load relaxation experiments to extract the elastic and transport properties of hydrogels and soft tissues with the goal to inform the design of tissue simulants and computational models of impact response of soft tissues. Polyacrylamide gels were chosen as a model material to study validation of this approach for μm -scale contact radii and contact depths where the poroelastic relaxation times are much shorter compared to those calculated from experiments conducted at macroscale length scales. Experiments were conducted both at macroscale and microscale length scales; elastic and transport properties extracted from these experiments exhibited excellent agreement with each other. This approach significantly reduced the required experiment time scale from $>10\text{s}$ of hours to $<10\text{s}$ of seconds, extending the applicability of contact-based analysis of poroelasticity to biological tissues that can degrade quickly with time. Next, same approach was applied on heart

and liver tissue to study the structure-property relationships. For the experiments conducted on these soft tissues, even though the dominance of poroelastic relaxation was not evident, calculated properties were in the range of values reported in literature. Elastic and transport properties of heart were found to be direction specific, given the layered structure of the tissue. For liver tissue, the presence of a capsule was found to increase the overall stiffness and decrease the permeability. These findings inform the future development of tissue simulant materials that exhibit similar layered structures to heart and liver, and computational models of tissue mechanics.

6.2 Suggestions for future research

This section discusses the possible extensions of this thesis research.

6.2.1 Computational modeling of gel response to high-rate deformation

While our work presented in Chapters 3 and 4 has produced viable candidates for engineered tissue simulants of heart and liver, further improvements must be made to more closely and simultaneously match all the desired design metrics between the gels and aforementioned tissues as well as other target tissues. As laboratory measurements are time consuming and costly due to the numerous variables that characterize such polymer systems (e.g., molecular weight, composition, and macromolecular structure, etc., all conferring unique mechanical performance suitable for the particular application), future experimental studies could involve parallel studies via finite element analysis to study a variety of gel designs. These studies could include consideration of a multilayered laminate of PDMS gels, reminiscent of the striated biological tissues, and determine the effect of variation of order and thickness ratios of layers as inspired by the striated or layered structure of biological tissues. Computational modeling using multiscale analysis will provide an avenue for better-controlled tuning of the macroscale properties of the gels by enabling access to the definition of each of the gel components individually at the micro/nanoscale level. In addition, simulations provide the benefit of exploring tissue simulant behavior at higher impact velocities more representative of ballistic conditions.

6.2.2 Engineered protein based hydrogels as soft tissue simulants

Because of the complex hierarchical structures present in soft tissues, the interpretation of mechanical measurements and the elucidation of structure-property relationships may be

challenging. Protein engineering offers a unique opportunity to produce simple model systems that replicate many of the chemical and structural elements present in tissue, allowing simple structure-property relationships to be more easily elucidated. Artificial protein polymer hydrogels offer the opportunity to mimic specific structural elements from natural proteins within synthetic hydrogel systems, allowing systematic exploration of the effects of these protein constituents on the mechanical response of hydrated gels and tissues. Effects of protein interactions on the stiffness, impact penetration depth, and impact energy dissipation characteristics of gels could be investigated using these model physically associating gel systems. Initial impact indentation studies on preliminary protein-based gel systems show that these gels could be designed to exhibit similar impact resistances to heart and liver tissues (Figure 6.1a); however, those designed to date dissipate the impact energy more slowly compared to soft tissues (Figure 6.1b).

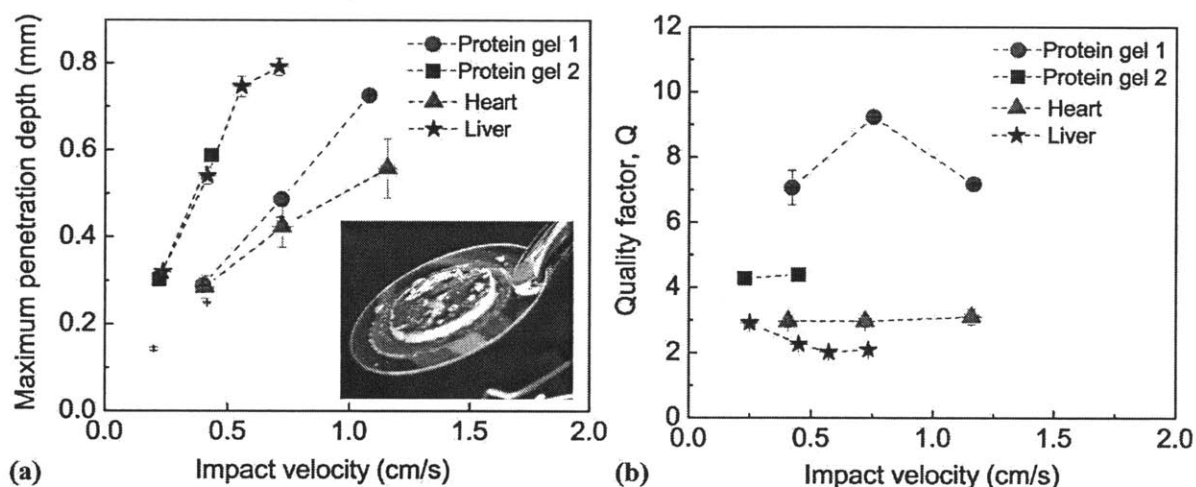


Figure 6.1 Quantitative analysis of maximum penetration depths as a function of impact velocity for protein-based hydrogels in comparison to soft tissue response, inset shows an image of the gel (courtesy of Matthew Glassman from Olsen Lab, MIT ChemE). (b) Quality factor Q related to energy dissipation rate of the gels and soft tissues as a function of impact velocity.

6.2.3 Poroviscoelastic analysis of soft tissues

Soft tissues are known to exhibit a poroelastic response due to their bi-phasic nature (i.e., solid-fluid interactions). Thus, in Chapter 5 we presented a contact-based approach where a poroelastic model was applied on the relaxation response of gels and tissues from heart and liver to simultaneously extract the elastic and transport properties, with the goal to inform the design of tissue simulant gels, and the development of computational models of tissue mechanics.

However, time dependent phenomena in gels and soft tissues may be attributed to a variety of mechanisms such as fluid squeezing out of the gel, viscous effects in the underlying polymeric network, or a combination of both. Although the dominant form of relaxation assumed in that study is poroelastic, in some cases the viscoelastic effects could occur over the same time scale as fluid permeation and would thus complicate the interpretation of the experimental results. Recently, Chester et al. has presented a continuum mechanical theory to describe coupled fluid permeation and large viscoelastic deformations in non-ionic polymeric gels via indentation⁵⁶. The determination of specific constitutive forms that take both poroelastic and viscoelastic contribution into consideration, and the accompanying material parameters from indentation experiments will likely be essential for accurate quantitative measurements of mechanical properties of gels and soft tissues over a wide range of length- and time-scales.

References

- 1 Fackler, M. L., Surinchak, J. S., Malinowski, J. A. & Bowen, R. E. Bullet fragmentation: a major cause of tissue disruption. *Journal of Trauma-Injury Infection & Critical Care* **24**, 35 (1984).
- 2 Juliano, T. F., Foster, A. M., Drzal, P. L., Weesoorya, T., Moy, P. & VanLandingham, M. R. Multiscale Mechanical Characterization of Biomimetic Physically Associating Gels. *Journal of Materials Research* **21**, 2084 (2006).
- 3 Leung, A. C., Kirth E. Simmonds, Matic, P. & Geltmacher, A. B. Surrogate Human Thorax Modal Frequency Response. *ABAQUS Users' Conference*, 303 (2006).
- 4 Joshi, M. *Chennai doctors perform Robot-assisted heart surgery*, <<http://www.topnews.in/health/chennai-doctors-perform-robot-assisted-heart-surgery-2446>> (2008).
- 5 Keel, T. *Jell-O Shots*, <<https://www.usconcealedcarry.com/ccm-columns/ballistic-basics/jell-o-shots/>> (2010).
- 6 Miller, K. Method of testing very soft biological tissues in compression. *Journal of Biomechanics* **38**, 153 (2005).
- 7 Tamura, A., Omori, K., Miki, K., Lee, J. B., Yang, K. H. & King, A. I. Mechanical Characterization of Porcine Abdominal Organs. *46th Stapp Car Crash Conference* **46** (2002).
- 8 Kroekera, S. G., Morleya, P. L., Jonesa, C. F., Bilston, L. E. & Crompton, P. A. The development of an improved physical surrogate model of the human spinal cord—Tension and transverse compression *Journal of Biomechanics* **42**, 878 (2009).
- 9 Fung, Y. C. Elasticity of Soft Tissues in Simple Elongation., *American Journal of Physiology* **213**, 1532 (1967).
- 10 Miller, K. & Chinzei, K. Mechanical properties of brain tissue in tension. *Journal of Biomechanics* **35**, 483 (2002).
- 11 Nava, A., Mazza, E., Furrer, M., Villiger, P. & Reinhart, W. H. In vivo mechanical characterization of human liver. *Medical Image Analysis* **12**, 203 (2008).
- 12 Kaufman, J. D., Miller, G. J., Morgan, E. F. & Klapperich, C. M. Time-dependent mechanical characterization of poly(2-hydroxyethyl methacrylate) hydrogels using nanoindentation and unconfined compression. *Journal of Materials Research* **23**, 1472 (2008).
- 13 Hu, Y., You, J.-O., Auguste, D. T., Suo, Z. & Vlassak, J. J. Indentation: A simple, nondestructive method for characterizing the mechanical and transport properties of pH-sensitive hydrogels. *Journal of Materials Research* **27**, 152 (2012).
- 14 Hu, T. & Desai, J. P. A Biomechanical Model of the Liver for Reality-Based Haptic Feedback. *The 6th International Conference on Medical Image Computing and Computer Assisted Intervention (MICCAI)* **2878**, 75 (2003).
- 15 Al-ja'afreh, T., Zweiri, Y., Seneviratne & Althoefer, K. A new soft-tissue indentation model for estimating circular indenter 'force-displacement' characteristics. *Proceedings of the IMechE Part H: Journal of Engineering in Medicine* **222**, 805.
- 16 Carter, F. J., T.G. Frank, Davies, P. J., McLean, D. & Cuschieri, A. Measurements and modelling of the compliance of human and porcine organs. *Medical Image Analysis* **5**, 231 (2001).
- 17 Barnes, S. L., Lyshchik, A., Washington, M. K., Gore, J. C. & Miga, M. I. Development of a mechanical testing assay for fibrotic murine liver. *Medical Physics* **34**, 4439 (2007).

- 18 Ulijaszek, S. J., Johnston, F. E. & M.A.Preece. *The Cambridge Encyclopaedia of Human Growth and Development*. (Cambridge University Press, 1998).
- 19 Nicollea, S. & Paliarne, J. F. Dehydration effect on the mechanical behaviour of biological soft tissues: Observations on kidney tissues. *Journal of the mechanical behavior of biomedical materials* **3**, 630 (2010).
- 20 Rho, J.-Y. & Pharr, G. M. Effects of drying on the mechanical properties of bovine femur measured by nanoindentation. *Journal of Materials Science:Materials in Medicine* **10**, 485 (1999).
- 21 Hengsberger, S., A. Kulik & Zysset, P. Nanoindentation discriminates the elastic properties of individual human bone lamellae under dry and physiological conditions. *Bone* **30**, 178 (2002).
- 22 Balooch, M., Wu-Magidi, I.-C., Balazs, A., Lundkvist, A. S., Marshall, S. J., Marshall, G. W., Siekhaus, W. J. & Kinney, J. H. Viscoelastic properties of demineralized human dentin in water with AFM-based indentation. *Journal of Biomedical Material Research* **40**, 539 (1998).
- 23 Bushby, A. J., Ferguson, V. L. & Boyde, A. Nanoindentation of bone: Comparison of specimens tested in liquid and embedded in polymethylmethacrylate. *Journal of Materials Research* **19**, 249 (2004).
- 24 Mann, A. B. & Pethica, J. B. Nanoindentation Studies in a Liquid Environment. *Langmuir* **12**, 4583 (1996).
- 25 Ebenstein, D. M. & Pruitt, L. A. Nanoindentation of soft hydrated materials for application to vascular tissues. *Journal of Biomedical Material Research* **69A**, 222 (2004).
- 26 Darvish, K. K. & Crandall, J. R. Nonlinear viscoelastic effects in oscillatory shear deformation of brain tissue *Medical Engineering & Physics* **23**, 633 (2001).
- 27 Yuan, Y. & Verma, R. Measuring microelastic properties of stratum corneum. *Colloids and Surfaces B: Biointerfaces* **48**, 6 (2006).
- 28 Kaufman, J. D. & Klapperich, C. M. Surface detection errors cause overestimation of the modulus in nanoindentation on soft materials. *Journal of the Biomechanical Behavior of Biomedical Materials* **2**, 312 (2009).
- 29 Deuschle, J., Enders, S. & Artz, E. Surface detection in nanoindentation of soft polymers. *Journal of Materials Research* **22**, 3107 (2007).
- 30 Carrillo, F., Gupta, S., Balooch, M., Marshall, S. J., Marshall, G. W., Pruitt, L. & Puttlitz, C. M. Nanoindentation of polydimethylsiloxane elastomers: Effect of crosslinking, work of adhesion, and fluid environment on elastic modulus. *Journal of Materials Research* **20**, 2820 (2005).
- 31 Ebenstein, D. M. & Wahl, K. J. A comparison of JKR-based methods to analyze quasi-static and dynamic indentation force curves. *Journal of Colloid and Interface Science* **298**, 652 (2006).
- 32 Johnson, K. L. *Contact Mechanics*. (Cambridge University Press, 1985).
- 33 Lin, Y. Y., Hui, C. Y. & Baney, J. M. Viscoelastic contract, work of adhesion and the JKR technique. *Journal of Physics D: Applied Physics* **32**, 2250 (1999).
- 34 Haiat, G., Huy, M. C. P. & Barthel, E. The adhesive contact of viscoelastic spheres. *Journal of the Mechanics and Physics of Solids* **51**, 69 (2003).
- 35 Hiratsuka, S., Mizutani, Y., Toda, A., Fukushima, N., Kawahara, K., Tokumoto, H. & Okajima, T. Power-Law Stress and Creep Relaxations of Single Cells Measured by Colloidal Probe Atomic Force Microscopy. *Japanese Journal of Applied Physics* **48**, 08JB17 (2009).
- 36 Burtovyy, R., Liu, Y., Zdyrko, B., Tregub, A., Moinpour, M., Buehler, M. & Luzinov, I. AFM Measurements of Adhesion between CMP Slurry Particles and Copper. *Materials Research Society Symposium Proceedings* **914** (2006).

- 37 Franke, O., Durst, K., Maier, V., Goken, M., Birkholz, T., Schneider, H., Hennig, F. & Gelse, K. Mechanical properties of hyaline and repair cartilage studied by nanoindentation. *Acta Biomaterialia* **3**, 873 (2007).
- 38 Pruitt, L. & King, K. Nanoindentation differentiates tissue-scale functional properties of native articular cartilage. *Journal of Biomedical Material Research A* **78**, 729 (2006).
- 39 Angkera, L., Swain, M. V. & Kilpatrick, N. Characterising the micro-mechanical behaviour of the carious dentine of primary teeth using nano-indentation. *Journal of Biomechanics* **38**, 1535 (2005).
- 40 Nia, H. T., Han, L., Li, Y., Ortiz, C. & Grodzinsky, A. Poroelasticity of Cartilage at the Nanoscale. *Biophysical Journal* **101**, 2304 (2011).
- 41 Cheng, Y.-T., Ni, W. & Cheng, C.-M. Nonlinear Analysis of Oscillatory Indentation in Elastic and Viscoelastic Solids. *Physical Review Letters* **97**, 075506 (2006).
- 42 Odegard, G. M., Gates, T. S. & Herring, H. M. Characterization of viscoelastic properties of polymeric materials through nanoindentation. *Experimental Mechanics* **45**, 130 (2005).
- 43 Franke, O., Göken, M., Meyers, M. A., Durst, K. & Hodge, A. M. Dynamic nanoindentation of articular porcine cartilage. *Materials Science and Engineering C* **31**, 789 (2011).
- 44 Lee, E. H. & Radok, J. R. M. The contact problem for viscoelastic bodies. *Journal of Applied Mechanics* **27**, 438 (1960).
- 45 Ting, T. C. T. Contact stresses between a rigid indenter and a viscoelastic half-space. *Journal of Applied Mechanics* **33**, 845 (1966).
- 46 VanLandingham, M. R., Chang, H. K., Drzal, P. L., White, C. C. & Chang, S. H. Viscoelastic Characterization of Polymers Using Instrumented Indentation. I. Quasi-Static Testing. *Journal of Polymer Science Part B: Polymer Physics* **43**, 1794 (2005).
- 47 Fischer-Cripps, A. C. A simple phenomenological approach to nanoindentation creep. *Medical Image Analysis* **9**, 481 (2005).
- 48 Biot, M. A. General theory of three-dimensional consolidation. *Journal of Applied Physics* **12**, 155 (1941).
- 49 Terzaghi, K. *Sitzungber. Akad. Wiss Wien Math.-Naturwiss. Kl., Abt, Ila* **132**, 125 (1923).
- 50 Hu, Y., Chen, X., Whitesides, G. M., Vlassak, J. J. & Suo, Z. Indentation of polydimethylsiloxane submerged in organic solvents. *Journal of Materials Research* **26**, 785 (2011).
- 51 Hu, Y., Zhao, X., Vlassak, J. J. & Suo, Z. Using indentation to characterize the poroelasticity of gels. *Applied Physics Letters* **96**, 121904 (2010).
- 52 Oyen, M. L. Poroelastic nanoindentation responses of hydrated bone. *Journal of Materials Research* **23**, 1307 (2008).
- 53 Galli, M., Comley, K. S. C., Shean, T. A. V. & Oyen, M. L. Viscoelastic and poroelastic mechanical characterization of hydrated gels. *Journal of Materials Research* **24**, 973 (2009).
- 54 Lin, W.-C., Shull, K. R., Hui, C.-Y. & Lin, Y.-Y. Contact measurement of internal fluid flow within poly(n-isopropylacrylamide) gels *Journal of Chemical Physics* **127**, 094906 (2007).
- 55 Lin, Y.-Y. & Hu, B.-W. Load relaxation of a flat rigid circular indenter on a gel half space. *Journal of Non-Crystalline Solids* **352**, 4034 (2006).
- 56 Chester, S. A. A constitutive model for coupled fluid permeation and large viscoelastic deformation in polymeric gels. *Soft Matter* **8**, 8223 (2012).
- 57 Fung, Y. C. *Biomechanics: Mechanical Properties of Living Tissues*. (Springer, 1993).
- 58 Yamada, H. *Strength of Biological Materials*. (Williams&Wilkins, 1970).
- 59 Liu, Z. & Bilston, L. On the viscoelastic character of liver tissue: experiments and modelling of the linear behaviour. *Biorheology* **37**, 191 (2000).
- 60 Valtorta, D. & Mazza, E. Dynamic measurement of soft tissue viscoelastic properties with a torsional resonator device. *Medical Image Analysis* **9** 481 (2005).

- 61 Shergold, O. A., Fleck, N. A. & Radford, D. The uniaxial stress versus strain response of pig skin and silicone rubber at low and high strain rates. *International Journal of Impact Engineering* **32**, 1384 (2006).
- 62 Moy, P., Weerasooriya, T., Juliano, T. F. & VanLandingham, M. R. Dynamic Response of an Alternative Tissue Simulant, Physically Associating Gels (PAG). *Proc. 2006 SEM Annu. Conf. Exp. Mech.* (2006).
- 63 Saraf, H., Ramesh, K., Lennon, A., Merkle, A. & Roberts, J. Measurement of the dynamic bulk and shear response of soft human tissues. *Experimental Mechanics* **47**, 439 (2007).
- 64 Pervin, F., Chen, W. W. & Weerasooriya, T. Dynamic compressive response of bovine liver tissues. *Journal of the Mechanical Behavior of Biomedical Materials* **4**, 76 (2011).
- 65 Song, B., Chen, W., Ge, Y. & Weerasooriya, T. Dynamic and quasi-static compressive response of porcine muscle. *Journal of Biomechanics* **40**, 2999 (2007).
- 66 Sligtenhorst, C., Cronin, D. & Brodland, G. High strain rate compressive properties of bovine muscle tissue determined using a split hopkinson bar apparatus. *Journal of Biomechanics* **39**, 1852 (2006).
- 67 Saraf, H., Ramesh, K., Lennon, A., Merkle, A. & Roberts, J. Mechanical properties of soft human tissues under dynamic loading. *Journal of Biomechanics* **40**, 1960 (2007).
- 68 Varga, F., Drzik, M., Handl, M., Chlpik, J., Kos, P., Filova, E., Rampichova, M., Necas, A., Trc, T. & Amler, E. Biomechanical characterization of cartilages by a novel approach of blunt impact testing. *Physiological Research* **56 (Suppl.1)**, 561 (2007).
- 69 Robinovitch, S. N., McMahon, T. A. & Hayes, W. C. Force attenuation in trochanteric soft tissues during impact from a fall. *Journal of Orthopaedic Research* **13**, 956 (1995).
- 70 Lau, V.-K. & Viano, D. C. Influence of Impact velocity on the severity of nonpenetrating hepatic injury. *Journal of Trauma* **21**, 115 (1981).
- 71 Talantikite, Y., Brun-Cassan, F., Lecoz, J. Y. & Tarriere, C. *Proceedings of the International Conference on the Biomechanics of Impacts* (1993).
- 72 Snedker, J., Barbezat, M., Niederer, P., Schmidlin, F. & Farshad, M. Strain energy density as a rupture criterion for the kidney: impact tests on porcine organs, finite element simulation, and a baseline comparison between human and porcine tissues. *Journal of Biomechanics* **38**, 993 (2005).
- 73 Lewis, J. L., Deloria, L. B., Oyen-Tiesma, M., Jr., R. C. T., Ericson, M. & Jr., T. R. O. Cell death after cartilage impact occurs around matrix cracks. *Journal of Orthopaedic Research* **21** 881 (2003).
- 74 Nicholas, N. C. & Welsch, J. R. *Ballistic Gelatin*. (Penn State Applied Research Laboratory, Happy Valley, PA, 2004).
- 75 Peterson, B. *Ballistic Gelatin Lethality Performance of 0.375-in Ball Bearing and MAAWS 401B Flechettes*. *Army Research Laboratory Technical Report ARL-TR-4153* (2007).
- 76 Moy, P., Foster, M., Gunnarsson, C. A. & Weerasooriya, T. Loading Rate Effect on Tensile Failure Behavior of Gelatins under Mode I. *Proceedings of the SEM Annual Conference* (2010).
- 77 Fackler, M. L. Wound ballistics: A target for error. *International Defense Review* **8**, 895 (1988).
- 78 Amato, J. J., Billy, L. J., Gruber, R. P., Lawson, N. S. & Rich, N. M. Vascular injuries: An experimental study of high and low velocity missile wounds. *Archives of Surgery* **101**, 167 (1970).
- 79 Seitz, M. E., Burghardt, W. R., Faber, K. T. & Shull, K. R. Self-Assembly and Stress Relaxation in Acrylic Triblock Copolymer Gels. *Macromolecules* **40**, 1218 (2007).

- 80 Mrozek, R. A., Cole, P. J., Otim, K. J., Shull, K. R. & Lenhart, J. L. Influence of solvent size on the mechanical properties and rheology of polydimethylsiloxane-based polymeric gels. *Polymer* **52**, 3422 (2011).
- 81 Constantinides, G., Kalcioğlu, I. Z., McFarland, M., Smith, J. F. & Van Vliet, K. J. Probing mechanical properties within fully hydrated gels and tissues. *Journal of Biomechanics* **41**, 3285 (2008).
- 82 Thompson, M. T., M.C. Berg, Tobias, I. S., Rubner, M. F. & Van Vliet, K. J. Tuning compliance of nanoscale polyelectrolyte multilayers to modulate cell adhesion. *Biomaterials* **26**, 6836 (2005).
- 83 Ho, S. P., Balooch, M., Goodis, H. E., Marshall, G. W. & Marshall, S. J. Ultrastructure and nanomechanical properties of cementum dentin junction. *J Biomed Mater Res A* **68**, 343 (2004).
- 84 Tweedie, C. A., Anderson, D. G., Langer, R. & Van Vliet, K. J. Combinatorial Material Mechanics: High-Throughput Polymer Synthesis and Nanomechanical Screening. *Advanced Materials* **17**, 2599 (2005).
- 85 Ebenstein, D. & Pruitt, L. Nanoindentation of biological materials. *NanoToday* **1**, 26 (2006).
- 86 Tweedie, C. A., Constantinides, G., Lehman, K. E., Brill, D. J., Blackman, G. S. & Van Vliet, K. J. Enhanced stiffness of amorphous polymer surfaces under confinement of localized contact loads. *Advanced Materials* **19**, 2540 (2007).
- 87 Van Vliet, K. J., Prchlik, L. & Smith, J. F. Direct measurement of indentation frame compliance. *Journal of Materials Research* **19**, 325 (2004).
- 88 Oliver, W. C. & Pharr, G. M. An improved technique for determining hardness and elastic modulus using load and displacement sensing indentation experiments. *Journal of Materials Research* **7**, 1564 (1992).
- 89 Constantinides, G., Ravi Chandran, K. S., Ulm, F.-J. & Van Vliet, K. J. Grid indentation analysis of composite microstructures: Principles and validation. *Materials Science and Engineering A* **430**, 189 (2006).
- 90 Thompson, M. T., Berg, M. C., Tobias, I. S., Rubner, M. F. & Van Vliet, K. J. Tuning compliance of nanoscale polyelectrolyte multilayers to modulate cell adhesion. *Biomaterials* **26**, 6836 (2005).
- 91 Cheng, L., Xia, X., Scriven, L. E. & Gerberich, W. W. Spherical-tip indentation of viscoelastic material. *Mechanics of Materials* **37**, 213 (2005).
- 92 Yeung, T., Georges, P. C., Flanagan, L. A., Marg, B., Ortiz, M., Funaki, M., Zahir, N., Ming, W., Weaver, V. & Janmey, P. A. Effects of substrate stiffness on cell morphology, cytoskeletal structure, and adhesion. *Cell Motility and the Cytoskeleton* **60**, 24 (2005).
- 93 Oyen, M. L. & Cook, R. F. Load-displacement behavior during sharp indentation of viscous-elastic-plastic materials. *Journal of Materials Research* **18**, 139 (2003).
- 94 Cheng, Y. T. & Cheng, C. M. Scaling, dimensional analysis, and indentation measurements. *Materials Science and Engineering R* **44**, 91 (2004).
- 95 Matzelle, T. R., Geuskens, G. & Kruse, N. Elastic Properties of Poly(N-isopropylacrylamide) and Poly(acrylamide) Hydrogels Studied by Scanning Force Microscopy. *Macromolecules* **36**, 2926 (2003).
- 96 Schmidt, D. J., Cebeci, F. C., Kalcioğlu, Z. I., Wyman, S. G., Ortiz, C., Van Vliet, K. J. & Hammond, P. T. Electrochemically Controlled Swelling and Mechanical Properties of a Polymer Nanocomposite. *ACS Nano* **3**, 2207 (2009).
- 97 Nelson, A. Stimuli-Responsive Polymers: Engineering Interactions. *Nature Materials* **7**, 523 (2008).
- 98 Ganta, S., Devalapally, H. & Amiji, A. S. M. A review of stimuli-responsive nanocarriers for drug and gene delivery. *Journal of Controlled Release* **126**, 187 (2008).

- 99 Mano, J. F. Stimuli-responsive polymeric systems for biomedical applications. *Advanced Engineering Materials* **10**, 515 (2008).
- 100 Mendes, P. M. Stimuli-responsive surfaces for bio-applications. *Chemical Society Reviews* **37**, 2512 (2008).
- 101 Ahn, S. K., Kasi, R. M., Kim, S. C., Sharma, N. & Zhou, Y. X. Stimuli-responsive polymer gels. *Soft Matter* **4**, 1151 (2008).
- 102 Discher, D. E., Janmey, P. & Wang, Y. L. Tissue cells feel and respond to the stiffness of their substrate. *Science* **310**, 1139 (2005).
- 103 Favier, V., Cavaille, J. Y., Canova, G. R. & Shrivastava, S. C. Mechanical percolation in cellulose whisker nanocomposites. *Polymer Engineering & Science* **37**, 1732 (1997).
- 104 Flandin, L., Bidan, G., Brechet, Y. & Cavaille, J. Y. New nanocomposite materials made of an insulating matrix and conducting fillers: Processing and properties. *Polymer Composites* **21**, 165 (2000).
- 105 DeLongchamp, D. M. & Hammond, P. T. High-contrast electrochromism and controllable dissolution of assembled Prussian blue/polymer nanocomposites. *Advanced Functional Materials* **14**, 224 (2004).
- 106 Dimitriadis, E. K., Horkay, F., Maresca, J., Kachar, B. & Chadwick, R. S. *Biophysical Journal* **82**, 2798 (2002).
- 107 Dubas, S. T. & Schlenoff, J. B. Swelling and smoothing of polyelectrolyte multilayers by salt. *Langmuir* **17**, 7725 (2001).
- 108 Jaber, J. A. & Schlenoff, J. B. Mechanical properties of reversibly cross-linked ultrathin polyelectrolyte complexes. *Journal of the American Chemical Society* **128**, 2940 (2006).
- 109 Peyton, S. R., Kalcioğlu, Z. I., Cohen, J. C., Runkle, A. P., Van Vliet, K. J., Lauffenburger, D. A. & Griffith, L. G. Marrow-Derived Stem Cell Motility in 3D Synthetic Scaffold Is Governed by Geometry Along With Adhesivity and Stiffness. *Biotechnology and Bioengineering* **108**, 1181 (2011).
- 110 Pelham, R. J. & Wang, Y. Cell locomotion and focal adhesions are regulated by substrate flexibility. *PNAS* **94**, 13661 (1997).
- 111 Peyton, S. R. & Putnam, A. J. Extracellular matrix rigidity governs smooth muscle cell motility in a biphasic fashion. *Journal of Cellular Physiology* **204**, 198 (2005).
- 112 Engler, A. J., Sen, S., Sweeney, H. L. & 2006, D. E. D. Matrix elasticity directs stem cell lineage specification. *Cell* **126**, 677 (2006).
- 113 Stachowiak, A. N. I., D. J. . Inverse opal hydrogel-collagen composite scaffolds as a supportive microenvironment for immune cell migration. *Journal of Biomedical Material Research A* **85**, 815 (2008).
- 114 Harley, B. A., Leung, J. H., Silva, E. C. & Gibson, L. J. Mechanical characterization of collagen-glycosaminoglycan scaffolds. *Acta Biomaterialia* **3**, 463 (2007).
- 115 Gibson, L. J. & Ashby, M. *Cellular Solids: Structure and Properties*. 2 edn, Vol. 1 (Cambridge University Press, 1999).
- 116 Jain, A., Rogojevic, S., Gill, W. N., Plawsky, J., Matthew, I., Tomozawa, M. & Simonyi, E. Effects of processing history on the modulus of silica xerogel films. *Journal of Applied Physics* **90**, 5832 (2001).
- 117 Stachowiak, A. N., Bershteyn, A., Tzatzalos, E. & Irvine, D. J. Bioactive hydrogels with an ordered cellular structure combine interconnected macroporosity and robust mechanical properties. *Advanced Materials* **17**, 399 (2005).
- 118 Mei, Y., Saha, K., Bogatyrev, S. R., Yang, J., Hook, A. L., Kalcioğlu, Z. I., Cho, S.-W., Mitalipova, M., Pyzocha, N., Rojas, F., Van Vliet, K. J., Davies, M. C., Alexander, M. R., Langer, R., Jaenisch, R. & Anderson, D. G. Combinatorial development of biomaterials for clonal growth of human pluripotent stem cells. *Nature Materials* **9**, 768 (2010).

- 119 Gearhart, J. New potential for human embryonic stem cells. *Science* **282**, 1061 (1998).
- 120 Daley, G. Q. & Scadden, D. T. Prospects for stem cell-based therapy. *Cell* **132**, 544 (2008).
- 121 Urbach, A., Schuldiner, M. & Benvenisty, N. Modeling for Lesch-Nyhan disease by gene targeting in human embryonic stem cells. *Stem Cells* **22**, 635 (2004).
- 122 Ebert, A. D., Yu, J., Rose, F. F., Mattis, V. B., Lorson, C. L., Thomson, J. A. & Svendsen, C. N. Induced pluripotent stem cells from a spinal muscular atrophy patient. *Nature* **457**, 277 (2009).
- 123 Saha, K. & Jaenisch, R. Technical challenges in using human induced pluripotent stem cells to model disease. *Cell Stem Cell* **5**, 584 (2009).
- 124 Anderson, D. G., Tweedie, C. A., Hossain, N., Navarro, S. M., Brey, D. M., Van Vliet, K. J., Langer, R. & Burdick, J. A. A Combinatorial Library of Photocrosslinkable and Degradable Materials. *Advanced Materials* **18**, 2614 (2006).
- 125 Anderson, D. G., Levenberg, S. & Langer, R. Nanoliter-scale synthesis of arrayed biomaterials and application to human embryonic stem cells. *Nat Biotechnol* **22**, 863 (2004).
- 126 Anderson, D. G., Putnam, D., Lavik, E. B., Mahmood, T. A. & Langer, R. Biomaterial microarrays: rapid, microscale screening of polymer-cell interaction. *Biomaterials* **26**, 4892 (2005).
- 127 Mei, Y., Gerecht, S., Taylor, M., Urquhart, A., Bogatyrev, S. R., Cho, S. W., Davies, M. C., Alexander, M. R., Langer, R. S. & Anderson, D. G. Mapping the Interactions among Biomaterials, Adsorbed Proteins, and Human Embryonic Stem Cells. *Advanced Materials* **21**, 2781 (2009).
- 128 Kalcioğlu, Z. I., Qu, M., Strawhecker, K. E., Shazly, T., Edelman, E., VanLandingham, M. R., Smith, J. F. & Van Vliet, K. J. Dynamic impact indentation of hydrated biological tissues and tissue surrogate gels. *Philosophical Magazine* **91**, 1339 (2011).
- 129 Mehdizadeh, S., Khoshgoftar, M., Najarian, S., Farmanzad, F. & Ahmadi, S. A. H. Comparison between Brain Tissue Gray and White Matters in Tension Including Necking Phenomenon. *American Journal of Applied Sciences* **5**, 1701 (2008).
- 130 Ghaemi, H., Behdian, K. & Spence, A. D. In vitro technique in estimation of passive mechanical properties of bovine heart part I. Experimental techniques and data. *Medical Engineering & Physics* **31**, 76 (2009).
- 131 Buschmann, M. D., Soulhat, J., Shirazi-Adl, A., Jurvelin, J. S. & Hunziker, E. B. Confined compression of articular cartilage: Linearity in ramp and sinusoidal tests and the importance of interdigitation and incomplete confinement. *Journal of Biomechanics* **31**, 171 (1998).
- 132 Chui, C., Kobayashi, E., Chen, X., Sakuma, I. & Hisada, T. Transversely isotropic properties of porcine liver tissue: experiments and constitutive modeling. *Medical & Biological Engineering & Computational* **45**, 99 (2007).
- 133 Roan, E. & Vegemanti, K. The nonlinear material properties of the liver tissue determined from no-slip uniaxial compression experiments. *Journal of Biomechanical Engineering* **129**, 450 (2007).
- 134 Ebenstein, D. M., Kuo, A., Rodrigo, J. J., Reddi, A. H., Ries, M. & Pruitt, L. A nanoindentation technique for functional evaluation of cartilage repair tissue. *Journal of Materials Research* **19** 273 (2004).
- 135 Evans, D. W. *A Nanoindentation Device and the Scale-Dependent Mechanical Properties of Native and Decellularized Liver Tissue* Master of Science thesis, Virginia tech-Wake Forest University, (2011).
- 136 Park, S. & Ateshian, G. Dynamic response of immature bovine articular cartilage in tension and compression, and nonlinear viscoelastic modeling of the tensile response. *Journal of Biomechanical Engineering* **128**, 623 (2006).

- 137 Rosen, J., Brown, J. D., De, S., Sinanan, M. & Hannaford, B. Biomechanical Properties of Abdominal Organs In Vivo and Postmortem Under Compression Loads. *Journal of Biomechanical Engineering* **130**, 021020 (2008).
- 138 Bowen, R. *Hepatic Histology: The Lobule*, 2003).
- 139 Ashley, E. A. & Niebauer, J. *Cardiology Explained*. (Remedica Medical Education and Publishing, 2005).
- 140 Guyton, A. C. & Hall, J. E. *Textbook of medical physiology*. (Elsevier Saunders, 2006).
- 141 Uhal, B. D. & Roehrig, K. L. Effect of dietary state on hepatocyte size. *Bioscience Reports* **2**, 1003 (1982).
- 142 Roberts, W. C. Pericardial heart disease: its morphologic features and its causes. *BUMC Proceedings* **18**, 38 (2005).
- 143 Rémy-Jardin, M. & Rémy, J. *Integrated Cardiothoracic Imaging with MDCT*. (Springer-Verlag, 2009).
- 144 Lieber, S. C., Aubry, N., Pain, J., Diaz, G., Kim, S.-J. & Vatner, S. F. Aging increases stiffness of cardiac myocytes measured by atomic force microscopy nanoindentation. *American Journal of Physiology - Heart and Circulatory Physiology* **287**, H645 (2004).
- 145 Hunter, P. J., McCulloch, A. D. & Keurs, H. E. D. J. t. Modelling the mechanical properties of cardiac muscle. *Progress in Biophysics & Molecular Biology* **69**, 289 (1998).
- 146 Quintana, J. R., Hernaez, E. & Katime, I. Thermoreversible gelation of mixed triblock and diblock copolymers in n-octane *Polymer* **43**, 3217 (2002).
- 147 Sliozberg, Y., Andzelm, J., Brennan, J. K., Vanlandingham, M. & Ganesan, V. Modeling Viscoelastic Properties of Triblock Copolymers: A DPD Simulation Study. *Journal of Polymer Science part B: polymer physics* **1**, 15 (2010).
- 148 Grunlan, J. C., Xia, X. Y., Rowenhorst, D. & Gerberich, W. W. High-resolution capacitive load-displacement transducer and its application in nanoindentation and adhesion force measurements. *Review of Scientific Instruments* **72**, 2804 (2001).
- 149 Fisher-Cripps, A. C. *Nanoindentation*. 2nd edn, (Springer-Verlag, 2004).
- 150 Constantinides, G., Silva, E., Blackman, G. S. & Van Vliet, K. J. Dealing with imperfection: quantifying potential length scale artefacts from nominally spherical indenter probes. *Nanotechnology* **18**, 305503 (2007).
- 151 Laurer, J. H., Khan, S. A., Spontak, R. J., Satkowski, M. M., Grothaus, J. T., Smith, S. D. & Lin, J. S. Morphology and rheology of SIS and SEPS triblock copolymers in the presence of a midblock-selective solvent *Langmuir* **15**, 7947 (1999).
- 152 Juliano, T. F., VanLandingham, M. R., Tweedie, C. A. & Van Vliet, K. J. Multiscale creep compliance of epoxy networks at elevated temperatures. *Experimental Mechanics* **47**, 99 (2007).
- 153 Engelmayer-Jr, G., Cheng, M., Bettinger, C. J., Borenstein, J. T., Langer, R. & Freed, L. E. Accordion-like honeycombs for tissue engineering of cardiac anisotropy. *Nature Materials* **7**, 1003 (2008).
- 154 Kalcioğlu, Z. I., Strawhecker, K., VanLandingham, M. R. & Van Vliet, K. J. Multiscale characterization of relaxation times of tissue surrogate gels and soft tissues. *27th Army Science Conference* (2010).
- 155 Du, P., Lu, H. & Zhang, X. Measuring the Young's Relaxation Modulus of PDMS Using Stress Relaxation Nanoindentation. *Materials Research Society Symposium Proceedings* **1222** (2010).
- 156 Williams, G. & Watts, D. C. Non-Symmetrical Dielectric Relaxation Behavior Arising from a Simple Empirical Decay Function. *Transactions of the Faraday Society* **66**, 80 (1970).

- 157 Harding, J. W. & Sneddon, I. N. The elastic stresses produced by the indentation of the plane surface of a semi-infinite elastic solid by a rigid punch. *Mathematical Proceedings of the Cambridge Philosophical Society* **41**, 16 (1945).
- 158 Hotta, A., Clarke, S. M. & Terentjev, E. M. Stress Relaxation in Transient Networks of Symmetric Triblock Styrene-Isoprene-Styrene Copolymer. *Macromolecules* **35**, 271 (2002).
- 159 Wang, A., Jiang, L., Mao, G. & Liu, Y. Direct Force Measurement of Silicone- and Hydrocarbon-Based ABATriblock Surfactants in Alcoholic Media by Atomic Force Microscopy. *Journal of Colloid and Interface Science* **256**, 331 (2002).
- 160 Okajima, T., Tanaka, M., Tsukiyama, S., T. Kadowaki, Yamamoto, S., Shimomura, M. & Tokumoto, H. Stress relaxation of HepG2 cells measured by atomic force microscopy. *Nanotechnology* **18**, 1 (2007).
- 161 Seitz, M. E., Burghardt, W. R., Faber, K. T. & Shull, K. R. Self-Assembly and Stress Relaxation in Acrylic Triblock Copolymer. *Macromolecules* **40**, 1218 (2007).
- 162 Hiratsuka, S., Mizutani, Y., Toda, A., Fukushima, N., Kawahara, K., Tokumoto, H. & Okajima, T. Power-Law Stress and Creep Relaxations of Single Cells Measured by Colloidal Probe Atomic Force Microscopy. *Japanese Journal of Applied Physics* **48**, 1 (2009).
- 163 Fackler, M. L. & Malinowski, J. A. The Wound Profile: A Visual Method for Quantifying Gunshot Wound Components *The Wound Profile: A Visual Method for Quantifying Gunshot Wound Components* **25**, 522 (1985).
- 164 Mavrillas, D., Sinouris, E., Vynios, D. & Papageorgakopoulou, N. Dynamic mechanical characteristics of intact and structurally modified bovine pericardial tissues. *Journal of Biomechanics* **38**, 761 (2005).
- 165 Nasser, S., Bilston, L. E. & Phan-Thien, N. Viscoelastic properties of pig kidney in shear, experimental results and modelling. *Rheologica Acta* **41**, 180 (2002).
- 166 Matice, J. M., Lau, A. G., Oyen, M. L. & Kent, R. W. Spherical indentation load-relaxation of soft biological tissues. *Journal of Materials Research* **21**, 2003 (2006).
- 167 Constantinides, G., Tweedie, C. A., Holbrook, D. M., Barragan, P., Smith, J. F. & Van Vliet, K. J. Quantifying deformation and energy dissipation of polymeric surfaces under localized impact. *Materials Science and Engineering A* **489**, 403 (2008).
- 168 Constantinides, G., Tweedie, C. A., Savva, N., Smith, J. F. & Van Vliet, K. J. Quantitative Impact Testing of Energy Dissipation at Surfaces. *Experimental Mechanics* **49**, 511 (2009).
- 169 *MSDS solutions*
- 170 French, A. P. *Vibrations and Waves*. (W.W. Norton and Company, 1971).
- 171 Pain, H. J. *The Physics of Vibrations and Waves*. (John Wiley & Sons Ltd., 2005).
- 172 Trelewicz, J. R. *Nanostructure Stabilization and Mechanical Behavior of Binary Nanocrystalline Alloys* Ph.D. thesis, Massachusetts Institute of Technology, (2008).
- 173 Bibbo, M. A. & Valles, E. M. Influence of pendant chains on the loss modulus of model networks. *Macromolecules* **17**, 360 (1984).
- 174 Roth, L. E., Vega, D. A., Valles, E. M. & Villar, M. A. Viscoelastic properties of networks with low concentration of pendant chains. *Polymer* **45**, 5923 (2004).
- 175 Villar, M. A. & Valles, E. M. Influence of Pendant Chains on Mechanical Properties of Model Poly(dimethylsiloxane) Networks. 2. Viscoelastic Properties. *Macromolecules* **29**, 4081 (1996).
- 176 Kawamura, T., Urayama, K. & Kohjiya, S. Multiaxial Deformations of End-Linked Poly(dimethylsiloxane) Networks. III. Effect of Entanglement Density on Strain-Energy Density Function. *Journal of Polymer Science Part B: Polymer Physics* **40**, 2780 (2002).
- 177 Patel, S. K., Malone, S., Cohen, C., Gillmot, J. R. & Colby, R. H. Elastic Modulus and Equilibrium Swelling of Poly(dimethylsiloxane) Networks. *Macromolecules* **25**, 5241 (1992).

- 178 Vega, D. A., Villar, M. A., Alessandrini, J. L. & Valles, E. M. Terminal Relaxation of Model Poly(dimethylsiloxane) Networks with Pendant Chains. *Macromolecules* **34**, 4591 (2001).
- 179 Urayama, K. Network Topology–Mechanical Properties Relationships of Model Elastomers. *Polymer Journal* **40**, 669 (2008).
- 180 Ferry, J. D. (John Wiley & Sons, New York, 1980).
- 181 Mrozek, R. A., Cole, P. J., Cole, S. M., Schroeder, J. L., Schneider, D. A., Hedden, R. C. & Lenhart, J. L. Design of nonaqueous polymer gels with broad temperature performance: Impact of solvent quality and processing conditions. *Journal of Materials Research* **25** (2010).
- 182 Obukhov, S. P., Rubinstein, M. & Colby, R. H. Network modulus and superelasticity *Macromolecules* **27**, 3191 (1994).
- 183 Vicente, J. D. *Rheology*. (InTech, 2012).
- 184 Gent, A. N., Liu, G. L. & Mazurek, M. J. Experimental study of molecular entanglement in polymer networks. *Journal of Polymer Science Part B: Polymer Physics* **32**, 271 (1994).
- 185 Doi, M. & Edwards, S. F. *The theory of Polymer dynamics*. (Clarendon Press, 1986).
- 186 Pearson, D. S. & Helfand, E. Viscoelastic properties of star-shaped polymers. *Macromolecules* **17**, 888 (1984).
- 187 Curro, J. G. & Pincus, P. A theoretical basis for viscoelastic relaxation of elastomers in the long-time limit. *Macromolecules* **16**, 559 (1983).
- 188 Gennes, P.-G. *Scaling concepts in polymer physics.*, (Cornell University Press, 1979).
- 189 Urayama, K., Yokoyama, K. & Kohjiya, S. Viscoelastic Relaxation of Guest Linear Poly(dimethylsiloxane) in End-Linked Poly(dimethylsiloxane) Networks. *Macromolecules* **34**, 4513 (2001).
- 190 Sivasailan, K. & Cohen, C. Monte Carlo simulations of free chains in end-linked polymer networks. *ournal of Rheology* **44**, 897 (2000).
- 191 Kalcioğlu, Z. I., Mahmoodian, R., Hu, Y., Suo, Z. & Van Vliet, K. J. From macro- to microscale poroelastic characterization of polymeric hydrogels via indentation *Soft Matter* **8**, 3393 (2012).
- 192 Galli, M. & Oyen, M. L. Spherical indentation of a finite poroelastic coating. *Applied Physics Letters* **93**, 031911 (2008).
- 193 Galli, M. & Oyen, M. L. Fast identification of poroelastic parameters from indentation tests. *CMES* **48**, 241 (2009).
- 194 Oyen, M. L. *Handbook of nanoindentation with biological applications*. (Pan Stanford, 2011).
- 195 Scherer, G. W. Drying Gels: VIII. Revision and Review. *Journal of Non-Crystalline Solids* **109**, 171 (1989).
- 196 Scherer, G. W. Measurement of Permeability: I. Theory. *Journal of Non-Crystalline Solids* **113**, 107 (1989).
- 197 C-Y. Hui, Y. Y. Lin, F-C. Chuang, K. R. Schull & W-C. Lin. A contact mechanics method for characterizing the elastic properties and permeability of gels. *J. Polym. Sci., Part B: Polym. Phys.* **44**, 359 (2006).
- 198 Scherer, G. W. Bending of gel beams: method of characterizing mechanical properties and permeability. *Journal of Non-Crystalline Solids* **142**, 18 (1992).
- 199 Lin, Y.-Y. & Hu, B.-W. Load relaxation of a flat rigid circular indenter on a gel half space. *Journal of Non-Crystalline Solids* **352**, 4034 (2006).
- 200 Sneddon, I. N. The relation between load and penetration in the axisymmetric Boussinesq problem for a punch of arbitrary profile. *Internat. J. Engrg. Sci* **3**, 47 (1965).
- 201 Hecht, A. M. & Geissler, E. Pressure-induced deswelling of gels. *Polymer* **21**, 1358 (1980).
- 202 Geissler, E. & Hecht, A. M. The Poisson ratio in polymer gels. 2. *Macromolecules* **14**, 185 (1981).

- 203 Hecht, A. M., Geissler, E. & Chosson, A. Dynamic light scattering by gels under hydrostatic
pressure. *Polymer* **22**, 877 (1981).
- 204 Pavesi, L. & Rigamonti, A. Diffusion constants in polyacrylamide gels. *Physical Review E* **51**,
3318 (1995).
- 205 Weiss, N. & Silberberg, A. Inhomogeneity of polyacrylamide gel structure from permeability
and viscoelasticity. *British Polymer Journal* **9**, 144 (1977).
- 206 Engler, A., Bacakova, L., Newman, C., Hategan, A., Griffin, M. & Discher, D. Substrate
compliance versus ligand density in cell on gel responses. *Biophysical Journal* **86**, 617
(2004).
- 207 Grattoni, C. A., Al-Sharji, H. H., Yang, C., Muggeridge, A. H. & Zimmerman, R. W. Rheology and
Permeability of Crosslinked Polyacrylamide Gel. *Journal of Colloid and Interface Science* **240**,
601 (2001).
- 208 Tsaturyan, A. K. Extracellular fluid filtration as the reason for the viscoelastic behaviour of
the passive myocardium. *Journal of Biomechanics* **17**, 749 (1984).
- 209 Yang, M. & Taber, L. A. The possible role of poroelasticity in the apparent viscoelastic
behavior of passive cardiac muscle. *Journal of Biomechanics* **24**, 587 (1991).
- 210 Smoluk, L. T. & Protsenko, Y. L. Mechanical Properties of Passive Myocardium: Experiment
and Mathematical Model. *Biophysics* **55**, 769 (2010).
- 211 Dokos, S., Smaill, B. H., Young, A. A. & LeGrice, I. J. Shear properties of passive ventricular
myocardium. *American Journal of Physiology - Heart and Circulatory Physiology* **283**, H2650
(2002).
- 212 Lee, J. M. & Boughner, D. R. Mechanical properties of human pericardium. Differences in
viscoelastic response when compared with canine pericardium. *Circulation Research* **57**,
475 (1985).
- 213 Huyghe, J. M., Campen, D. H. V., Arts, T. & Heethaar, R. M. The Constitutive Behaviour of
Passive Heart Muscle Tissue: A quasilinear viscoelastic formulation. *Journal of
Biomechanics* **24**, 841 (1991).
- 214 Tamura, A., Omori, K., Miki, K., Lee, J. B., Yang, K. H. & King, A. I. *Stapp Car Crash Journal* **46**,
55 (2002).
- 215 Miller, K. Constitutive Modeling of Abdominal Organs. *Journal of Biomechanics* **33**, 367
(2000).
- 216 Kerdok, A. E. *Characterizing the nonlinear mechanical response of liver to surgical
manipulation* Ph.D. thesis, Harvard University, (2006).
- 217 Kerdok, A. E., Ottensmeyer, M. P. & Howe, R. D. Effects of perfusion on the viscoelastic
characteristics of liver. *Journal of Biomechanics* **39**, 2221 (2006).
- 218 Mak, A. F., Lai, W. M. & Mow, V. C. Biphasic indentation of articular cartilage—I. Theoretical
analysis. *Journal of Biomechanics* **20**, 703 (1987).
- 219 Gupta, S., Lin, J., Ashby, P. & Pruitt, L. A fiber reinforced poroelastic model of
nanoindentation of porcine costal cartilage: a combined experimental and finite element
approach. *Journal of Mechanical Behavior of Biomedical Materials* **2**, 326 (2009).
- 220 Miller, G. J. & Morgan, E. F. Use of microindentation to characterize the mechanical
properties of articular cartilage: comparison of biphasic material properties across length
scales. *Osteoarthritis Cartilage* **18**, 1051 (2010).
- 221 Yang, M., Taber, L. A. & Clark, E. B. A Nonlinear Poroelastic Model for the Trabecular
Embryonic Heart. *Journal of Biomechanical Engineering* **116**, 213 (1994).
- 222 Ng, E. Y. K., Ghista, D. N. & Jegathese, R. C. Perfusion studies of steady flow in
poroelastic myocardium tissue. *Computer Methods in Biomechanics and Biomedical
Engineering* **8**, 349 (2005).

- 223 Chapelle, D., Gerbeau, J.-F., Sainte-Marie, J. & Vignon-Clementel, I. E. A poroelastic model
valid in large strains with applications to perfusion in cardiac modeling. *Computational
Mechanics* **46**, 91 (2012).
- 224 Raghunathan, S., Evans, D. & Sparks, J. L. Poroviscoelastic Modeling of Liver Biomechanical
Response in Unconfined Compression. *Annals of Biomedical Engineering* **38**, 1789 (2010).
- 225 Jordana, P., Socrate, S., Zicklera, T. E. & Howea, R. D. Constitutive modeling of porcine liver in
indentation using 3D ultrasound imaging. *Journal of the mechanical behavior of biomedical
materials* **2**, 192 (2009).
- 226 Kvalseth, T. O. Cautionary Note About R2. *The American Statistician* **9**, 279.
- 227 Sacks, M. S. & Chuong, C. J. Biaxial mechanical properties of passive right ventricular free
wall myocardium. *Journal of Biomechanical Engineering* **115**, 202 (1993).
- 228 Garrido, L., Wedeen, V. J., Kwong, K. K., Spencer, U. M. & Kantor, H. L. Anisotropy of water
diffusion in the myocardium of the rat. *Circulation Research* **74**, 789 (1994).
- 229 Zocchi, L., Raffaini, A., Agostoni, E. & Cremaschi, D. Diffusional permeability of rabbit
mesothelium. *Journal of Applied Physiology* **85**, 471 (1998).
- 230 Swartz, M. A. & Fleury, M. E. Interstitial Flow and Its Effects in Soft Tissues. *Annual Review of
Biomedical Engineering* **9**, 229 (2007).
- 231 Mansour, J. M. & Mow, V. C. The Permeability of Articular Cartilage under Compressive
Strain and at High Pressures. *The Journal of Bone and Joint Surgery* **58-A**, 509 (1976).
- 232 Lakes, R. S. Deformation mechanisms of negative Poisson's ratio material: Structural
aspects. *Journal of Materials Science* **26**, 2287 (1991).
- 233 Hollenstein, M., A Nava, D. V., Snedeker, J. & Mazza, E. Mechanical Characterization of the
Liver Capsule and Parenchyma. *Lecture Notes Computational Science* **4072**, 150 (2006).
- 234 Cross, S. E., Jin, Y.-S., Rao, J. & Gimzewski, J. K. Nanomechanical analysis of cells from cancer
patients. *Nature Nanotechnology* **2**, 780 (2007).
- 235 Gu, W. Y., Mao, X. G., Foster, R. J., Weidenbaum, M., Mow, V. C. & Rawlins, B. A. The
anisotropic hydraulic permeability of human lumbar anulus fibrosus. Influence of age,
degeneration, direction, and water content. *Spine* **24**, 2449 (1999).
- 236 Cheng, S. & Bilston, L. E. Unconfined compression of white matter. *Journal of Biomechanics*
40, 117 (2007).
- 237 Chadwick, R. S. Axisymmetric Indentation of a Thin Incompressible Elastic Layer. *SIAM
Journal on Applied Mathematics* **62**, 1520 (2002).
- 238 A. Wang, L. Jiang, G. Mao & Liu, Y. Direct Force Measurement of Silicone- and Hydrocarbon-
Based ABATriblock Surfactants in Alcoholic Media by Atomic Force Microscopy. . *Journal of
Colloid and Interface Science* **256**, 331 (2002).
- 239 Wu, Z. & Hjort, K. Surface modification of PDMS by gradient-induced migration of embedded
Pluronic. *Lab on a Chip* **9**, 1500 (2009).

Appendix A

Determination of Elastic Modulus of a Thin Layer Using Nanoindentation

For accurate characterization of the mechanical properties of thin samples via atomic force microscopy enabled indentation, Dimitriadis et al.¹⁰⁶ and Chadwick²³⁷ have derived corrections to the Hertz model for finite sample thickness. They reported that for nonbonded samples, when $h < 0.1R$:

$$F_m(t) = \left(\frac{2\pi}{3h}\right) ER\delta(t)^2 \quad (\text{A.1})$$

where h is defined as sample thickness, F_m is the force calculated from the model, E is the elastic modulus, R is the radius of the probe, and δ is the indentation depth during the loading period. For the PB/LPEI nanocomposites characterized in Chapter 2, given that $R=5 \mu\text{m}$, and $h=224 \text{ nm}$, we adopted Equation A.1 to calculate film elastic modulus from nanoindentation experiments. For each force displacement response, the sum of error SoE was calculated as:

$$SoE = \sum_{i=1}^n (F_{m,i} - F_{exp,i})^2 \quad (\text{A.2})$$

where $F_{exp,i}$ is the measured force at each time point, i during the loading period. Finally, utilizing Microsoft excel solver that uses iterative numerical methods, E was calculated by minimizing SoE for a given force displacement response. Figure A.1 shows a representative force vs. displacement response from the loading period of an experiment, and the fit using Equation A.1.

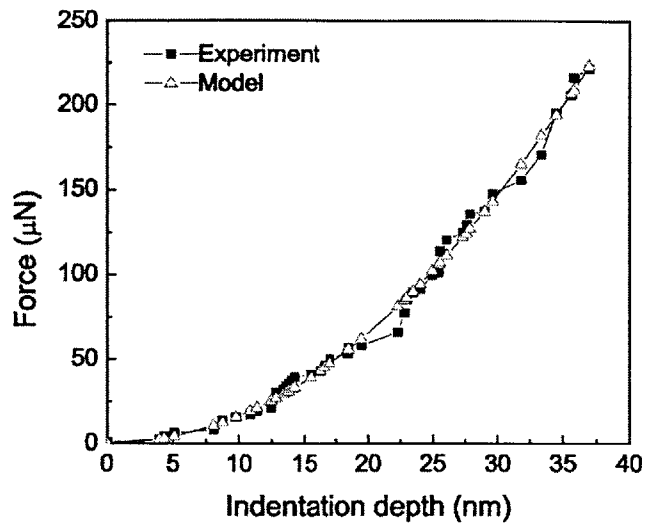


Figure A.1 Comparison between the experimental data and the model fit shows excellent agreement.

Appendix B

Effect of Pluronic® F108 on Adhesive Forces

This appendix aims to extend the study on Section 3.2.4 to test whether pluronic® F108 is effective for minimizing adhesive forces on material systems other than styrenic copolymer systems. The two material systems presented here are (1) synthetic Polydimethylsiloxane (PDMS) gels, and (2) biological tissues from rat heart.

B.1 Polydimethylsiloxane (PDMS) gels

B.1.1 Experimental methods

Polydimethylsiloxane (PDMS) elastomer samples were prepared by mixing a siloxane base with a cross-linking agent (Sylgard Elastomer 184, Dow Corning Corporation) at a ratio of 10:1. The solution was stirred for 10 min at room temperature and poured into a rectangular mold, degassed in vacuum for 1 h, and then cured at 65°C for 24 h. Microscale AFM-enabled indentation and load relaxation experiments (3D-MFP, Asylum Research) were performed via modified plateau probes (PL2-FM, Nanosensors), which have nominal spring constants of ~1-5 N/m. PL2-FM probes have geometries similar to a “flat punch” with a plateau diameter of 1.8 $\mu\text{m} \pm 0.5 \mu\text{m}$. Experiments were conducted in air, in phosphate buffered saline (PBS), and in PBS+ 3 vol-% Pluronic F108 solution. Elastic modulus E was calculated from quasistatic indentation experiments (maximum forces F_{max} of 50 nN-400 nN, displacement rate of the piezo = 6 μs , $n=10$ repeats per immersion environment) by fitting the loading part of the load vs. time response, using the solution for indentation of a rigid flat punch indenter into a homogeneous, linear elastic and isotropic material assuming a Poisson’s ratio ν of 0.5:

$$h = P(1 - \nu^2)/(2hR) \quad (\text{B.1})$$

For the load relaxation experiments, maximum indentation depths h_{max} were held at 200 nm for 5 s with a loading time of 0.1 s ($n=15$ repeats per immersion environment). To calculate the relaxation time scales τ , normalized force vs. time responses were described using a stretched exponential of the KWW type¹⁵⁶:

$$x(t) = x_{\infty} + x_0 e^{-(t/\tau)^{\beta}} \quad (\text{B.2})$$

where β describes the distribution of relaxation times with values between zero and unity.

B.1.2 Results and Discussion

In general, pluronic surfactants are known to adsorb on a hydrophobic surface with the hydrophilic PEO block extending into the solution and the more hydrophobic PPO block anchoring as loops and trains²³⁸. Previous studies have shown that the hydrophobic surface of PDMS can be made hydrophilic via modifying the surface with pluronic surfactants²³⁹. Here, we adapt this method, and observe that the immersion of PDMS samples in PBS containing 3%Pluronic® F108 results in minimization of the adhesive forces (Figure B.1). For the load relaxation experiments on PDMS gels tested in air, there was too much electrostatic interaction between the probe and the material that no reliable data could be collected, therefore only the results from tests conducted in PBS and in PBS+3% Pluronic® F108 are reported.

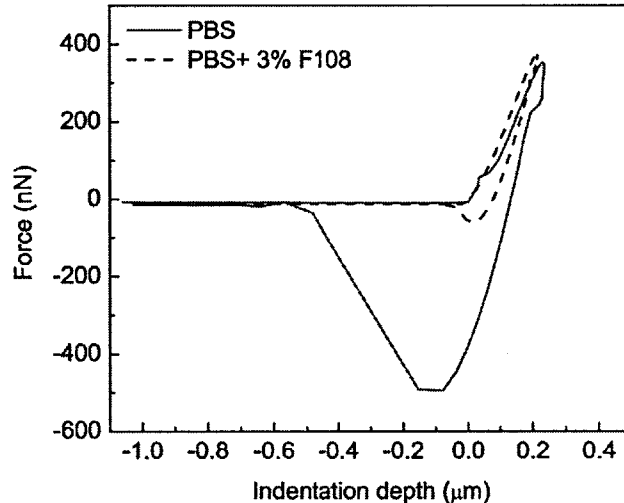


Figure B.1 Representative load vs. displacement response from load relaxation experiments on PDMS gels immersed in PBS and PBS containing 3% Pluronic® F108 shows that adhesive forces between the probe and the sample surface are minimized when the gels are immersed in the solution containing pluronic.

To investigate the effect of immersion environment on the surface mechanical properties of the gel, quasistatic indentation experiments were conducted via AFM. Young's moduli E were calculated from the load vs. indentation depth responses via Equation B.1. The results showed that E did not change significantly as a function of environment (Table B.1). Thus, we concluded that this surfactant reduced adhesion without changing the surface mechanical properties.

Table B.1 Young's Elastic Modulus of PDMS as a function of the immersion environment. Data are represented as mean \pm standard deviation.

Sample	E_{Air} (kPa)	E_{PBS} (kPa)	$E_{\text{PBS+3%F108}}$ (kPa)
PDMS	1024.15 ± 14.75	930.41 ± 21.72	993.79 ± 3.61

Even though immersing the PDMS gel in PBS+3% Plurionic® F108 did not affect the surface mechanical properties, removal of the adhesive forces affected the relaxation responses. Qualitative comparison between the normalized force $F(t)/F(0)$ vs. time responses in different immersion environments showed that the gel relaxed more in the presence of adhesive forces between the probe and the sample surface (in PBS, Figure B.2a). However, relaxation times τ calculated by Equation B.2 were not affected by the removal of adhesion (Figure B.2b).

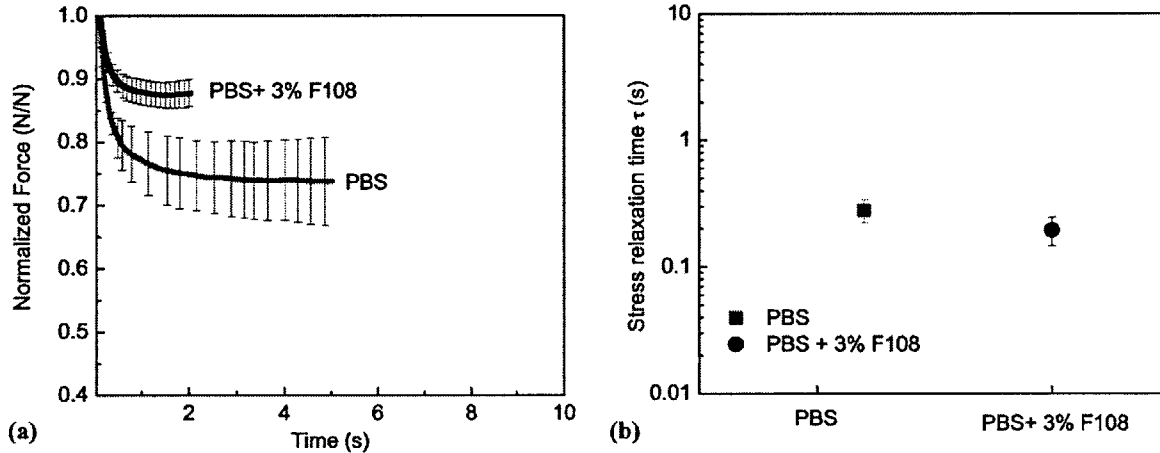


Figure B.2 (a) Normalized force vs. time responses, and (b) calculated relaxation time τ values at different immersion environments. Data are represented as mean \pm standard deviation.

In conclusion, we extended the study conducted on styrenic triblocks in Section 3.2.4 by immersing the PDMS gels in a solution that contains Pluronic® F108. Similar to what is reported in Section 3.2.4, here we were able to minimize the adhesive forces between the probe surface and the PDMS gel surface. Immersing the sample in solution and thus minimizing the adhesive forces did not affect the surface mechanical properties, and the calculated relaxation times, but affected the relaxation response, and must be taken into account for accurate characterization. This methodology could be further utilized for minimization of adhesive forces in other

experimental techniques such as impact indentation experiments on PDMS gels reported in Chapter 4.

B.2 Tissues from rat heart

In order to study whether immersing the tissue in a solution that includes surfactant would minimize the adhesive forces between the probe and the tissue surface, tissue sample from rat heart was first immersed in Krebs-Henseleit buffer. The resulting load vs. displacement responses from stress relaxation tests indicated the presence of adhesive forces between the spherical probe ($R= 22.5 \mu\text{m}$) and the sample surface, although these forces were much smaller compared to the maximum forces attained (Figure B.3a). Next, the same tissue sample was tested immersed in Krebs-Henseleit +0.5 Pluronic® F108 buffer. Even though addition of Pluronic® F108 was shown to minimize adhesion between the probe surface and the sample surface for both the triblock/diblock gels and the PDMS gels, immersing the heart tissue in a solution that included this surfactant did not minimize the adhesion between the probe and the tissue surface significantly (Figure B.3a). Increasing the concentration of the surfactant in the solution from 0.5% to 3%, or substituting Pluronic® F018 with Triton X or bovine serum did not affect the magnitude of the adhesive forces (data not shown). No correlation was found between the magnitude of the adhesive forces and the amount of time that passed after the start of the experiment, suggesting that the degradation of the tissue did not affect the measured adhesive forces (Figure B.3b).

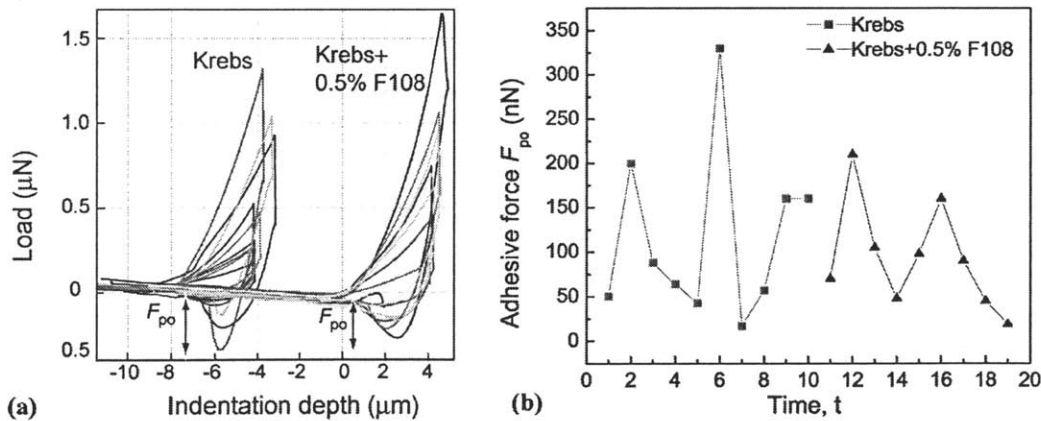


Figure B.3 (a) Load vs. displacement response of heart tissue in direction A; immersed in Krebs-Henseleit buffer vs. Krebs-Henseleit buffer+ 0.5 Pluronic®F108. (b) Adhesion force F_{po} as a function of time in the presence and lack of Pluronic®F108. Note that the values in the time axis

are arbitrary, i.e. they do not represent the real time intervals, and the total time of the experiment is 3 hours (i.e. at $t=20$, real time is 3 h).

Appendix C

Designing Experiments to Extract Poroelastic Relaxation Times

This section aims to explain in detail the design of experiments for accurate characterization of poroelastic relaxation times from atomic force microscopy enabled stress relaxation experiments, in order to guide the reader for future experiments on other material systems. Based on the discussion in Section 5.2.4, rise times t_R (s) must be at least an order of magnitude smaller than the poroelastic relaxation times τ (s), in order to capture the relaxation of the gel:

$$\tau \geq 10t_R \quad (\text{C.1})$$

Rise time t_R is calculated from $t_R = h_{\max}/v_{\max}$ where h_{\max} is the maximum displacement of the probe and v_{\max} is the displacement rate. Relaxation times are calculated from $\tau \sim a^2/D$ where contact radius a is defined as $a \sim (Rh)^{1/2}$, and D is the diffusivity. Plugging these into equation C.1 leads to:

$$\frac{Rh_{\max}}{D} \geq 10 \frac{h_{\max}}{v_{\max}} \quad (\text{C.2})$$

Rearranging equation C.2 results in:

$$\frac{Rv_{\max}}{D} \geq 10 \quad (\text{C.3})$$

Given an estimate of D from literature, and the maximum v_{\max} available for a given instrument, Equation C.3 will give estimation for a lower boundary value for R of the probe that should be chosen. For the PAAm hydrogels characterized in Section 5.2.4, assuming $v_{\max} = 100 \mu\text{m/s}$ and $D=10^{-10} \text{ m}^2/\text{s}$ requires $R \geq 10 \mu\text{m}$.

Next, let's assume that in order to conduct these experiments on materials that can degrade over time, relaxation times should be less than 30 s, but longer than some amount of time “ x ” to ensure that poroelastic relaxation is the dominant mechanism. The value of x must be chosen to be at least an order of magnitude larger than t_R and the value of the reported viscoelastic relaxation times. This assumption leads to:

$$x \leq \frac{R h_{max}}{D} \leq 30 \quad (C.4)$$

Obviously, h_{max} can never be larger than R , and if h_{max} is chosen to be equal to R , the strain s for a spherical probe calculated from $s=a/R$ will be 100%. In order to be in the linear viscoelastic regime, if we assume that the strain must be smaller than a certain value s_{max} then:

$$\sqrt{R h_{max}/R} \leq s_{max} \quad (C.5)$$

Thus, $h_{max} \leq R s_{max}^2$. We can also define a minimum strain value s_{min} we would like to achieve; $h_{max} \geq R s_{min}^2$. Plugging these relations into Equation C.4 results in:

$$\frac{x D}{s_{min}^2} \leq R^2 \leq \frac{30 D}{s_{max}^2} \quad (C.6)$$

For example, for the PAAm hydrogels, given that $x=1$ s $s_{max}=0.6$, $s_{min}=0.4$ and $D=10^{-10}$ m²/s requires $25 \mu\text{m} \leq R \leq 90 \mu\text{m}$.

In addition to the probe radius, another parameter that needs to be considered and affects the maximum attainable displacement value h_{max} , and hence the relaxation times is the spring constant k of the probe. Using the solution for indentation of a spherical indenter into a homogeneous, linear elastic and isotropic material, we can calculate the displacement attained in an experiment from the forces applied according to³²:

$$h_{max} = \left(\frac{3F(1-\nu^2)}{4ER^{1/2}} \right)^{2/3} \quad (C.7)$$

where F is the applied force, ν is the Poisson's ratio of the material, R is the radius of the probe and E is the elastic modulus of the material. For AFM enabled experiments, F is calculated as $F=k\delta$ where δ is the measured deflection (m) and k is the spring constant of the cantilever (N/m). Note that the maximum values attainable for δ depends both on the range of the piezo (in volts), and the calibration factor (m/volts). Plugging equation C.7 into C.4 leads to:

$$x \leq R^{2/3} \left(\frac{3k\delta(1-\nu^2)}{4ED^{3/2}} \right)^{2/3} \leq 30 \quad (C.8)$$

Equation C.8 suggests that given an initial guess for E , D and ν choosing a cantilever that has a small spring constant might require the radius of the probe R to be chosen larger in order to satisfy the limitations. If the characterized material is very compliant ($\sim <10$ kPa) and k is chosen to be too large, the cantilever will be too stiff such that it will penetrate through the sample and

not bend (i.e., not deflect) when in contact with the sample. To avoid that, a larger probe radius could be chosen.